Friction and diffusion dynamics of adsorbates at surfaces

een wetenschappelijke proeve op het gebied van
de Natuurwetenschappen, Wiskunde en Informatica

Proefschrift

ter verkrijging van de graad van doctor
aan de Radboud Universiteit Nijmegen
op gezag van de Rector Magnificus Prof. Dr. C. W. P. M. Blom,
volgens besluit van het College van Decanen
in het openbaar te verdedigen op dinsdag 5 juli 2005
des namiddags om 1.30 uur precies
door

Claudio Fusco

geboren op 11 juni 1976
te Rome (Italië)

Promotores:
Prof. Dr. A. Fasolino
Prof. Dr. T. W. J. M. Janssen

Manuscriptcommissie:
Prof. Dr. M. I. Katsnelson
Prof. Dr. S. E. Speller
Prof. Dr. D. E. Wolf (Universität Duisburg-Essen)

ISBN

The work described in this thesis was carried out as a part of a research program of the 'Stichting voor Fundamenteel Onderzoek der Materie' (FOM), with financial support from the 'Nederlandse Organisatie voor Wetenschappelijk Onderzoek' (NWO), under project 015.000.031.

The aim of science is not to open the door to infinite wisdom, but to set a limit to infinite error

Bertolt Brecht

Contents

Chapter 1

Introduction

In this introductory chapter we give a flavour of the topics investigated in this work, underlining the motivations, the problematics, and presenting an overview of the experimental techniques and computational methods used to probe atomic-scale processes at surfaces.

1.1 Pushing, pulling and sliding: a nonequilibrium and nonlinear world

Suppose we were able to discern individual atoms on a surface and to follow their movement. Then, the surface would not appear as a lifeless frozen landscape, but as a playground filled with fidgety children, who vivaciously run around, spontaneously jump up and down, come close or far to each other, form groups or remain apart. From this picture, the surface becomes an animated arena, where various events take place: atoms can migrate from one position to another, spending some time in a stable location, and, like those restless children, they can interact with each other or break apart. A deep understanding of such a diverse world poses of course big challenges. In this work, we will consider two important phenomena occurring at surfaces, namely *surface diffusion* and *atomic-scale friction*, studying them from a theoretical point of view.

The stimuli for surface diffusion studies are manifold: any surface physical or chemical process, which involves displacement of surface atoms or molecules, naturally depends on surface diffusion in an important way. An attempt to make a full list of all these processes is going to fail but, just to name the most significant, surface diffusion plays a vital role in crystal growth [1], including epitaxial growth of thin films widely used in microelectronics, heterogeneous catalysis [2], without which the modern chemical industry could hardly be imagined, and tribology, e.g. the science of friction, wear and lubrication [3]. As an example, we illustrate in Fig. 1.1 the occurrence of diffusion in epitaxial growth: during the growth, steps are formed on the surface and new atoms land on it, which can diffuse until they meet a step or another atom, thus forming a dimer and eventually a larger island. Therefore, the kinetics of the growth and the morphology of the film will be affected by the

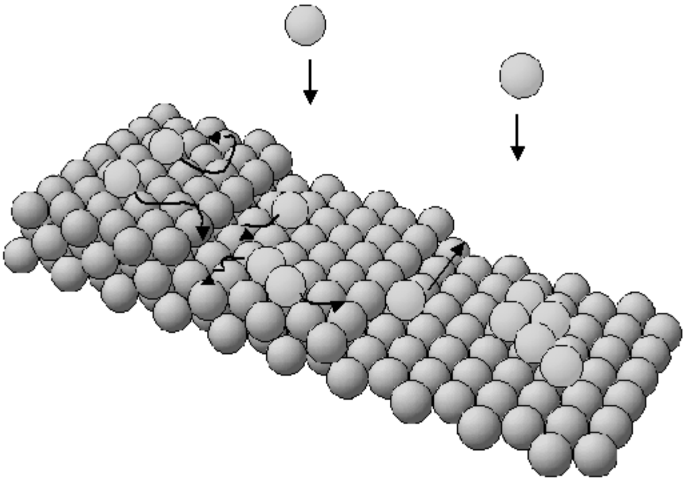

Figure 1.1: Sketch of the growth process on a surface: atoms land on the surface and an diffuse along the steps.

diffusion in the early stages of the process. The role of surface diffusion in influencing the performance characteristics and long-term stability of functional elements in electronics and other technologies grows rapidly with processing device miniaturization. For this reason, it is critical in such modern technologies as growth of nanostructures, fabrication of modern semiconductor lasers, magnetic multilayer recording heads based on giant magnetoresistance etc. Pushing, pulling and sliding of atoms and molecules is the new frontier of nanotechnology [4]. Firm knowledge of the basic mechanisms of single atom manipulation and of the *molecular mechanics* of such devices is fundamental for nanostructuring [5]. In fact, when we create nanostructures and nanodevices, the elemental building blocks are actually still individual atoms and molecules. We must therefore understand how they can be moved and move themselves, and how strongly they stick to each other and to the substrate. Thus, surface diffusion is an interdisciplinary problem of immense relevance. But, as soon as we try to approach these kind of processes, we immediately have to cope with many conceptual problems: we are dealing with phenomena characterized by a complex, nonequilibrium dynamical behaviour, governed by nonlinear interatomic interactions, giving rise to unexpected and unpredictable effects, such as anomalous diffusion, highly nonlinear response and chaos. In general, such nonlinearities in surface diffusion remain so far almost unexplored.

When an atomic or molecular adsorbate diffuses, or is pulled, on a surface it unavoidably experiences friction. During the sliding of a nanometer sized tip on a surface, the atoms in contact have to overcome an energy barrier similar to atoms diffusing on a crystal surface. Thus, these two apparently different phenomena are intimately related. New biomolecular mechanical nanodevices and tip-induced atom repositioning are some examples of the key role played today by friction forces at the atomic scale. It is therefore important to investigate the fundamental mechanisms responsible for friction and energy dissipation at the nanoscale [4, 6]. Frictional phenomena are familiar to everybody from the experiences of daily life. Friction is not always an unwanted phenomenon: it makes us hear the sound of a violin and it allows us to walk up a hill and to come back down, usually in a controlled way. Thus, it is not surprising that sliding friction is one of the oldest problems in physics and certainly one of the most relevant both from a fundamental and a practical point of view [3]. While the knowledge of friction between macroscopic objects is well established and the empirical laws governing it have been known for five centuries, the behaviour of atomic-scale friction calls for a deeper theoretical insight. Frictional forces oppose the mutual movement of two objects and are nonconservative, transforming part of the mechanical energy into heat. In most experimental conditions, for a given pair of macroscopic contacting surfaces, the friction force is just proportional to the load and is independent of the contact area, surface roughness and sliding velocity. The force needed to put a body in motion is higher than that needed to keep it in motion, namely static friction is higher than dynamic friction. How can we explain these phenomenological laws? Can we derive them from fundamental atomic or molecular principles? Do they have an atomic-scale counterpart? What is the origin of the static and kinetic friction forces? And how can we control friction? These are the most outstanding questions one has to face. Answering them is not easy, and we are still far from a complete understanding of such phenomena: this is why the field of tribology attracts much interest from the scientific community. To clarify where these complications come from, we first notice that surfaces can be smooth or rough, hard or soft, elastic or plastic, brittle or ductile, dry or lubricated, and of very different chemistries. When two macroscopic surfaces slide relatively to each other, they interact through many asperities, more species (e.g. lubricants) can be present at the interface and roughness manifests itself at the micrometer scale (see Fig. 1.2(a)). The single asperities, however, extend on a nanometer length scale: at this level, we can ideally have contact between clean, flat and well-defined materials, whose *dry friction* (i. e. friction without lubricants) can be studied (see Fig. 1.2(b)). Macroscopic friction is believed to be the sum of the frictional effects occurring at all these small individual asperities. Thus, it is inextricably linked to microscopic properties, and the starting point for any microscopic picture of friction is that of a single asperity sliding on a flat surface. The field of *nanotribology*, which is the study of the frictional properties of a single asperity moving on a surface, has thus flourished in the last years, also thanks to the de-

Figure 1.2: Simplified sketch of two sliding surfaces at the macroscale (a) and at the nanoscale (b).

velopment of experimental tools, such as the atomic force microscope (see Sec.1.3.4) [6, 7]. The nanoscale description is relevant to many technological nanodevices, where the high surface-to-volume ratio makes the old, simple empirical laws of friction inadequate; moreover, conventional tribological and lubrication techniques used for large objects can be ineffective at the nanometer scale, which requires new methods for control. At the conceptual and theoretical levels, the modelling of dissipation processes at the atomic scale is still in its first stages. Recent advances have revealed the enormous complexity of even the simplest tribological processes at the nanoscale. In this regime, dissipation of energy is dominated by interatomic interactions, surface registry, vibrational and excitation spectra: these are extreme conditions that cannot always be treated by linear theories.

1.1.1 Aim of this work

The aim of this work is to investigate some of the complex phenomena presented above by using simple theoretical models. Specifically, we point out the importance of the nonequilibrium adsorbate dynamics in surface diffusion of interacting particles, where nonlinear effects lead to an exchange of energy between translational and vibrational motion and where resonant mechanisms and chaotic behaviour can strongly affect the diffusive motion. We will study the validity of the phenomenological laws of friction at the nanoscale, finding that such nonlinear dynamics is responsible for nonlinear relation between friction and load, highly nonlinear velocity dependence and the possibility, in certain circumstances, of frictionless sliding.

1.2 Structure of this work

This work is organized as follows.

In the rest of this chapter, we give a brief survey of the experimental techniques used to probe atomic and molecular diffusion and nanoscale friction (Sec. 1.3), and we introduce simple models particularly useful to describe these phenomena (Sec. 1.4) and the methods employed for computer simulations (Sec. 1.5), with a specific emphasis on how to include thermal effects (Sec. 1.6).

In Chap. 2 we review the basic concepts of surface diffusion of an adatom in a periodic potential, both with and without an external driving force, presenting comparatively analytical and numerical approaches to this problem.

Chap. 3 is devoted to the problem of interacting particles moving on a periodic substrate: we present original results about the diffusive dynamics of a dimer, both at zero and finite temperatures, emphasizing the role of the internal motion on the diffusive dynamics and the occurrence of nonlinear effects, which result in chaotic behaviour and anomalous diffusion. The relation between chaos and diffusion is analysed and comparisons with experimental findings are suggested.

Chap. 4 deals with the problem of the velocity dependence of atomic-scale friction: in the framework of the Tomlinson model (see Sec. 1.4.2), we find an appreciable dependence of friction on velocity in the small velocity regime that is relevant to Atomic Force Microscopy (AFM) experiments (see Sec. 1.3.4). We quantify this dependence and show the role of thermal effects.

In Chap. 5 we introduce a more realistic $3D$ model to study nanoscale friction, which is applied to AFM on graphite. We discuss the load dependence of atomistic friction in this case, finding departures from the linear relation expected for macroscopic systems, and we analyse in detail the dynamics of the tip sliding of the surface: dynamical effects of the tip motion can have a strong influence on the frictional behaviour, and states of very low friction can be achieved due to the incommensurability between the tip and the substrate.

1.3 Experimental techniques: probing atomic motion and friction at surfaces

The earliest observations of surface mobility date back some 80 years ago from now [8, 9]. In particular, it was noted that the growth speed of small mercury crystallites from a supersaturated vapor proceeding along specific directions on a crystal substrate was much faster than the rate of condensation from the gas phase [9]. These findings led to the statement that '*adsorbates molecules can migrate on the surface by virtue of thermal motion*' [10]. More direct observations of surface diffusion were accomplished around 1930 by thermionic methods [11], which suggested the concept of '*hopping atoms*'. These ideas constitute the foundation for the interpretation of surface mobility observation in the following years.

In this section we will briefly review the working principles, advantages and limitations of the most commonly used scanning probe methods to measure adsorbate diffusion and friction on a surface.

1.3.1 Field Ion Microscopy (FIM)

This technique, invented by Müller in the early 1950s [12], allows to image surfaces with atomic resolution (~ 1 Å) and to monitor the movement of individual atoms adsorbed on the surface [13]. The FIM provides an image of the adsorbate atoms at the apex of a sharp needle, commonly referred to as a tip. Such an image is obtained by applying a high positive potential to the tip in the presence of a background gas, called the imaging gas. The high electric field ionizes the imaging gas atoms, and accelerates them to an image detector where image spots are formed. FIM was successfully applied to investigate the diffusion of single metal adatoms and clusters strongly bounded at metal surfaces [14, 15]. The main limitation of FIM is its narrow range of applicability, so far only to a selected number of noble and transition metals.

1.3.2 Scanning Tunneling Microscopy (STM)

The advent of STM has had a tremendous impact on surface science. STM allows in particular for structure determination and direct observation of atomistic processes on any conducting surface, which greatly enhances the spectrum of FIM. Binnig and Rohrer developed the first STM [16], for which they were awarded the Nobel Prize in 1986. The principle of the STM is based on the strong distance dependence of the quantum mechanical tunneling effect (see Fig. 1.3). A thin metal tip is brought in close proximity of the sample surface. A bias negative potential of few volts or less is applied between the tip and the surface. At a distance of only a few Å, due to the large overlap of tip and sample electron wavefunctions, the bias potential induces a tunneling current I_T, which is given by $I_T \sim \exp(-2kd)$, where d denotes the tip-surface distance and k is a constant depending on the height of the potential barrier. Typically, for metals k is of the order of 1 Å^{-1}. Hence, an increase of the tunneling distance of only 1 Å changes the tunneling current by about one order of magnitude. If the tip is scanned over the sample surface while an electronic feedback loop keeps the tunneling current constant (constant current mode), the tip height follows a contour of constant local density of states and provides information on the topography of the sample surface. The high, atomic-scale resolution of STM is due to the tunneling nature of the current. There are at least four different operation modes which can be used to study surface diffusion by STM:

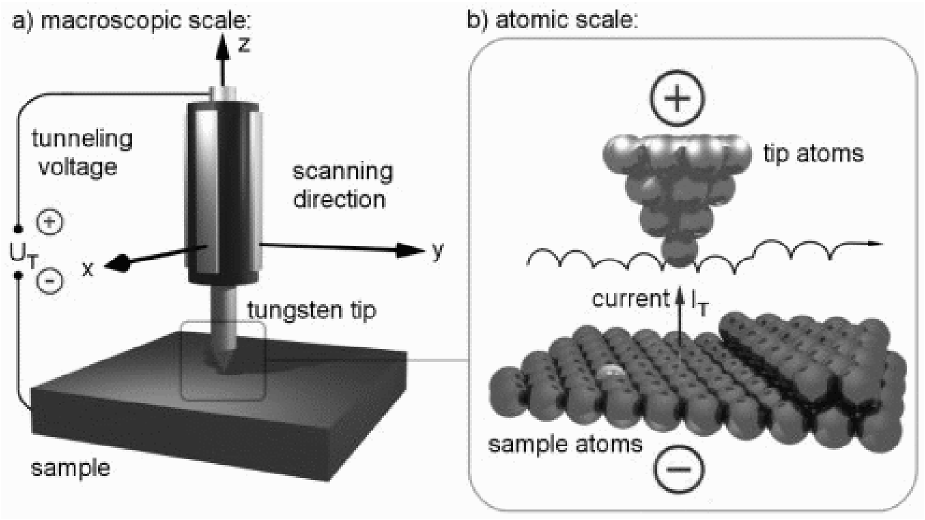

Figure 1.3: Working principle of STM: applying a negative sample voltage yields electron tunneling from occupied states at the surface into unoccupied states of the tip. [From Ref. [17]].

(a) monitoring the fluctuations in the tunneling current caused by highly mobile adsorbate atoms underneath the tip. Thus, adsorbate diffusion can be measured by recording the current fluctuations [18, 19];
(b) counting the density of islands formed by the diffusing atoms and deducing the diffusion from classical nucleation theory [20];
(c) direct imaging of the displacements of the diffusing species by thermal annealing, in analogy to the working principle of FIM [21];
(d) atom tracking, the most recent and appealing method, where the STM tip automatically follows the positions and the migration path of an individual moving adsorbate [22].

When fancy instruments have been developed, surface mobility can even be recorded at video rates and visualized by STM movies [23].
Each of these approaches has its merits and limitations, but collectively the power of STM in surface diffusion measurements is superior to that of FIM. The major advantages of STM are atomic resolution, its transparency and versatility, allowing to use the same tip to image a wide variety of systems, and the appeal for direct visualization. Limitations of STM are the possible effect of the tip-surface interactions in the measurements and the fact that only rather low diffusivity ranges are accessible.

1.3.3 Quasielastic Helium Atom Scattering (QHAS)

This technique provides a mirror image in reciprocal space to the real-space information of random motions in two dimensions obtained by microscopic measurements [24, 25]. QHAS is the surface analogous to quasielastic scattering of neutrons, which was extensively applied to bulk phenomena. Inelastic scattering techniques were already used in the 70s to study phonon dynamics at surfaces. However, the application of this technique to surface diffusion dates back only to about 15 years ago [24]. In a QHAS experiment, an atomic He beam with a sharp energy distribution is directed on a surface. In the presence of a mobile adsorbate layer, diffusively scattered He experiences energy exchanges with the adatoms, which lead to a slight broadening of the energy distribution of the reflected He beam. The width of the so-called quasielastic peak is thus related to the adatom diffusivity. It can be determined by time-of-flight measurements of the reflected He beam at different temperatures, allowing a systematic investigation of the mobility of the adsorbate. The striking feature of QHAS is that it provides additional information on the dynamics of the adsorbate, which is very important for the diffusivity, as we will illustrate in Chap. 3, and that non-diffusive processes are also reflected in the peak broadening. However, QHAS is only limited to high diffusivities.

1.3.4 Atomic Force Microscopy (AFM)

Since its introduction in 1986 [26], AFM has turned out to be a unique tool to detect frictional forces on the length scales of atomic dimensions. AFM is a powerful technique to measure friction between a sharp tip and a smooth sample surface with atomic-scale resolution. AFM studies have contributed significantly to the understanding of friction on the nanometer scale since 1987, when Mate et al. performed their pioneering work in detecting frictional forces on a graphite surface and correlating them with atomic-scale processes [27].

The working principle of AFM is rather simple and resembles that of a record player. A sketch of a typical experimental set-up is shown in Fig. 1.4. A tip, which is mounted on a soft leaf spring, the so-called cantilever, is brought in close proximity with a sample surface, in a fashion similar to STM tip-sample approach mechanisms, and it is laterally moved over it. Forces acting between the tip and the sample will result in deflections of the cantilever. When the tip is brought into contact with the surface, the cantilever experiences a normal bending, and when it is shifted with respect to the sample (or vice versa), it is

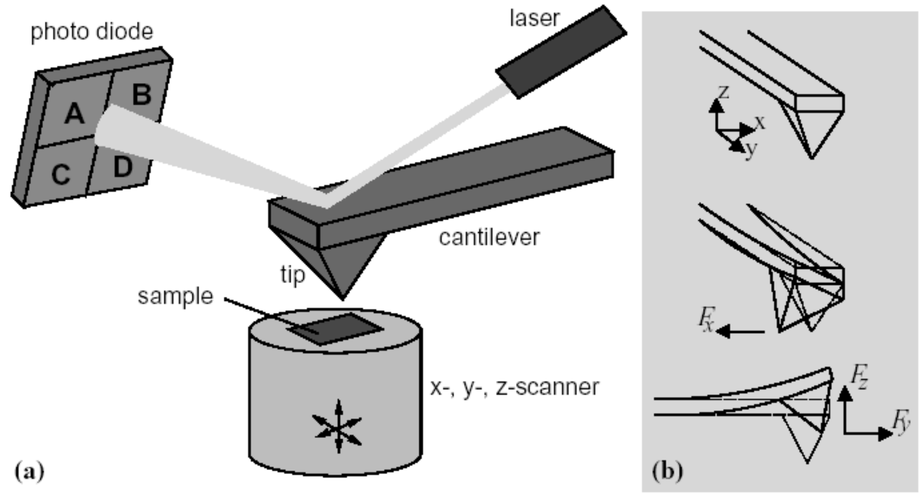

Figure 1.4: (a) A sketch of an atomic force microscope: bending and torsion of the cantilever are measured simultaneously by measuring the lateral and vertical deflection of a laser beam while the sample is scanned. (b) The torsion of the cantilever (middle) is solely due to lateral forces F_x acting in the x (scanning) direction, whereas both forces acting normal to the surface (F_z) as well as in plane in y direction (F_y) cause a bending of the cantilever (bottom). [From Ref. [28]].

also twisted laterally. The advantage of AFM is that it can measure both the normal and the lateral deflections of the cantilever, by using a laser beam which is reflected from the rear of the cantilever into a four-quadrant photodetector. The normal and lateral forces acting on the cantilever can be deduced from the normal and lateral signals acquired with the photodetector, provided that the spring constants of the cantilever and the sensitivity of the photodetector are known. When lateral and normal forces are measured at the same time, we have the so-called Friction Force Microscope (FFM). In such a sense, the FFM tip resembles an isolated asperity of a surface, where sub-nanonewton forces can be easily detected. Due to the small tip size, typically between 10 and 100 nm, FFM can be successfully used to map friction forces with extraordinary resolution. Cantilevers are usually made of silicon, silicon nitride, tungsten or diamond, and can be fabricated with a variety of force constants, ranging from 0.01 to 100 N/m. The calibration of cantilevers with different shape often requires analytical evaluation or finite element analysis [29]. As an alternative, an *in situ* calibration of lateral forces on samples with well-defined profiles is also possible [30]. The characterization of the shape of the tip is also important to have an idea of the geometry of the tip-surface contact. *In situ* determination of the tip shape [31] and *ex situ* tip imaging by transmission electron microscopy have been performed [32]. Typical scanning velocities in AFM are rather low, usually between 1 nm/s and 100 μm/s.

Depending on the details of the normal force experienced by the tip as it is brought towards the sample surface, the AFM can operate in two different force regimes:

(a) the *attractive regime*, where interaction forces (van der Waals, electrostatic etc.) attract the tip to the sample, but actual mechanical contact does not occur;
(b) the *contact (repulsive) regime*, where the outer electronic configuration of the tip and surface atoms provides electrostatic and Pauli repulsive forces.
To achieve the contact mode, usually an external load is applied to the cantilever. This mode is ideal for nanotribological applications, and makes it possible to measure the load dependence of friction at the nanoscale, which is a very important issue in nanotribology, since it can markedly differ from the macroscopic behaviour (we will discuss this point more thoroughly in Chap. 5). The disadvantage of this mode is that the tip can break or be damaged when it is moved over the sample. A typical measurement of the lateral force at the atomic scale, using a tungsten tip on graphite, is reported in Fig. 1.5. Two important features can be observed:
(i) saw -tooth pattern of the lateral force, which is called *stick-slip*;
(ii) hysteresis between forward and backward scan directions, giving rise to the so-called friction loop.
These features can be reproduced by simple atomistic models, as we will see in Sec. 1.4.2.

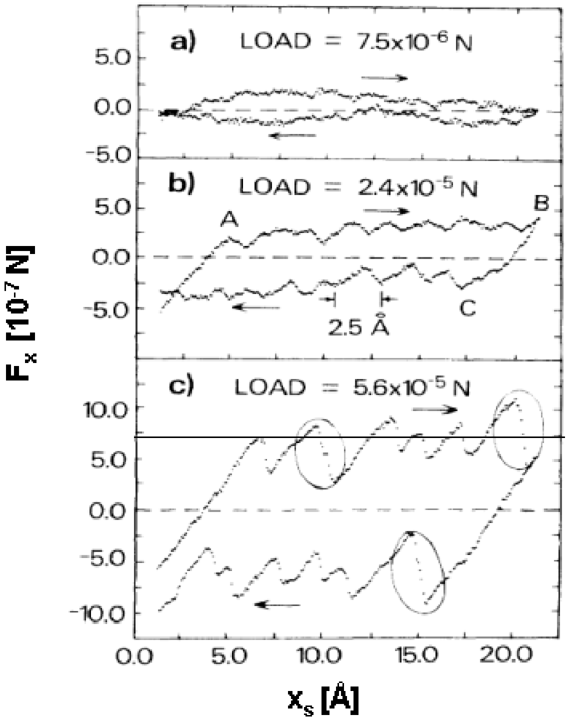

Figure 1.5: Lateral force F_x in the scanning direction as a function of the scanning position of the support x_s for three different values of the applied load. Notice the stick-slip behaviour and the hysteresis of F_x between forward and backward scanning. The dashed lines indicate $F_x = 0$, while the solid line in c) is the value of the friction force, calculated as the average of F_x. Friction increases for increasing load. [From Ref. [27]].

Notice that the friction force can be calculated as the average of the stick-slip force, which is proportional to the area of the friction loop (see Sec. 1.4.2). It is seen that the friction force, and thus the area of the hysteresis loop, increases when the load is increased. We will explain these effects in more detail in Sec. 1.4.2 and in Chap. 5.

In the attractive mode, AFM is a powerful topographic technique, i. e. it can be used to image surface with very high resolution. In this case, a feedback system, which controls the vertical z position of the tip, keeps the deflection of the cantilever, and thus the vertical force between tip and surface, constant. A very suggestive image of graphite obtained with this method is shown in Fig. 1.6. Other methods can be used to image in the attractive (non-contact) regime, such as the *force modulation* technique [34], which has been demonstrated to achieve true atomic resolution on surfaces. In this technique the cantilever oscillates above the surface with constant amplitude and frequency. The frequency shift is related to the tip-surface interaction and can provide an indirect measurement of it (see also Sec. 5.3.3 of Chap. 5).

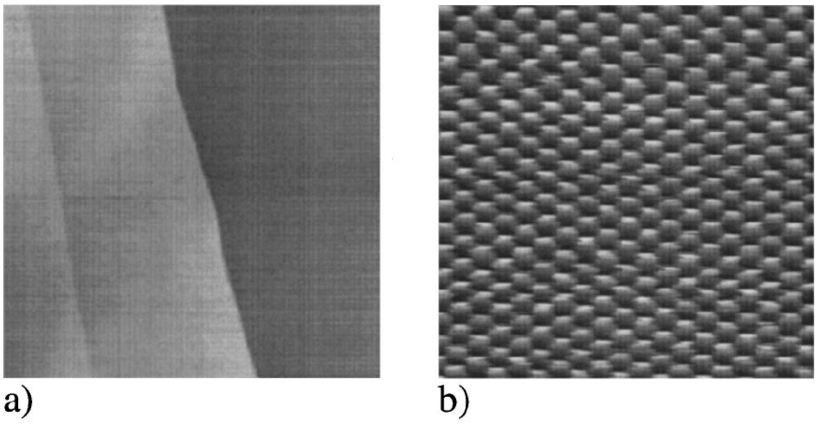

Figure 1.6: Images of a graphite surface by AFM at two different length scales: a) 3μm $\times$ 3μm, b) 5 nm $\times$ 5 nm. In a) the steps on the surfaces can be seen, while in b) the hexagonal lattice periodicity of graphite can be appreciated. [From Ref. [33]].

Finally, we would like to mention that AFM is also used for more exotic applications in biology, to image DNA [35] and biomolecules [36] and to study living cells [37].

1.4 Modelling surface diffusion and friction: a "minimalistic" approach

A large variety of theoretical approaches have been adopted to study processes at surfaces from a microscopic point of view. Of course, the key goal of these approaches is to explain the experimental findings and to predict new phenomena. From a general point of view, we essentially have two main ways to look at the problem: we can try to analyse atomic processes and structures in great detail and keeping a close quantitative relation to real systems and experiments, or we can go for “simple (minimalistic) models”, which are based on simplified interatomic interactions and focus only on the most relevant degrees of freedom of the system, trying to retain the most important features. Both methods have their strengths and weaknesses. Large-scale simulations allow to reproduce quite accurately some experimental features, but are not really well suited to extract general information at a fundamental level; minimalistic models have the advantage of being computationally cheap and simple enough to enable us to work out the general mechanisms of the problem, which are not system specific, and to provide a deeper physical understanding of the processes at play. In this respect, the latter approach is quite efficient and, as we will illustrate below, it can explain phenomena of high complexity. Moreover, these models allowed to make predictions which were later verified experimentally. Thus, in the present work we have opted for the microscopic minimalistic approach, which has been used to study surface diffusion of adatoms and dimers, and atomic-scale friction.

1.4.1 Freezing the surface atoms and overcoming the barrier

In considering the motion of a single adsorbed atom (in the following referred to as adatom or monomer) on a surface, it is natural to begin by assuming that the adatom sees a one-dimensional ($1D$) static corrugated potential, which effectively represents its interaction with a periodic arrangement of atoms forming the surface. A typical example of such a potential, which has been intensively studied during the last decades, is a sinusoidal function of the form

$$\boxed{U_{sub}(x) = U_0(1 - \cos(2\pi x/a)),} \tag{1.1}$$

whose period a is equal to the surface lattice parameter and whose amplitude $2U_0$ gives a measure of the strength of the interaction between the adatom and the surface, which is equivalent to the diffusion barrier. Although a $1D$ description seems to be rather simplified, $1D$ atomic motion has been observed in real systems: diffusion along surface steps or on channeled-metal surfaces has a quasi $1D$ character [38]. A sketch of the model is illustrated in Fig. 1.7.

We can think of three “energetic sources” which might enable the adatom to move over the potential barrier:
(a) initial kinetic energy $E_{kin}^{(0)} = \frac{1}{2}mv_0^2$ possessed by the particle (m is the mass of the particle and v_0 is its initial velocity);
(b) an external force field F (for example an electric field E acting on a particle of charge q, whereby $F = qE$);
(c) thermal fluctuations.
In the absence of energetic source (c) a threshold is required for sources (a) and (b) in order to initiate the motion of the adatom, namely $E_{kin}^{(0)} \geq 2U_0$ and $F \geq \frac{2\pi U_0}{a}$. In this situation the particle will have a preferential direction for its motion. If only source (c) is present the motion of the particle will be completely random and it will have the same probability to move in the forward or in the backward direction. This case is known as *Brownian motion*.

We can formalize the qualitative picture outlined above by writing an equation of

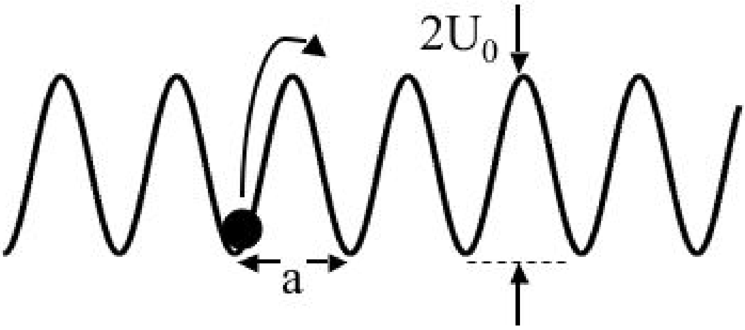

Figure 1.7: Sketch of the model of monomer diffusion on a periodic potential considered in Chap. 2.

motion for the adatom coordinate $x(t)$ in the periodic potential. Based on a merely deterministic description of the problem, this equation will have the form

$$m\ddot{x} = -\frac{2\pi U_0}{a} \sin\left(\frac{2\pi x}{a}\right) + F. \tag{1.2}$$

Eq. (1.2), however, takes into account neither thermal effects nor possible dissipative mechanisms to which the adatom can be subjected. Friction is usually incorporated in the equation of motion as a force opposing the movement of the particle, which is proportional to the particle velocity. Thus, in the presence of a frictional force, Eq. (1.2) becomes

$$m\ddot{x} = -\frac{2\pi U_0}{a} \sin\left(\frac{2\pi x}{a}\right) + F - m\eta\dot{x}. \tag{1.3}$$

The form of the friction force in Eq. (1.3) is purely phenomenological and the damping η is usually an unknown parameter, which has to be fitted to experimental or simulation data. However, it is possible to give an estimate of η from the energy exchange between the adatom and the substrate. A quite detailed analysis of this issue is given in the review book of Persson [39]. In particular, the energy exchange between the adatom and the substrate occurs via phononic and electronic excitations, and is due to the collisions between the adatom and the substrate atoms. Eq. (1.3) still lacks thermal effects. An effective way to deal with thermal fluctuations is presented in Sec. 1.6. A more extensive treatment of the adatom diffusion in a periodic potential will be reported in Chap. 2.

Eq. (1.3) is meant to describe the motion of a single atom on a periodic surface, or can be used in situations where the interaction between the particles forming the adsorbate is so weak that it can be neglected. Thus, how can we model interacting particles moving on a periodic surface? The simplest case is to consider a dimer, i. e. two coupled adatoms, which interact via a harmonic potential, as sketched in Fig. 1.8. Eq. (1.3) would then be

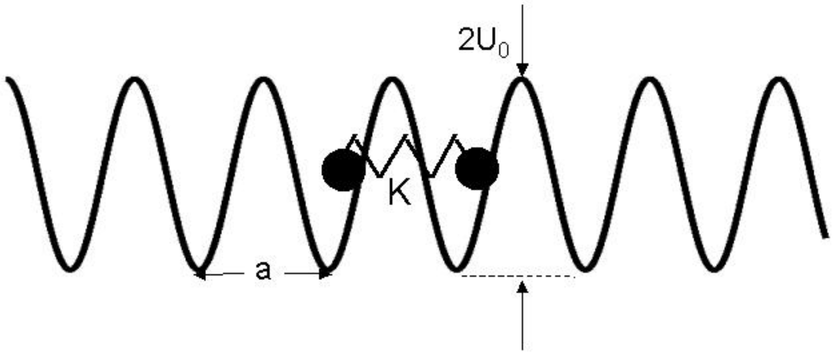

Figure 1.8: Sketch of the model of dimer diffusion on a periodic potential considered in Chap. 3.

replaced by two equations for the atoms coordinates x_1 and x_2 of the form

$$\begin{aligned} m\ddot{x}_1 &= K(x_2 - x_1 - l) - \frac{2\pi U_0}{a}\sin\left(\frac{2\pi x_1}{a}\right) + F - m\eta\dot{x}_1 \\ m\ddot{x}_2 &= K(x_1 - x_2 + l) - \frac{2\pi U_0}{a}\sin\left(\frac{2\pi x_2}{a}\right) + F - m\eta\dot{x}_2 \end{aligned} \tag{1.4}$$

The dimer model will be studied in detail in Chap. 3.

1.4.2 The Tomlinson model: to stick or to slip?

It is quite surprising that the main features of atomic-scale friction can be accounted for by a very simple and instructive mechanical model, which dates back to 1929, when it was introduced by Tomlinson [40]. This model can explain the occurrence of static and kinetic friction, the origin of the stick-slip behaviour observed in the experiments (see Fig. 1.6) and the transition to sliding states. It has been successfully used to describe the motion of a tip and to model the scan process in AFM [41, 42, 43, 44]. Here, we illustrate the properties of this model and its extraordinary versatility to capture the nonlinear nature of frictional dynamics.

We consider for simplicity the $1D$ Tomlinson model at $T = 0$. A cantilever tip of mass m interacts with the surface via a periodic potential V_{TS} and is attached by a spring of elastic constant K to a support (cantilever) moving at constant velocity v_s along the x direction (see the sketch in Fig. 1.9). For the $1D$ case we choose V_{TS} of the form

$$V_{TS}(x) = U_0[1 - \cos(2\pi x/a)], \tag{1.5}$$

where a is the lattice constant of the substrate. The elastic interaction between the tip and the support is

$$V_{el}(x) = \frac{1}{2}K(x - x_s)^2, \tag{1.6}$$

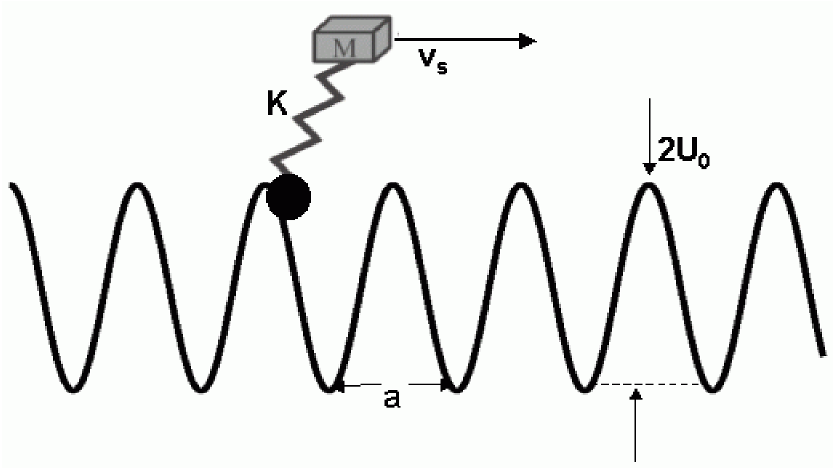

Figure 1.9: Sketch of the $1D$ Tomlinson model for atomistic friction.

where the support position x_s is

$$x_s = v_s t. \tag{1.7}$$

It is assumed that the tip is a point-like object, representing the average over many atoms of the real tip-surface contact. Energy dissipation in this model is introduced by adding a damping term proportional to the tip velocity in the equation of motion. Thus, the equation of motion in $1D$ becomes

$$\boxed{m\ddot{x} + m\eta\dot{x} = -\frac{2\pi U_0}{a}\sin\left(\frac{2\pi x}{a}\right) - K(x - v_s t).} \tag{1.8}$$

Also for the Tomlinson model, thermal fluctuations can be taken into account in the framework of the Langevin approach of Sec. 1.6. The solution of Eq. (1.8) is periodic, with period na/v_s [45]:

$$x(t + na/v_s) = x(t) + na \qquad \text{for integer } n. \tag{1.9}$$

Typically $n = 1$ for not too small η, while in the strongly underdamped regime the periodicity of the solution can be an integer multiple of the lattice constant. The damping η is often an unknown parameter in experiments and thus one has to adopt an *ad hoc* choice. Usually a critical damping, $\eta = 2\sqrt{K_x/m}$ [44], is assumed in order to reduce the oscillations of the tip and to avoid multiple jumps. The underdamped regime is, however, characterized by a very complex dynamical behaviour [45], as we will mention in Chap. 4.

The character of the motion in the Tomlinson model crucially depends on the interplay between the tip-substrate potential (1.5) and the elastic potential (1.6), or more specifically on the value of the cantilever stiffness K and of the surface corrugation U_0. For example, suppose we keep U_0 fixed and we change K. By varying the cantilever stiffness, two kinds of potential energy surfaces $V_{tot} = V_{TS} + V_{el}$ appear, as pictorially shown in Fig. 1.10. When the cantilever is stiff, i. e. K is large, the curvature of V_{el} is large and V_{tot} is

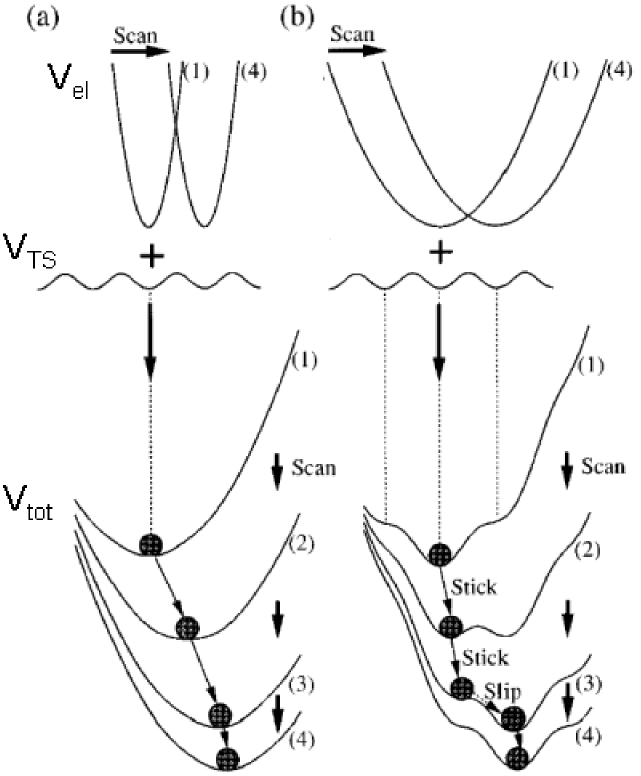

Figure 1.10: Sketch of the energy landscape in the Tomlinson model for a stiff cantilever (a) and a soft cantilever (b). In (a) the total potential V_{tot} has only one minimum and the tip slides continuously on the surface, while in (b) V_{tot} possesses many minima (metastable states), which give rise to the stick-slip behaviour. [From Ref. [46]].

nearly parabolic, with a single minimum (Fig. 1.10(a)). Therefore, the tip atom is always moving trapped in a minimum of the potential energy and shifts continuously during the scan: in this situation the tip performs a *sliding motion*. On the other hand, for the soft cantilever, i. e. for small K, the curvature of V_{el} is small and the potential energy surface has many minima, which correspond to many metastable states (Fig. 1.10(b)). In this case, the tip atom is trapped in one of these minima for a period of the scan, but it makes a sudden jump from one minimum to another deeper minimum, when the barrier between two minima disappears: this gives rise to the *stick-slip motion*. The stick time (i. e. the time spent around the minimum) is much larger than the slip time (i. e. the time needed to go from one minimum to the other). Thus, the characteristic ingredient, which makes the Tomlinson model so powerful in describing the AFM dynamics, is the coexistence of *trapped* and *sliding* states. More quantitatively, it can be shown that elastic instabilities leading to nonadiabatic jumps between metastable states occur when [41, 44]

$$K < -\left.\frac{\partial^2 V_{TS}}{\partial x^2}\right|_{x=x_m}, \quad \text{i.e.} \quad \tilde{U}_0 \equiv \frac{4\pi^2 U_0}{K a_x^2} > 1, \tag{1.10}$$

where $x_m = na_x$ $(n = 1, 2, \ldots)$ denotes the position of the minima of V_{TS}. From what we have just said, it is clear that the main mechanism of energy dissipation in the model is determined by these elastic instabilities, and therefore we expect a more pronounced contribution to kinetic friction in the stick-slip regime. The kinetic friction force F_{fric} is defined as the average of the lateral force $F_x = K(v_s t - x)$. By assuming a periodic motion of the type of Eq. (1.9), F_{fric} can be written as

$$\boxed{F_{fric} =< F_x >\equiv \frac{v_s}{na} \int_0^{na_x/v_s} F_x dt.} \tag{1.11}$$

It is easy to show that the definition Eq. (1.11) is equivalent to calculating the friction force from the energy dissipation ΔW in one period

$$\Delta W = m\eta \int_0^{na_x/v_s} \dot{x}^2 dt. \tag{1.12}$$

The friction force is then given by

$$F_{fric} = \frac{\Delta W}{na_x}. \tag{1.13}$$

This is derived analytically in the appendix of this chapter. Notice that F_{fric} is different from the *static friction force*, i. e. the force needed to put the object in motion, which is simply given by the force necessary to overcome the potential barrier:

$$F_{static} = \frac{2\pi U_0}{a}. \tag{1.14}$$

A typical behaviour of the position, the velocity and the lateral force of the tip, obtained by solving Eq. (1.8) numerically, is shown in Fig. 1.11 for two values of $\tilde{U}_0$, one below and the other above the threshold $\tilde{U}_0 = 1$. For $\tilde{U}_0 < 1$, the position evolves rather continuously in time, and at the same time the behaviour of the velocity is smooth. Instead, for $\tilde{U}_0 > 1$, the stick-slip motion is observed in the tip coordinate, the velocity is almost vanishing in the sticking parts, and it is peaked reaching high values when the tip slips. Almost all the energy is dissipated during these events, where the tip velocity is very large. This trend reflects itself in the evolution of the lateral force F_x, which is smoothly oscillating for $\tilde{U}_0 < 1$ and has a sharp saw-tooth shape for $\tilde{U}_0 > 1$. The friction force is thus much higher in the latter case, as indicated by the horizontal lines in Fig. 1.11(c). Moreover, as it can be seen in Fig. 1.12(a), for $\tilde{U}_0 < 1$, the total energy $E_{tot} = m\dot{x}^2/2 + V_{tot}$ follows adiabatically the potential energy surface, while for $\tilde{U}_0 > 1$ it has a significant contribution from the kinetic energy. Fig. 1.12(b) suggests that the dynamics of the Tomlinson model is also very sensitive to the choice of the damping: for $\eta = 0$ many oscillations, with different periodicities, are superimposed to the smoother behaviour of the damped case. The parameter $\tilde{U}_0$, defined in Eq. (1.10) is the quantity that regulates the transition between stick-slip and sliding motion, and thus between high friction to low friction. This kind of transition has been recently observed experimentally

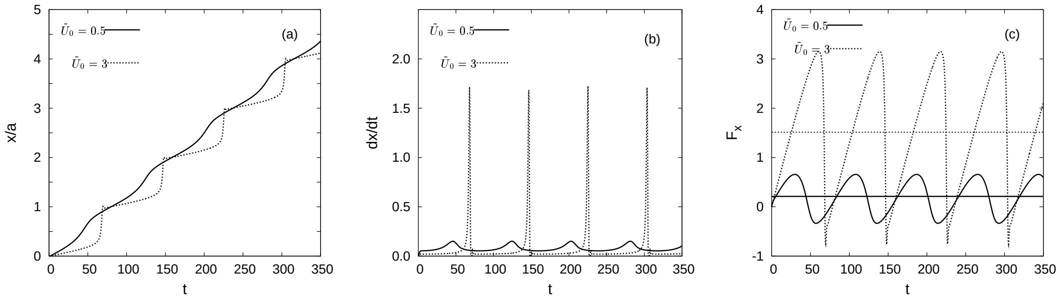

Figure 1.11: Time behaviour of the tip coordinate (rescaled to the lattice parameter a) (a), tip velocity (b) and lateral force (c), for two values of the reduced corrugation: $\tilde{U}_0 = 0.5$ (below the threshold) and $\tilde{U}_0 = 3$ (above the threshold). The horizontal lines in (c) indicate the values of the friction force for the two cases ($F_{fric} = 0.21$ for $\tilde{U}_0 = 0.5$ and $F_{fric} = 1.51$ for $\tilde{U}_0 = 3$). While the tip coordinate slides continuously and the lateral force is smooth for $\tilde{U}_0 = 0.5$, stick-slip occurs for $\tilde{U}_0 = 3$, and the tip velocity has sharp peaks corresponding to the slip events. Energy dissipation, and thus friction, is much higher in the latter case. The scanning velocity used in the simulations is $v_s = 0.08$ and the damping is assumed to be critical ($\eta = 2$). All quantities are in dimensionless units (see the appendix at the end of this chapter).

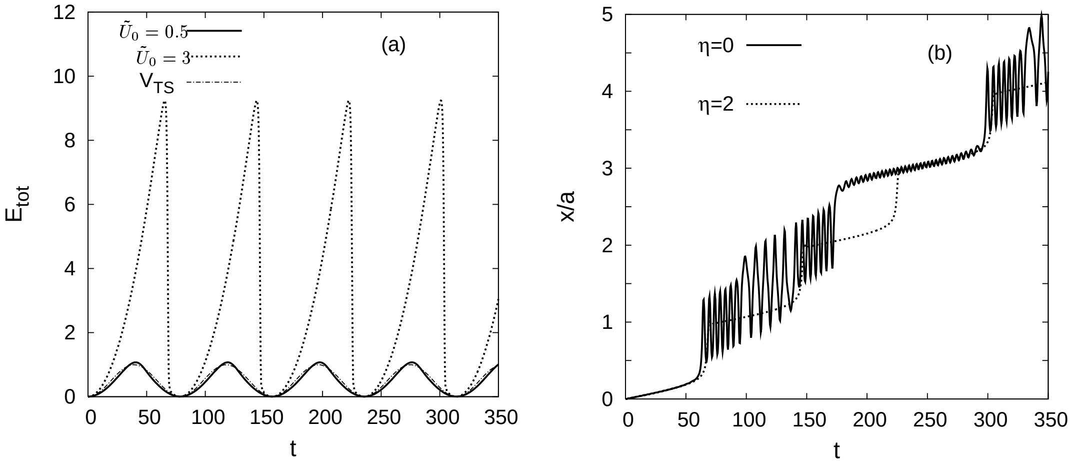

Figure 1.12: (a) Time behaviour of the total energy E_{tot} for $\tilde{U}_0 = 0.5$ and $\tilde{U}_0 = 3$ and $\eta = 2$. While, for $\tilde{U}_0 = 0.5$, the total energy adiabatically follows the tip-surface potential V_{TS}, for $\tilde{U}_0 = 3$ E_{tot} is peaked in proximity of the slip events, due to the contribution of the kinetic energy. (b) Comparison of the tip coordinate (rescaled to the lattice parameter a) for the undamped and the critically damped case, for $\tilde{U}_0 = 3$. The scanning velocity is $v_s = 0.08$. All quantities are in dimensionless units (see the appendix at the end of this chapter).

in an AFM study on NaCl [47]. When stick-slip instabilities cease to exist, a new regime of ultralow friction is encountered. Experimentally, the transition is driven by changing the applied load. However, since, as we will see in Chap. 5, the applied load modifies the effective corrugation U_0 of the tip-substrate interaction, different loads correspond to different values of $\tilde{U}_0$, and thus the experimental observations can be simply described in the framework of the Tomlinson model. Fig. 1.13 compares the experimental results for different loads with the simulations of Eq. (1.8) for different values of $\tilde{U}_0$. The qualitative behaviour is the same, and interestingly, the stick-slip behaviour and the hysteresis loop become less and less evident when the load (or $\tilde{U}_0$ in our terminology) is decreased. These results are very relevant, because they suggest a way to control friction at the nanoscale without the use of lubricants (see discussion in Sec. 5.6 of Chap. 5) and emphasize the strength of the Tomlinson model to describe the frictional dynamics.

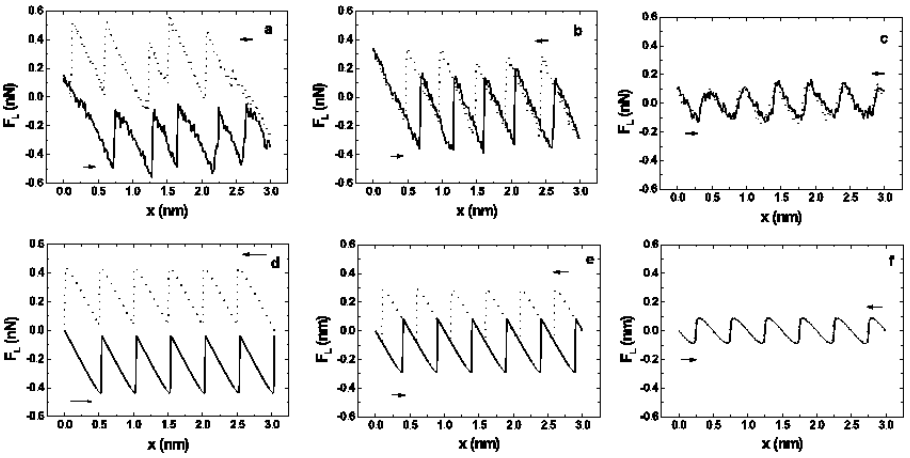

Figure 1.13: Lateral force as a function of the tip position, as obtained by AFM experiments on NaCl (a-c) and by simulations of the Tomlinson model (d-f). The normal applied loads in the experiments are $F_{load} = 4.7$ nN (a), $F_{load} = 3.3$ (b) and $F_{load} = -0.47$ (c), while the values of $\tilde{U}_0$ are $\tilde{U}_0 = 5$ (d), $\tilde{U}_0 = 3$ (e) and $\tilde{U}_0 = 1$ (f). Notice the transition from stick-slip to sliding by decreasing the load in the experiments and by decreasing the effective corrugation $\tilde{U}_0$ in the simulations. The hysteresis loop disappears for low loads (low $\tilde{U}_0$), indicating that the energy dissipation is vanishing. [From Ref. [47]].

We will employ the Tomlinson model in Chap. 4 to study the velocity dependence of atomic-scale friction.

1.4.3 A unifying approach

So far, we have presented two different minimalistic models, one for the surface diffusion of adsorbates and the other for the description of atomistic friction. Is there a way to combine these two apparently different models in one approach, and possibly enhance the complexity of the description? We propose a model, shown in Fig. 1.14, which is suitable both for surface diffusion and for frictional dynamics. It contains the crucial ingredients

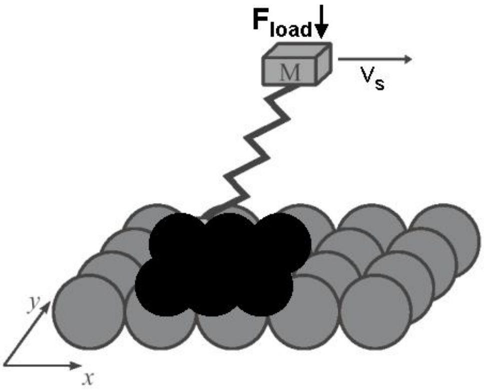

Figure 1.14: Our $3D$ atomistic model for surface diffusion and frictional dynamics (AFM).

that are relevant to both problems. An adsorbate, which can be an adatom, a molecule, a cluster of atoms, an island, or the tip-surface contact in AFM, is moved over a $2D$ surface, which is formed by a periodic arrangement of atoms. If we are interested in modelling AFM, this adsorbate can be attached by means of a spring to a support moving at constant velocity v_s, and possibly an external load along z can be applied. Otherwise, we are reduced to the case of pure diffusion of the adsorbate on the surface. Notice that an appropriate interatomic interaction between the adsorbate and the surface has to be chosen, and in general we do not assume that it can be reduced to a simple sinusoidal potential. Moreover, the substrate can be rigid or mobile, depending whether we include or not thermal fluctuations in our description. Thus, such model is quite versatile, and is based on the fact that AFM can be thought as a driven diffusion problem, as we will underline in Chap. 5, where this model will be used.

1.5 Computational approaches: an overview

Since the equations of motion of an adsorbate moving on a substrate are in general not solvable analytically, one has to resort to computer simulations. Before going into the details of the specific simulations we have used in this work, we would like to briefly summarize the computational methods typically used to study the motion of adsorbates on surfaces. They can basically be divided into four main classes.
(a) *Ab initio calculations*: this is a first-principles method, which allows to calculate explicitly the force field between all the atoms in the system quantum-mechanically within some approximations, such as density functional theory. The great advantage of this method is that there are in principle no fitting parameters. The main task of first-principles calculations in surface diffusion is to obtain quantitative estimates for diffusion barriers [48], to be compared to experimental values or to be used for other computational approaches. They can also serve as a tool to measure the interaction between the tip and the surface in AFM experiments, which is thus relevant to frictional problems [49]. Both static and dynamic calculations at finite temperature (for example using the Car-Parrinello method [50]) are

possible within the ab initio framework. The drawbacks of these simulations are that they are highly computationally demanding, and that they are very costly for the study of diffusion events at finite temperatures. They are limited to rather small systems and to short time scales (of the order of 100 ps).

(b) *Total energy calculations*: they elucidate the potential energy surface relevant in surface migration of adsorbates. For this purpose, the surface corrugation is mapped by calculating the energies for different static configurations. The positions of the atoms are relaxed by local energy minimization procedures similar to steepest descent [51]. There are numerous example of application of this method in surface diffusion [52] and in AFM simulations [46, 53]. The disadvantage of this approach is that it cannot account for the dynamical aspects of the problem, which nevertheless can be very relevant, as we will see in Chaps. 3 - 5.

(c) *Molecular Dynamics (MD) simulations*: with such simulations the dynamics is calculated by solving the classical mechanics equations of motion [54]. The temporal and spatial evolution of an adsorbate interacting with surface atoms are thus obtained. In MD calculations the form of the potential energy is given explicitly as a function of the positions of the atoms. There are many classes of such potentials, varying in their degree of complexity and relation to first-principles calculations. They range from simple two-body empirical potentials, such as the harmonic potential, to more complicated many-body interactions [58]. The main advantage of using classical phenomenological potentials is that the MD method is immediately feasible, while the main drawback is the fitting procedure which has to be done and tested for each case separately. Thermal effects can be taken into account in the simulations keeping the temperature constant through a thermostat or by treating them in an effective way in the Langevin approach, which is based on stochastic equations that consider the coupling to a heat bath and the effect of dissipation (see Sec. 1.6). Ref. [59] contains a review of applications of MD simulations to surface diffusion. MD is also widely used to investigate friction between solid surfaces [60]. Although MD simulations can give very accurate results and are able to follow the dynamical details of the system, they are mostly limited to short time scale (or the order of 100 ns), since the typical time step used is very small (of the order of femtoseconds). Moreover, MD calculations of surface diffusion can be rather time-consuming, especially at low temperatures, at which the atoms spend most of the time oscillating around the potential minima. The rate of transitions between different metastable states (minima of the potential) is proportional to $\exp(-E_a/k_BT)$, where E_a is the activation energy for diffusion, and thus this factor is very low for small temperatures ($k_BT \ll E_a$). Recently, an accelerated MD dynamics method has been proposed to overcome this problem [61], thus extending the time scale of MD simulations. The basic idea of this method, called hyper-MD, consists in adding a bias potential to the potential energy, which is constructed in such a way to keep the total potential at the saddle point unchanged, leading to an enhanced escape rate from the minimum.

(d) *Monte Carlo (MC) simulations*: at very low temperatures and with relatively weak interatomic interactions, the adatoms are mostly localized around the adsorption sites, and move among these sites with a rate that is much smaller than the typical vibration frequencies. In this case the lattice-gas model, characterized by a lattice-gas Hamiltonian and a prescribed dynamical algorithm for transitions between different configurations, becomes a very useful model of surface diffusion [62]. The evolution of the lattice gas can be described by a master equation, which governs the time behaviour of the probability $P(\mathbf{n})$ for the system to be in a certain configuration $\mathbf{n}$. The MC method [54] calculates this probability, assuming a specific form of the transition rate $w(\mathbf{n}, \mathbf{n}')$ between two different configurations $\mathbf{n}$ and $\mathbf{n}'$. In the standard implementation of MC simulations for dynamical studies, at each step in the simulation a particle is randomly chosen. Then a jump direction is chosen, again randomly, towards a possible arrival site. If the arrival site is full, the move is rejected; if it is empty, the transition probability $w(\mathbf{n}, \mathbf{n}')$ is computed, according to the specifically chosen algorithm (for example Metropolis [54]) and a random number $0 < r \leq 1$ is generated. If $r \leq w(\mathbf{n}, \mathbf{n}')$, the move is accepted, otherwise it is rejected. Each MC step corresponds to one unit of time whose precise microscopic interpretation is difficult. For simple systems, this can be compared with MD simulations to map out the dynamics back to real time. The main shortcoming of this implementation of MC simulations becomes evident at low temperatures, where the transition probabilities are very small. Thus, a larger part of the computing time is spent in attempting moves which are rejected. This drawback may be overcome by a MC scheme in which moves are chosen according to their *a priori* probability, so that no moves are rejected. This is the basis of the so-called time-dependent MC method. Compared to MD, which has a natural dynamics arising from the Hamiltonian description, MC is much less detailed from the microscopic point of view, since the dynamics is superimposed to the Hamiltonian description.

1.6 Switching on the temperature: Langevin dynamics

Consider the motion of an adatom over a $1D$ substrate. In principle, we should take into account not only the motion of the adatom, but also that of the atoms forming the substrate, which interact with each other with a potential V that we assume to be pairwise, for example harmonic (see Fig. 1.15). Indicating by U the interaction between the adatom and each of the substrate atoms and supposing we consider a chain of N substrate atoms (possibly with periodic boundary conditions), one has to solve the equations for the adatom coordinate x and for the coordinates x_i of the substrate atoms $(i = 1, N)$:

$$\left\{ \begin{array}{lcl} m\ddot{x} & = & -\frac{\partial U}{\partial x} \\ m\ddot{x}_i & = & -\frac{\partial U}{\partial x_i} - \frac{\partial V}{\partial x_i} \qquad i = 1, N \end{array} \right. \tag{1.15}$$

These are $N + 1$ equations and solving them can be a rather time consuming task if N is large. However, in surface diffusion problems we are mainly interested in the dynamics of the adsorbate and not in the motion of the substrate atoms around their equilibrium positions. Therefore, the natural solution to this problem is to integrate out *all* the substrate degrees of freedom in the equations of motion, leaving only an effective equation for the adatom. This the basis of the Langevin approach for the study of surface diffusion. In this treatment, the substrate atoms are frozen to their equilibrium positions and the vibrations are treated effectively as a heat bath coupled to the adsorbate. In this way, thermal effects are automatically included. Thus, in the case of an adatom diffusing on a

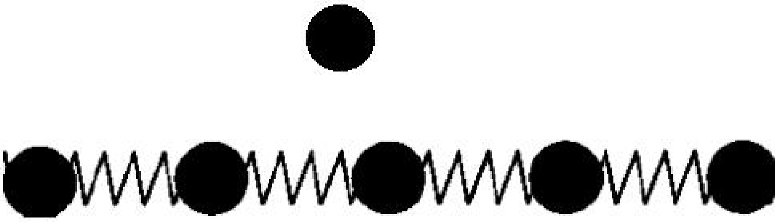

Figure 1.15: An adatom interacting with a chain of atoms forming the substrate. The interactions between the substrate atoms (V) and between the adatom and the substrate atoms (U) are assumed to be pairwise.

periodic potential, the Langevin equation generalizes Eq. (1.3), and has the form [63]

$$\boxed{m\frac{d^2x}{dt^2} + m\eta\frac{dx}{dt} = -\frac{2\pi U_0}{a}\sin\left(\frac{2\pi x}{a}\right) + F + f(t).} \tag{1.16}$$

The term $f(t)$ in Eq. (1.16) is a stochastic force randomly acting on the particle and satisfying the conditions

$$\langle f(t)\rangle = 0 \tag{1.17}$$

$$\boxed{\langle f(t)f(0)\rangle = 2m\eta k_B T\delta(t)} \tag{1.18}$$

where $\langle\cdot\rangle$ denotes an ensemble average, k_B is the Boltzmann's constant and T is temperature. A stochastic force obeying Eqs. (1.17)-(1.18) is called *white noise.* This stochastic force arises from the non-adiabatic coupling between the adatom and the electronic and vibrational excitations of the substrate. This coupling leads to fluctuations in the energy and momentum of the adatom as well as to damping of its motion. Thus, the heat bath pumps energy through the stochastic force f in a random fashion, which is then removed via some dissipation channels accounted for by the phenomenological damping term $m\eta\frac{dx}{dt}$. This is the reason for which the fluctuations of the stochastic forces are intimately related to dissipation, as expressed by Eq. (1.18), which is indeed also known as *fluctuation-dissipation* relation. The white noise approximation is justified when the time scale of the substrate motion is much faster than the adatom time scale. If this condition is not fulfilled any more, the simple form of the Langevin equation (1.16) does not hold and a time-dependent kernel $\Sigma(t,t')$, which includes memory effects, has to be introduced:

$$m\frac{d^2x}{dt^2} + m\int_{-\infty}^{t}\Sigma(t,t')x(t')dt' = -\frac{2\pi U_0}{a}\sin\left(\frac{2\pi x}{a}\right) + F + f(t). \tag{1.19}$$

Then, the fluctuation-dissipation relation (1.18) becomes

$$\langle f(t)f(0)\rangle = mk_B T\Sigma(t,0). \tag{1.20}$$

This situation occurs for example when the mass of the particle is light, or the adatom-substrate interaction is stiff [64]. The case of white noise is of course recovered when

$$\Sigma(t,t') = 2\eta\delta(t-t'). \tag{1.21}$$

1.6.1 Computational technicalities

There are several ways to solve the Langevin equation numerically. Basically one has to include stochastic forces in an algorithm used to solve deterministic equations, such as velocity Verlet or Runge-Kutta [54, 55, 56, 57]. In our simulations we have usually employed the velocity Verlet algorithm, which, at variance with the Runge-Kutta, is a symplectic algorithm (i. e. it retains many dynamical properties of the phase space that the exact trajectories are known to exhibit), and thus it is more robust and stable, preserving the microscopic time reversibility of the equations of motion. The velocity Verlet advances positions and velocities as follows (we consider for simplicity one particle in $1D$):

$$\left\{\begin{array}{rcl} v(t+\frac{\Delta t}{2}) & = & v(t) + \frac{F(t)}{m}\frac{\Delta t}{2} + O((\Delta t)^2) \\ x(t+\Delta t) & = & x(t) + v(t)\Delta t + \frac{F(t)}{m}\frac{(\Delta t)^2}{2} + O((\Delta t)^4) \\ v(t+\Delta t) & = & v(t+\frac{\Delta t}{2}) + \frac{F(t+\Delta t)}{m}\frac{\Delta t}{2} + O((\Delta t)^2) \end{array}\right. \tag{1.22}$$

In Eq. (1.22) $F(t)$ is the force at time t acting on the particle, which depends only on the position $x(t)$. The algorithm is self starting. Given their values at t, positions at $t+\Delta t$ and velocities at $t+\Delta t/2$ are calculated from the force at time t. Then $F(t+\Delta t)$ is computed from the advanced positions. The calculation of the forces is the most time consuming part. Finally, the velocity is advanced from $t+\Delta t/2$ to $t+\Delta t$.

In the presence of a frictional force proportional to v, the force acting on the particle will be

$$G(x,v) = F(x) - m\eta v. \tag{1.23}$$

In order to treat velocity dependent forces it is necessary to make some changes in Eq. (1.22), which now becomes

$$\left\{\begin{array}{rcl} v(t+\frac{\Delta t}{2}) & = & v(t)\left(1-\eta\frac{\Delta t}{2}\right) + \frac{F(t)}{m}\frac{\Delta t}{2} + O((\Delta t)^2) \\ x(t+\Delta t) & = & x(t) + v(t)\Delta t + \left(\frac{F(t)}{m} - \eta v(t)\right)\frac{(\Delta t)^2}{2} + O((\Delta t)^4) \\ v(t+\Delta t) & = & v(t+\frac{\Delta t}{2}) + \left(\frac{F(t+\Delta t)}{m} - \eta v(t+\Delta t)\right)\frac{\Delta t}{2} + O((\Delta t)^2) \end{array}\right. \tag{1.24}$$

It is easy to show that Eq. (1.22) is replaced by

$$\left\{\begin{array}{rcl} v(t+\frac{\Delta t}{2}) & = & v(t)\left(1-\eta\frac{\Delta t}{2}\right) + \frac{F(t)}{m}\frac{\Delta t}{2} + O((\Delta t)^2) \\ x(t+\Delta t) & = & x(t) + v(t)\Delta t + \left(\frac{F(t)}{m} - \eta v(t)\right)\frac{(\Delta t)^2}{2} + O((\Delta t)^4) \\ v(t+\Delta t) & = & \left(1+\eta\frac{\Delta t}{2}\right)^{-1}\left[v(t+\frac{\Delta t}{2}) + \frac{F(t+\Delta t)}{m}\frac{\Delta t}{2}\right] + O((\Delta t)^2) \end{array}\right. \tag{1.25}$$

It has been recognized that the issue of temperature regulation is a very delicate one in MD study of surface friction. Compared to other types of thermostats, the Langevin approach has the advantage of removing heat where it is generated, the viscous damping being proportional to the particle velocity. The stochastic force f is drawn at each time step from a Gaussian distribution with zero mean and variance given by

$$\langle f^2(t) \rangle = 2m\eta k_B T/\Delta t, \tag{1.26}$$

where Δt is the time step used in the simulation. Usually Δt is of the order of $10^{-15}s$. The method of Box and Muller [54] is particularly useful to generate Gaussian distributed numbers. It consists in generating a couple of uniform random numbers r_1 and r_2 in $(0, 1)$ and calculating

$$\zeta_- = (-2 \ln r_1)^{1/2} \cos(2\pi r_2) \tag{1.27}$$

and

$$\zeta_+ = (-2 \ln r_1)^{1/2} \sin(2\pi r_2). \tag{1.28}$$

In this way ζ_- and ζ_+ are Gaussian random numbers with zero mean and unit variance. A Gaussian number with mean c and variance σ can be simply obtained by the transformation

$$f_\pm = c + \sigma\zeta_\pm. \tag{1.29}$$

In our case $c = 0$ and $\sigma = 2m\eta k_B T/\Delta t$. The stochastic force $f(t)$ at time t is calculated as the average of f_+ and f_-:

$$f(t) = \frac{1}{2}(f_+ + f_-). \tag{1.30}$$

In particular, it is convenient to extract f_- and f_+ according to Eqs. (1.27)-(1.29) at the beginning of the simulation, and then to use for f_- at each time step the value of f_+ calculated at the previous time step and so on. In this way only one Gaussian number has to be calculated every time step (except the first), thus avoiding to perform an extra calculation of f_-, which saves computational time, since the logarithm and the square root are quite expensive operations.

In order to have statistically well-defined physical quantities, the Langevin dynamics requires to sample many trajectories characterized by different "realizations" of the random forces and to perform averages of the quantities of interest over these trajectories. In this way, the noise associated with the stochastic forces can be reduced. For diffusion problems the number of realizations needed depends on the value of $U_0/k_B T$, and it is typically of the order of 10^3. For example, in Fig. 1.16 two trajectories of the monomer are reported, one for a very small and the other for a large value of the driving force F: it is seen that the spatial coordinate evolves linearly in time in both cases, but while for large forces only few tens of realizations are enough, in the case of a very low force (i. e. a high diffusion barrier) even for hundreds of realizations we still observe many fluctuations due to the random noise.

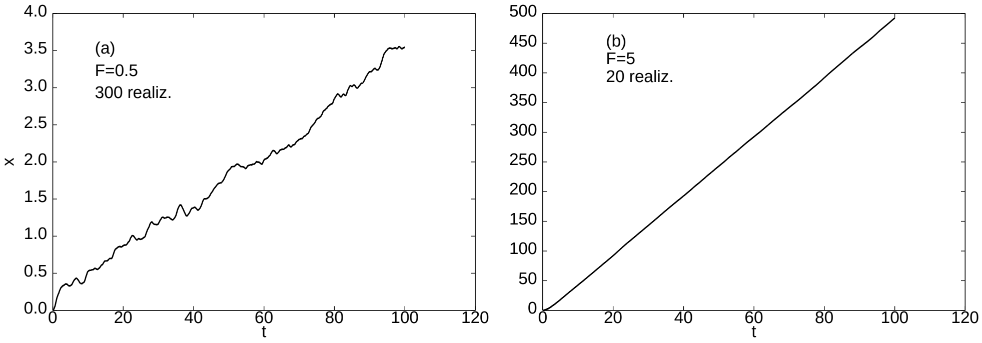

Figure 1.16: Averaged trajectory of the monomer in the driven case for $F = 0.5$ (a) and $F = 5$ (b), $m = 1$, $U_0 = 2.5$ and $\eta = 1$ ($k_BT = 1$). The number of realizations used in (a) is much larger than that in (b) and still $x(t)$ in (a) displays many fluctuations due to the stochastic forces. All quantities are in dimensionless units (see Sec. 2.1).

Appendix: equivalence between friction and energy dissipation

In this appendix we show the equivalence between the definition of the friction force calculated as the average of the lateral force (Eq.(1.11)) and that obtained from the energy dissipation (Eq.(1.13)). For simplicity we introduce the adimensional units

$$\tilde{x} = \frac{2\pi x}{a}, \quad \tilde{t} = \sqrt{\frac{K}{m}}t, \quad \tilde{\eta} = \sqrt{\frac{m}{K}}\eta, \quad \tilde{U_0} = \frac{(2\pi)^2}{Ka^2}U_0, \quad \tilde{v}_s = \frac{2\pi}{a}\sqrt{\frac{m}{K}}v_s$$

and rewrite Eq. (1.8) as

$$\ddot{\tilde{x}} + \tilde{\eta}\dot{\tilde{x}} + \tilde{U_0}\sin\tilde{x} + \tilde{x} - \tilde{v}_s\tilde{t} = 0 \tag{1.31}$$

In the following we will omit the tildes for simplicity. The expression of the energy dissipated in one period $2\pi/v_s$ becomes

$$\Delta W = \eta \int_0^{2\pi/v_s} \dot{x}^2 dt \tag{1.32}$$

and the friction force is

$$F_{fric} = \Delta W/(2\pi). \tag{1.33}$$

Now we can multiply both sides of Eq.(1.31) by $\dot{x}$ and integrate over one period:

$$\int_0^{2\pi/v_s} \dot{x}\ddot{x}dt + \eta\int_0^{2\pi/v_s} \dot{x}^2 dt + U_0\int_0^{2\pi/v_s} \dot{x}\sin x dt + \int_0^{2\pi/v_s} \dot{x}x dt - v_s\int_0^{2\pi/v_s} t\dot{x}dt = 0 \tag{1.34}$$

Let us calculate each term separately:

$$\int_0^{2\pi/v_s} \dot{x}\ddot{x}dt = \frac{1}{2}\dot{x}^2\Big|_0^{2\pi/v_s} \tag{1.35}$$

$$\eta \int_0^{2\pi/v_s} \dot{x}^2 dt \equiv 2\pi F_{fric} \tag{1.36}$$

$$U_0 \int_0^{2\pi/v_s} \dot{x} \sin x dt = -U_0 \int_0^{2\pi/v_s} d\cos x = U_0(1-\cos x)|_0^{2\pi/v_s} \tag{1.37}$$

$$\int_0^{2\pi/v_s} \dot{x} x dt = \frac{1}{2}\int_0^{2\pi/v_s} dx^2 = \frac{1}{2}x^2\Big|_0^{2\pi/v_s} \tag{1.38}$$

$$-v_s \int_0^{2\pi/v_s} t\dot{x} dt = -v_s \int_0^{2\pi/v_s} t dx = -v_s \frac{2\pi}{v_s} x\left(\frac{2\pi}{v_s}\right) + v_s \int_0^{2\pi/v_s} x dt =$$

$$-2\pi x\left(\frac{2\pi}{v_s}\right) + v_s \int_0^{2\pi/v_s} x dt \tag{1.39}$$

Inserting this expressions into (1.34) we have

$$\frac{1}{2}\dot{x}^2\Big|_0^{2\pi/v_s} + 2\pi F_{fric} + U_0(1-\cos x)|_0^{2\pi/v_s} + \frac{1}{2}x^2\Big|_0^{2\pi/v_s} + v_s \int_0^{2\pi/v_s} x dt - 2\pi x\left(\frac{2\pi}{v_s}\right) = 0. \tag{1.40}$$

Assume that $x(t)$ is periodic, i. e.

$$x(t + 2\pi/v_s) = x(t) + 2\pi. \tag{1.41}$$

Then $x(2\pi/v_s) = x(0) + 2\pi$ and Eq. (1.40) becomes

$$2\pi F_{fric} - \frac{1}{2}(2\pi)^2 + v_s \int_0^{2\pi/v_s} x dt = 0 \tag{1.42}$$

We introduce $\xi = x - v_s t$. We can thus rewrite the last expression obtaining

$$2\pi F_{fric} = \frac{1}{2}(2\pi)^2 - v_s \int_0^{2\pi/v_s} \xi dt - v_s^2 \int_0^{2\pi/v_s} t dt = \frac{1}{2}(2\pi)^2 - v_s \int_0^{2\pi/v_s} \xi dt - \frac{v_s^2}{2}\left(\frac{2\pi}{v_s}\right)^2 =$$

$$-v_s \int_0^{2\pi/v_s} \xi dt. \tag{1.43}$$

Since $v_s t - x = -\xi$ is the lateral force F_x, we have an alternative expression of the friction force

$$F_{fric} = \frac{v_s}{2\pi} \int_0^{2\pi/v_s} F_x dt \equiv < F_x > \tag{1.44}$$

where $< \cdot >$ indicates a time average. Thus, finally we have proved that

$$\frac{\eta}{2\pi} \int_0^{2\pi/v_s} \dot{x}^2 dt = \frac{v_s}{2\pi} \int_0^{2\pi/v_s} F_x dt \tag{1.45}$$

Bibliography

[1] H. Brune, Surf. Sci. Rep. **31**, 121 (1998).

[2] R. Imbihl and G. Ertl, Chem. Rev. **95**, 697 (1995).

[3] F. P. Bowden and D. Tabor, *An Introduction to Tribology*, Anchor Press/Doubleday, Garden City (1973).

[4] J. K. Gimzewski and C. Joachim, Science **283**, 168 (1999).

[5] L. Bartels, G. Meyer and K.-H. Rieder, Phys. Rev. Lett. **79**, 697 (1997).

[6] E. Meyer, R. M. Overney and K. Dransfeld, *Nanoscience: Friction and Rheology on the Nanometer Scale*, World Scientific, Singapore (1998).

[7] E. Gnecco, R. Bennewitz, T. Gyalog and E. Meyer, J. Phys. Condens. Matter **13**, R619 (2001).

[8] L. Hamburger, Kolloid Z. **23**, 12 (1918).

[9] M. Volmer and I. Estermann, Z. Phys. **7**, 13 (1921).

[10] M. Volmer, Trans. Faraday Soc. **28**, 359 (1925).

[11] I. Langmuir and J. B. Taylor, Phys. Rev. **40**, 463 (1932).

[12] E. W. Müller, Z. Phys. 131, 136 (1951).

[13] G. Ehrlich and F. G. Hudda, J. Chem. Phys. **44**, 1039 (1966).

[14] T. T. Tsong and R. Casanova, Phys. Rev. Lett. **47**, 113 (1981).

[15] G. L. Kellogg, J. Chem. Phys. **83**, 852 (1985).

[16] G. Binning and H. Rohrer, Helv. Phys. Acta **55**, 726 (1982).

[17] http://www.ieap.uni-kiel.de/surface/ag-kipp/stm/stm.htm.

[18] G. Binning, H. Fuchs and E. Stoll, Surf. Sci. **169**, L295 (1985).

[19] R. Gomer, Appl. Phys. A **39**, 1 (1986).

[20] J. A. Venables, Phil. Mag. **27**, 697 (1973).

[21] E. Ganz, S. K. Theiss, I.-S. Hwang and J. Golovchenko, Phys. Rev. Lett. **68**, 1567 (1992).

[22] B. S. Swartzentruber, Phys. Rev. Lett. **76**, 459 (1996).

[23] T. R. Linderoth, S. Horch, E. Laegsgaard, I. Stensgaard and F. Besenbacher, Phys. Rev. Lett. **78**, 4978 (1997).

[24] J. W. M. Frenken, J. P. Toennies, and Ch. Wöll, Phys. Rev. Lett. **60**, 1727 (1988).

[25] J. Ellis and J. P. Toennies, Phys. Rev. Lett. **70**, 2118 (1993).

[26] G. Binnig, C. F. Quate and Ch. Gerber, Phys. Rev. Lett. **68**, 930 (1986).

[27] C. M. Mate, G. M. McClelland, R. Erlandsson and S. Chiang, Phys. Rev. Lett. **59**, 1942 (1987).

[28] H. Hölscher and U. D. Schwarz, *Friction at the Nanometer-Scale– Nanotribology Studied with the Scanning Force Microscope*, Caesar preprint (2002).

[29] J. M. Neumeister and W. A. Ducker, Rev. Sci. Instrum. **65**, 2527 (1994).

[30] D. F. Ogletree, R. W. Carpick and M. Salmeron, Rev. Sci. Instrum. **67**, 3298 (1996).

[31] R. W. Carpick, N. Agraït, D. F. Ogletree and M. Salmeron, J. Vac. Sci. Technolog. B **14**, 1289 (1996).

[32] U. D. Schwarz, O. Zwörner, P. Köster and R. Wiesendanger, *Micro/Nanotribology and Its Applications*, edited by B. Bhushan, Kluwer Academic Publishers, Doordrecht (1997).

[33] U. D. Schwarz, O. Zwörner, P. Köster and R. Wiesendanger, Phys. Rev. B **56**, 6987 (1997).

[34] F.-J. Giessibl, Science **267**, 68 (1995).

[35] G. U. Lee, L. A. Chrisey and R. J. Colton, Science **266**, 771 (1994).

[36] A. Engel, Y. Lyubchenko and D. Muller, Trens Cell Biol. **9**, 77 (1999).

[37] S. A. Schneider, K. C. Sritharan, J. P. Geibel, H. Oberleithner and B. P. Jena, Proc. Nat. Acad. Sci. **94**, 316 (1997).

[38] See for example U. Kürpick, Phys. Rev. B **63**, 045409 (2001); P. J. Feibelman, Phys. Rev. B **61**, R2452 (2000); F. Montalenti and R. Ferrando. Surf. Sci. **432**, 27 (1999).

[39] B. N. J. Persson, *Sliding Friction: Physical Principles and Applications*, Springer, Berlin (1998).

[40] G. A. Tomlinson, Philos. Mag. **7**, 905 (1929).

[41] D. Tománek, W. Zhong and H. Thomas, Europhys. Lett. **15**, 887 (1991).

[42] T. Gyalog, M. Bammerlin, R. Lüthi, E. Meyer and H. Tomas, Europhys. Lett. **31**, 269 (1995).

[43] H. Hölscher, U. D. Schwarz and R. Wiesendanger, Europhys. Lett. **36**, 19 (1996).

[44] H. Hölscher, U. D. Schwarz and R. Wiesendanger, Surf. Sci. **375**, 395 (1997).

[45] J. S. Helman, W. Baltensperger and J. A. Hołyst, Phys. Rev. B **49**, 3831 (1994).

[46] N. Sasaki, K. Kobayashi and M. Tsukada, Phys. Rev. B **54**, 2138 (1996).

[47] A. Socoliuc, R. Bennewitz, E. Gnecco and E. Meyer, Phys. Rev. Lett. **92**, 134301 (2004).

[48] See for example G. Boisvert and L. J. Lewis, Phys. Rev. B **56**, 7643 (1997).

[49] See for example W. Zhong and D. Tománek, Phys. Rev. Lett. **64**, 3054 (1990); S. H. Ke, T. Uda, R. Pérez, I. Štich and K. Terakura, Phys. Rev. B **60**, 11631 (1999).

[50] R. Car and M. Parrinello, Phys. Rev. Lett. **55**, 2741 (1985).

[51] W. H. Press, S. A. Teukolsky, W. T. Vetterling and B. P. Flannery, *Numerical Recipes: The Art of Scientific Computing*, Cambridge University Press, New York (1992).

[52] See for example R. Wang and K. A. Fichthorn, Phys. Rev. B **48**, 18288 (1993); D. S. Sholl and K. A. Fichthorn, Phys. Rev. Lett. **79**, 3569 (1997).

[53] M. R. Sørensen, K. W. Jacobsen and P. Stoltze, Phys. Rev. B **53**, 2101 (1996).

[54] M. P. Allen, D. J. Tildesley, *Computer Simulation of Liquids*, Clarendon Press, New York (1988).

[55] D. Frenkel and B. Smit, Understanding Molecular Simulation (Academic Press, London, 2002).

[56] H. C. J. Berendsen and W. F. van Gunsteren, in Dynamics Simulation of Statistical-Mechanical Systems, edited by G. P. F. Ciccotti and W. G. Hoover (North Holland, Amsterdam, 1986), pp. 43-65.

[57] P. Procacci and M. Marchi, in Advances in the Computer Simulations of Liquid Crystals, edited by P. Pasini and C. Zannoni (Kluwer Academic Publishers).

[58] See for example M. S. Daw and M. I. Baskes, Phys. Rev. B **29**, 6443 (1984); F. Ercolessi, E. Tosatti and M. Parrinello, Phys. Rev. Lett. **57**, 719 (1986).

[59] K. A. Fichthorn and J. S. Raut, in *Surface Diffusion: Atomistic and Collective Processes*, edited by M. Tringides, Plenum Press, New York, p. 409 (1997).

[60] See for example M. H. Müser, Comp. Phys. Comm. **146**, 54 (2002).

[61] A. F. Voter, Phys. Rev. Lett. **78**, 3980 (1997).

[62] See for example J. S. Raut and K. A. Fichthorn, J. Chem. Phys. **110**, 587 (1999).

[63] H. Risken, *The Fokker-Planck Equation*, 2nd ed., Springer (1989).

[64] A. Cuchetti and S. C. Ying, Phys. Rev. B **54**, 3300 (1996).

Chapter 2

Diffusion model of an adatom in a periodic potential

In this chapter we introduce the basic concepts of stochastic motion and its applications to the phenomenon of adatom diffusion on periodic surfaces. Some analytical and numerical approaches to this problem will be comparatively presented both for the driven motion and for the pure diffusion on the surface.

2.1 Introduction

As already emphasized in Chap. 1, the diffusion of isolated adatoms (i. e. atoms adsorbed on a surface) is one of the most fundamental processes in surface science and is of crucial importance in very diverse areas such as crystal and thin film growth and catalysis [1, 2, 3, 4, 5].

Consider the motion of a particle in a $1D$ sinusoidal potential

$$U_{sub}(x) = U_0(1 - \cos(2\pi x/a)), \tag{2.1}$$

which can be viewed as the simplest approach to model adatom surface diffusion (see Fig. 2.1). Qualitatively, the stable situation for the adatom is to be in a well of the periodic potential, while it can migrate to the nearest well only if it has sufficient energy to overcome the diffusion barrier. As explained in Sec. 1.4.1, the motion of the particle over the substrate can be initiated by an initial kinetic energy, by an external force F or by thermal fluctuations. The Langevin equation (1.16) describes the dynamics of the adatom at finite temperature T. In the following we will work with the dimensionless Langevin equation

$$\boxed{\frac{d^2\tilde{x}}{d\tilde{t}^2} + \tilde{\eta}\frac{d\tilde{x}}{d\tilde{t}} = -\tilde{U}_0 \sin\tilde{x} + \tilde{f} + \tilde{F}}, \tag{2.2}$$

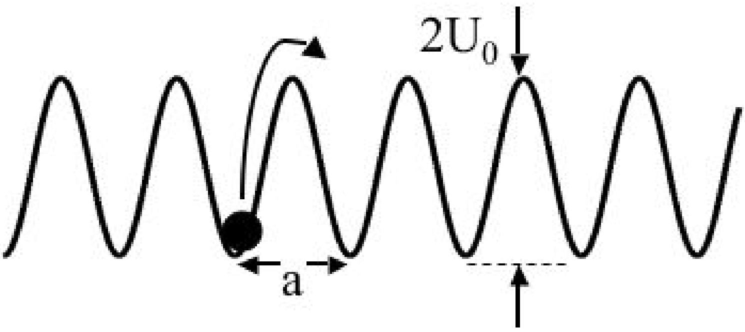

Figure 2.1: Sketch of the model of adatom diffusion considered in this chapter.

which is obtained from Eq. (1.16) by defining the characteristic time

$$\tau = \left(\frac{ma^2}{4\pi^2 k_B T}\right)^{1/2}$$

and the dimensionless variables

$$\tilde{x} = kx, \quad \tilde{t} = t/\tau, \quad \tilde{\eta} = \eta\tau, \quad \tilde{U}_0 = U_0/(k_B T), \quad \tilde{f} = f/(kk_B T), \quad \tilde{F} = F/(kk_B T).$$

The fluctuation-dissipation relation Eq. (1.18) in dimensionless variables becomes

$$\langle \tilde{f}(\tilde{t})\tilde{f}(0)\rangle = 2\tilde{\eta}\delta(\tilde{t}). \tag{2.3}$$

We will omit the tildes in the following. In order to have an idea of the order of magnitude of the physical quantities, we note that in a typical case $m \sim 2 \cdot 10^{-26}$ kg, $T \sim 200$ K, $a \sim 2 \cdot 10^{-10}$ m, so that $\tau \sim 2.5 \cdot 10^{-13}$ s.

The Langevin equation for an adatom has been investigated to great extent in the literature: the most comprehensive review on this topic is to be found in Risken's textbook [6], where the diffusion is analysed within the framework of the Fokker-Planck equation, and in the review of Hänggi et al. [7]. Besides, Eq. (2.2) is also connected to a variety of systems of practical importance, such as the damped pendulum [8], superionic conductors [9], Josephson tunneling junctions [10] and rotation of dipoles driven by a constant field [11]. The present chapter does not aim at covering this topic exhaustively, but it presents an overview of the adatom motion in a periodic potential, combining computer simulations with existing theories, and stressing some problematics which are still open. In particular, we will show that, despite of the simplicity of the model, the nonlinearities arising from the form of the substrate potential Eq. (2.1) make the dynamics quite complex, resulting for example in a nonlinear response of the particle velocity to an external force, with the occurrence of bistability and hysteresis. Thus, the deterministic case $T = 0$ is already interesting as an example of nonlinear dynamical system and we will devote to it a part of the present chapter.

The chapter is organized as follows. Sec. 2.2 analyses the deterministic motion of the adatom without including thermal fluctuations. Sec. 2.3 considers the motion of the adatom under the action of an external field with thermal fluctuations. Finally, Sec. 2.4 is devoted to the thermal diffusion problem on a periodic substrate, i. e. the stochastic motion without any external driving field.

2.2 Motion without thermal fluctuations

In this section we deal with the motion of the adatom as given by Eq. (2.2) with $f = 0$. This implies studying the deterministic dynamics of a dissipative system. The response of the system will be then a delicate function of the damping. We will first consider the case in which $F = 0$ and $v_0 \neq 0$ and then we will focus on the behaviour of the system when $v_0 = 0$ and $F \neq 0$.

2.2.1 Dynamics without external driving

When the particle possesses an initial kinetic energy $E_{kin}^{(0)}$ (or initial velocity v_0) and it starts from one local minimum of the potential energy (for example $x = 0$) it will be able to overcome the diffusion barrier only if $E_{kin}^{(0)} \geq 2U_0$, otherwise it will perform an oscillatory motion within the potential well. If the threshold is overcome and $\eta = 0$, the particle will slide on the substrate with average velocity $\langle v \rangle$, which can be easily calculated from energy conservation:

$$\langle v \rangle = \frac{1}{2}\left(v_0 + \sqrt{v_0^2 - 4U_0}\right). \tag{2.4}$$

For finite damping η, energy will be dissipated and the particle will stop in one of the potential wells in a time of the order of $1/\eta$. Thus, the instantaneous velocity $v \equiv \dot{x}$ will relax to $v = 0$ in a finite time. Depending on the value of η, it can display oscillations around zero: this will happen if the particle is underdamped, i. e. when $\eta < \omega_{sub}$, where

$$\omega_{sub} = \sqrt{\frac{d^2U_{sub}}{dx^2}}\Bigg|_{x=x_{min}} \tag{2.5}$$

is the frequency of oscillation of the particle around the local minimum x_{min} of the potential $U_{sub}(x)$. For the sinusoidal potential

$$\omega_{sub} = \sqrt{U_0}. \tag{2.6}$$

The different behaviour of the velocity relaxation in the underdamped and overdamped regime can be observed in Fig. 2.2, which illustrates the time behaviour of v for $U_0 = 1$ and three values of η ($\eta = 0, 0.5, 1.5$). Fig. 2.3 shows the trajectory of the particle in the phase space for the same values of η as in Fig. 2.2. For $\eta = 0$ and $E_{kin}^{(0)} > 2U_0$ the only stable motion is that in which the particle runs along the potential with periodically varying velocity: this attractor has the whole phase space as basin of attraction. For $\eta \neq 0$ and whatever value of v_0 the dynamics has an attractor corresponding to a minimum of the periodic potential, which has a finite basin of attraction.

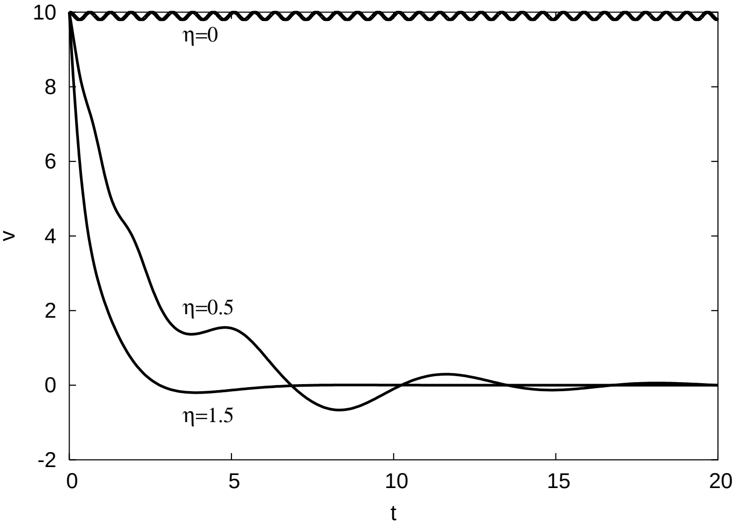

Figure 2.2: Time behaviour of velocity for $f = 0$, $F = 0$, $U_0 = 1$ and three values of η: undamped ($\eta = 0$), underdamped ($\eta = 0.5$) and overdamped ($\eta = 1.5$).

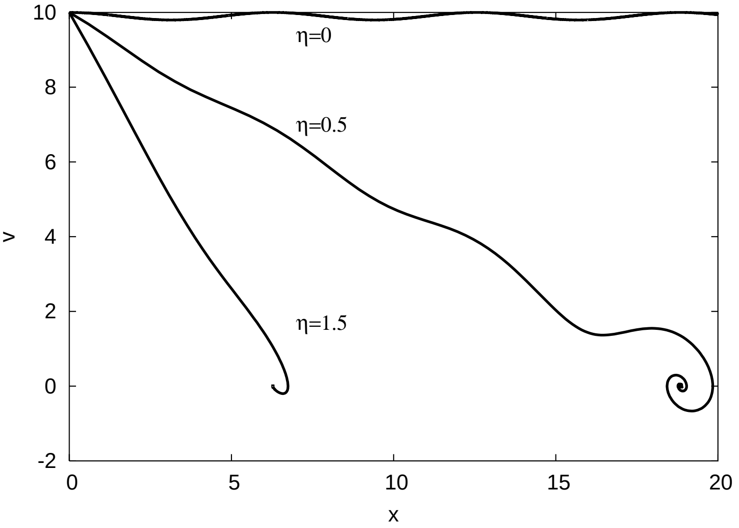

Figure 2.3: Trajectory in the phase space for $f = 0$, $F = 0$, $U_0 = 1$ and three values of η: undamped ($\eta = 0$), underdamped ($\eta = 0.5$) and overdamped ($\eta = 1.5$).

2.2.2 Driven motion

When a constant external force F is applied to the particle, the total potential energy $U_{tot}(x)$ becomes

$$U_{tot}(x) = U_{sub}(x) - Fx = U_0(1 - \cos x) - Fx. \tag{2.7}$$

Thus, the periodic potential $U_{sub}(x)$ will be tilted in the rightward direction, with an average slope determined by the value F. As it can be seen in Fig. 2.4, for small values of F, U_{tot} has minima and maxima and the particle will be in a locked state for $v_0 = 0$, since it cannot overcome the diffusion barrier. On the other hand, for large enough forces, the minima and maxima of U_{tot} disappear and the particle can be in a running state. The critical force F_{c1} at which this happens is determined by imposing that the first and second derivative of U_{tot} are equal to zero: this is equivalent to say that U_{tot} has a saddle point. Working out this condition, it is easy to find that

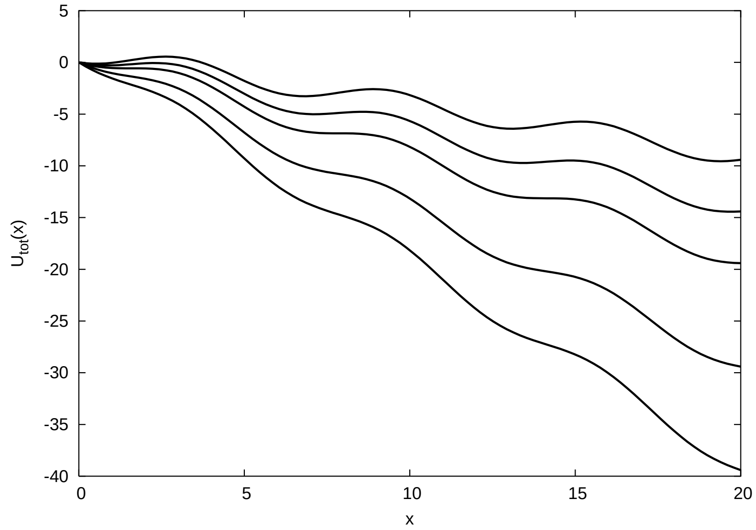

Figure 2.4: Total potential energy for $U_0 = 1$ and different values of the applied forces F: from top to bottom $F = 0.5, 0.75, 1, 1.5, 2$. For $F > F_{c1} = U_0 = 1$, U_{tot} does not have any minima and maxima.

$$F_{c1} = U_0. \tag{2.8}$$

Notice that F_{c1} corresponds to the *static friction force*, i. e. the force needed for the particle to overcome the threshold for the motion. For $F > F_{c1}$ the particle will perform a drift motion in the direction of the force with an average velocity $\langle v \rangle$ (here $\langle \cdot \rangle$ indicates a time average). The plot of the applied force F as a function of the drift velocity $\langle v \rangle$ is called velocity-force characteristic, which can be used to define the mobility μ as

$$\mu = \frac{\langle v \rangle}{F}. \tag{2.9}$$

For very large forces, the effect of the substrate potential becomes negligible and $F \simeq \eta\langle v\rangle$, so that the mobility will reach the asymptotic value $\mu = 1/\eta$. The fact that $\mu = 1/\eta$ can be easily found by time averaging Eq. (2.2) with $f = 0$ and noting that for long times $\langle\ddot{x}\rangle = 0$ and $\langle\sin x\rangle \simeq \langle\sin(\langle v\rangle t)\rangle = 0$. Since $\mu = 0$ for $F < F_{c1}$, it will have a discontinuity at $F = F_{c1}$ from zero to a finite value. Deviations of $F - \eta\langle v\rangle$ from 0 are an indication of a nonlinear response, due to the nonlinear interaction of the particle with the substrate. This will happen for not too high values of the applied forces, when the coupling to the substrate is important. Thus, the crucial question is to study the departures from the linear behaviour in the velocity-force characteristic, which we will show below.

A. Overdamped case

Different authors have treated analytically the overdamped limit ($\eta \gg \omega_{sub}$) [6, 12], where the inertial term $\ddot{x}$ can be neglected in the equation of motion. Thus Eq. (2.2) becomes

$$\eta\frac{dx}{dt} = F - U_0\sin x. \tag{2.10}$$

We can integrate this equation by separating the variables:

$$\frac{\eta dx}{F - U_0\sin x} = dt. \tag{2.11}$$

Defining t_{per} as the time the particle needs to travel the distance of one period $a = 2\pi$ of the substrate potential, it can be seen from Eq. (2.11) that, for $F > U_0$

$$t_{per} = \int_0^{2\pi}\frac{\eta dx}{F - U_0\sin x} = \frac{2\pi\eta}{\sqrt{F^2 - U_0^2}}. \tag{2.12}$$

Hence, the average velocity $\langle v\rangle$ can be calculated from Eq. (2.12) as $\langle v\rangle = 2\pi/t_{per}$. Thus

$$\begin{cases} \langle v\rangle = 0 & F < U_0 \\ \langle v\rangle = \frac{\sqrt{F^2 - U_0^2}}{\eta} & F \geq U_0 \end{cases} \tag{2.13}$$

For very large forces F, such that $F \gg U_0$, the second equation (2.13) can be approximated by

$$\boxed{\langle v\rangle \simeq \frac{F}{\eta}\left(1 - \frac{U_0^2}{2F^2}\right)} \qquad F \gg U_0, \quad \eta \gg \sqrt{U_0}. \tag{2.14}$$

This means that the nonlinear part of the friction force $F - \eta\langle v\rangle$ has a $1/F$ (or equivalently $1/\langle v\rangle$) dependence as leading term:

$$\boxed{F - \eta\langle v\rangle \simeq \frac{U_0^2}{2F} \simeq \frac{U_0^2}{2\eta\langle v\rangle}} \qquad F \gg U_0, \quad \eta \gg \sqrt{U_0}. \tag{2.15}$$

In Fig. 2.5(a) we show the velocity-force characteristic for the overdamped case, obtained by numerical simulations of Eq. (2.10), and the prediction of Eq. (2.13) for $F > U_0$. As

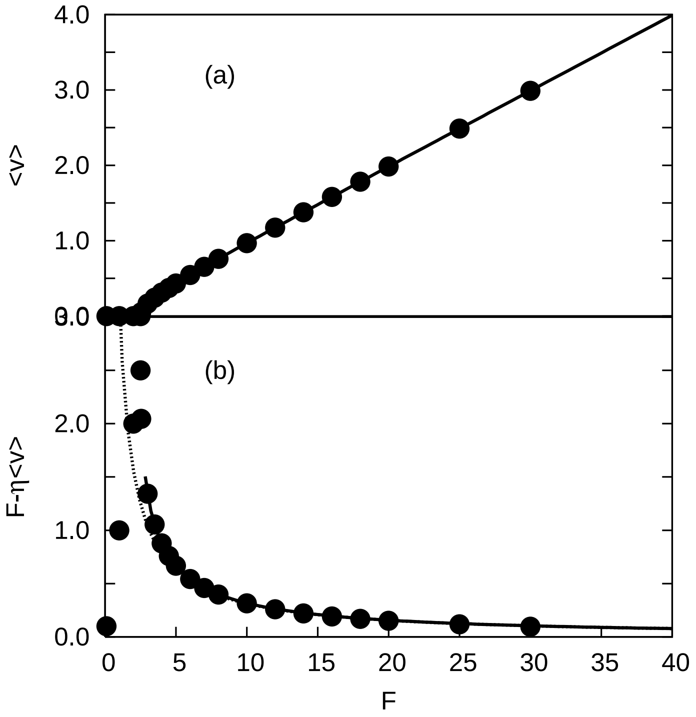

Figure 2.5: Velocity-force characteristic (a) and nonlinear part of the friction force $F - \eta\langle v\rangle$ (b) as a function of F, at $T = 0$, in the overdamped case ($\eta = 10$ and $U_0 = 2.5$). The solid circles are the result of numerical simulations, while the solid lines are obtained by using $\langle v\rangle$ from the second Eq. (2.13). The dotted line in (b) is given by Eq. (2.15). From (b) it is evident that the nonlinear part is well described by the theoretical curve.

it can be seen from Fig. 2.5(b), where we plot the nonlinear part of the frictional force $F - \eta\langle v\rangle$, the agreement between the simulation and the analytical expression is very good. Moreover, the approximate Eq. (2.15) overlaps with the exact formula (2.13) for not too small forces.

B. Arbitrary damping

In the case of moderate damping, we can find an approximate analytic expression for the mobility in the limit of large forces considering the full equation of motion

$$\ddot{x} + \eta\dot{x} = F - U_0 \sin x. \tag{2.16}$$

For $F \gg U_0$ we know that there will be a drift motion with average velocity $\langle v\rangle$ and a small modulation $u(t)$:

$$x(t) = \langle v\rangle t + u(t) \tag{2.17}$$

with $|u| \ll \pi$. Thus Eq. (2.16) can be rewritten as

$$\ddot{u} + \eta\langle v\rangle + \eta\dot{u} = F - U_0 \sin(\langle v\rangle t + u). \tag{2.18}$$

Since u is very small we can expand the sin term up to first order in u:

$$\ddot{u} + \eta\langle v\rangle + \eta\dot{u} \simeq F - U_0 \sin(\langle v\rangle t) - U_0 \cos(\langle v\rangle t)u. \tag{2.19}$$

Averaging Eq. (2.19) and noting that $\langle \ddot{u}\rangle = 0$ and $\langle \dot{u}\rangle = 0$, we obtain

$$F - \eta\langle v\rangle = U_0\langle u \cos(\langle v\rangle t)\rangle. \tag{2.20}$$

Thus we can approximate Eq. (2.19) by

$$\ddot{u} + \eta\dot{u} \simeq -U_0 \sin(\langle v\rangle t), \tag{2.21}$$

which can be solved for u giving

$$u(t) = U_0 \frac{\sin(\langle v\rangle t + \phi)}{\langle v\rangle(\langle v\rangle^2 + \eta^2)^{1/2}}, \tag{2.22}$$

where $\tan\phi \equiv \eta/\langle v\rangle$. Plugging the solution (2.22) into Eq. (2.20) and noting that

$$\begin{aligned}
\langle u \cos(\langle v\rangle t)\rangle &= U_0 \frac{\cos\phi\langle\cos(\langle v\rangle t)\sin(\langle v\rangle t) > + \sin\phi\langle\cos^2(\langle v\rangle t)\rangle}{\langle v\rangle(\langle v\rangle^2 + \eta^2)^{1/2}} \\
&= \frac{U_0 \sin\phi}{2\langle v\rangle(\langle v\rangle^2 + \eta^2)^{1/2}} \\
&= \frac{U_0\eta}{2\langle v\rangle(\langle v\rangle^2 + \eta^2)},
\end{aligned} \tag{2.23}$$

we obtain

$$F = \eta\langle v\rangle + \frac{U_0^2\eta}{2\langle v\rangle(\langle v\rangle^2 + \eta^2)} \simeq \eta\langle v\rangle\left(1 + \frac{U_0^2}{2\langle v\rangle^4}\right), \tag{2.24}$$

where we have neglected the term η^2 with respect to $\langle v\rangle^2$ in the denominator. The nonlinear friction force $F - \eta\langle v\rangle$ has in this case a $1/\langle v\rangle^3$ (or $1/F^3$) dependence:

$$\boxed{F - \eta\langle v\rangle \simeq \frac{U_0^2\eta}{2\langle v\rangle^3} \simeq \frac{U_0^2\eta^4}{2F^3}} \qquad F \gg U_0. \tag{2.25}$$

Inverting Eq. (2.24) and using $F = \eta\langle v\rangle$, we can express $\langle v\rangle$ as a function of F:

$$\boxed{\langle v\rangle = \frac{F}{\eta}\left(1 - \frac{U_0^2\eta^4}{2F^4}\right)} \qquad F \gg U_0. \tag{2.26}$$

Notice that the approximation we have made in Eq. (2.24) implies that Eqs. (2.25) and (2.26) are valid only for small damping with respect to the drift velocity, i. e. $\eta \ll \langle v\rangle$. Fig. 2.6 shows the velocity-force characteristic and the nonlinear friction force obtained by

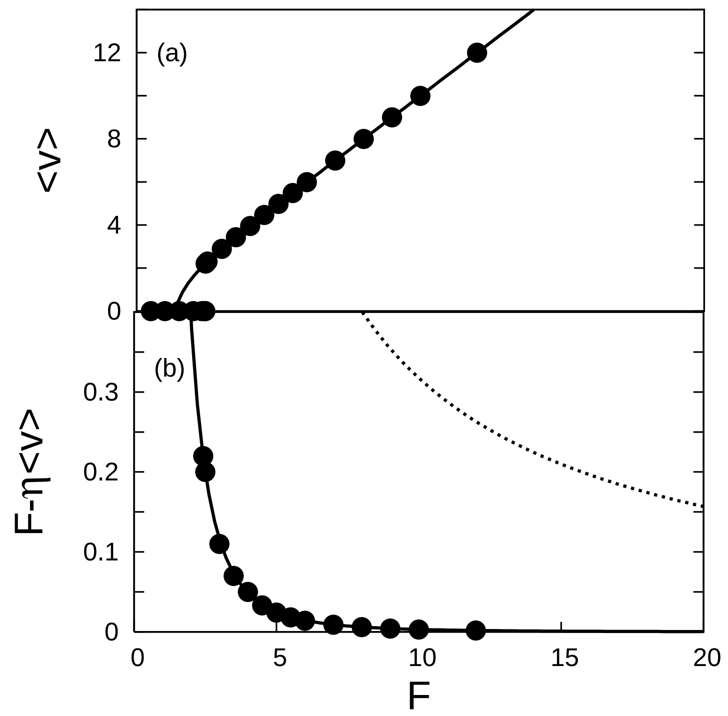

Figure 2.6: Velocity-force characteristic (a) and nonlinear part of the friction force $F-\eta\langle v\rangle$ (b) as a function of F, at $T=0$, in the case of moderate damping ($\eta=1$ and $U_0=2.5$). The solid circles are obtained by numerical simulations, while the solid lines in (a) and (b) are obtained from Eqs. (2.26) and (2.25) respectively. The dotted line in (b), given by the second equation (2.13), does not correctly describe the nonlinear friction in this damping regime.

numerical simulations together with the analytic form predicted by Eqs. (2.25) and (2.26), revealing a very good agreement between them. On the other, as it can be seen from Fig. 2.6(b), the overdamped expression Eq. (2.13) drastically fails to reproduce the result of the simulation. From these findings, it appears that there should be a transition between the $1/F^3$ and $1/F$ behaviour of the nonlinear friction by increasing the value of the damping. In fact, for an intermediate value of the damping parameter, both Eqs. (2.13) and (2.25) are ineffective to describe the behaviour of $F-\eta\langle v\rangle$ for all the range of forces: expression (2.13) can reproduce the behaviour at smaller forces, while at larger forces the nonlinear friction is more accurately fitted by the $1/F^3$ tail (see Fig. 2.7).

At the beginning of this subsection we have mentioned that a critical force F_{c1} exists for the particle to pass from the locked to the running state. This is true when the particle starts at rest from the potential minimum and the force is increased starting from $F=0$. What happens when we decrease the force adiabatically (i. e. in small steps) starting

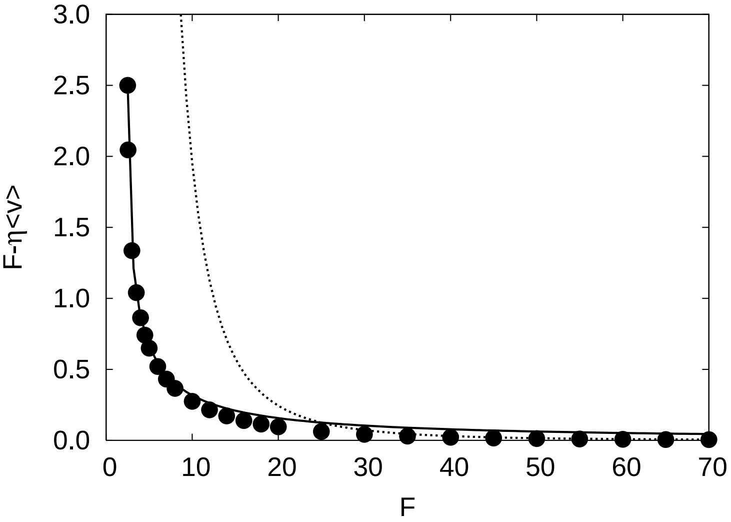

Figure 2.7: Nonlinear part of the friction force $F - \eta\langle v\rangle$ as a function of F, at $T = 0$, for an intermediate value of the damping ($\eta = 5$ and $U_0 = 2.5$). The solid circles are the result of numerical simulations, the solid line is obtained by using the expression of $\langle v\rangle$ for the overdamped case (Eq. (2.13)) and the dotted line is the analytic curve Eq. (2.25). It is evident the crossover between two kinds of behaviour at small and large forces.

from the running state? This is shown in Fig. 2.8, where the increasing and decreasing force curves are indicated by the arrows. It is immediately seen that decreasing the force results in the same velocity-force characteristic for $F > F_{c1}$, but in a strikingly different behaviour for $F < F_{c1}$. This is due to the fact that, for not too high damping, a bistability between the locked and running solution exists for $F < F_{c1}$. In this region the particle is either locked or running depending on its initial velocity. A second critical force F_{c2} can be identified where the mobility vanishes upon decreasing the force. In other words, when the force is decreased, the particle has already an initial excess kinetic energy that enables it to move even when $F < F_{c1}$, and when $F = F_{c2}$ the drift velocity abruptly vanishes. This results in a hysteretic behaviour of the velocity-force characteristic. The condition for the occurrence of hysteresis is found to be $\eta/\sqrt{U_0} < 1.19$ [6] and the value of the critical force F_{c2}, for very small η ($\eta \ll \sqrt{U_0}$), is related to the model parameters by the formula

$$F_{c2} = 4\sqrt{U_0}\eta/\pi. \tag{2.27}$$

2.3 Mobility at finite temperature

Now we turn to the problem of driven motion in the presence of thermal fluctuations, which is described by the Langevin equation Eq. (2.2). As already mentioned in Sec. 1.6, the Langevin equation represents an effective way to deal with thermal fluctuations, which treats the substrate as a thermal bath pumping thermal energy to the adsorbate.

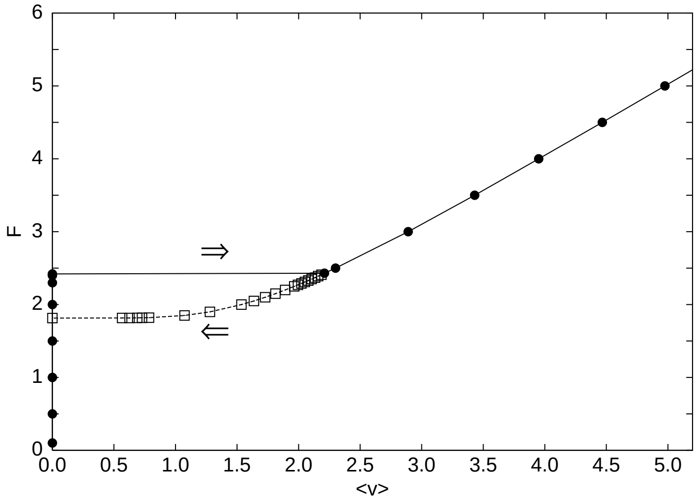

Figure 2.8: Velocity-force characteristic at $T = 0$, $U_0 = 2.5$ and $\eta = 1$. The solid circles are the points obtained increasing the force from the locked state, while the open squares are obtained by decreasing the force from the running state. Notice the hysteresis between the locked and the running solution for $F < F_{c1} \equiv U_0$. In this case $F_{c2} \simeq 1.815$ is slightly smaller than the value predicted by Eq. (2.27), i. e. $F_{c2} \simeq 2$, because the condition $\eta \ll \sqrt{U_0}$ is not satisfied.

2.3.1 Mapping to the Fokker-Planck equation

The theoretical analysis of the Langevin equation was first performed by Kramers already in 1940 in the celebrated paper "Brownian motion in a Field of Force and the Diffusion Model of Chemical Reactions" [13]. The primary interest of Kramers was to model rate processes in chemical reactions by the motion of a particle in a $1D$ double-well potential, where the coordinate x corresponds to the reaction coordinate: the purpose was to calculate the transition rate from one metastable state to the other, improving the Transition State Theory (TST), which was the simplest approach widely used in the chemical physics community. Thus, he pictured the escape process as governed by Brownian motion dynamics driven by thermal forces, connected with friction and temperature by means of Eq. (2.3).

The Langevin equation can be mapped to a Fokker-Planck equation for the probability distribution function $P(x, v, t)$ (i. e. the probability to find the particle at position x and with velocity v at time t), which is also known as Klein-Kramers equation [6, 7, 13, 14]:

$$\frac{\partial P(x,v,t)}{\partial t} = \left[-\frac{\partial}{\partial x} v + \frac{\partial}{\partial v} \left(U'_{tot}(x) + \eta v \right) + \eta k_B T \frac{\partial^2}{\partial v^2} \right] P(x,v,t). \tag{2.28}$$

The first term on the right hand side of Eq. (2.28) represents a drift diffusion, the second term comes from the velocity dependent force $-\left(U'_{tot}(x) + \eta v\right)$ in Eq. (2.2), and the last term accounts for thermal fluctuations assuming a white noise satisfying Eq. (2.3).

Kramers' analysis of Eq. (2.28) was restricted to the case

$$k_B T \ll E_b, \tag{2.29}$$

where E_b is the diffusion barrier, i. e. the difference in energy between one local minimum (metastable state) and its adjacent maximum (unstable state). In this situation the random force is acting only as a small perturbation, and the particle will relax towards one of the minima of the potential U_{tot} and will stay there for an extremely long time until eventually it will be kicked by the random force into a neighbouring metastable state. This is a rare event, occurring however in a finite time, which is called the escape time. In this limit, it is possible to separate the time scales, e.g. the escape time is much larger than the other typical time scales involved in the problem, for example the time associated with the motion of the particle inside the potential well. When Eq. (2.29) is satisfied, the diffusive motion of the particle is said to be *activated*. On the other hand, if the thermal energy $k_B T$ is comparable with the diffusion barrier, the particle can move almost freely between metastable states and there is no separation of time scales: in this situation Kramers' rate description makes no sense, and thus we will not consider this case here. In our problem $U_{tot}(x)$ is a tilted periodic potential given by Eq. (2.7). This potential is different from the prototypical case considered by Kramers, because it contains an external driving term, representing an energy source for the system. Thus Eq. (2.28) can be written as

$$\frac{\partial P(x,v,t)}{\partial t} = \left[-\frac{\partial}{\partial x} v + \frac{\partial}{\partial v} \left(U_0 \sin x - F + \eta v \right) + \eta k_B T \frac{\partial^2}{\partial v^2} \right] P(x,v,t). \tag{2.30}$$

In his work, Kramers analysed separately the regimes of strong and weak damping η, considering also the case of moderate damping. For all these three situations he gave the explicit analytic expression of the transition rate R for the particle to go from one metastable state to next, overcoming the diffusion barrier E_b. We will also consider these three damping regimes separately in the following. In the case of the driven motion of the dimer the relation between the transition rate and the average drift velocity is

$$\langle v \rangle = aR = 2\pi R. \tag{2.31}$$

Qualitatively we expect that in presence of thermal fluctuations the particle has always the chance to overcome the diffusion barrier, even at very small driving forces. This means that $\langle v \rangle$ should go to zero continuously as $F \to 0$, or in other words $F_{c1} = 0$. The idea is that the noise provided by stochastic force is responsible for transitions between the locked and the running state, which make both the threshold related to the diffusion barrier and the hysteresis related to the bistability disappear. The fact that drift motion is attained even for very small forces at finite temperature can be appreciated in Fig. 1.16(a).

2.3.2 Highly overdamped case

The overdamped case is of interest for some applications, such as dc Josephson junctions and transport of charged particles, which can be modelled by Eq. (2.2) neglecting the inertial term $\ddot{x}$ in Eq. (2.2). For very strong damping, the thermal relaxation is much shorter than the spatial diffusion time (*spatial-diffusion-limited* regime), thus we can integrate out the velocity in the Fokker-Planck equation (2.28) by defining the reduced probability

$$P(x,t) = \int_{-\infty}^{\infty} P(x,v,t)dv, \tag{2.32}$$

which is simply the distribution function for x. The time evolution of $P(x,t)$ is governed by the Smoluchowski equation (see for example Ref. [6]), which, for the potential U_{tot} defined by Eq. (2.7), has the form

$$\frac{\partial P(x,t)}{\partial t} = \frac{1}{\eta}\frac{\partial}{\partial x}\left(U_0 \sin x - F\right)P(x,t) + \frac{k_B T}{\eta}\frac{\partial^2 P(x,t)}{\partial x^2}. \tag{2.33}$$

In order to determine the steady-state transition rate R, the original idea of Kramers was to consider a steady state situation in which a steady probability current from one local minimum to the next is maintained by sources and sinks. The sources provide particles at energy few times $k_B T$ below the diffusion barrier E_b, which thermalize and eventually leave the well, overcoming the barrier. Following this argument, the escape rate R is given by the total probability current j divided by the population n_0 of particles at the potential well:

$$R = j/n_0. \tag{2.34}$$

It is possible to show that the stationary probability distribution $P_{st}(x)$ of the Smoluchowski equation (2.33) is

$$P_{st}(x) = \frac{\eta j}{k_B T}\exp(-U_{tot}(x)/k_B T)\int_{x}^{x_+}\exp(U_{tot}(y)/k_B T)dy, \tag{2.35}$$

where x_+ is the position of the sink. Since $n_0 = \int_{-\infty}^{x_{max}} P_{st}(x)dx$, R^{-1} becomes

$$R^{-1} = \int_{-\infty}^{x_{max}}\exp(-U_{tot}(x)/k_B T)dx\int_{x}^{x_+}\frac{\exp(U_{tot}(y)/k_B T)}{k_B T/\eta}dy, \tag{2.36}$$

where x_{max} is the location of the local maximum of the potential. Assuming the condition for activated behaviour $E_b \gg k_B T$, it can be shown that Eq. (2.36) becomes

$$R = \frac{(\omega_{min}|\omega_{max}|)}{2\pi\eta}\exp(-E_b/k_B T), \tag{2.37}$$

where ω_{min} and ω_{max} are the oscillations frequency at the minimum and at the maximum of U_{tot} respectively. Coming back to our problem, where U_{tot} is given by Eq. (2.7), we can easily calculate ω_{min}, ω_{max} and E_b. We find

$$\omega_{min} = |\omega_{max}| = \omega_{sub}(1 - F^2/U_0^2)^{1/4} \tag{2.38}$$

(notice that ω_{max} is imaginary) and

$$E_b = U_{tot}(x_{max}) - U_{tot}(x_{min}) = 2U_0\left(\sqrt{1-\frac{F^2}{U_0^2}} - \frac{F}{U_0}\arccos\left(\frac{F}{U_0}\right)\right). \tag{2.39}$$

As expected, $E_b(F=0)=2U_0$. Moreover, Eq.(2.39) contains the fact that the barrier disappears when $F>U_0$, since the argument of the square root becomes negative: this is in agreement with the discussion presented at the beginning of subsection 2.2.2. Thus finally we have, according to Eq. (2.31), that the drift velocity in the steady state is related to the driving force by

$$\boxed{\langle v\rangle = \frac{U_0\sqrt{1-\frac{F^2}{U_0^2}}}{\eta}\exp(-E_b(F)/k_BT)} \qquad E_b \gg k_BT, \quad \eta \gg \sqrt{U_0} \tag{2.40}$$

with $E_b(F)$ given by Eq. (2.39). The comparison between the simulations and Eq. (2.40) is reported in Fig. 2.9 for two values of U_0. It is clearly seen that Eq. (2.40) well reproduces the simulation results at low forces for large U_0, but fails when U_0 becomes comparable to the thermal energy.

Corrections to the original result of Kramers Eq. (2.40) have been proposed on the basis of perturbative expansions in $1/\eta$ [12, 15]. Exact results for the overdamped case, which are based on the solution of the steady-state Smoluchowski equation, have been reported by different authors [10, 16, 17]. Parris et al. [17] obtained an expression for the mobility that is applicable to any temperature and any kind of potential:

$$\langle v\rangle = (1-\exp(-Fl/k_BT))\frac{k_BT/\eta}{\int_0^l \exp(-Fy/k_BT)C(l,y)dy}. \tag{2.41}$$

The finite-space correlation function $C(l,y)$ in Eq. (2.41) is given by

$$C(l,y) = \frac{1}{l}\int_0^l \exp\left(-\frac{U_{sub}(x)-U_{sub}(x+y)}{k_BT}\right)dy, \tag{2.42}$$

where l is a typical length of the system. For a sinusoidal potential, where $l=a=2\pi$, the correlation function can be easily calculated and Eq. (2.41) becomes

$$\boxed{\langle v\rangle = (1-\exp(-2\pi F/k_BT))\frac{k_BT/\eta}{\int_0^{2\pi}\exp(-Fy/k_BT)I_0\left(\frac{2U_0}{k_BT}\sin\left(\frac{y}{2}\right)\right)dy}} \tag{2.43}$$

where $I_0(z)$ is the modified Bessel function of order 0 [18]. Notice that from Eq. (2.43) we recover the linear behaviour in the limit of large forces $F \gg U_0$. In fact, $I_0(z)\simeq 1$ for small z, $\exp(-2\pi F/k_BT)\simeq 0$ in the numerator for large force, and

$$\int_0^{2\pi}\exp\left(-\frac{Fy}{k_BT}\right)dy = \frac{k_BT}{F}\left[1-\exp\left(-\frac{2\pi F}{k_BT}\right)\right] \simeq \frac{k_BT}{F}$$

in the denominator. Thus

$$\langle v\rangle \simeq F/\eta \qquad F \gg U_0. \tag{2.44}$$

The analytical expression (2.43) is plotted in Fig. 2.9 together with the results of the simulations and Kramers' rate equation (2.40). While Kramers' rate theory has a limited

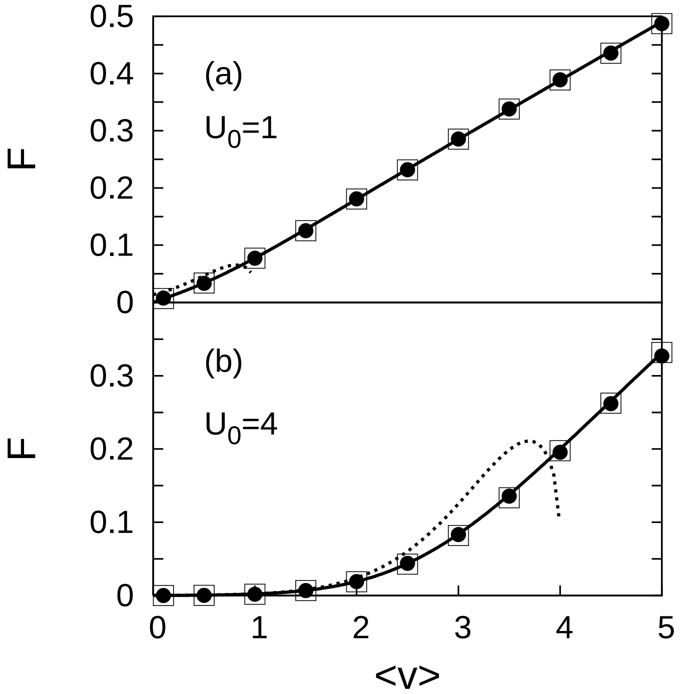

Figure 2.9: Velocity-force characteristic at finite temperature ($k_BT = 1$) in the overdamped case ($\eta = 10$) for $U_0 = 1$ (a) and $U_0 = 4$ (b). The solid circles and the open squares are obtained by simulations of the Langevin equation (2.2) without and with the inertial term $\ddot{x}$ respectively, the dotted lines are given by the Kramers' analytical expression Eq. (2.40) and the solid lines represent the exact result Eq. (2.43). While the latter describes the simulation results very well in the whole range of forces, Kramers' expression fails for large forces and when U_0 becomes comparable to the thermal energy. Notice that for this high value of η the simulations of the full Langevin equation produce results which are almost indistinguishable from those obtained by neglecting the inertial term in Eq. (2.2).

range of application, Eq. (2.43) can reproduce the results of the simulations very accurately for any value of F and U_0. Moreover, as shown in Fig. 2.9, the simulations of the complete equation (2.2) (including the inertial term) give results that are practically identical to those obtained by considering the overdamped equation, meaning that the approximation of neglecting the inertial term is very well justified for high values of the damping. However, when η is decreased, Eq. (2.43) becomes less and less accurate and for generic values of the damping one has to develop different approaches to correctly describe the mobility (see Sec. 2.3.4). This can be appreciated in Fig. 2.10, where the relation between $\langle v \rangle$ and F is plotted for different η both for the simulations and the analytic formula (2.43).

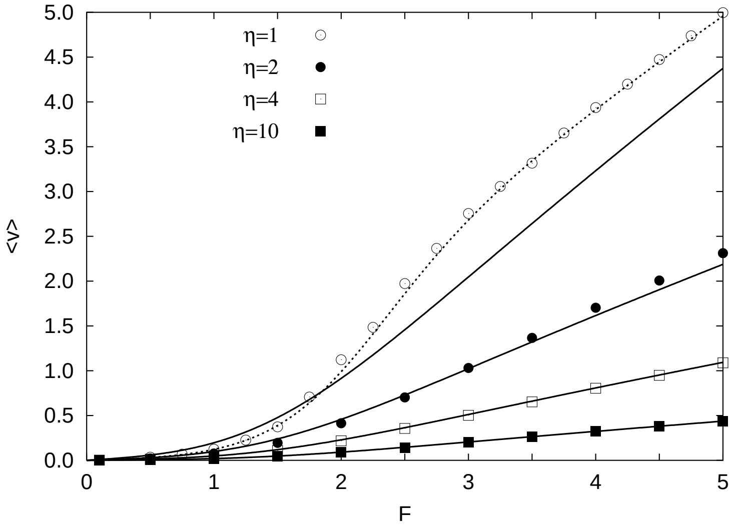

Figure 2.10: Velocity-force characteristic at finite temperature ($k_BT = 1$) for $U_0 = 2.5$ and different values of the damping. The symbols are the results of the simulations, while the solid lines are obtained by the analytic expression Eq. (2.43) for the overdamped case and the dotted line by the matrix continued-fraction method Eq. (2.62) for $\eta = 1$. Note that the solid curves become less accurate in describing the behaviour of the mobility as the damping is decreased. In particular, for $\eta = 1$, the matrix continued-fraction method provides a much better agreement.

2.3.3 Highly underdamped case

In the case of very low η the particle is exposed to very little damping and very little noise and, as a result, it will follow the unperturbed conservative equations of motion for a long time. Thus the energy or, equivalently, the action

$$I(E) = m \int v dx \tag{2.45}$$

is almost constant along the trajectory, compared with the rapidly changing angle variable ϕ (*energy-diffusion-limited* regime). Then, starting from Eq. (2.28), the averaging procedure over the angle ϕ will yield a diffusion equation for the probability density of the action [13]:

$$\frac{\partial P}{\partial t}(I,t) = \eta \frac{\partial}{\partial I} I \left(1 + \frac{2\pi k_B T}{\omega(I)} \frac{\partial}{\partial I}\right) P, \tag{2.46}$$

where $\omega(I)$ is the angular frequency at the action I:

$$\frac{\partial E}{\partial I} = \frac{\omega(I)}{2\pi}. \tag{2.47}$$

It can be immediately seen from Eq. (2.46) that the stationary probability distribution $P_{st}(I)$ is linked to the probability current j by

$$j = -\eta I \left(1 + \frac{2\pi k_B T}{\omega(I)} \frac{\partial}{\partial I}\right) P_{st}(I) \qquad 0 < I \leq I_b \tag{2.48}$$

where $I_b \equiv I(E_b)$. The first term in Eq. (2.48) represents the relaxation due to damping and describes a downward drift in energy towards the local minimum, while the second term is the effect of thermal fluctuations and describes the diffusive process which permits particles to get away from the potential minimum. Imposing $P_{st}(I_b) = 0$ (absorption of particles overcoming the diffusion barrier) and using Eq. (2.47), one finds from Eq. (2.48)

$$P_{st}(I) = j(\eta k_B T)^{-1} \exp(-E(I)/k_B T) \int_I^{I_b} \frac{\exp(E(I')/k_B T)}{I'} \frac{\omega(I')}{2\pi} dI'. \tag{2.49}$$

At $T = 0$, $P_{st}(I)$ has a logarithmic singularity originated from the fact that the probability source is concentrated at $I = 0$. However, for $E_b/k_B T \gg 1$, this singularity does not contribute to the population n_0 in the well:

$$n_0 = \int_0^{I_b} P_{st}(I) dI. \tag{2.50}$$

Using Eqs. (2.31), (2.34), (2.48) and (2.50), in the limit $E_b/k_B T \gg 1$, the expression for the drift velocity becomes

$$\boxed{\langle v \rangle = \frac{\eta I_b \omega_{min}}{k_B T} \exp(-E_b/k_B T)} \qquad E_b/k_B T \gg 1, \quad \eta I_b \ll k_B T. \tag{2.51}$$

Note the proportionality between $\langle v \rangle$ and the damping η. For the driven monomer in a sinusoidal potential, ω_{min} has the form (2.38), E_b obeys Eq. (2.39) and, for F close to U_0, I_b is given by [19]

$$I_b = \frac{24}{5} \sqrt{U_0} [2(1 - F/U_0)]^{5/4}. \tag{2.52}$$

Büttiker et al. extended Kramers' treatment for the highly underdamped limit to cover a wider range of damping constants, taking into account that at energies just above E_b, the stationary distribution is controlled both by uphill diffusion in energy and by flow out of the well [20]. This case is of interest to understand the voltage-current characteristics in extremely underdamped Josephson-junction circuits and to model chemical reactions, where the damping is usually very small. The final result for the drift velocity is

$$\langle v \rangle = \frac{[1 + (4\alpha k_B T/\eta I_b)]^{1/2} - 1}{[1 + (4\alpha k_B T/\eta I_b)]^{1/2} + 1} \frac{\eta I_b \omega_{min}}{k_B T} \exp(-E_b/k_B T), \tag{2.53}$$

where $\alpha \simeq 1$. For $\eta \to 0$, Eq. (2.53) reduces to Eq. (2.51).

Generally, Kramers-like approximations for the transition rate are not always good and they have a limited range of validity. This can be clearly observed in Fig. 2.11, where we show the velocity-force characteristic for two values of U_0 and for a very small value of η. Eq. (2.53) is only slightly different from Kramers' original result Eq. (2.51), and both of them overlap with the results of the simulations for $F \to 0$, but cannot reproduce the behaviour of the mobility when the force is increased. This is due to the fact that both

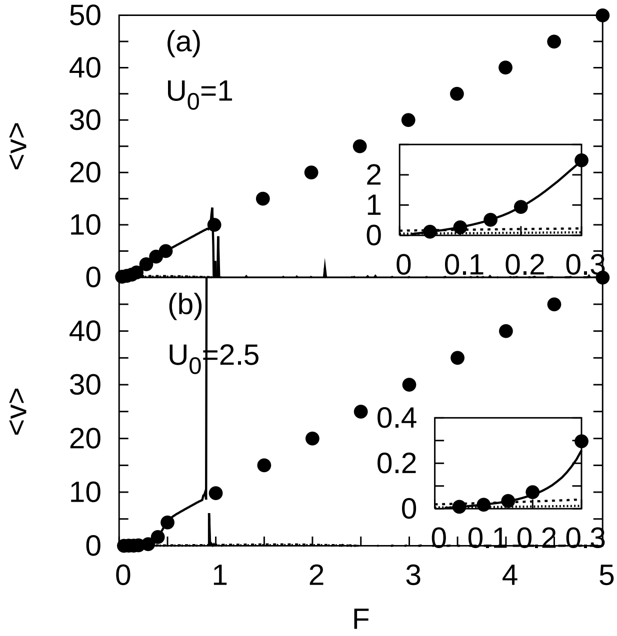

Figure 2.11: Velocity-force characteristic at finite temperature ($k_B T = 1$) in the strongly underdamped case ($\eta = 0.1$) for $U_0 = 1$ (a) and $U_0 = 2.5$ (b). The solid circles are obtained by numerical simulations of Eq. (2.2), while the dashed and dotted lines are the analytical expressions Eqs. (2.51) and (2.53) respectively. Note that the agreement between the analytic results and the simulations is good only for very small forces (see insets) and for large U_0. The solid lines are the expressions of the matrix continued-fraction method Eq. (2.62): they can describe the mobility quite well for not too large forces ($F < 1$), but fail for larger values of F due to the instability of the continued fraction for small η, signalled by the divergence at $F \simeq 1$.

the conditions expressed in Eq. (2.51) have to be satisfied at the same time, restricting the range of forces for its applicability. For large U_0 this range is expected to be larger.

2.3.4 Arbitrary damping

Kramers developed a theory also in the case of arbitrary (moderate) damping [13]. After calculating the stationary probability distribution function $P_{st}(x,v)$ that satisfies the steady state of Eq. (2.30), it is possible to find the expressions of the probability current $j = \int_{-\infty}^{\infty} vP_{st}(x_{max},v)dv$ and of the population in the well $n_0 = \int_{-\infty}^{x_{max}} P_{st}(x,v)dxdv$, which give easily the transition rate R using Eq. (2.34). The final celebrated result is

$$R = \frac{\omega_{min}}{2\pi|\omega_{max}|}\left[\left(\frac{\eta^2}{4}+|\omega_{max}|^2\right)^{1/2}-\frac{\eta}{2}\right]\exp(-E_b/k_BT) \qquad E_b \gg k_BT. \tag{2.54}$$

In the limit of large damping $\eta \gg |\omega_{max}|$, Eq. (2.54) reduces to the overdamped expression Eq. (2.37). In the limit $\eta \to 0$, Eq. (2.54) can be approximated by the result of the TST [21]:

$$R_{TST} = \frac{\omega_{min}}{2\pi}\exp(-E_b/k_BT) \qquad E_b \gg k_BT. \tag{2.55}$$

In this limit, the transition rate does not depend on the damping. Using Eq. (2.31), the drift velocity $\langle v\rangle$ as a function of the driving force is given by

$$\boxed{\langle v\rangle = \frac{\omega_{min}}{|\omega_{max}|}\left[\left(\frac{\eta^2}{4}+|\omega_{max}|^2\right)^{1/2}-\frac{\eta}{2}\right]\exp(-E_b/k_BT)} \qquad E_b \gg k_BT. \tag{2.56}$$

Eq. (2.56) is derived under the assumption that the motion is activated, which is satisfied for $E_b \gg k_BT$, i. e. for small values of the driving force. For large forces the role of thermal fluctuations becomes less important and the argument presented in Sec. 2.2.2, leading to Eq. (2.26), can be applied for finite T as well, resulting in a F^{-3} correction to the linear behaviour.

A different method to calculate the mobility at finite temperature has been introduced by Risken [6]. It consists in expanding the stationary solution of the Fokker-Planck equation in Hermite functions ψ_n:

$$P_{st}(x,v) = \psi_0(v)\sum_{n=0}^{\infty} c_n(x)\psi_n(v). \tag{2.57}$$

From the normalization of P_{st} it is immediately seen that $c_0 = (2\pi)^{-1}$. Inserting the expansion (2.57) into the Fokker-Planck equation (2.28), a hierarchy of equations for the coefficients c_n is obtained. From the first equation of this hierarchy it follows that $c_1(x) = c = \text{const}$. The drift velocity is directly connected to c:

$$\langle v\rangle = \int_0^{2\pi}\int_{-\infty}^{\infty} vP_{st}(x,v)dxdv = \int_0^{2\pi}\int_{-\infty}^{\infty} v\psi_0(v)\sum_{n=0}^{\infty} c_n(x)\psi_n(v)dxdv = \sqrt{k_BT}2\pi c. \tag{2.58}$$

In order to solve the hierarchy of equations Risken proposed to expand the periodic coefficients c_n into a truncated Fourier series:

$$c_n(x) = (2\pi)^{-1/2} \sum_{p=-Q}^{Q} c_n^p \exp(ipx). \tag{2.59}$$

After some lengthy calculations, a relation between c_0^p and a matrix H is found:

$$c_0^p = H^{p0} c\sqrt{2\pi}. \tag{2.60}$$

H is the matrix continued fraction:

$$\mathbf{H} = -\eta\hat{\mathbf{D}}^{-1}\left\{\mathbf{I} - \frac{1}{\eta^2}\mathbf{D}\left[\mathbf{I} - \frac{1}{2\eta^2}\mathbf{D}\left[\mathbf{I} - \frac{1}{3\eta^2}\mathbf{D}[\mathbf{I}...]^{-1}\hat{\mathbf{D}}\right]^{-1}\hat{\mathbf{D}}\right]^{-1}\hat{\mathbf{D}}\right\}, \tag{2.61}$$

where **I** represents the identity matrix. The normalization condition requires $c_0^0 = (2\pi)^{-1/2}$, so that the drift velocity (2.58) is given by

$$\langle v\rangle = \sqrt{k_BT}2\pi c = \sqrt{k_BT}/H^{00}. \tag{2.62}$$

Thus, the main task in determining the drift velocity is calculating the matrix continued fraction (2.61) and this is the reason for which this approach is called *matrix continued-fraction method* (MCFM). To evaluate this infinite continued fraction, Eq. (2.61) is approximated by its Nth approximant. N and the truncation number Q are determined in such a way that a convergence of $\langle v\rangle$ within a certain accuracy is obtained. It turns out that $N_0 = 20\sqrt{k_BT}/\eta$ and $Q = 12$ are sufficient to give accurate results up to $U_0 = 4$[6]. A comparison of $\langle v\rangle$ obtained by Eq. (2.62) with the simulations and with the overdamped expression (2.43) for $\eta = 1$ is displayed in Fig. 2.10. It is clear that the MCFM reproduces the behaviour of the mobility very well, and gives a very good agreement where the overdamped approach fails. However, the MCFM shows problems for very small η, since in this situation the convergence of the continued fraction is not always guaranteed. This is clearly seen in Fig. 2.11, where the MCFM can accurately describe the simulations for small F, but it is not applicable for $F > 1$. An instructive example of all the approximations presented in this subsection is shown in Fig. 2.12 for a moderate value of the damping ($\eta = 1$ and $U_0 = 2.5$).

2.4 Purely thermal diffusion

2.4.1 Determination of the diffusion coefficient

So far we have analysed the motion of a monomer under the action of an external driving. Now we consider the situation $F = 0$, $v_0 = 0$ and $T \neq 0$, i. e. the case in which the motion of the particle on the substrate is only due to thermal effects. This is the problem of purely thermal diffusion, which is very important in surface science, in particular for

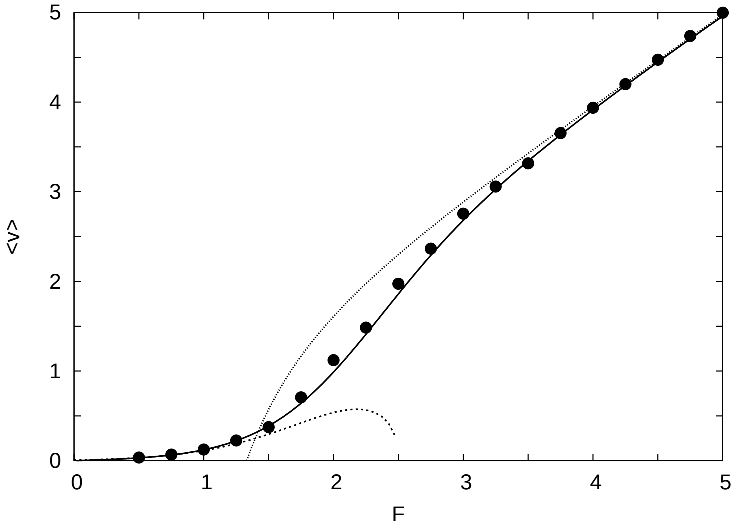

Figure 2.12: Velocity-force characteristic at finite temperature ($k_BT = 1$) for a moderate value of the damping ($\eta = 1$ and $U_0 = 2.5$). The solid circles are obtained by numerical simulations, the dashed line is the Kramers' expression Eq. (2.56), the dotted line is the analytical behaviour for large forces given by Eq. (2.26) and the solid line is the evaluation of the drift velocity from Eq. (2.62) using the MCFM. While the validity of Kramers' theory is restricted to small forces, the MCFM can give a reasonable description of the numerical data in the whole range of applied forces. Notice the F^{-3} correction to the linear behaviour at large forces ($F > 4$) expressed by Eq. (2.26).

crystal growth, where the diffusion of the adatoms along the steps can influence the kinetics of the growth process. Here we will mainly focus on the diffusion of an adatom in $1D$. The case $F = 0$ was indeed the problem originally treated by Kramers for a metastable potential well [13]. The diffusive motion of the adatom is characterized by the diffusion coefficient D, which is defined from the mean square displacement $\langle x^2(t)\rangle$ as

$$D = \lim_{t\to\infty} \frac{\langle x^2(t)\rangle}{2t}. \tag{2.63}$$

For low enough temperatures ($k_BT \ll E_b$, where $E_b = 2U_0$), the diffusion proceeds by uncorrelated thermally activated jumps and the diffusion coefficient has an Arrhenius dependence on the activation energy E_b with prefactor D_0:

$$\boxed{D = D_0 \exp(-E_b/k_BT).} \tag{2.64}$$

The activation energy is the crucial quantity related to the activated motion and can be measured experimentally using the techniques outlined in Sec. 1.3 [22] or it can be calculated by *ab initio* simulations with reasonable accuracy (see Sec. 1.5) [23]. Typically the prefactor D_0 ranges from 10^{-1} to 10^{-5} cm^2/s, and the activation energy varies between 0.1 and 1 eV (for example in the case of diffusion of Pt adatoms on Pt(111) it was found $D_0 = 2 \cdot 10^{-3}$ cm^2/s and $E_b = 0.26$ eV [24]). D_0 contains the real dynamical information and in general it depends on the damping η, which characterizes the strength of the coupling to the substrate excitations. The Arrhenius behaviour is valid both in the overdamped and underdamped case, as it can be seen by taking the appropriate limits of the exact results. In fact, it is known that [6]

$$D = k_B T \lim_{F \to 0} \mu, \tag{2.65}$$

where μ is the mobility defined in Eq. (2.9). For the overdamped case it was found that Eq. (2.65) assumes the form [10]

$$D = D_f I_0^{-2}(U_0/k_B T), \tag{2.66}$$

where $D_f \equiv k_B T/\eta$ is the diffusion coefficient for the Brownian motion of a free particle (without external potential). From Eq. (2.66) the Arrhenius dependence at low temperatures ($k_B T \ll E_b$) follows:

$$D \simeq \frac{E_b}{2\eta} \exp\left(-\frac{E_b}{k_B T}\right). \tag{2.67}$$

On the other hand, when $E_b/k_B T$ is small, the particle diffuses almost freely:

$$D \simeq D_f[1 - (E_b/k_B T)^2/8]. \tag{2.68}$$

In the underdamped limit $\eta \to 0$ it was shown by Risken [6] that

$$D = D_f G(E_b/k_B T), \tag{2.69}$$

with

$$G(x) = (x/2\pi)^{1/2} \exp(x) I_0^{-1}(x) J(x),$$

where $J(x) = \int_0^1 du u^{-3/2} \exp(-2x/u) \mathbf{E}^{-1}(u)$ and $\mathbf{E}(u)$ is the complete elliptic integral of the second kind. The limit for low temperatures of Eq. (2.69) gives an Arrhenius behaviour as well, with the same activation energy but with a different prefactor:

$$D \simeq \pi D_f/2 \exp(-E_b/k_B T). \tag{2.70}$$

Fig. 2.13 shows a plot of the diffusion coefficient as a function of $E_b/k_B T$ as obtained by numerical simulations, together with the Arrenhius plot: it is seen that the data follow the Arrenhius behaviour for large E_b ($E_b/k_B T > 3$), while a deviation due to finite barrier effects at small E_b is found. In general, the diffusion coefficient can be found numerically with practically any desired accuracy using the MCFM presented in Sec. 2.3.4.

2.4.2 Long jumps in surface diffusion

From what we have just said, the diffusion coefficient seems to be univocally related to the adatom/surface system. However, the question is much more complex, since the Kramers' problem in a periodic potential is qualitatively different from the escape problem

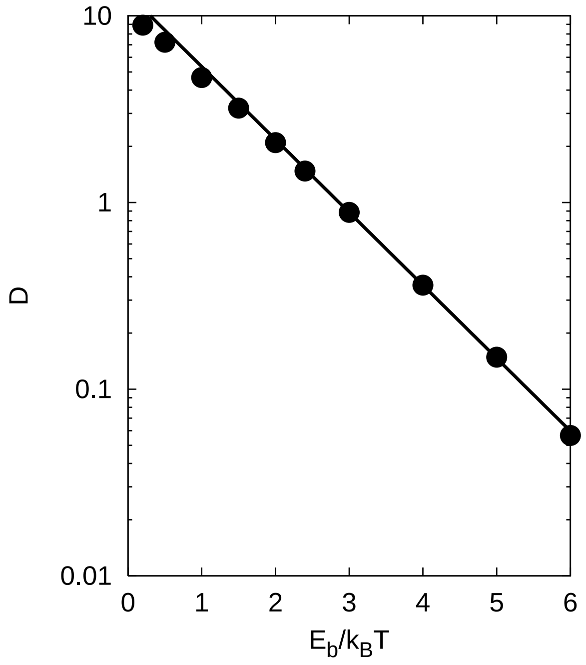

Figure 2.13: Plot of the diffusion coefficient as a function of the rescaled energy barrier for the underdamped case $\eta = 0.1$. The solid circles are obtained by numerical simulations, while the solid line an Arrenhius plot of the form $D = D_0 \exp(-E_b/k_BT)$, where $D_0 \propto 1/\eta$ and E_b/k_BT is the rescaled activation energy. The data follow the Arrhenius behaviour only for small enough temperatures ($k_BT < 3E_b$), while at high temperatures a deviation from the exponential (i. e. from the linear slope in lin-log scale) is observed, due to finite barrier effects.

out of a metastable well, to which most of Kramers' work was devoted. In fact, the periodic potential is multistable and the escaped particle may again be trapped, due to the presence of thermal fluctuations, in any other well; this means that jumps of a single lattice spacing or of many lattice spacings are possible. In the overdamped regime, most of the energy is dissipated in the jumps from one potential well to the other and the long-time dynamics can be describe as a random walk between adjacent potential wells; this means that only jumps of one lattice parameter occur. On the contrary, the underdamped dynamics is more complex, since jumps of any length are possible. This can appreciated for example in Fig. 2.14, where the trajectory of the monomer for two values of the damping is shown. The literature concerning the possibility of long jumps is extensive: experiments [28, 29, 30, 31] and molecular dynamics simulations [32, 33, 34] have demonstrated the occurrence of long jumps both on flat surfaces as well as along surface steps. Despite that, the origin of this phenomenon is not completely understood yet and a full theoretical description is still lacking. This is a significant problem in surface diffusion, since activation of multiple jumps is a clear evidence of low-friction diffusion [35], and can be used to estimate an upper bound of the friction coefficient η, which remains

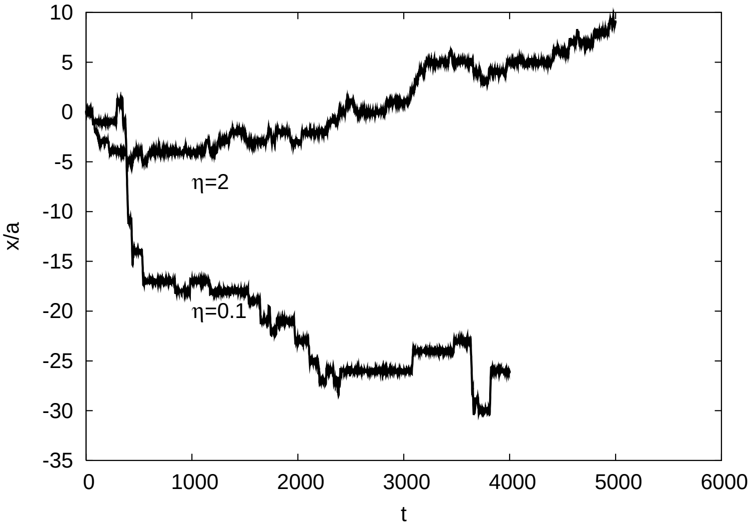

Figure 2.14: Time behaviour of the position of the monomer x rescaled to the lattice parameter $a = 2\pi$ for $U_0 = 1.5$ and for two values of the damping ($\eta = 0.1$ and $\eta = 2$). Notice the occurrence of jumps of single lattice spacing for $\eta = 2$ and of many lattice parameters for $\eta = 0.1$.

an unknown parameter in experiments [35, 36]: this is why the discussion on long jumps is still alive [37].

In the underdamped case, the complete jump-length probability distribution has to be evaluated. This can be seen from the definition of D in the jump regime [6]:

$$D = \frac{1}{2} R \langle l^2 \rangle, \tag{2.71}$$

where R is the jump rate and $\langle l^2 \rangle$ is the mean-square jump length. For R we can use the results of Sec. 2.3 for $F = 0$, but $\langle l^2 \rangle$ has to be calculated from the distribution of the jump lengths.

The problem is trivial for the overdamped case, since $\langle l^2 \rangle = a^2$ and the only knowledge of the rate is sufficient to determine D. From Eq. (2.37) it follows that $R \propto \eta^{-1}$, thus $D \propto \eta^{-1}$.

In the case of intermediate friction ($\eta \simeq \omega_{sub} \equiv \sqrt{U_0}$) $\langle l^2 \rangle = a^2$, but the jump rate can be adequately described by TST (Eq. (2.55)) [6, 7], which is independent of η, so that $D \propto \eta^0$. For moderate or large damping ($\eta \gtrsim \omega_{sub}$), for which $\langle l \rangle = a$, the formula

$$R = R_{TST} B(\eta) \tag{2.72}$$

with $B(\eta) = [(\eta/(2\omega_{sub}))^2 + 1]^{1/2} - \eta/(2\omega_{sub})$, provides an interpolation between the TST and the overdamped limits [13].

In the underdamped limit ($\eta \ll \omega_{sub}$), $R \propto \eta$ (see Eq. (2.51)), but the probability of atomic jumps over many lattice parameters is highly increased, so that $\langle l^2 \rangle > a^2$. The dependence of $\langle l \rangle$ on η can be estimated by a simple argument: $\langle l \rangle \sim \langle v_{barr} \rangle t_{fl}$, where $\langle v_{barr} \rangle \sim \sqrt{E_b}$ is an average velocity of the atoms that cross the energy barrier E_b and $t_{fl} \sim \eta^{-1}$ is the flight time, thus yielding $\langle l \rangle \propto \eta^{-1}$, and $D \propto \eta^{-1}$, as in the overdamped case. Analytical results are known for the $1D$ case in the limit $\eta \rightarrow 0$ only [6, 25, 26]. Numerical simulations have also been performed, but they are too time consuming in the low damping limit [27]. The dependence of D on η, resulting from numerical simulations, is displayed in Fig. 2.15: power laws with the same exponent $\simeq 1$ but with different prefactors are found in the underdamped and overdamped regime.

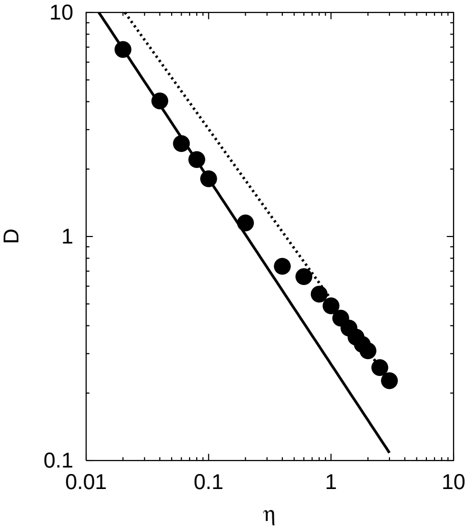

Figure 2.15: Behaviour of the diffusion coefficient as a function of the damping for $U_0 = 1.5$. The solid circles are the result of numerical simulations, while the solid and dotted lines are power law fits $D \propto \eta^{-\alpha}$ to the underdamped ($\eta < 0.1$) and overdamped ($\eta > \sqrt{U_0} \simeq 1.2$) regimes respectively. Notice that in both limits the fits to $D(\eta)$ have a similar slope ($\alpha \simeq 1$), but a different prefactor.

The diffusion coefficient is not only a delicate function of the damping, but depends also on the topology of the surface potential. For example, it was shown that $2D$ diffusion may significantly reduce the jump length, since the trajectory of long jumps which goes through several saddle points may not correspond to a straight line. This effect has to reduce the probability of long jumps, so one could expect a dependence of the form $\langle l \rangle \propto \eta^{-\sigma_l}$, with $\sigma_l < 1$. Since the escape rate R in a multidimensional system should still behave as $R \propto \eta$ (see Ref. [38]), we come to the dependence $D \propto \eta^{-\sigma}$, with $\sigma = 2\sigma_l - 1 < 1$. In particular, it was found by numerical simulations that $\sigma = 0.5$ for a substrate potential with centered-rectangular symmetry [39] and it was conjectured that, in the limit $\eta \rightarrow 0$, D is independent of η for all nonseparable $2D$ substrate potentials [27]. For $2D$ separable potentials the same dependence of D on η as in $1D$ should be recovered [40]. In general, σ is not universal but depends on the geometry of the substrate potential [41].

Bibliography

[1] R. Gomer, Rep. Prog. Phys. **53**, 917 (1990).

[2] G. L. Kellogg, Surf. Sci. Rep. **21**, 1 (1994).

[3] H. Brune, Surf. Sci. Rep. **31**, 121 (1998).

[4] B. Ala-Nissila, R. Ferrando, S. C. Ying, *Adv. Phys.* **2002**, 51, 949.

[5] R. Imbihl and G. Ertl, Chem. Rev. **95**, 697 (1995).

[6] H. Risken, *The Fokker-Planck Equation*, 2nd ed., Springer (1989), chap. 11.

[7] P. Hänggi, P. Talkner and M. Borkovec, Rev. Mod. Phys. **62**, 251 (1990).

[8] E. Ben-Jacob, D. J. Bergman, B. J. Matkowsky and Z. Schuss, Phys. Rev. A **26**, 2805 (1982).

[9] P. Fulde, L. Pietronero, W. R. Schemer and S. Strässler, Phys. Rev. Lett. **35**, 1776 (1975).

[10] V. Ambegaokar and B. I. Halperin, Phys. Rev. Lett. **22**, 1364 (1969).

[11] W. T. Coffey, Yu. P. Kalmykov and E. S. Massawe, Phys. Rev. E **48**, 699 (1993).

[12] T. Schneider, E. P. Stoll and R. Morf, Phys. Rev. B **18**, 1417 (1978).

[13] H. A. Kramers, Physica (Utrecht) **7**, 284 (1940).

[14] Z. Zheng and G. Hu, Phys. Rev. E **52**, 109 (1995).

[15] R. S. Larson and M. D. Kostin, J. Chem. Phys. **69**, 4821 (1978).

[16] A. R. Bishop and S. E. Trullinger, Phys. Rev. B **17**, 2175 (1978).

[17] P. E. Parris, M. Kuś, D. H. Dunlap and V. M. Kenkre, Phys. Rev. E **56**, 5295 (1997).

[18] *Handbook of Mathematical Functions*, edited by M. Abramowitz and A. Stegun (Dover, New York, 1964).

[19] M. Büttiker and R. Landauer, Phys. Rev. A **23**, 1397 (1981).

[20] M. Büttiker, E. P. Harris and R. Landauer, Phys. Rev. B **28**, 1268 (1983).

[21] See for example H. Eyring, J. Chem. Phys. **3**, 107 (1935).

[22] See for example E. Ganz, S. K. Theiss, I.-S. Hwang and J. Golovchenko, Phys. Rev. Lett. **68**, 1567 (1992).

[23] See for example G. Boisvert and L. J. Lewis, Phys. Rev. B **56**, 7643 (1997).

[24] K. Kyuno, A. Gölzhäuser and G. Ehrlich, Surf. Sci. **397**, 191 (1998).

[25] R. Ferrando, R. Spadacini and G. E. Tommei, Phys. Rev. E **48**, 2437 (1993).

[26] R. Ferrando, R. Spadacini and G. E. Tommei, Phys. Rev. E **51**, 126 (1995).

[27] O. M. Braun and R. Ferrando, Phys. Rev. E **65**, 061107 (2002).

[28] G. Ehrlich, Surf. Sci. **246**, 1 (1991).

[29] D. Cowell Senft and G. Ehrlich, Phys. Rev. Lett. **74**, 294 (1995)

[30] J. Ellis and J. P. Toennies, Phys. Rev. Lett. **70**, 2118 (1993).

[31] T. R. Linderoth, S. Horch, E. Laegsgaard, I. Stensgaard and F. Besenbacher, Phys. Rev. Lett. **78**, 4978 (1997).

[32] K. D. Dobbs and D. J. Doren, J. Chem. Phys. **97**, 3722 (1992).

[33] R. Ferrando and G. Treglia, Phys. Rev. B **50**, 12104 (1994).

[34] F. Montalenti and R. Ferrando, Phys. Rev. B **59**, 5881 (1999).

[35] A. P. Graham, F. Hofmann, J. P. Toennies, L. Y. Chen and S. C. Ying, Phys. Rev. Lett. **78**, 3900 (1997).

[36] H. Xu and I. Harrison, J. Phys. Chem. B **103**, 11233 (1999).

[37] G. Antczak and G. Ehrlich, Phys. Rev. Lett. **92**, 166105 (2004).

[38] M. Borkovec and B. J. Berne, J. Chem. Phys. **82**, 794 (1985).

[39] L. Y. Chen, M. R. Baldan and S. C. Ying, Phys. Rev. B **54**, 8856 (1996).

[40] L. Y. Chen and S. C. Ying, Phys. Rev. Lett. **71**, 4361 (1993).

[41] G. Caratti, R. Ferrando, R. Spadacini and G. E. Tommei, Phys. Rev. E **55**, 4810 (1997).

Chapter 3

Diffusion and nonlinear dynamics of non rigid dimers on surfaces

This chapter is based on the following papers:

- C. Fusco, A. Fasolino and T. Janssen, Eur. Phys. J. B **31**, 95 (2003).
- C. Fusco and A. Fasolino, Thin Solid Films **428**, 34 (2003).
- C. Fusco and A. Fasolino, in “Modeling and Simulating Materials Nanoworld” (Advances in Science and Technology), edited by P. Vincenzini and F. Zerbetto, Techna Group, Vol. 44, pp. 293-300 (2004).
- C. Fusco and A. Fasolino, *Nonlinear dynamics and surface diffusion of diatomic molecules*, to be published in ChemPhysChem.

The dynamics of interacting particles on a surface is a complex phenomenon. Even for the simplest cluster, i. e. a dimer, a very rich dynamical behaviour, characterized by nonlinear effects, resonances and chaos, is found. We will present different aspects of the dimer dynamics on a periodic substrate at zero and finite temperatures, underlining the role of the interparticle interaction on the dimer motion and thermal diffusion, and suggesting connections to real systems and to experimental findings.

3.1 Introduction: beyond single atom diffusion

In the previous chapter we have analysed the adatom diffusion dynamics, emphasizing the role it plays in the microscopic understanding of crystal growth, thin film formation and other surface phenomena. Once individual adatoms are adsorbed on the surface they can meet, thus forming larger clusters. Therefore, the natural subsequent step is the study of small-cluster diffusion, starting from the simplest case, i. e. a dimer. However, even for this simple object a complete understanding of the mobility and the diffusion mechanisms on a surface has not been reached yet and some important questions are still open. The interest of the surface physics community on this topic is witnessed by several recent theoretical works [1, 2, 3, 4].

Interacting particles moving on a surface represent a system displaying complex dynamical features, with the possibility of anomalous diffusive behaviour. With the refinement of the experimental methods described in Chap. 1, it has been possible to follow the dynamical details of surface diffusion (using STM) [5] and to image physisorbed clusters (using FIM) [6]. Furthermore, the "atom tracking" technique allows to resolve every diffusive event, enabling to monitor the path of the cluster with high accuracy [7, 8]. Early FIM investigations showed enhanced diffusion rates of adsorbed small metal clusters [9] and more recent experiments have reported high diffusion coefficients for large gold or antimony clusters [10]. In the same fashion, a diffusion coefficient 4 orders of magnitude higher than that of single particle was found for small iridium clusters (Ir_7 and Ir_{19}), with a significant contribution of long jumps to the diffusivity [11]. The effect of long jumps on the diffusion of small $1D$ platinum clusters [12] and of large molecules adsorbed on metal surfaces [13] has also been highlighted in recent variable-temperature STM experiments. Different diffusion mechanisms for metal clusters have been proposed: concerted jumps, i. e. jumps of the cluster as a whole, leap-frog events, i.e the possibility for one end-atom to migrate to the other end of the cluster [12, 14], or dissociation-reassociation processes [15]. Interestingly, a theoretical study of diffusion of some molecular clusters in molecular sieves has revealed that concerted mechanisms involving simultaneous motion of the whole cluster result in strongly size dependent activation energies, with "magic numbers" associated to very low activation energy for diffusion of clusters of specific sizes [16]. A similar behaviour has also been observed for heteroepitaxial island diffusion of Ag on Ru(0001) [17]. Furthermore, unique molecular features, including non-nearest-neighbour hops, conformal correlations and directional anisotropy, have been found in theoretical studies of diffusion of $n-$alkanes chains on Pt(111) [18].

These peculiar diffusive characteristics, which, at first sight, may seem related to the motion of large atomic clusters, have been indeed observed even for dimers. Experimental studies of dimer diffusion on a crystalline surface by using STM show a very rich phenomenology [19]. An increase of the mobility of dimers by a factor of 2 to 5 with respect to that of adatoms has been found for platinum by FIM [20] and was explained by exchange processes with substrate atoms. The role of long jumps for this system has also been reported [21] and the distribution of jump lengths has been studied theoretically in the framework of random walk models [15, 22]. A particularly interesting model system for its applications in the microelectronic industry is represented by Si_2 on Si(001). It is known that Si(001) reconstructs in dimer rows with different characteristic lengths. It has been shown that the diffusion of Si_2 on Si(001) proceeds by one atom at a time rather than as a two-atom unit and that two possible diffusion configurations (on top of dimer rows or in troughs between dimer rows) are possible [19, 23]. Furthermore, in a recent STM study on water molecules adsorbed on Pd(111) at $T = 40$ K a very striking finding emerged: the diffusion coefficient of the water dimer is 4 orders of magnitude higher than that of the single water molecule [8].

From this various landscape of experimental observations and of different diffusion phenomena, it is clear that a solid theoretical understanding of the fundamental mechanism governing the diffusion of interacting particles on a surface is needed. The scope of this chapter is to address this problem for the simple but important case of a dimer physisorbed on a $1D$ periodic substrate, trying to link the macroscopic diffusive behaviour to microscopic degrees of freedom. In fact, most theoretical works have focussed on the determination of energy barriers for diffusion in different systems, usually on the basis of energy arguments and neglecting the role of internal degrees of freedom (see for example Refs. [3, 24, 25, 26]). However, it has been suggested that the diffusion dynamics can be strongly affected by the presence of intramolecular motion [17, 27, 28] and that the activation barrier for the dimer motion can dramatically depend on the relation between the dimer natural length and the substrate lattice parameter [4, 8, 28, 29, 30, 31]. The coupling between degrees of freedom gives rise to the so-called entropy barriers [32], which are responsible for a nonmonotonic dependence of the diffusivity on the dimer's parameters. Specifically, we will show that the coupling between translational and intramolecular motion of the dimer produces a complex dynamical behaviour, dominated by non-linear effects, parametric resonances and chaos. Moreover, the dynamical misfit induced by thermal vibrations on the intramolecular motion accounts for deviations from activated behaviour of the diffusion coefficient (see also Refs. [17, 27]). The relation between diffusive regime, chaotic motion and non-Arrhenius behaviour is of particular interest: it has been recognized that deterministic chaos can induce transport phenomena not considered in conventional statistical mechanics (for instance an anomalous growth of the mean square displacement) [33] and that sometimes a diffusionlike transport can be driven by deterministic chaos instead of thermal stochastic noise. For example, it has been seen that molecular motion in zeolites [34] can be reproduced by noiseless Molecular Dynamics (MD) simulations [35], suggesting that the diffusive mechanisms are not driven by any stochastic force; besides, this behaviour can account for the observed non-Arrhenius nonequilibrium diffusivity in zeolites [36].

The chapter is organized as follows. In Sec. 3.2 we describe the model we have employed in our theoretical investigations. Sec. 3.3 contains the relevant results for the Hamiltonian dynamics of the system: analytical treatment combined with numerical simulations shows intriguing nonlinear effects and different dynamical regimes, ranging from oscillatory to drift motion, with the possibility of chaotic features and stochastic ("quasi-diffusive") motion. In Sec. 3.4 we will present the peculiarities of thermal diffusive dynamics of the dimer and in Sec. 3.5 we will emphasize the connection between non-Arrhenius behaviour and deterministic chaos. Sec. 3.6 is devoted to the driven motion of the dimer, both at $T = 0$ and $T \neq 0$, which is relevant to the frictional dynamics of interacting particles (see the analogous problem for the monomer in Secs. 2.2 and 2.3 of Chap. 2).

3.2 Model

Our model contains in a a simple way the salient features of a diatomic molecule physisorbed on a periodic substrate. We consider a dimer moving on a periodic $1D$ substrate at zero and finite temperature. Although simplistic, a $1D$ model can be relevant since $1D$

dimer diffusion occurs in real systems, in particular along steps and on channeled (110) metal surfaces [37]. The particle-substrate interaction is modelled by a periodic function:

$$U_{sub}(x_1, x_2) = U_0 \left[2 - \cos\left(\frac{2\pi x_1}{a}\right) - \cos\left(\frac{2\pi x_2}{a}\right) \right], \tag{3.1}$$

where x_i represents the spatial coordinate of particle i ($i = 1, 2$), $2U_0$ is the diffusion barrier per particle and a is the substrate lattice constant. Most of the results presented here have been obtained using a harmonic interatomic potential:

$$V(x_1, x_2) = \frac{K}{2}(x_2 - x_1 - l)^2, \tag{3.2}$$

where K is the force constant and l is the spring equilibrium length. We have also used short range interatomic interactions, such as the Lennard-Jones (LJ) potential (see Sec. 3.3.2B). In the framework of the Langevin dynamics the equations of motion are

$$\left\{ \begin{array}{lcl} m\ddot{x}_1 + m\eta\dot{x}_1 & = & K(x_2 - x_1 - l) - \frac{2\pi U_0}{a} \sin\left(\frac{2\pi x_1}{a}\right) + f_1 + F \\ m\ddot{x}_2 + m\eta\dot{x}_2 & = & K(x_1 - x_2 + l) - \frac{2\pi U_0}{a} \sin\left(\frac{2\pi x_2}{a}\right) + f_2 + F \end{array} \right. \tag{3.3}$$

where m is the mass of each particle and F is the external driving force. The stochastic forces satisfy

$$\langle f_i \rangle = 0 \tag{3.4}$$

and the fluctuation-dissipation relation

$$\langle f_i(t) f_j(0) \rangle = 2m\eta k_B T \delta_{ij} \delta(t). \tag{3.5}$$

Our model is sketched in Fig. 3.1. It is convenient to rewrite the equation of motion in adimensional units by introducing a characteristic time

$$\tau = \frac{a}{2\pi} \left(\frac{m}{k_B T} \right)^{1/2}$$

and defining

$$\tilde{x} = \frac{2\pi}{a} x, \quad \tilde{t} = \frac{t}{\tau}, \quad \tilde{\eta} = \eta\tau, \quad \tilde{U_0} = \frac{U_0}{k_B T}$$

$$\tilde{f} = \frac{a}{2\pi k_B T} f, \quad \tilde{F} = \frac{a}{2\pi k_B T} F, \quad \tilde{l} = \frac{2\pi}{a} l, \quad \tilde{K} = \frac{a^2}{4\pi^2 k_B T} K.$$

In this way Eq. (3.3) becomes (in the following we will only use these adimensional units and will omit the tildes for simplicity)

$$\left\{ \begin{array}{lcl} \ddot{x}_1 + \eta\dot{x}_1 & = & K(x_2 - x_1 - l) - U_0 \sin x_1 + f_1 + F \\ \ddot{x}_2 + \eta\dot{x}_2 & = & K(x_1 - x_2 + l) - U_0 \sin x_2 + f_2 + F, \end{array} \right. \tag{3.6}$$

and the fluctuation-dissipation relation Eq. (3.5)

$$< f_i(t) f_j(0) >= 2\eta \delta_{ij} \delta(t). \tag{3.7}$$

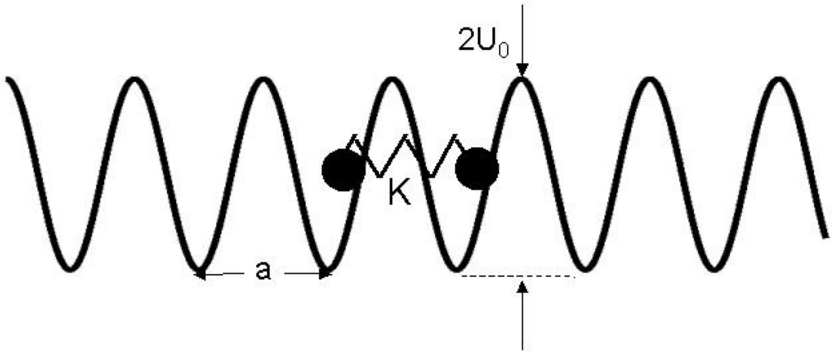

Figure 3.1: Sketch of the model of dimer diffusion on a periodic potential considered in this chapter.

It is useful to introduce the centre of mass and internal coordinates, defined by

$$x_{CM} = (x_1 + x_2)/2 \qquad x_r = x_2 - x_1 - l. \tag{3.8}$$

In this new coordinate system Eq. (3.6) becomes

$$\begin{cases} \ddot{x}_{CM} & = & -\eta\dot{x}_{CM} - U_0\cos((x_r + l)/2)\sin x_{CM} + F + f_{CM} \\ \ddot{x}_r & = & -\eta\dot{x}_r - 2Kx_r - 2U_0\sin((x_r + l)/2)\cos x_{CM} + f_r \end{cases} \tag{3.9}$$

where f_{CM} and f_r are defined as

$$f_{CM} = (f_1 + f_2)/2 \qquad f_r = f_2 - f_1 \tag{3.10}$$

We perform MD simulations, integrating the equations of motion (3.6) using a velocity-Verlet algorithm, with time step $\Delta t = 10^{-4}\tau$, averaging the trajectories calculated at $T \neq 0$ over several hundreds of realizations ($\simeq 300$ in driven case and $\simeq 3000$ in the undriven case with $F = 0$), in order to reduce the statistical noise due to the stochastic term.

3.3 Nonlinear Hamiltonian dynamics

In this section we consider the deterministic non-dissipative and non-driven dynamics of Eq. (3.6), i. e. without stochastic forces f_i and for $\eta = 0$ and $F = 0$. For this choice we have a purely Hamiltonian (conservative) system. We will study in detail the dynamics of the system as a function of the initial kinetic energy. Furthermore, we focus on the commensurate case in which $l = a = 2\pi$, i. e. when the spring natural length is equal to the period of the substrate potential. In this situation the minimum energy configuration does not depend on K (namely $x_1 = 0$ and $x_2 = a$ minimize the total potential energy) and moreover a linearization around $x_r = 0$ offers the possibility to treat the problem in a semi-analytical way. This has the advantage to give a closer insight into the dynamical features of this system.

3.3.1 Dynamics of the linearized system

When $x_r \simeq 0$, as at the beginning of the motion starting from equilibrium, we can linearize in x_r the equations of motion (3.9):

$$\ddot{x}_{CM} \simeq U_0 \sin x_{CM} \tag{3.11}$$

$$\ddot{x}_r \simeq -2K(1 - \frac{U_0}{2K} \cos x_{CM})x_r. \tag{3.12}$$

As initial conditions we choose

$$\begin{array}{ll} x_{CM}(0) = x_0 = a/2 & \dot{x}_{CM}(0) = v_0 \\ x_r(0) = 0 & \dot{x}_r(0) = 0. \end{array}$$

In this way we give an initial kinetic energy to the dimer at equilibrium (alternatively one could have chosen to give an initial potential energy, i. e. $\dot{x}_{CM}(0) = 0$ and $x_{CM}(0) \neq a/2$). Notice that the initial kinetic energy for this choice coincides with the total energy of the system. In order to excite the internal motion we apply an infinitesimal perturbation ($x_r \simeq 10^{-8}$) to the system from its equilibrium state. The minimum kinetic energy for the CM to get out of the potential is $v_0^2 = 4U_0$ if $v_1 = v_2 = v_0$ (v_i is the initial velocity of particle i). Below this threshold value (namely $v_0 < \sqrt{4U_0}$) Eq. (3.11) coincides with the equation of a classical pendulum for which the amplitude as a function of the period of oscillation is known in terms of an elliptic integral [38], as shown in Fig. 3.2(a). The maximum amplitude of oscillation of the CM is determined by v_0. In this case

$$x_{CM} \simeq x_0 + \frac{C}{2} \sin(\omega t). \tag{3.13}$$

with $\omega = \omega(v_0)$ (see Fig. 3.2(b)). This means that

$$\cos x_{CM} \simeq A + B \cos(2\omega t) \tag{3.14}$$

with A and B depending on v_0 via ω. Inserting (3.14) into the equation of motion for x_r (3.12) we obtain the equation of a parametric oscillator:

$$\ddot{x}_r = -\omega_{0eff}^2(1 + h \cos(2\omega t))x_r \tag{3.15}$$

where $\omega_{0eff} \equiv \sqrt{2K - AU_0}$ and $h \equiv BU_0/\omega_{0eff}^2$. The relation between the initial velocity v_0 and the frequency ω_{0eff} is shown in Fig. 3.2(c) for several values of $v_0 < \sqrt{4U_0}$. It is worth noting that the stretching frequency of the free dimer $\sqrt{2K}$ becomes $\sqrt{2K + U_0}$ in the external potential (this is true when the CM is fixed at the equilibrium position). But in Eq. (3.12) the motion of x_r is further affected by the oscillatory behaviour of the CM and its natural frequency changes into $\omega_{0eff} \equiv \sqrt{2K - AU_0}$. Conversely, when $v_0 > \sqrt{4U_0}$ the CM performs a drift motion, i. e.

$$x_{CM} \simeq x_0 + \langle v_{CM} \rangle t, \tag{3.16}$$

where $< \cdot >$ denotes a time average and $\langle v_{CM} \rangle$ is the drift average CM velocity. By defining ω as $\omega = \langle v_{CM} \rangle/2$ the equation for x_r remains in the form (3.15) with $\omega_{0eff} \equiv \sqrt{2K}$ and $h \equiv U_0/(2K)$ (i. e. $A = 0$ and $B = 1$).

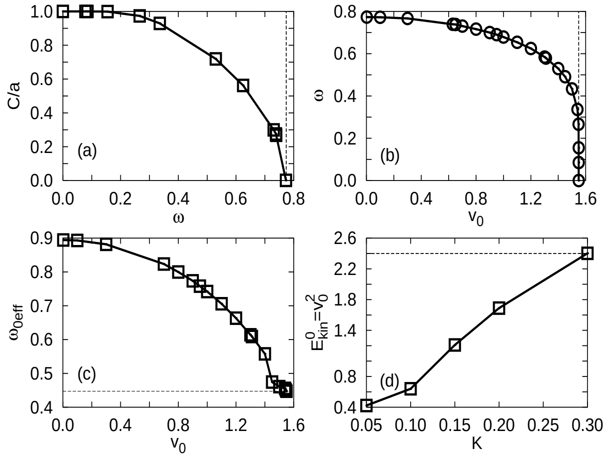

Figure 3.2: Relation between amplitude C (rescaled to lattice parameter a) and frequency of oscillation as given by the solution of Eq. (3.11) (a), between CM frequency of oscillation and CM initial velocity (b) and between the effective stretching frequency and CM initial velocity (c), obtained by numerical calculations for $U_0 = 0.6$ (solid lines). The lower energy borders of instability regions as a function of K are plotted in (d). The vertical dashed lines in (a) and in (b) indicate respectively the frequency of small oscillations $\sqrt{U_0} = 0.774$ and the velocity corresponding to the threshold for drift motion $\sqrt{4U_0} = 1.5492$. The horizontal dashed lines in (c) and (d) correspond respectively to $\omega_{0eff} = \sqrt{2K}$ ($K = 0.1$), which is reached when $v_0 \geq \sqrt{4U_0}$, and to the energy threshold for drift motion $4U_0$.

The CM motion (either oscillatory or drifting), as considered in the linearized Eq. (3.11), drives parametrically the internal motion of the dimer. We establish the instability ranges by monitoring for which values of the initial velocity v_0 an exponential increase of x_r is found. In order to understand the energy threshold for the excitation of parametric resonances, we plot the lower borders of the instability regions as a function of K in Fig. 3.2(d) when the total initial kinetic energy $E^0_{kin} = v_0^2$ is less than the potential barrier $4U_0$. In this way we can identify a critical value $K = K_c$ above which the parametric resonance can be excited only if the CM performs a drift motion (e.g. $E^0_{kin} > 4U_0$). It turns out that $K_c \simeq 0.3$ for $U_0 = 0.6$. Since ω_{0eff} is determined by K, by considering different values of K we can construct the standard picture for parametric instabilities relating h to ω. One can recognize the main resonance for $\omega = \omega_{0eff}$ (Fig. 3.3). The boundaries of the region of instability are given by the stars in Fig. 3.3. The different curves represent h as a function of ω for different values of K. Note that, at fixed K, h increases when ω decreases (e.g. when the amplitude of oscillation increases and $v_0 < \sqrt{4U_0}$), but when the CM overcomes the barrier, h reaches the constant value $U_0/(2K)$. Moreover, the range of frequency in which instability is observed is larger for smaller values of K. An example of parametric resonance is shown in Fig. 3.4(a): x_r oscillates and its amplitude increases exponentially. In Fig. 3.4(b) a blow up of the behaviour of x_r and of the drive x_{CM}, oscillating at the same frequency, is also shown.

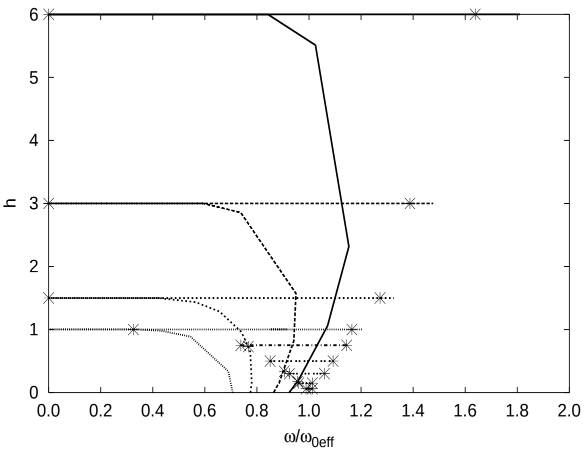

Figure 3.3: Relation between frequency and the parameter h of Eq. (3.15) for different values of K (from top to bottom: $K = 0.05, 0.1, 0.2, 0.3, 0.4, 0.6, 1, 2, 5$) and $U_0 = 0.6$. The region in which the parametric resonance occurs is bounded by the stars.

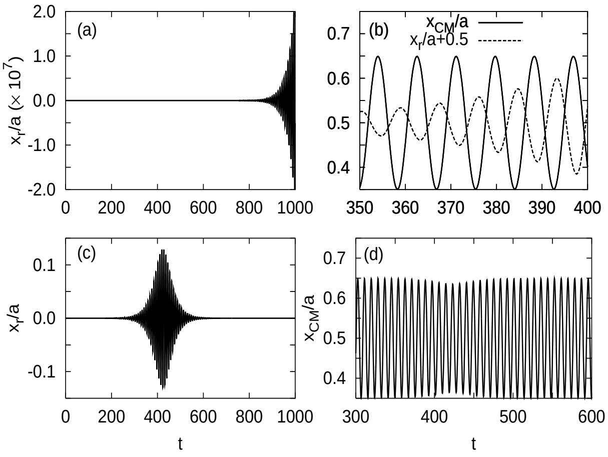

Figure 3.4: Comparison between internal and CM motion of the linearized system Eqs. (3.11) and (3.12) (upper panel) and those obtained by integrating the complete system Eq. (3.6) (lower panel). The internal motion plotted in (a) is the numerical result of the integration of Eq. (3.15). Notice the scale of the y axis in (a), which is due to the large exponential increase of the amplitude of the oscillations. Only the envelope of the rapid oscillations of x_r is visible on the left panels ((a) and (c)). (b) shows that x_r and x_{CM} in the linearized system oscillate with the same frequency. The initial exponential increase of x_r for the full system in (c) is suppressed by the coupling of x_r to x_{CM}, which brings x_r out of the instability region of the parametric oscillator. The CM of the full system is shown in (d), where we note a decrease of the amplitude at the point in which the internal motion starts to decrease in (c). The parameters used in the simulation are $U_0 = 0.6$, $K = 0.05$ and $v_0 = 0.7$. All lengths are rescaled to the substrate lattice constant a.

3.3.2 Dynamics of the full system

A. Harmonic case

Now we consider the original system of equations of motion (3.9). The linearization given by Eqs. (3.11) and (3.12) allows to understand some of the dynamical features of the full system. However, the CM and internal motion equations are coupled and this results in a qualitatively different behaviour with respect to the simple approximation discussed in Sec. 3.3.1. In particular, we note that the feedback of x_r on x_{CM} drives the CM out of the instability window found for the linearized system Eq. (3.15). An example is illustrated in Fig. 3.4, where we compare the motion of the complete and of the linearized system. As we can see in Fig. 3.4(c), the parametric increase of x_r found for the linearized equations is followed by a decrease, due to the fact that the feedback of x_r on x_{CM} causes a change of the amplitude of the CM at that point ($t \simeq 400$ in Fig. 3.4(d)). However, when x_r decreases, the instability reappears and the internal motion increases again (at later times not shown in the figure). The system gets in and out the instability window, because we are considering a case that is almost at the border. Instead, in Fig. 3.5 we show a case which is in the centre of the region of instability: we can note that after an initial transient the internal motion is always excited, and its behaviour is more irregular so that it is not possible to identify a clear unique frequency of oscillation and a unique rate of increase. This behaviour is caused by the shift in position inside the instability window, which in turn produces a shift in frequency and rate of increase. Note that the excitation of the internal motion leads to a CM motion which would not have occurred if the dimer had been rigid. In that case the CM would have kept the initial oscillatory behaviour around the equilibrium position. Here, instead, the internal vibrations play a role similar to that of a heat bath and drive the CM away from the minimum with jumps across one or more potential wells. In fact, for a non-rigid dimer, it is possible to get out of the well even if

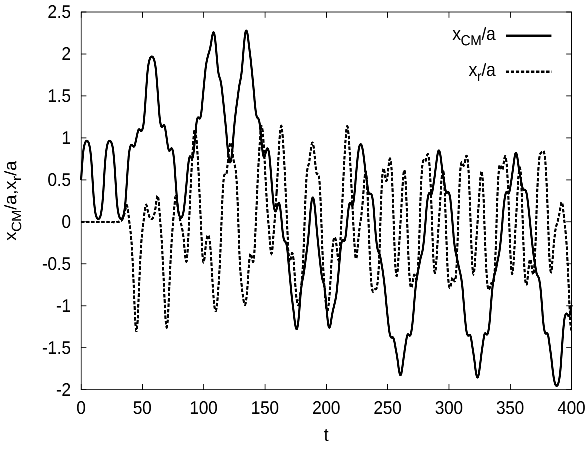

Figure 3.5: Numerical simulations of Eq. (3.9) for $U_0 = 0.6$, $K = 0.05$ and $v_0 = 1.54$. The CM (solid line) and internal motion (dashed line), rescaled to the substrate lattice constant a, are shown.

$v_0 < \sqrt{4U_0}$. This happens because if the internal motion is excited, it is possible that one particle remains in the minimum whereas the other reaches the nearest maximum. In this way the energy balance is:

$$E^0_{kin} = \frac{1}{2}v_1^2 + \frac{1}{2}v_2^2 = 2U_0 + \frac{1}{2}K(a/2)^2 \qquad (3.17)$$

and if K is sufficiently small the right-hand side is smaller than $4U_0$ (we assume $v_1 = v_2 = v_0$). Thus vibrational energy can be effective in overcoming the barrier. The resulting motion of the dimer (Fig. 3.5) can be characterized as chaotic, as shown later in Sec. 3.3.3.

It is interesting that the chaotic motion described above occurs at velocities below and above the threshold $\sqrt{4U_0}$ for drift motion in the linearized system. This is due to a coexistence of long jumps with localized motion, which persists for a certain range of initial energies. This behaviour is similar to that reported in Ref. [39] for a monomer moving on a $2D$ surface. In Fig. 3.6(a) we show the case where $v_0 = \sqrt{4U_0}$. At the beginning, the CM performs a step-like motion: every time it overcomes a barrier it gets stuck for a while in the next minimum before overcoming the next barrier. In this initial stage $x_r = 0$. After x_r gets excited, this step-like motion disappears. The parametric resonance which one would have expected in this case for the simplified system is not visible because of the reciprocal influence of CM and internal motion, which inhibits the increase of amplitude of x_r. Note that when the internal motion is excited almost all the energy is transferred to the vibrational modes, as it can be seen by the corresponding peaks in Fig. 3.6(d).

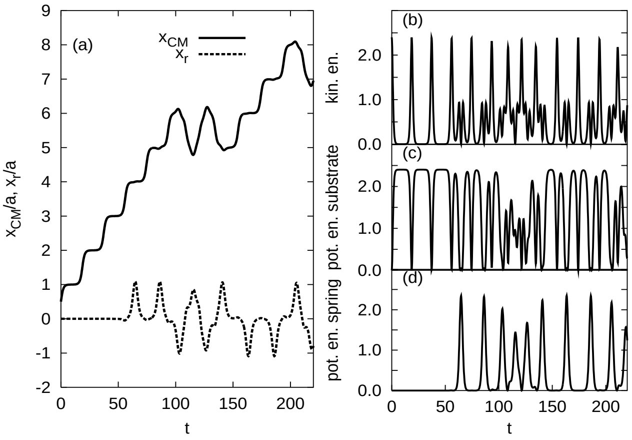

Figure 3.6: Numerical simulations of Eq. (3.9) for $U_0 = 0.6$, $K = 0.1$ and $v_0 = \sqrt{4U_0} \simeq 1.5492$: (a) CM trajectory (solid line) and internal motion (dashed line); (b) kinetic energy; (c) substrate potential energy; (d) spring potential energy.

By further increasing the initial kinetic energy the dynamics becomes again non chaotic, and the CM performs a drift motion with constant velocity unless the conditions for parametric excitation given by Eq. (3.15) are met. This does not occur for the small values of K considered up to now. In fact, a dimer presents only one characteristic frequency so that conditions for parametric excitation are generally met either in the oscillatory or in the drift regime. The situation would be different for a larger molecule where different vibrational modes could be excited for different values of v_0. In Fig. 3.7 we show one situation for large K where the drift CM motion excites the internal motion through a parametric resonance for drift velocity twice the dimer natural stretching frequency $\omega_0 = \sqrt{2K}$. When the internal motion acquires a large amplitude, deviations from the linear behaviour of x_{CM} are observed.

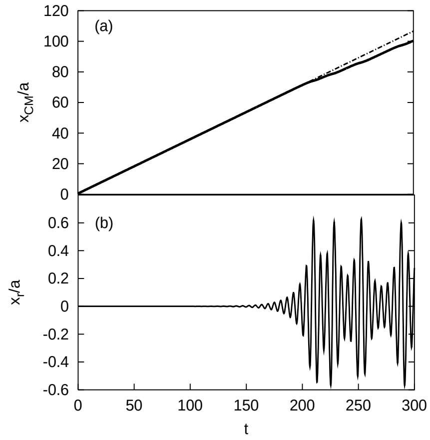

Figure 3.7: Numerical simulations of Eq. (3.9) for $U_0 = 0.6$, $K = 0.5$ and $v_0 = 2.5$. In (a) we show the CM motion (solid line) with a linear fit for $t < 200$ (dot-dashed line), while the internal coordinate is plotted in (b).

In Fig. 3.8 we summarize, for three values of K, the effect of different v_0 (at fixed U_0) on the CM motion. Increasing v_0, a complex transition from oscillatory regular motion to chaotic motion and then to a drift regime can take place depending on the value of K. For $K = 0.05$ (Fig. 3.8(a)), resonant excitation of the internal motion occurs for $v_0 > 0.65$ as given in Fig. 3.2(d). Above this value, first a regime with recursive excitation of x_r, as in Fig. 3.4(c), takes place so that $< x_{CM} >= a/2$ and $\langle v_{CM} \rangle = 0$. At $v_0 > 1.3$ the escape from the well described by Eq. (3.17) becomes possible. The resulting (chaotic) behaviour of x_{CM} in this regime is shown by the dashed line in Fig. 3.8(a) for $v_0 = 1.65$. The CM motion in this regime has a transient behaviour which follows $< x_{CM}^2 > \simeq t^\alpha$ $(1 < \alpha < 2)$ with $\langle v_{CM} \rangle \simeq 0$, i. e. it is "quasi-diffusive", that is to say neither purely diffusive nor ballistic. This behaviour extends up to $v_0 < 1.68$, i. e. well above the "threshold" $\sqrt{4U_0}$. Above, a drift motion $x_{CM}(t) \simeq x_0 + \langle v_{CM} \rangle t$ occurs. For a larger $K = 0.3$ (Fig. 3.8(b)) the quasi-diffusive motion starts occurring at values of $v_0 \simeq \sqrt{4U_0}$ up to $v_0 = 2.2$, where drift motion is recovered. Lastly for $K = 0.5$ (Fig. 3.8(c)), there is no chaotic regime. The drift motion starts at $v_0 = \sqrt{4U_0}$ and deviations only occur for a narrow range of velocities where x_r becomes parametrically excited, as shown in Fig. 3.7.

We may estimate from Eq. (3.17) the critical K value above which the internal motion

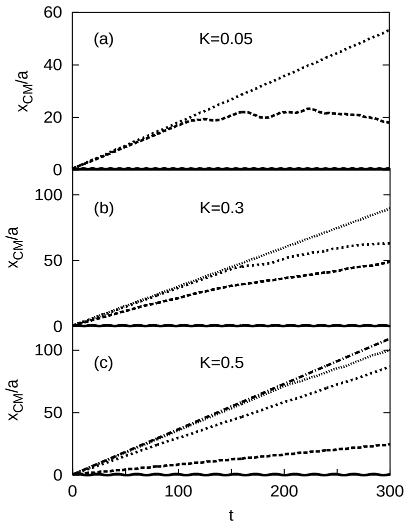

Figure 3.8: Numerical simulations of Eq. (3.9) for $U_0 = 0.6$, three values of K and several values of v_0. In this case the threshold velocity is $v_0 = \sqrt{4U_0} \simeq 1.5492$. The CM motion is plotted for $K = 0.05$ (a), $K = 0.3$ (b) and $K = 0.5$ (c). The different curves in each panel are obtained with different initial velocities. From bottom to top in each graph $v_0 = 0.63, 1.65, 1.68$ (a), $v_0 = 1.5, 1.85, 2.15, 2.2$ (b), $v_0 = 1.54, 1.55, 2.2, 2.5, 2.55$ (c). Note the deviation from linear behaviour in (c) for $v_0 = 2.5$ (see Fig. 3.7 and text).

is not effective in making the CM overcome the potential barrier for $v_0 < \sqrt{4U_0}$. Namely

$$2U_0 + \frac{1}{2}K_c\pi^2 = 4U_0, \tag{3.18}$$

and for $U_0 = 0.6$ we find $K_c \simeq 0.35$. As a consequence, for $K > K_c$ no chaotic motion is found.

B. Lennard-Jones case

Now we consider the effect of replacing the harmonic interaction (3.2) with a finite-range potential. As a simple choice, we take the LJ potential, given by

$$V_{LJ}(r) = 4\epsilon \left[\left(\frac{\sigma}{r}\right)^{12} - \left(\frac{\sigma}{r}\right)^{6} \right] \tag{3.19}$$

with $r \equiv |x_2 - x_1|$ and a cutoff at $r = 2.5\sigma$. To recover the harmonic interaction close to the minimum, we impose the equilibrium distance to be equal to the spring equilibrium length and the second derivative of V_{LJ} to be equal to the spring constant, namely:

$$\left\{ \begin{array}{ccccc} r_{min} & = & \sqrt[6]{2}\sigma & = & l \\ \left.\frac{d^2V_{LJ}}{dr^2}\right|_{r=r_{min}} & = & \frac{24\epsilon}{\sigma^2}\left[\frac{26}{\sqrt[3]{128}} - \frac{7}{\sqrt[3]{16}}\right] & = & K \end{array} \right. \tag{3.20}$$

whence

$$\begin{cases} \sigma &= \frac{l}{\sqrt[6]{2}} \\ \epsilon &= \frac{Kl^2}{72} \end{cases} \tag{3.21}$$

At variance with harmonic interactions, a finite-range potential allows dissociation of particles. This is clearly seen in Fig. 3.9, where the time behaviour of the CM and internal motion is plotted comparing the harmonic and LJ potentials. The CM is the same in the two cases when $x_r = 0$, i. e. at the beginning of the motion. Then, as the internal motion starts to increase, x_r given by LJ is found very similar to the harmonic x_r, but then the amplitude of the oscillations due to the LJ potential becomes larger. At $t \simeq 420$ the two particles dissociate and x_r starts to increase very fast since only one particle moves.

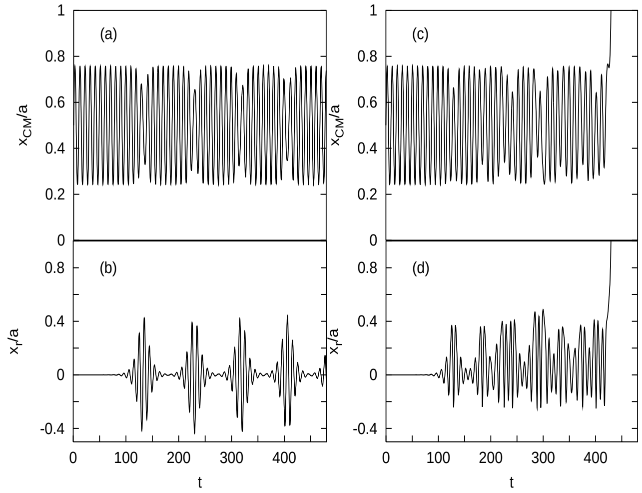

Figure 3.9: Numerical simulations of the equation of motion of a dimer for harmonic (a)-(b) and LJ interactions (c)-(d). The CM and internal motion are shown. The parameters are $U_0 = 0.6$, $K = 0.05$ and $v_0 = 1.12$ for the harmonic potential. The parameters of the LJ have been chosen according to Eq. (3.21): $\sigma \simeq 5.598$ and $\epsilon \simeq 0.0274$.

In Fig. 3.10 we show a similar process for the case where the CM performs a drift motion. We observe that the increase of amplitude of x_r occurs approximately at the same time for both harmonic and LJ interactions. As just noted above, at this point a departure from the linear behaviour of the CM takes place. While large oscillations persist in the harmonic x_r, breaking of the interparticle bond is found in the LJ case. This shows that the resonant excitation of internal vibrations could be effective in leading to dissociation of molecular bonds and can have applications in catalysis and in dissociative adsorption of molecules [40, 41].

3.3.3 Chaotic dynamics

The dynamics described in Sec. 3.3.2A shows very complex features, in spite of the simplicity of our model. The quasi-diffusive, irregular motion found for small values of K, as in

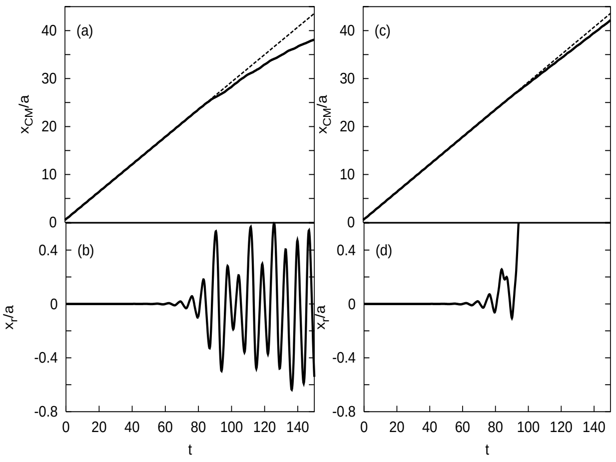

Figure 3.10: Numerical simulations of the equation of motion of a dimer for harmonic (a),(b) and LJ interactions (c),(d). The CM and internal motion are shown. The dashed lines in (a) and (c) are linear fits to x_{CM} for $t < 80$. The parameters are $U_0 = 0.6$, $K = 0.4$ and $v_0 = 2.15$ for the harmonic potential. The parameters of the LJ have been chosen according to Eq. (3.21): $\sigma \simeq 5.598$ and $\epsilon \simeq 0.219$.

Fig. 3.5, resembles characteristics peculiar to a chaotic regime. This is confirmed by looking at the temporal evolution of two trajectories starting at infinitesimally distant points. For example, Fig. 3.11 shows two long CM trajectories with initial spatial conditions differing by 10^{-6}. The behaviour of the CM is unpredictable and the trajectories diverge for the entire simulation time. This is a qualitative signature of chaotic dynamics (see the appendix at the end of the chapter). Chaotic motion can occur in nonlinear dynamical systems with at least three degrees of freedom. Much studied is the case of systems characterized by a single spatial coordinate subjected to an external drive [42, 43, 44, 45, 46]. Besides, a system of interacting particles can exhibit chaotic motion with "quasi-diffusive" features in one dimension [47, 48, 49]. This can happen even without the presence of an external drive, as we will show below. In view of the sinusoidal potential and of the phase space dimension, our model bears some resemblance to an undriven double pendulum [50, 51, 52]. However, in our case, the possibility to perform either oscillatory or drift motion leads to the appearance and subsequent disappearance of chaos for increasing initial kinetic energy.

In order to characterize more quantitatively the chaotic motion, we have numerically computed the Lyapunov exponent, which measures the rate of divergence of nearby trajectories (see [53, 54]):

$$\delta x(t) \sim \delta x(0)\mathrm{e}^{\lambda t}, \tag{3.22}$$

where $\delta x(t)$ denotes the separation between nearby trajectories and λ is the Lyapunov exponent. In an $n-$ dimensional phase space n Lyapunov exponents can be calculated, but we limit ourselves to the computation of the maximal Lyapunov exponent λ_{max} (see Eq. (3.45)), which is sufficient to signal the occurrence of chaos. If $\lambda_{max} > 0$ the motion

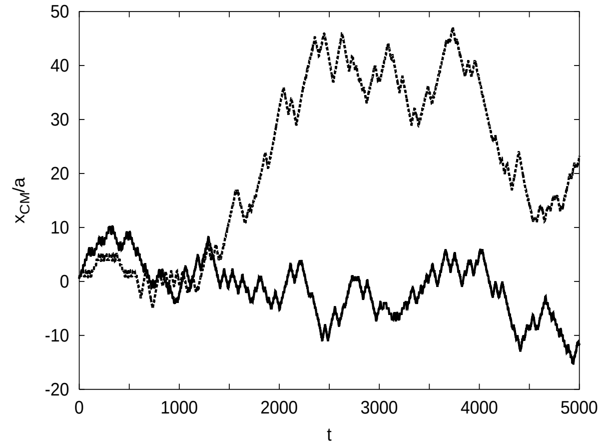

Figure 3.11: CM motion for $U_0 = 0.6$, $K = 0.1$ and $v_0 = \sqrt{4U_0} \simeq 1.5492$, starting from initial conditions differing by 10^{-6}.

is unstable and chaos may occur, while if $\lambda_{max} < 0$ we have a regular stable motion ($\lambda_{max} = 0$ corresponds to a stable quasi-periodic motion). We show λ_{max} as a function of time for a small value of K ($K = 0.05$ and $U_0 = 0.6$) in Fig. 3.12 for different v_0. The saturation values of the different curves give a measure of the corresponding maximal

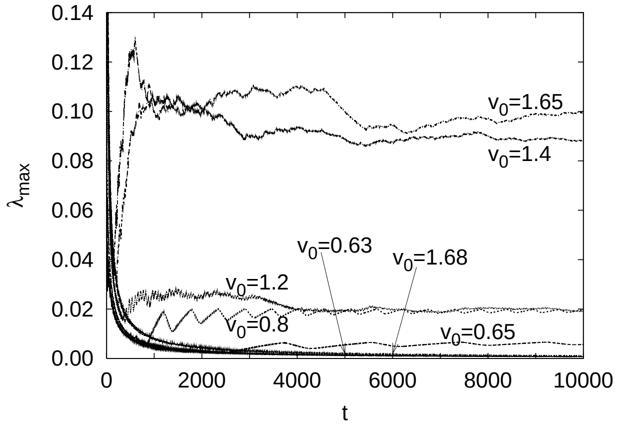

Figure 3.12: Temporal behaviour of the maximal Lyapunov exponent for $U_0 = 0.6$, $K = 0.05$ and different initial velocities v_0, which are reported beside each curve.

Lyapunov exponent. We note that for low values of v_0 ($v_0 = 0.63$ in the figure) $\lambda_{max} = 0$, meaning that the motion in this range is regular: x_{CM} oscillates periodically and $x_r \simeq 0$. When the internal motion starts to be excited ($0.65 \leq v_0 < 1.4$) λ_{max} jumps to a positive small value ($\lambda_{max} \simeq 0.02$), signalling that a weak chaotic dynamics is induced by x_r. For larger values of v_0 ($1.4 \leq v_0 < 1.68$), as the CM gets out of the minimum of the potential well and performs an irregular motion of the type shown in Fig. 3.5, the magnitude of

λ_{max} suddenly increases of about one order of magnitude ($\lambda_{max} \simeq 0.1$), but jumps again discontinuously to zero when v_0 is high enough for the CM to perform a drift motion and $x_r \simeq 0$. In this way, we have a complex transition from non-chaotic to chaotic motion and vice versa as a function of the initial velocity, as sketched in Fig. 3.13. This behaviour is different from that of the double pendulum, where the non-chaotic regime is not recovered for large initial velocities [50, 51].

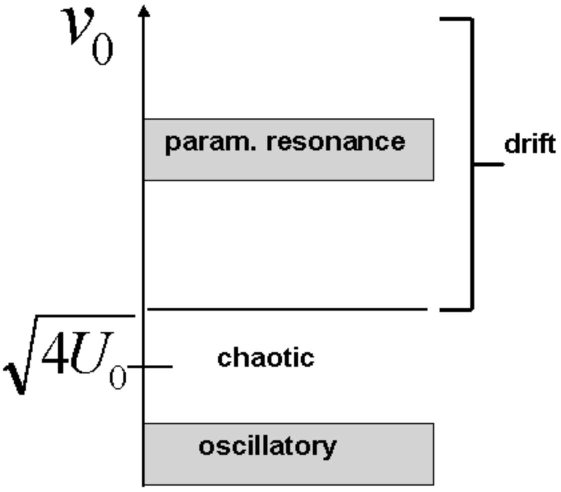

Figure 3.13: Sketch of the dynamical regimes for the dimer as a function of the initial velocity of the CM of the dimer. For low velocities oscillatory motion occurs, while, for intermediate velocities in a region around the threshold $\sqrt{4U_0}$, chaotic motion appears. For higher velocities, drift motion and possible parametric resonances characterize the dimer dynamics. For $K = 0.05$ chaos is found for $0.7 \leq v_0 \leq 1.65$ ($0.49 \leq E^{(0)}_{kin} \leq 2.72$), for $K = 0.1$ in the range $0.9 \leq v_0 \leq 1.78$ ($0.81 \leq E^{(0)}_{kin} \leq 3.168$) and for $K = 0.3$ in the range $1.5 \leq v_0 \leq 2.15$ ($2.25 \leq E^{(0)}_{kin} \leq 4.62$).

Further insight into such a dynamical behaviour is found by looking at the phase space projected on the (x_{CM}, v_{CM}) plane in Fig. 3.14, for four different initial velocities. The phase plot in (a) is a simple closed loop corresponding to a regular oscillatory motion where $\lambda_{max} = 0$. As the initial velocity increases more complex features appear: in the weak chaotic regime (b) extra loops are present, while the phase plot in (c) becomes very much folded and irregular. The regular dynamics is restored again in (d), where there is a drift motion of the CM, with v_{CM} oscillating around the drift velocity.

Power spectrum analysis is usually considered as an additional effective method to detect chaos. We have calculated the power spectra of x_r by using a fast Fourier transform and we show them in Fig. 3.15 for the same values of U_0, K and v_0 as in Fig. 3.14. The power spectrum for the regular motion (a) is smooth and has few peaks, at $\omega_{osc}, 3\omega_{osc}, 5\omega_{osc}, \ldots$, i. e. the harmonics expected for a parametric oscillator. In (b) each peak broadens, developing further lateral features. For the most chaotic motion (c) the power spectrum

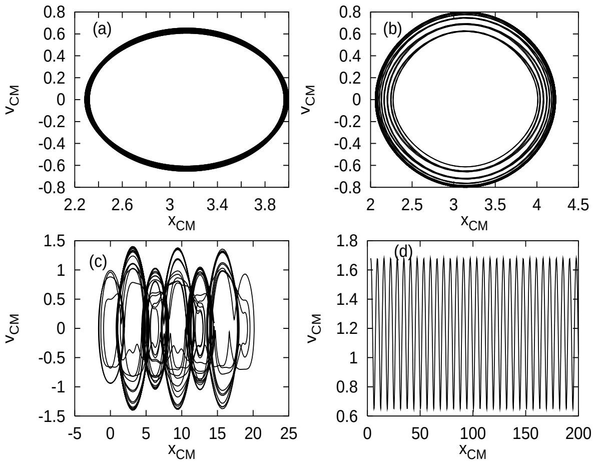

Figure 3.14: Phase space plot projected on the (x_{CM}, v_{CM}) plane for $U_0 = 0.6$, $K = 0.05$ and four values of v_0: $v_0 = 0.63$ (a), $v_0 = 0.8$ (b), $v_0 = 1.4$ (c) and $v_0 = 1.68$ (d).

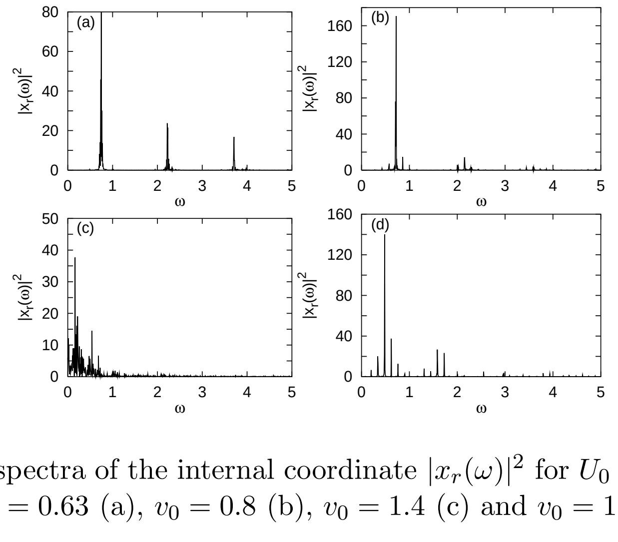

Figure 3.15: Power spectra of the internal coordinate $|x_r(\omega)|^2$ for $U_0 = 0.6$, $K = 0.05$ and four values of v_0: $v_0 = 0.63$ (a), $v_0 = 0.8$ (b), $v_0 = 1.4$ (c) and $v_0 = 1.68$ (d).

becomes very irregular with a large number of peaks. This chaoticity disappears for higher velocities (d), where the motion is regular and the power spectrum is again smooth with a large peak at $\omega = \sqrt{2K}$ corresponding to the dimer stretching frequency.

3.3.4 Discussion

In this section we have presented some aspects of the nonlinear Hamiltonian dynamics of a dimer moving on a $1D$ periodic substrate with period equal to the equilibrium length of the dimer. A complex dynamical behaviour as a function of the energy is found, with occurrence of resonant instabilities and chaotic motion. However, some features have been neglected or not fully considered in the model, and we will comment briefly on them.

1. **Role of incommensurability.** In the previous discussion we have only studied the commensurate case, both for the possibility of a semi-analytical description and for its relevance to a number of physical systems, such as diffusion of small metal clusters on surfaces of the same material (see for example Ref. [37]). However, different ratios between the dimer equilibrium length and the substrate lattice parameter are also of interest, for example for heteroepitaxial crystal growth. In this case the equilibrium configuration of the dimer in the periodic potential depends on the value of the diffusion barrier and of the force constant. The dynamical behaviour of the incommensurate dimer is qualitatively the same, with the occurrence of chaotic motion. However, since the incommensurate configuration has a higher potential energy, the escape of the particle from the local minimum occurs at lower initial kinetic energies than in the commensurate case, thus enlarging the range of initial velocities where the chaotic behaviour takes place.

2. **Pulling the particles apart.** In our investigation we have imposed an initial equal velocity to both particles in the same direction. A worthy question is what happens when the initial condition is changed, for example when the two particles are pulled in opposite directions. In this situation the dimer performs two kind of motions: localized vibrations with the CM fixed at the equilibrium position and chaotic motion. It is interesting that upon increasing the energy the order in which these regimes occur is inverted with respect to the case where the particles are driven in the same direction. In fact, there is a transition from localized vibrations to chaos at low energies, then a range of energies of oscillatory motion again and another transition to chaos at higher energies [1]. While in the case discussed in Sec. 3.3.2 the CM oscillatory motion parametrically drives the internal motion and receives a feedback from it, here the oscillatory motion of the internal coordinate x_r excites the CM and can drive the chaotic behaviour.

3. **Influence of dissipation and noise.** A realistic description of surface diffusion should include temperature and dissipation, for example in the framework of the Langevin formalism, as done in Sec. 2.4. Although in this section we have neglected thermal fluctuations, we can try to make some qualitative predictions concerning the effect of a finite substrate temperature, modelled by stochastic forces and a damping

term, on the diffusive dynamics. The introduction of these effects could smear out all the deterministic features. The stable periodic orbits become attracting centres via dissipation, so that the regular and chaotic motions would be only transient. On the other hand, temperature should be effective to provide energy to escape from an attractor, giving rise to a diffusive motion. Nevertheless, we expect that for small temperatures and small friction coefficients, the thermal equilibration time should be bigger than the equilibration time due to the deterministic chaotic dynamics. Thus, under such circumstances, the effects explained in this section could be significant also for real systems at finite temperature, at short time scales. The relation between chaotic dynamics and thermal diffusion will be discussed in more detail in Sec. 3.5.

4. **Relevance to experiments.** An example of applicability of our results concerns the chaotic dynamics. Chaos in surface diffusion is a novel feature, which gives rise to interesting anomalous behaviour, and has recently attracted much attention [39]. In particular, anomalous diffusion observed in the motion of Na particles on Cu(001) in $2D$ [39], by means of quasielastic helium atom scattering (see Sec. 1.3.3 of Chap. 1), has been related to chaotic dynamics. This has been inferred by studying the phase space structure and the power spectra. Such a behaviour is connected to the low-damping diffusion occurring in this system, where $\eta \simeq 10^{-12}$ ps^{-1}. Another system where chaotic motion can be relevant is Xe on Pt(111), in which the extreme case of ideal gas behaviour, with zero effective friction and no influence of the adiabatic potential, has been observed experimentally [59] (see Fig. 3.16). For this situation our deterministic description is fully justified.

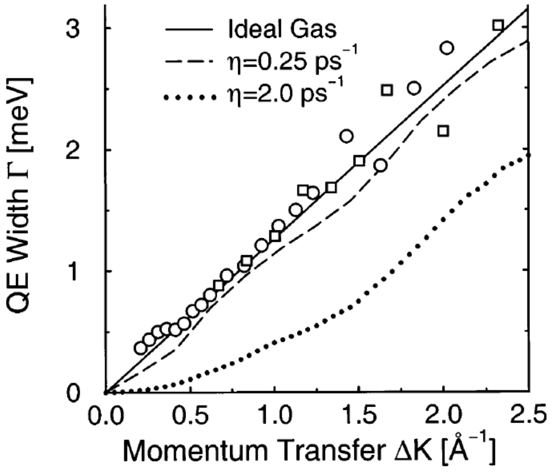

Figure 3.16: Momentum transfer dependence of the quasielastic helium atom peak broadening. The circles and the squares correspond to experimental data for two different incident energies of the beam for scattering from Xe adsorbed on a Pt(111) surface at $T = 105$ K. The solid line is the theoretical prediction for an ideal gas at the same temperature, while the dotted and dashed line are obtained by MD simulations for two different values of the damping η. [From Ref. [59]].

In Sec. 3.1 we have pointed out that our model can be thought a simple description of diffusive processes occurring during crystal growth and thin film formation. There are also experiments in which gas molecules, for example CH_4 (which can be thought as a dimer formed by a group CH_3 and an H atom), are adsorbed on a metal surface at high translational energies, using supersonic molecular beams, and can eventually dissociate [41, 55, 56]. The angle between the beam and the surface can be changed, and the sticking probability of the molecule to the surface is found to be a pronounced function of the incident angle [55]. Specifically, our model mimics the case of a beam parallel to the surface. It can be interesting to examine in which experimental conditions the effects predicted by our model about the occurrence of resonant effects are important: this should happen when the condition for parametric resonance

$$v = v_{res} \simeq 2\nu_0 a, \tag{3.23}$$

is satisfied. In Eq. (3.23) $\nu_0 = \omega_0/(2\pi)$ is the vibrational frequency of the molecule and a is the lattice parameter of the surface. For CH_4 on Pt(110) $\nu_0 \simeq 8.4 \cdot 10^{13}$ Hz and $a \simeq 2.77 \cdot 10^{-10}$ m. Thus $v_{res} \simeq 3 \cdot 10^4$ m/s, which is very high in comparison to the typical velocities in experiments, which are one order of magnitude smaller (the maximum initial translational energy is of the order of 1 eV). This means that the nonlinear resonant effects are not easily observed in this kind of experiments. Nevertheless, the coupling between translational and internal motion that plays a crucial role in our study is found to be very important in the dissociative dynamics of methane [57]. However, the resonant velocity given by Eq. (3.23) is much lower for commensurate metal dimers. For example, for Al_2 on Al(110) [26] one finds $\nu_0 \simeq 2.8 \cdot 10^{12}$ s^{-1} and $a \simeq 4 \cdot 10^{-10}$ m, yielding $v_{res} \simeq 2300$ m/s, thus an order of magnitude less than for CH_4. We thus predict these kinds of effects to occur at high enough incident translational energies, which are currently not achievable in experimental situations.

3.4 Non-Arrhenius thermal diffusion

Analogously to what discussed for the monomer in Sec. 2.4, we present here the thermal diffusive dynamics of the dimer, which is studied in the Langevin approach. Thus $v_0 = 0$ and $F = 0$ in Eq. (3.6). The diffusion coefficient is defined in this case from the mean square displacement of the CM of the dimer:

$$D = \lim_{t\to\infty} \frac{< x_{CM}^2(t) >}{2t}. \tag{3.24}$$

At variance with the adatom case, for which the diffusion coefficient follows an Arrhenius behaviour at not too large temperatures (see Fig. 2.13), we will show here that pronounced deviations from the activated exponential behaviour can occur for the dimer. This is immediately seen in Fig. 3.17(a), where the diffusion coefficient of the adatom and of the dimer for different equilibrium lengths is plotted. Two striking features emerge from this figure:

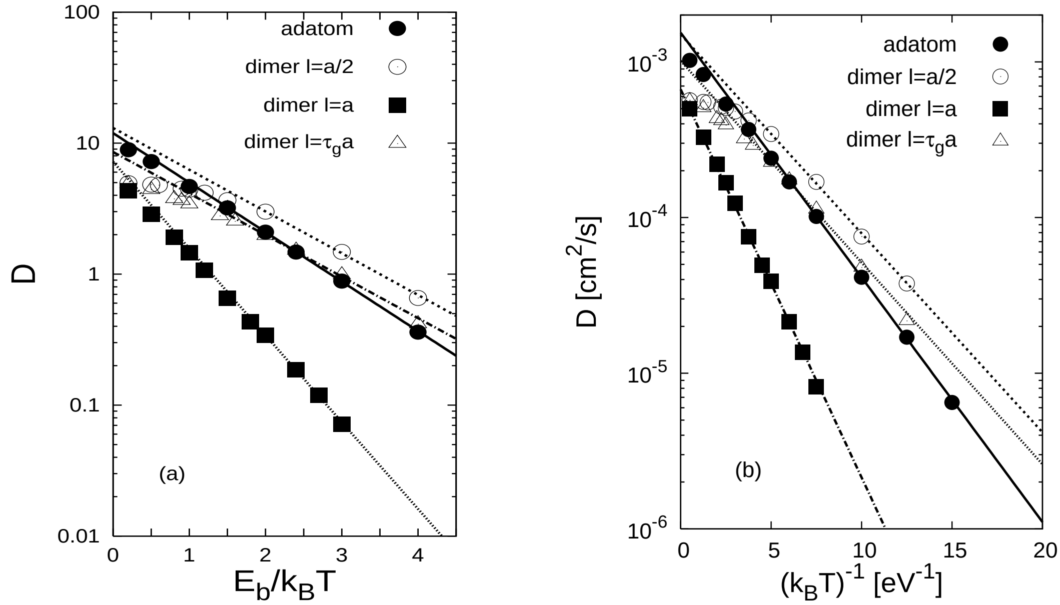

Figure 3.17: (a) Diffusion coefficient D as a function of the potential barrier E_b (rescaled to k_BT) for the adatom and the dimers with $K = 1$, $\eta = 0.1$ and different values of l. (b) Same data as in (a) plotted in physical units. Here $a = 0.25$ nm, $U_0 = 0.2$ eV, $m = 5 \cdot 10^{-26}$ kg, $K = 2$ N/m and $\eta = 0.7$ ps^{-1}. The points are the data from the simulations and the lines represent fits to the data in the low temperature regime. Notice that the the diffusion coefficient of the dimer with $l = a/2$ at $E_b = 36$ is about 3 orders of magnitude larger than that of the adatom. $\tau_g = (1 + \sqrt{5})/2$ is the golden mean, which is a prototypical example of incommensurate ratio [60].

- The dimer can diffuse faster than the monomer for some values of the intramolecular spacing (for example $l = a/2$), with a lower activation energy.
- The behaviour of the dimer deviates from the activated form in the high temperature (or equivalently low potential barrier) region.

The fact that the diffusivity of the dimer can be higher than that of the monomer is also found by Monte Carlo studies [16] and by an analytical approach [30]. This is explained by the fact that for certain intramolecular lengths the dimer is “out of phase” with respect to the surface potential, creating a misfit which weakens the energy barrier and thus results in a higher diffusion. Furthermore, experiments on water diffusion on Pd(111) performed at low temperatures ($T \simeq 40$ K) showed that the mobility of dimers and larger clusters is 3-4 orders of magnitude larger than that of adatoms [8]. This is due to the mismatch between the oxygen-oxygen distance in the dimer, which is $2.96 \cdot 10^{-10}$ m and the lattice constant of Pd(111), which is $2.75 \cdot 10^{-10}$ m: the misfit prevents both molecules from forming bonds to the substrate, thus reducing the diffusion barrier of the dimer. Also in our case, extrapolating the fits to the data of Fig. 3.17 to very low temperatures, it is possible to see that the dimer diffusion can be orders of magnitude higher than that of the adatom.

The non-Arrhenius behaviour of the diffusion coefficient observed in Fig. 3.17 is due to the dependence of the activation energy on temperature (or equivalently on the diffusion barrier). We attribute this to the role of internal vibrations, which can account for a temperature dependent equilibrium length, affecting the diffusive behaviour especially in the high temperature (or low E_b) regime. A similar mechanism was also proposed in a study of heteroepitaxial island diffusion of small Ag clusters on Ru(0001) [17]. We elucidate the effect of the intramolecular motion on the diffusive behaviour in Fig. 3.18(a), where we compare the diffusion constant of the incommensurate dimer for l fixed to its equilibrium value to that of the non rigid incommensurate dimer. It is clear that we can

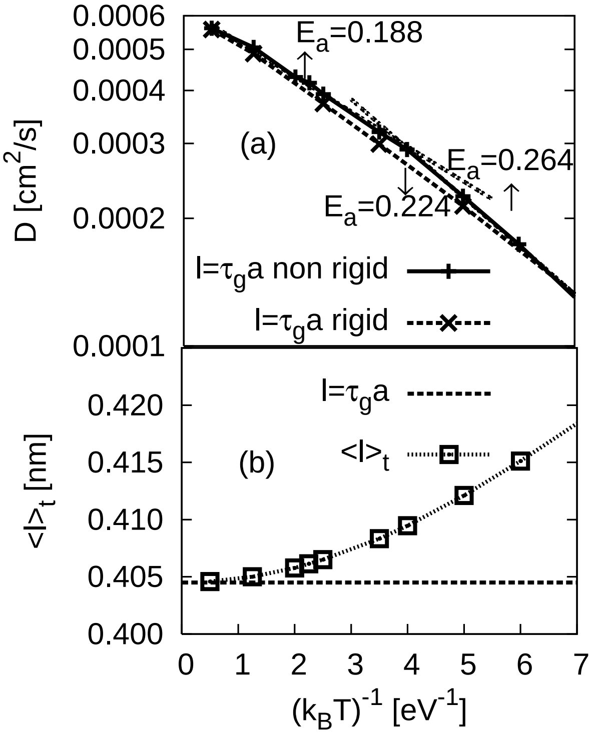

Figure 3.18: (a) Diffusion coefficient as a function of $1/(k_B T)$ for the incommensurate dimer with $l = \tau_g a$ and the same parameters as in Fig. 3.17. The intramolecular length is kept fixed or not fixed, as indicated by the labels. Fitted activation energies (in eV) are also reported. (b) Dynamical equilibrium length $< l >_t$ as a function of $1/(k_B T)$.

define a unique value of the activation energy E_a for the rigid dimer, whereas the activation energy is in general temperature dependent when the dimer is allowed to vibrate. The temperature dependence of E_a is linked a temperature dependent misfit $< l_t >$ induced by the dynamics, as shown in Fig. 3.18(b): $< l_t >$ is the intramolecular spacing averaged over time, which can be viewed as a dynamical equilibrium length.

The effect of the internal motion on the activation energy for diffusion of the dimer can be analytically taken into account by a simple argument. The interaction between the dimer and the substrate (Eq. 3.1) is separable and can be written as

$$U_{sub}(x_1, x_2) = U(x_1) + U(x_2) \tag{3.25}$$

where $U(x)$ is the single particle interaction potential

$$U(x) = U_0 \left[1 - \cos\left(\frac{2\pi x}{a_x}\right)\right]. \tag{3.26}$$

It is easy to see that U_{sub} can be written as

$$U_{sub} = U(x_{CM} + \delta x) + U(x_{CM} - \delta x), \tag{3.27}$$

where $\delta x = \frac{1}{2}(x_2 - x_1) = \frac{1}{2}(x_r + l)$. Considering $\delta x \ll l/2$ (this assumption is rather well-founded for the commensurate case) and expanding Eq. (3.27) around x_{CM} up to the fourth order in δx, we get

$$U_{sub}(x_{CM}, \delta x) = 2U_0 \left[1 - \cos\left(\frac{2\pi x_{CM}}{a_x}\right) + \cos\left(\frac{2\pi x_{CM}}{a_x}\right)(\delta x)^2 - \cos\left(\frac{2\pi x_{CM}}{a_x}\right)(\delta x)^4\right] \tag{3.28}$$

Averaging Eq. (3.28) over the internal vibrations and using the equipartition theorem

$$< (\delta x)^2 >= \frac{1}{2m\omega_0^2} k_B T \tag{3.29}$$

$$< (\delta x)^4 > \simeq (< (\delta x)^2 >)^2 = \frac{1}{4m^2\omega_0^4}(k_B T)^2 \tag{3.30}$$

we obtain $< U_{sub} > (x_{CM})$, i. e. the average of U_{sub} over δx as a function of x_{CM}, as

$$< U_{sub} > (x_{CM}) = 2U_0 \left[1 - \cos\left(\frac{2\pi x_{CM}}{a_x}\right) + \frac{\cos\left(\frac{2\pi x_{CM}}{a_x}\right)}{2m\omega_0^2} k_B T - \frac{\cos\left(\frac{2\pi x_{CM}}{a_x}\right)}{4m^2\omega_0^4}(k_B T)^2\right]. \tag{3.31}$$

The activation energy is given by

$$E_a =< U_{sub} > (x_{CM,max}) - < U_{sub} > (x_{CM,min}) \tag{3.32}$$

At $T = 0$, $x_{CM,max} = \pi$ and $x_{CM,min} = 0$, so that we can approximate the expression of E_a for finite T by

$$E_a \simeq< U_{sub} > (\pi) - < U_{sub} > (0) = 4U_0 \left[1 - \frac{k_B T}{2m\omega_0^2} + \frac{(k_B T)^2}{4m^2\omega_0^4}\right]. \tag{3.33}$$

This shows that the activation energy depends on temperature. Computing the values of $E_a/2U_0$ from Eq. (3.33) for different K we get numbers very close to those obtained from the numerical results of Fig. 3.17. For example, for $l = a$, $K = 2$ N/m and using for the other parameters the values reported in the caption of Fig. 3.17, we obtain $E_a/2U_0 \simeq 1.5$ from the simulations and $E_a/2U_0 \simeq 1.6$ from Eq. (3.33). For $l = a$ and $K = 0.2$ N/m, $E_a/2U_0 \simeq 1.2$ from the simulations and $E_a/2U_0 \simeq 1.25$ from Eq. (3.33).

The diffusion coefficient is also a sensitive function of the strength of the intramolecular coupling. This is illustrated in Fig. 3.19 for the commensurate case $l = a$ and for the incommensurate case $l = \tau_g a$. While in the commensurate situation the diffusion decreases when increasing the force constant K, the diffusion coefficient for the incommensurate dimer is higher at larger K. In fact, a rigid dimer ($K \to \infty$) with $l = a$ is equivalent to a monomer and it perfectly fits in the substrate potential. Thus, the possibility to excite the internal motion of the commensurate dimer leads to a looser fit with the periodic potential and can promote the diffusive motion: this is analogous to what found for the deterministic motion in Sec. 3.3, where the escape of the dimer over the barrier is enhanced by the intramolecular vibrations. A complex dependence of the dimer diffusivity on the force constant for $l = a$ has also been reported in a recent study [32]: for low temperatures D is a decreasing function of K. The behaviour of the CM and internal motion for $l = a$ and two values of the force constant in one stochastic realization of the dynamics is illustrated in Fig. 3.20: for small K, the jumps of the CM are clearly correlated with the internal vibrations and usually occur just after large displacements of x_r. Conversely, for large K,

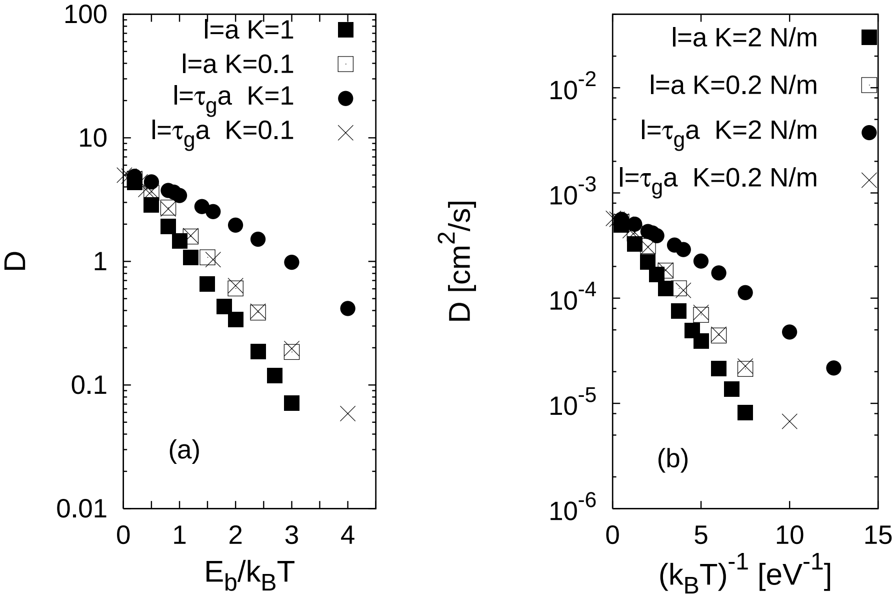

Figure 3.19: (a) Diffusion coefficient as a function of the energy barrier (scaled to $k_B T$) for the commensurate ($l = a$) and incommensurate ($l = \tau_g a$) dimer, each for two different values of K ($K = 0.1$ and $K = 1$), and $\eta = 0.1$. (b) Same data as in (a) plotted in physical units (see parameters in the caption of Fig. 3.17). While in the commensurate case the diffusion is higher for smaller K, an increase of D with K is observed for the incommensurate dimer.

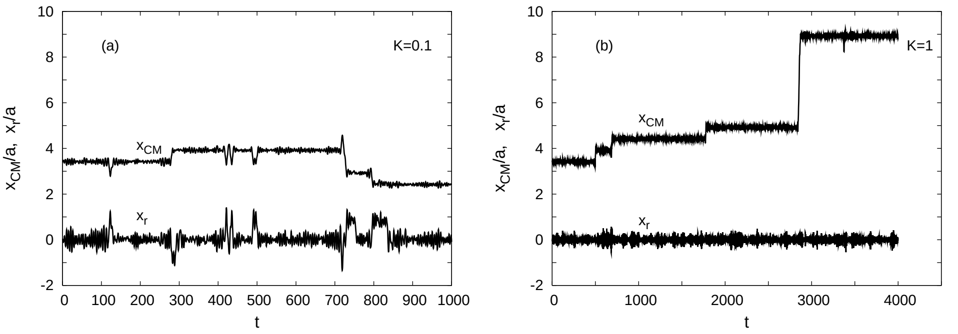

Figure 3.20: Temporal evolution of CM and internal motion (rescaled to the lattice parameter a) for the commensurate dimer ($l = a$), $U_0 = 1.5$, $\eta = 0.1$ and two values of the force constant: $K = 0.1$ (a) and $K = 1$ (b). While the internal motion drives the CM in (a), the dimer motion is concerted in (b). Thus, the excitation of internal vibrations enhances the diffusive motion. Notice the extended time scale in (b), necessary to observe rare jumps events of the CM.

the internal coordinate oscillates smoothly around a constant value and the motion of the dimer is concerted, i. e. it moves over the barrier as a nearly rigid unit. Jumps of x_{CM} are very rare in this case, and the diffusion is lower than for small K. Thus, diffusion decreases with K in the commensurate case. On the other hand, the incommensurate rigid dimer has a lower barrier to overcome to diffuse and the main effect of the internal motion is to dissipate translational energy, thus inhibiting the diffusion. This can be appreciated in Fig. 3.21, where long jumps of the CM for large K, signalling enhanced diffusion, occur, while for small K shorter jumps together with larger oscillations in the internal motion are dominant. Thus, in this case, diffusion increases with K.

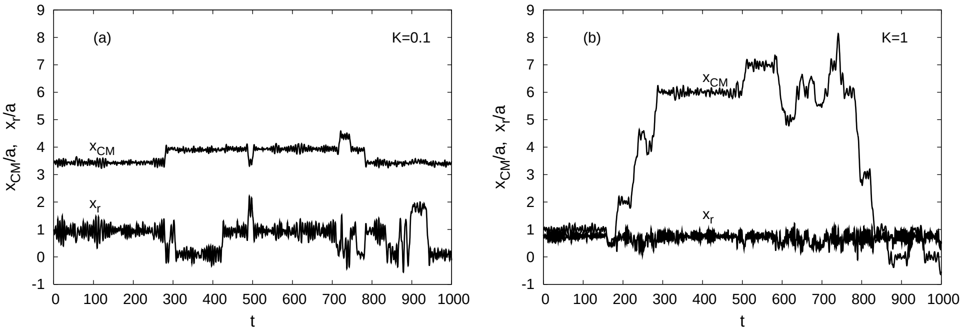

Figure 3.21: Temporal evolution of CM and internal motion (rescaled to the lattice parameter a) for the incommensurate dimer ($l = \tau_g a$), $U_0 = 1.5$, $\eta = 0.1$ and two values of the force constant: $K = 0.1$ (a) and $K = 1$ (b). Here we have an opposite trend with respect to Fig. 3.20: for small K, the diffusion is less pronounced, since the internal motion dissipates the translational energy of the CM. Instead, longer jumps of x_{CM} are seen for larger K.

In summary, the possibility to excite the internal degrees of freedom, even for a simple diatomic molecule, can affect the temperature dependence of the activation energy and determine a complex diffusive behaviour that is related to the lattice commensurability.

3.5 Relation between chaos, deterministic and thermal diffusion

In Sec. 3.3.2 we have seen that the dimer can undergo a chaotic, "stochastic-like" motion even in the absence of thermal fluctuations. This "anomalous" diffusion, which is called "deterministic diffusion", is caused by the interparticle interaction and thus it is absent for individual adatoms. Diffusive-like dynamics in a Hamiltonian system arises as a result of the instability of the motion in a bounded region of phase space. The rapid stochastization of the dynamics is a consequence of the chaotic coupling between the CM and the internal motion and is due to the excitations of parametric resonances in the system: in the "drift" of the dimer above the periodic relief a periodic force arises, which acts on the internal degree of freedom in a parametric way. The fact that dynamical chaos leads to spatial diffusion in configuration space is of exceptional interest, since it demonstrates that under certain conditions cluster diffusion can occur at $T = 0$, i. e. in the absence of thermal impacts due to a heat bath. In this case the role of the heat bath is played by the exchange between translational and internal motion, which, due to the nonlinearity of the system, can occur in a random manner. Fig. 3.22 shows a comparison between the deterministic and the thermal mean square displacements. At $T = 0$, $< x_{CM}^2 >$ represents

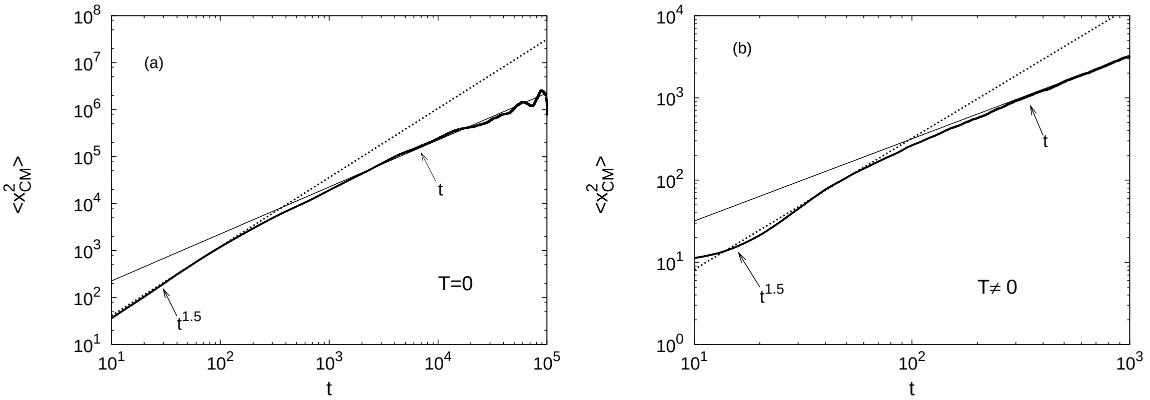

Figure 3.22: Mean square displacement for the deterministic (a) and thermal motion (b) for $U_0 = 0.6$ and $l = a$ (thick solid lines) . In (a) $K = 0.05$, $v_0 = 1.65$, $\eta = 0$ and in (b) $K = 0.1$, $\eta = 0.1$. The thin solid lines are linear fits for large t, while the dashed lines are power law fits with exponent ~ 1.5 for small t. The data plotted in (b) have been obtained by averaging the trajectory over 3000 realizations.

a time average taken by displacing the time origin [61], while at $T \neq 0$ it is an average over realizations. It can be seen that the long time behaviour is linear (diffusive) also for $T = 0$. Notice that in Fig. 3.22 a transient superdiffusive regime is present, both at $T = 0$ and at finite T. This is an indication of anomalous diffusion, which might signal the presence of chaotic effects with long jumps. In fact, signatures of the chaotic regime can be recognized in the jump length distribution: jumps of the adsorbate over many lattice parameters are predicted by theoretical models (see for instance [15, 62]) and observed experimentally (see [13]). In particular, diffusion should be highly promoted for weakly bound dimers for which we found the chaotic features. Indeed, as reported in Ref. [32], the diffusion coefficient decreases by about an order of magnitude with respect to the non-interacting case $K = 0$, when the elastic constant is increased from $K = 0$ to $K = 0.25$, at least for small values of the damping and of the temperature. Therefore, the relation between chaotic deterministic diffusion and stochastic thermal diffusion is an important topic currently under study [39].

As we have already mentioned in Sec. 3.3.2, the anomalous diffusion is due to the coexistence of regular and chaotic dynamics, which can be seen in the phase space as the coexistence of localized and unbounded motion (see for example Fig. 3.14(c)). Fig. 3.23 shows that this structure persists also at finite T for small force constants: some periodic patterns can be recognized in the chaotic phase space.

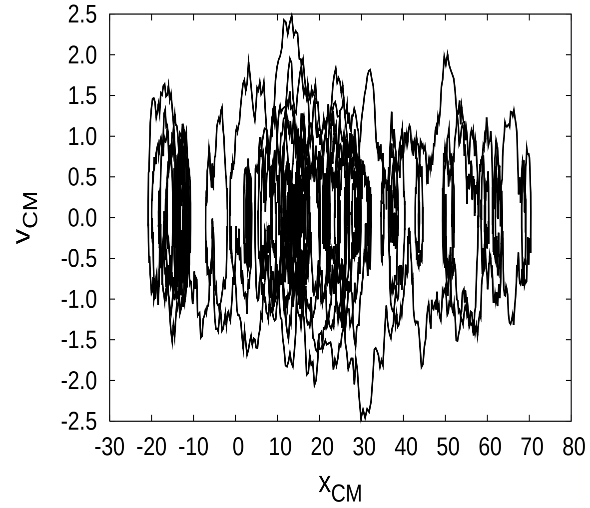

Figure 3.23: Phase space plot projected on the (x_{CM}, v_{CM}) plane at finite T for $U_0 = 0.6$, $\eta = 0.1$ and $K = 0.05$. Notice that a structure similar to that of Fig. 3.14(c) ($T = 0$), with periodic and unstable orbits, can be recognized. The more pronounced irregularity is due to thermal fluctuations.

Finally, we mention that a deterministic diffusive behaviour leads to a non-Arrhenius dependence of the thermal diffusion coefficient, as in Fig. 3.19, providing a further link between chaotic dynamics and thermal diffusion [63]. Deviations from the Arrhenius behaviour due to deterministic chaos have been reported for example for the diffusion of molecules through zeolite crystals [36].

3.6 Driven diffusion

The driven motion of the dimer is of importance to understand the frictional dynamics of the smallest cluster of interacting particles. In fact, we will show below that the interparticle interaction renders the problem more complex than for the driven motion of a monomer, giving rise to a richer dynamical behaviour. This can be immediately seen in Fig. 3.24, where we have plotted the velocity-force characteristics for different values of the intramolecular spacing l, namely $l = a$, $l = a/2$ and $l = \tau_g a$, both for $T = 0$ and $T \neq 0$. Notice that for each l we choose an initial configuration of the dimer which minimizes the total potential energy.

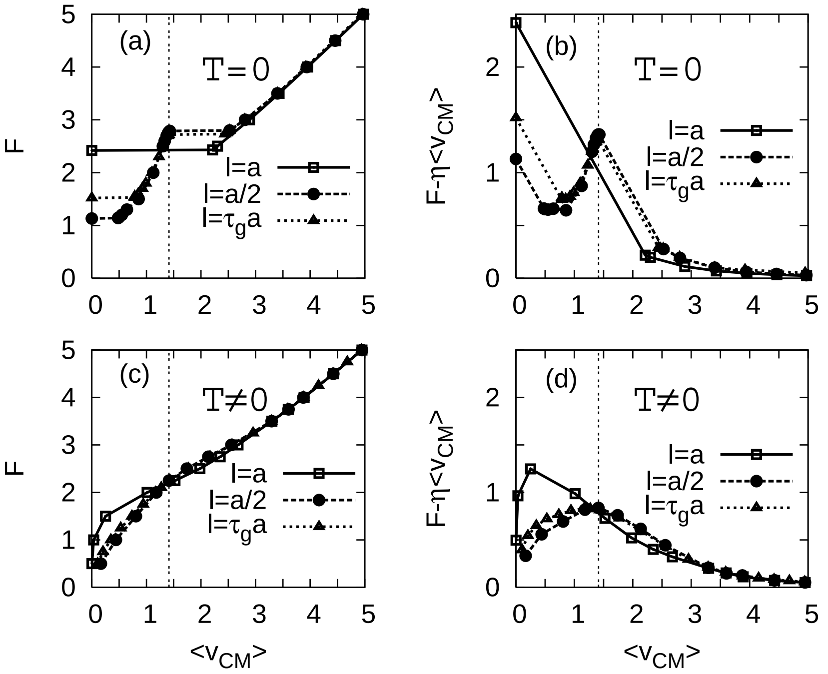

Figure 3.24: Velocity-force characteristic of the dimer for $T = 0$ (a),(b) and $T \neq 0$ (c),(d) for three values of l. The vertical dot-dashed line passes through $\langle v_{CM} \rangle = \omega_0$. The parameters used are $U_0 = 2.5$, $\eta = 1$ and $K = 1$. Notice that the critical value of the force F_{c1}^{dim} to start the motion of the dimer depends sensitively on l.

Let us first consider the case $T = 0$ (Figs. 3.24(a)-(b)). As for the monomer (see Sec. 2.2.2), a critical force F_{c1}^{dim}, which depends on the value of l, is needed to achieve the motion for $T = 0$. Then, for larger values of F, the velocity increases as a function of the external force, but at a certain value of the force F_{c3}^{dim} another plateau appears in the $(\langle v_{CM} \rangle, F)$ plane, signalling a dynamical crossover in the system. Finally, keeping on increasing the force, the linear regime is recovered (Fig. 3.24(a)). We note that the qualitative behaviour is the same for different l, but the values of F_{c1}^{dim} can differ significantly as a function of l. This is due to energetic reasons: the dimer with $l = a/2$ is favourite since, on average, it has to overcome a lower barrier, while for $l = a$ the two particles tend to be pinned in the minima and to behave like a monomer (in fact the velocity-force characteristic of the $l = a$ dimer is practically superimposed on that of the monomer). A closer comparison between the velocity-force characteristic of the monomer and that of the incommensurate dimer at $T = 0$ is presented in Fig. 3.25(a). The main differences

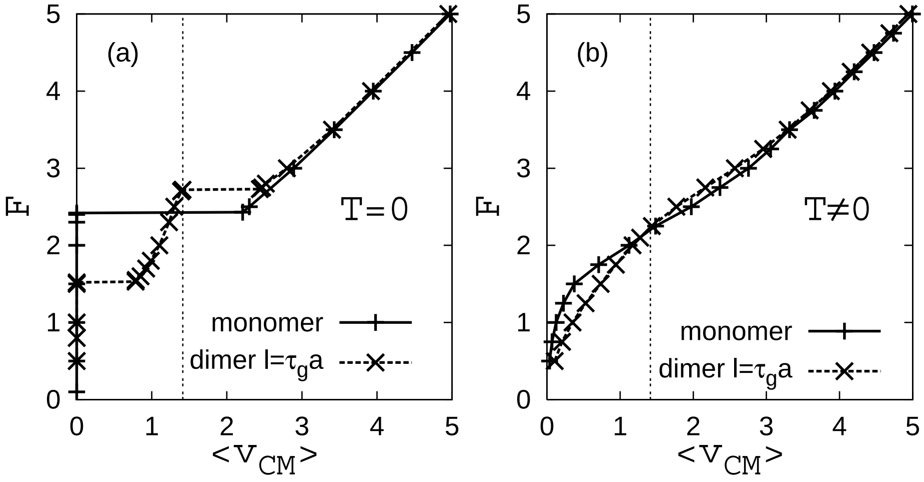

Figure 3.25: Comparison between the velocity-force characteristic of the monomer and of the dimer for $T = 0$ (a) and $T \neq 0$ (b). The vertical dot-dashed lines pass through $\langle v_{CM} \rangle = \omega_0$. The parameters used are the same as in Fig. 3.24. Notice the second "plateau" of $F(\langle v_{CM} \rangle)$ for the dimer at $T = 0$, which is absent for the monomer, and the crossover of the mobility at $T \neq 0$ near $\langle v_{CM} \rangle = \omega_0$.

are that the static friction F_{c1}^{dim} is lower than that for the monomer (where $F_{c1} = U_0$) and that the second plateau in the velocity-force characteristic is absent for the monomer; nevertheless, they follow the same asymptotic behaviour for large forces.

In the CM frame, the external potential leads, for a drift motion $x_{CM} \sim \langle v_{CM} \rangle t$, to a time-periodic force acting on the particles, with "washboard" frequency (i. e. the frequency associated to the drift motion over the periodic potential) given by $\langle v_{CM} \rangle$. The force F_{c3}^{dim}, where the second plateau appears, physically corresponds to the point where the washboard frequency is in resonance with the stretching frequency of the dimer $\omega_0 = (2K)^{1/2}$, exciting the internal degrees of freedom. This resonance mechanism was also found in the Frenkel-Kontorova model (periodic chain of interacting particles moving on a periodic substrate) in the low friction limit [64]. It is evident from Fig. 3.24(a) that, for $F < F_{c3}^{dim}$, an increase of the driving force F by a considerable amount leads only to a slight increase of the average drift velocity $\langle v_{CM} \rangle$. In other words, the differential mobility $d\langle v_{CM} \rangle / dF$ in this region is very low. This is due to the fact that not all the energy pumped by the force F is transferred into the translational motion of the CM, but when $\langle v_{CM} \rangle$ approaches the internal frequency of the dimer a sort of "swing" phenomenon occurs, for which most of the energy goes into excitations of the internal motion of the dimer. This means that the dissipation is maximum for $\langle v_{CM} \rangle \simeq \omega_0$. Such feature is highlighted in Fig. 3.24(b), where $F - \eta \langle v_{CM} \rangle$ is plotted as a function of $\langle v_{CM} \rangle$: a clear peak associated to the resonance appears at $\langle v_{CM} \rangle = \omega_0$ when $l \neq a$. In order to understand in more detail the mechanism giving rise to the resonance, one can study the second equation of motion (3.9) for the internal degree of freedom of the dimer, assuming that $x_r \ll 1$. The simplest approximation is the zeroth order, by which $x_r = 0$ inside the sine term of Eq. (3.9). Using the fact that $x_{CM} \sim \langle v_{CM} \rangle t$, we obtain the following approximate equation for the internal motion (note that $a = 2\pi$):

$$\ddot{x}_r + \eta \dot{x}_r + 2K x_r = 2U_0 \sin(l/2) \cos(\langle v_{CM} \rangle t). \tag{3.34}$$

We immediately recognize Eq. (3.34) to be the equation of a resonant oscillator, which has the solution

$$x_r(t) = 2U_0 \sin\left(\frac{l}{2}\right) \frac{1}{\sqrt{(\omega_0^2 - \langle v_{CM} \rangle^2)^2 + \eta^2 \langle v_{CM} \rangle^2}} \cos(\langle v_{CM} \rangle t - \delta), \tag{3.35}$$

where $\tan \delta = \eta \langle v_{CM} \rangle / (\omega_0^2 - \langle v_{CM} \rangle^2)$. At this point, we can use the balance of the energy dissipation rate to compute the sliding friction. In fact, the average power pumped by the driving force $\langle v_{CM} \rangle$ is dissipated in the CM motion and in the internal motion:

$$F \langle v_{CM} \rangle = \eta \langle v_{CM}^2 \rangle + \eta \langle v_r^2 \rangle, \tag{3.36}$$

where $v_r \equiv \dot{x}_r$ is the internal velocity. Using Eqs. (3.34) and (3.36) and approximating $\langle v_{CM}^2 \rangle$ by $\langle v_{CM} \rangle^2$, one finds, after some calculations, the nonlinear contribution to sliding friction:

$$F - \eta \langle v_{CM} \rangle = \frac{\eta}{2} U_0^2 \sin^2\left(\frac{l}{2}\right) \frac{\langle v_{CM} \rangle}{(\omega_0^2 - \langle v_{CM} \rangle^2)^2 + \eta^2 \langle v_{CM} \rangle^2}. \tag{3.37}$$

A comparison between the simulation and the analytical result is shown in Fig. 3.26. The agreement is very good, especially for small U_0 and large K [65]. For very large velocities we can neglect ω_0 with respect to $\langle v_{CM} \rangle$ in the denominator of Eq. (3.37):

$$F - \eta \langle v_{CM} \rangle \simeq \frac{\eta}{2} U_0^2 \sin^2\left(\frac{l}{2}\right) \frac{1}{\langle v_{CM} \rangle^3}. \tag{3.38}$$

This gives rise to a $\langle v_{CM} \rangle^{-3}$ behaviour of the nonlinear friction force for large F [4], which is the same law found for the monomer (see Eq. (2.25) of Chap. 2). However, this similarity is just incidental, because we have derived Eq. (3.37) on the basis of a resonant mechanism acting on the internal coordinate of the dimer, which is of course absent for a single particle. We also see from Eq. (3.35) that for the commensurate case $l = a = 2\pi$ no excitation of x_r takes place, as the sine term vanishes, and the description of the internal motion as that of a resonant oscillator is not effective. That is the reason for which no peak is observed in Fig. 3.24(b) for $l = a$.

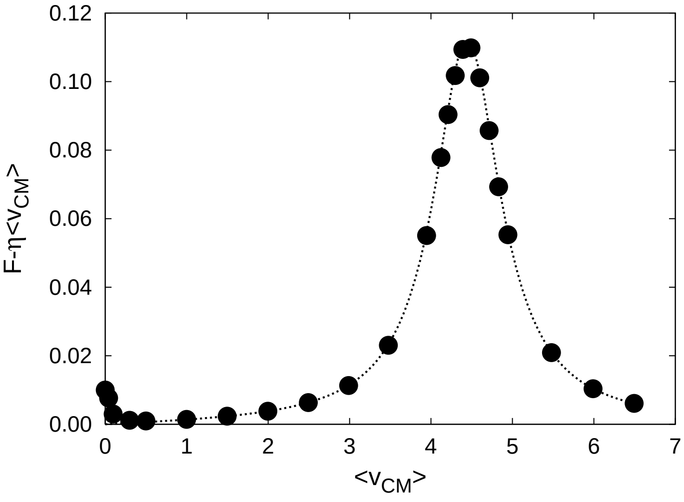

Figure 3.26: Velocity dependence of the nonlinear friction force for $U_0 = 1$, $\eta = 1$, $K = 10$ and $l = a/2$. The circles are the numerical result, while the dashed line is the theoretical curve obtained from Eq. (3.37). Notice the very good agreement between the theory and the data and the efficiency of Eq. (3.37) to reproduce the resonance at $\langle v_{CM}\rangle = \omega_0 = \sqrt{20}$.

A more thorough insight in the commensurate case can be gained by going to the first order approximation of the second equation (3.9). Linearizing the sine term for small x_r, we have

$$\ddot{x}_r + \eta\dot{x}_r + 2Kx_r = U_0\cos(\langle v_{CM}\rangle t)x_r. \tag{3.39}$$

Eq. (3.39) means that the commensurate dimer can be described in first approximation as a parametric oscillator. This is what we have just seen for the Hamiltonian dynamics in Sec. 3.3.1. From Eq. (3.39) an exponential increase of the amplitude of x_r is expected for $\langle v_{CM}\rangle \simeq 2\omega_0$ (thus not for $\langle v_{CM}\rangle = \omega_0$ as in the normal resonance) within a given instability window. We note that indeed the amplitude of x_r increases exponentially in a certain range of F, as shown in Fig. 3.27, but it saturates at long times. This is due to the fact that Eq. (3.39) assumes a constant CM velocity. Actually, in the full system Eq. (3.9), x_{CM} is coupled to x_r, so that v_{CM} decreases slightly during the dynamics as shown in Fig. 3.27(d). This is enough to shift $\langle v_{CM}\rangle$ out of the instability window, thus stopping the increase of x_r.

This shows how intramolecular vibrations can be resonantly excited due to the sliding on a periodic substrate and how the details of the resulting internal motion are non trivial. For instance, whether this could represent a mechanism for dissociation depends on the maximum excursion from the equilibrium distance. Moreover, the very nature of resonances makes the temporal behaviour very much dependent on the initial values of the interatomic spacing, which is in turn related to vibrational energy and temperature.

We have seen that two plateaus might be present in the velocity-force characteristic of the dimer, as in Fig. 3.25(a). What is their physical meaning? Indeed, if we decrease the force adiabatically (in small steps) from a high value to zero, we find hysteretic behaviour,

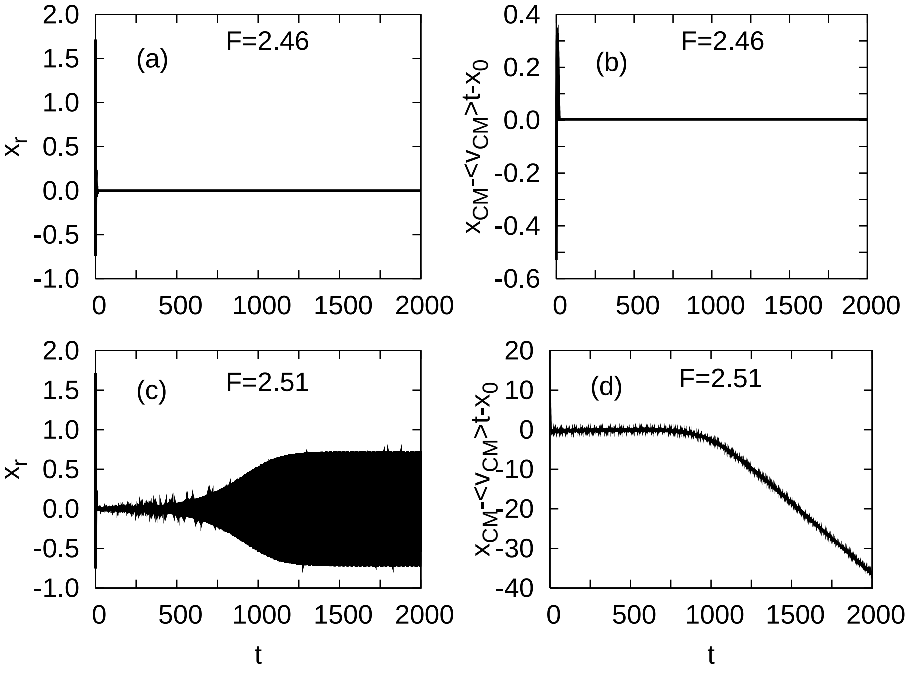

Figure 3.27: Internal and CM motion of the dimer for $l = a$ with initial condition $x_2 - x_1 = 1.27a$, for different values of the external driving F. x_r is shown in (a) and (c), while the deviation of $x_{CM} - x_0$ from $\langle v_{CM} \rangle t$ is plotted in (b) and (d) (x_0 is the initial position of the CM). The parameters used are the same as in Fig. 3.24. The saturation of the increase of x_r in (c) is due to the fact that v_{CM} is not really constant, but it decreases during the motion, as it can be seen in (d).

as it can be seen in Fig. 3.28: when F is decreased, a first hysteresis occurs in proximity of $\langle v_{CM} \rangle = \omega_0$, giving a critical value $F_{c4}^{dim} < F_{c3}^{dim}$, where the velocity-force characteristic has a discontinuous derivative, while a second hysteresis is found when F is decreased further from F_{c1}^{dim} and another critical value $F_{c2}^{dim} < F_{c1}^{dim}$, where $\langle v_{CM} \rangle = 0$, is obtained. However, these two hysteresis have a different origin. The latter (decreasing the force from F_{c1}^{dim}) is similar to that encountered for the monomer (see Fig. 2.8 of Chap. 2) and is related to the *static bistability* between the locked and the running state. On the other hand, the hysteresis from F_{c3}^{dim} to F_{c4}^{dim} is associated to a *dynamic bistability* between two running states. In fact, the theoretical curve plotted in Fig. 3.28 using Eq. (3.37) shows that there are two possible values of the velocity for a given force in the region of the plateau. In particular, it gives a negative slope of the mobility, i. e. $d\langle v_{CM} \rangle / dF < 0$, which signals an instability of the system. This is the reason why the dimer avoids this unphysical region and at a given force F_{c3}^{dim} has a discontinuous jump in the drift velocity. It can be shown that this bistable behaviour of the dimer critically depends on U_0, K and η. Specifically, for fixed K and η, it is observed when U_0 exceeds a certain critical value (or equivalently when η is lower than a critical value for fixed U_0 and K) [65]. Notice that the theoretical curve in Fig. 3.28 remarkably resembles the van der Waals curve for

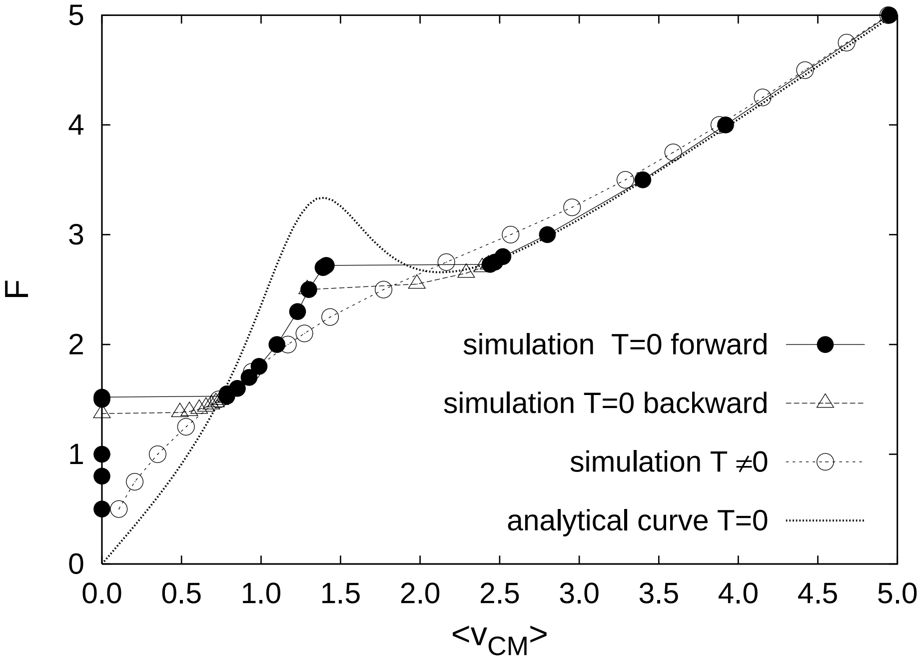

Figure 3.28: Velocity-force characteristic for the dimer with $l = \tau_g a$ at $T = 0$ in the forward (closed circles) and in the backward direction (open triangles), and at $T \neq 0$ in the forward direction (open circles). The parameters used are the same as in Fig. 3.24. The dotted line without points is the theoretical curve obtained from Eq. (3.37) adding the linear term $\eta\langle v_{CM}\rangle$. Note the two hysteresis at $T = 0$ and the absence of hysteresis at $T \neq 0$. The curve at $T \neq 0$ starts from $\langle v_{CM}\rangle = 0$ and smoothly crosses the regions of bistability. The theoretical curve is a two-valued function of $\langle v_{CM}\rangle$ in the region of dynamic bistability, while the interval where $dF/d\langle v_{CM}\rangle < 0$ signals a region of instability. The values of the critical forces at $T = 0$ are $F_{c1}^{dim} = 1.52$, $F_{c2}^{dim} = 1.37$, $F_{c3}^{dim} = 2.72$ and $F_{c4}^{dim} = 2.5$.

the gas-liquid phase transition in the Clapeyron plane (pressure-volume). We can think that in our system the role of the pressure is played by the applied force and the volume corresponds to the drift velocity. In this sense, Eq. (3.37) could be regarded as an equation of state of the system, analogously to van der Waals empirical equation relating pressure and volume. Both equations are however only approximate descriptions of the real system and cannot predict what happens in the transition region, where a coexistence of two different states is found. Pursuing this analogy more deeply, the “effective temperature” in our case is given by $1/U_0$ (at fixed η and K). Above a certain critical temperature the system displays no bistability.

The effects that we have shown at $T = 0$ are partially smeared out by thermal fluctuations. In Figs. 3.24(c)-(d) we see that the static friction force vanishes at finite T and that no plateaus in the velocity-force curve exist. The resonance peak at $\langle v_{CM}\rangle = \omega_0$ still survives, but is lower and somehow broader: temperature reduces the friction force and makes the slope of the velocity-force characteristic less steep. The mobility is sensitive to the value of l also at $T \neq 0$. The curves for different l still cross at $\langle v_{CM} \rangle = \omega_0$ and the crossover of the mobility can also be observed comparing the characteristics of the monomer and of the incommensurate dimer in Fig. 3.25(b). For $l = a$ a peak is found at small $\langle v_{CM} \rangle$ in Fig. 3.24(d): this is due to the fact that in the commensurate case, even though the static friction force found at $T = 0$ vanishes, a larger force is needed to reach the sliding state and this corresponds to the point of highest curvature in the velocity-force characteristic plotted in Fig. 3.24(c). To a certain extent this resembles the monomer case, where a very similar behaviour is found. Notice that no bistabilities and hysteresis are present at finite T, as it can be clearly seen from Figs. 3.24(c) and 3.25(b). This is even more evident in Fig. 3.28, where the characteristics of the incommensurate dimer at $T = 0$ and $T \neq 0$ are compared. The curve at $T \neq 0$ crosses the region of bistability in a smooth way, thus making clear how temperature can account for transitions between different dynamical states. A hysteretic behaviour in the low friction limit, at $T \neq 0$, has been reported for long periodic chains [66]. However, a preliminary investigation on the bistable behaviour of the dimer has shown that hysteresis can survive at very small T ($k_B T < U_0/20$) even for such a small cluster, as illustrated in Fig. 3.29 [65]. This opens the way for an understanding of the link between the dynamics of small systems of interacting particles and that of infinite linear chains.

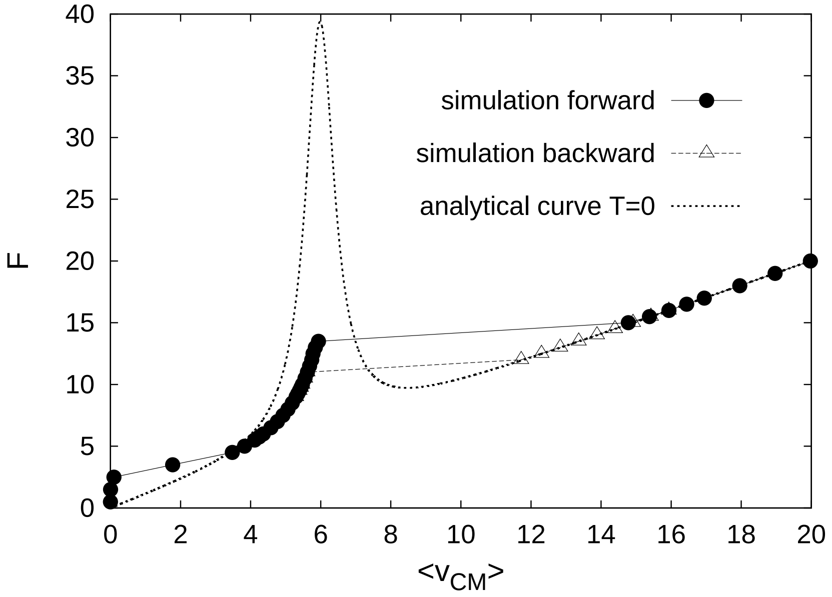

Figure 3.29: Velocity-force characteristic for the dimer at $T \neq 0$ in the forward (closed circles) and in the backward direction (open triangles), for $U_0 = 20$, $K = 18$, $\eta = 0.1$ and $l = a/2$. The dotted line without points is the theoretical curve obtained from Eq. (3.37) adding the linear term $\eta \langle v_{CM} \rangle$. Note that the hysteresis in the dynamical bistability region is present also in this case.

Appendix: Properties of chaotic systems

Chaotic dynamics appears generally in nonlinear dynamical systems, i. e. systems of first order differential equations. A dynamical system is said to be chaotic if it displays an exponentially sensitive dependence on initial conditions. For a nonlinear dynamical system chaos can occur if there are at least three variables. Therefore, for autonomous (time-independent) Hamiltonian systems, chaotic dynamics is possible with at least two degrees of freedom. The dynamics of a Hamiltonian system is governed by the set of first-order differential equations

$$\dot{\mathbf{x}} = \mathbf{F}(\mathbf{x}) \tag{3.40}$$

where $\mathbf{x}$ is a point of the phase space (e. g. positions and momenta). Whenever the Hamiltonian can be written as the sum of a kinetic energy part, depending only on the momenta, and a potential energy part, a necessary condition for the existence of chaotic dynamics is the non-separability of the potential energy function. On the other hand, systems described by time-dependent Hamiltonians may show chaos even in $1D$. Usually the phase space of a chaotic Hamiltonian system consists of regions of partial integrability, characterized by the existence of tori and dynamical stability, with interspersed regions of chaotic behaviour. By changing a parameter in the Hamiltonian, like some coefficient in the potential energy function or the total energy in the case of a conservative system, the degree of chaos or irregularity of a system can be varied. In this respect, a complete description of the motion is generally not needed, and one can look for a statistical approach: the evolution and relaxation towards equilibrium of certain average quantities can be studied, rather than the trajectory corresponding to a given set of initial conditions. Since chaos may already appear in Hamiltonian systems with only two degrees of freedom, statistical mechanics can be justified for small classical systems [67].

Let us consider some dynamical properties of chaotic Hamiltonian systems. The individual trajectories in phase space are given by the solution of Eq. (3.40), which can be written as

$$\mathbf{x} = \mathbf{\Phi}^t(\mathbf{x}_0), \tag{3.41}$$

where $\mathbf{\Phi}^t$ is the flow representing the evolution of the initial point $\mathbf{x}_0$ after a time t. In general it is a nonlinear function of initial conditions and time. The evolution of the phase-space volume is controlled by the Jacobian determinant which satisfies

$$|\det \partial_x \Phi^t| = \exp \int_0^t \nabla \cdot \mathbf{F} d\tau. \tag{3.42}$$

For Hamiltonian systems the phase-space volume is preserved and the divergence of the vector field vanishes: $\nabla \cdot \mathbf{F} = 0$. In this case the system is *conservative*. If $\nabla \cdot \mathbf{F} < 0$ in some region of the phase space the system is *dissipative*. A trajectory can be

(a) stationary if $\mathbf{\Phi}^t(\mathbf{x}) = \mathbf{x}$ for all t;
(b) periodic if $\mathbf{\Phi}^t(\mathbf{x}) = \mathbf{\Phi}^{t+T}(\mathbf{x})$ for a given minimum period T;
(c) aperiodic if $\mathbf{\Phi}^t(\mathbf{x}) = \mathbf{\Phi}^\tau(\mathbf{x})$ for all $t \neq \tau$.

Stationary points are usually equilibrium points of the potential energy function. Periodic trajectories can be stable or unstable, giving rise to quasiperiodic or chaotic behaviour, respectively, of nearby aperiodic orbits. The starting point for the investigation of the degree of irregularity of a complex dynamical system is therefore the analysis of the phase-space structure. This will give us a qualitative view of the main features of the system at a given value of the Hamiltonian parameters, i. e. it should reveal the presence of stability regions and chaos.

Chaotic motion can be characterized by a few quantities, which are often used as indicators of chaos:

1. *Poincaré section.* This is a mapping of the phase space obtained by means of keeping one of the dynamical variables fixed at a constant value. Evolving a properly chosen set of initial conditions, whenever the dynamical variable reaches this value for a trajectory, the other variables and the corresponding conjugate momenta are recorded, and this will be done for every trajectory of the initial ensemble. Periodic motions are seen as fixed points of the Poincaré map, quasiperiodic trajectories will give rise to regular islands and chaotic trajectories to randomly distributed points on the section.

2. *Lyapunov exponent.* Consider two nearby trajectories $\mathbf{x}$ and $\mathbf{x}' = \mathbf{x} + \delta\mathbf{x}$. For small $\delta\mathbf{x}$ the time evolution of the deviation $\delta\mathbf{x}$ will be given to linear order in $\delta\mathbf{x}$ by

   $$\delta\dot{\mathbf{x}} = \partial_{\mathbf{x}}\mathbf{F}(\mathbf{x})\delta\mathbf{x}, \tag{3.43}$$

   where $\partial_{\mathbf{x}}\mathbf{F}(\mathbf{x})$ denotes the Jacobian of the transformation. Since in MD simulations time is discretized in small steps δt, so that $t = n\delta t$ for $n = 0, 1, ...$, we can consider the discrete version of Eq. (3.43), obtained by replacing $\mathbf{x}(t)$ by $\mathbf{x}_n$ and $\delta\dot{\mathbf{x}}$ by $(\delta\mathbf{x}_{n+1} - \delta\mathbf{x}_n)/\delta t$:

   $$\delta\mathbf{x}_{n+1} = (\mathbf{I} + \delta t\ \partial_{\mathbf{x}}\mathbf{F}(\mathbf{x}_n))\delta\mathbf{x}_n \equiv \mathbf{J}(\mathbf{x}_n)\delta\mathbf{x}_n = \prod_{i=1}^{n}\mathbf{J}(\mathbf{x}_i)\delta\mathbf{x}_0, \tag{3.44}$$

   where $\mathbf{I}$ is the identity operator. In general, for a dynamical system with an $n-$dimensional phase space there will be n Lyapunov exponents, but the knowledge of the maximum Lyapunov exponent λ_{max} is sufficient to determine all the others [53]. λ_{max} is given by

   $$\lambda_{max} = \lim_{n\to\infty}\frac{1}{n}\ln\big|\prod_{i=0}^{n-1}\mathbf{J}(\mathbf{x}_i)\delta\mathbf{x}_0\big|. \tag{3.45}$$

   In practice, in computer simulations one calculates $\delta\mathbf{x}_n$ iteratively as $\delta\mathbf{x}_{n+1} = \mathbf{J}(\mathbf{x}_n)\delta\mathbf{x}_n$ and uses this result to calculate $\lambda^{(n)}_{max}$ at time $t = n\delta t$:

   $$\lambda^{(n)}_{max} = \frac{1}{n}\ln\big|\prod_{i=0}^{n-1}\mathbf{J}(\mathbf{x}_i)\delta\mathbf{x}_0\big|. \tag{3.46}$$

   Thus, λ_{max} as a function of t is obtained and its asymptotic value yields the maximal Lyapunov exponent:

   $$\lambda_{max} = \lim_{n\to\infty}\lambda^{(n)}_{max} \tag{3.47}$$

In the case treated in Sec. 3.3, i. e. the Hamiltonian dynamics of a dimer moving in a sinusoidal potential, the equations of motion (3.9) (for $\eta = 0$, $F = 0$, $f_{CM} = 0$ and $f_r = 0$) can be written in the form of Eq. (3.40)

$$\left\{ \begin{array}{lcl} \dot{x}_{CM} & = & v_{CM} \\ \dot{v}_{CM} & = & -U_0 \cos((x_r + l)/2) \sin x_{CM} \\ \dot{x}_r & = & v_r \\ \dot{v}_r & = & -2Kx_r - 2U_0 \sin((x_r + l)/2) \cos x_{CM} \end{array} \right. \tag{3.48}$$

and $\mathbf{J}_n$, i. e. $\mathbf{J}$ calculated at time $t = n\delta t$, is a 4×4 matrix depending on x_{CM} and x_r:

$$\mathbf{J}_n = \begin{pmatrix} 1 & \delta t & 0 & 0 \\ -U_0 \cos x_{CM} \cos\left(\frac{x_r+l}{2}\right) \delta t & 1 & U_0 \sin x_{CM} \sin\left(\frac{x_r+l}{2}\right) \frac{\delta t}{2} & 0 \\ 0 & 0 & 1 & \delta t \\ 2U_0 \sin x_{CM} \sin\left(\frac{x_r+l}{2}\right) \delta t & 0 & -\left[2K + U_0 \cos x_{CM} \cos\left(\frac{x_r+l}{2}\right)\right] \delta t & 1 \end{pmatrix} \tag{3.49}$$

We choose the time step δt to be equal to the time step Δt used to integrate numerically Eq. (3.48).

The Lyapunov exponent measures the rate of divergence (or convergence) of two nearby trajectories. Depending on the sign of λ_{max} different types of orbits can be found. In conservative systems, for $\lambda_{max} < 0$ nearby orbits approach each other along *stable* directions, for $\lambda_{max} > 0$ they separate exponentially along *unstable* directions, while for $\lambda_{max} = 0$ they maintain their distance along marginal directions. In dissipative systems it is useful to introduce the concept of *attractor*, which describes the long-time dynamics of the system: it is the orbit to which all nearby orbits asymptotically approach. The sign of λ_{max} determines different kinds of attractors:

- $\lambda_{max} < 0$: the orbits tend to a stable *fixed point* (this is what happens in the damped harmonic oscillator for instance);
- $\lambda_{max} = 0$: the orbits tend to a closed curve in phase space, a *limit cycle* (as in the case of two identical simple harmonic oscillators with different amplitudes);
- $\lambda_{max} > 0$: the orbit is unstable and chaotic. Nearby points will diverge to arbitrary separation and all neighbourhoods in phase space will be eventually visited. The phase space would be a tangled sea of wavy lines, like a pot of spaghetti. This however does not preclude any organization, as a pattern may emerge. For these reasons, the attractor in this case is called *strange attractor* and has a complex structure with a fractal geometry.

3. *Power spectrum.* The power spectrum of a dynamical variable $X(t)$ is defined from its Fourier transform $X(\omega) = \int \exp(i\omega t) X(t) dt$ as

$$P(\omega) = |X(\omega)|^2. \tag{3.50}$$

For a multiple periodic motion one obtains a set of discrete lines, one line for each frequency, while a chaotic motion, which is completely aperiodic, has a broad continuous power spectrum. Thus, a pronounced irregularity in the power spectrum is an indication of chaotic behaviour in the system. We have used power spectra to characterize the chaotic dynamics of the dimer in Fig. 3.15.

Bibliography

[1] A. S. Kovalev and A. I. Landau, Low Temp. Phys. **28**, 423 (2002).

[2] O. M. Braun, R. Ferrando and G. E. Tommei, Phys. Rev. E **68**, 051101 (2003).

[3] A. H. Romero, A. M. Lacasta and J. M. Sancho, Phys. Rev. E **69**, 051105 (2004).

[4] S. Gonçalves, V. M. Kenkre and A. R. Bishop, Phys. Rev. B **70**, 195415 (2004).

[5] E. Ganz, S. K. Theiss, I. Hwang, J. Golovchenko, Phys. Rev. Lett. **68**, 1567 (1992).

[6] G. L. Kellogg, Phys. Rev. Lett. **67**, 216 (1991).

[7] B. S. Swartzentruber, Phys. Rev. Lett. **76**, 459 (1996).

[8] T. Mitsui, M. K. Rose, E. Fomin, D. F. Ogletree and M. Salmeron, Science **297**, 1850 (2002).

[9] K. Stolt, W. R. Graham and G. Ehrlich, J. Chem. Phys. **65**, 3206 (1976).

[10] L. Bardotti, P. Jensen, A. Hoareau, M. Treilleux, B. Cabaud, A. Perez and F. Cadete Santos Aires, Surf. Sci. **367**, 276 (1996).

[11] S. C. Wang, U. Kürpick and G. Ehrlich, Phys. Rev. Lett. **81**, 4923 (1998)

[12] T. R. Linderoth, S. Horch, L. Petersen, S. Helveg, E. Laegsgaard, I. Stensgaard and F. Besenbacher, Phys. Rev. Lett. **82**, 1494 (1999).

[13] M. Schunack, T. R. Linderoth, F. Rosei, E. Laegsgaard, I. Stensgaard and F. Besenbacher, Phys. Rev. Lett. **88**, 156102 (2002).

[14] F. Montalenti and R. Ferrando, Phys. Rev. Lett. **82**, 1498 (1999).

[15] F. Montalenti and R. Ferrando, Phys. Rev. B **60**, 11102 (1999).

[16] D. S. Sholl, K. A. Fichthorn, Phys. Rev. Lett. 79, 3569 (1997).

[17] J. C. Hamilton, Phys. Rev. Lett. 77, 885 (1996).

[18] J. S. Raut, K. A. Fichthorn, J. Chem. Phys. 108, 1626 (1998).

[19] H. J. W. Zandvliet, B. Poelsema and B. S. Swartzentruber, Phys. Today **54**, 41 (2001).

[20] G. L. Kellogg and A. F. Voter, Phys. Rev. Lett. **67**, 622 (1991).

[21] T. R. Linderoth, S. Horch, E. Laegsgaard, I. Stensgaard, F. Besenbacher, Surf. Sci. **402**, 308 (1998).

[22] F. Montalenti and R. Ferrando, Phys. Rev. E **61**, 3411 (2000).

[23] B. Borovsky, M. Krueger and E. Ganz, Phys. Rev. B **59**, 1598 (1999).

[24] G. Boisvert and L. J. Lewis, Phys. Rev. B **56**, 7643 (1997).

[25] G. Brocks and P. J. Kelly, Phys. Rev. Lett. **76**, 2362 (1996).

[26] P. J. Feibelman, Phys. Rev. Lett. **58**, 2766 (1987).

[27] S. Yu. Krylov, Phys. Rev. Lett. **83**, 4602 (1999).

[28] P. Deltour, J.-L. Barrat and P. Jensen, Phys. Rev. Lett. **78**, 4597 (1997).

[29] O. M. Braun, Surf. Sci. **230**, 262 (1990).

[30] R. Tsekov and E. Ruckenstein, Surf. Sci. **344**, 175 (1995).

[31] R. Tsekov and E. Ruckenstein, J. Chem. Phys. **100**, 3808 (1994).

[32] O. M. Braun, Phys. Rev. E **63**, 011102 (2001).

[33] R. Metzler and J. Klafter, Phys. Rep. **339**, 1 (2000).

[34] J. Kärger and D. M. Ruthven, *Diffusion in Zeolites* (Wiley, New York, 1992).

[35] P. Demontis, G. B. Suffritti and P. Mura, Chem. Phys. Lett. **191**, 553 (1992).

[36] D. I. Kopelevich and H.-C. Chang, Phys. Rev. Lett. **83**, 1590 (1999).

[37] See for example U. Kürpick, Phys. Rev. B **63**, 045409 (2001); P. J. Feibelman, Phys. Rev. B **61**, R2452 (2000); F. Montalenti and R. Ferrando. Surf. Sci. **432**, 27 (1999).

[38] See for example *Berkeley Physics Course - Vol. 1 (Mechanics)*, pag. 225-227 (Mcgraw-Hill Book Company, New York, 1962).

[39] R. Guantes, J. L. Vega and S. Miret-Artés, Phys. Rev. B **64**, 245415 (2001).

[40] J. K. Norsko, Rep. Prog. Phys. **53**, 1253 (1990).

[41] A. V. Walker and D. A. King, J. Chem. Phys. **112**, 4739 (2000).

[42] A. Venkatesan and M. Lakshmanan, Phys. Rev. E **56**, 6321 (1997).

[43] S.-Y. Kim and B. Hu, Phys. Rev. E **58**, 3028 (1998); S.-Y. Kim and B. Hu, Phys. Rev. E **58**, 7231 (1998); S.-Y. Kim and Y. Kim, Phys. Rev. E **61**, 6517 (2000) .

[44] Y. Kao and C. Wang, Phys. Rev. E **48**, 2514 (1993).

[45] U. Parlitz and W. Lauterborn, Phys. Rev. A **36**, 1428 (1987).

[46] K. Murali and M. Lakshmanan, Phys. Rev. E **48**, R1624 (1993).

[47] T. Strunz and F.-J. Elmer, Phys. Rev. E **58**, 1612 (1998).

[48] B.-Y. Ou, X.-G. Zhao and S.-G. Chen, Physica B **269**, 145 (1999).

[49] S. Kocić, Lj. Ristovski and N. Burić, Chaos, Solitons and Fractals **12**, 1839 (2001) .

[50] T. Shinbrot, C. Grebogi, J. Wisdom and J. A. Yorke, Am. J. Phys. **60**, 491 (1992).

[51] R. B. Levien and S.M. Tan, Am. J. Phys. **61**, 1038 (1993).

[52] D. J. Christini, J. J. Collins and P. S. Linsay, Phys. Rev. E **54**, 4824 (1996).

[53] J.-P. Eckmann and D. Ruelle, Rev. Mod. Phys. **57**, 617 (1985).

[54] J.-P. Eckmann , S. Oliffson Kamphorst, D. Ruelle and S. Ciliberto, Phys. Rev. A **34**, 4971 (1986).

[55] A. V. Walker and D. A. King, Phys. Rev. Lett. **82**, 5156 (1999).

[56] M. B. Lee, Q. Y. Yang and S. T. Ceyer, J. Chem. Phys. **87**, 2724 (1987).

[57] S. Paavilainen and J.A. Nieminen, Surf. Sci. Lett. **486**, L489 (2001).

[58] A. P. Graham, F. Hofmann, J. P. Toennies, L. Y. Chen and S. C. Ying, Phys. Rev. Lett. **78**, 3900 (1997).

[59] J. Ellis, A. P. Graham and J. P. Toennies, Phys. Rev. Lett. **82**, 5072 (1999).

[60] See for example L. Consoli, H. J. F. Knops and A. Fasolino, Phys. Rev. Lett. **85**, 302 (2000).

[61] M. P. Allen, D. J. Tildesley, *Computer Simulation of Liquids*, Clarendon Press, New York, pp. 185-187 (1988).

[62] O. M. Braun and R. Ferrando, Phys. Rev. E **65**, 061107 (2002).

[63] A. J. Lichtenberg and M. A. Lieberman, *Regular and Stochastic Motion*, Springer-Verlag, New York (1982).

[64] T. Strunz and F.-J. Elmer, Phys. Rev. E **58**, 1601 (1998).

[65] S. Gonçalves, C. Fusco, V. M. Kenkre and A. R. Bishop, *Bistability and hysteresis in the sliding friction of a dimer*, submitted.

[66] O. M. Braun, T. Dauxois, M. V. Paliy and M. Peyrard, Phys. Rev. E **55**, 3598 (1997).

[67] P. Gaspard, *Chaos, Scattering and Statistical Mechanics*, Cambridge University Press (1998).

Chapter 4

Velocity dependence of atomic-scale friction: a comparative study of the one- and two-dimensional Tomlinson model

This chapter is based on the following paper:

- C. Fusco and A. Fasolino, Phys. Rev. B **71**, 045413 (2005).

We present a comparative analysis of the velocity dependence of atomic-scale friction for the Tomlinson model, at zero and finite temperatures, in $1D$ and $2D$, and for different values of the damping. Combining analytical arguments with numerical simulations, we show that an appreciable velocity dependence of the kinetic friction force F_{fric}, for small scanning velocities v_s (from 1 nm/s to 2 μm/s), is inherent in the Tomlinson model. In the absence of thermal fluctuations in the stick-slip regime, it has the form of a power-law, $F_{fric} - F_0 \propto v_s^{\beta}$ with $\beta = 2/3$, irrespective of dimensionality and value of the damping. Since thermal fluctuations enhance the velocity dependence of friction, we provide guidelines to establish when thermal effects are important and to which extent the surface corrugation affects the velocity dependence.

4.1 Introduction

As we have underlined in Sec.1.1, the empirical laws of macroscopic friction cannot always be applied at the atomic level. One fundamental issue concerns the velocity dependence of friction. For macroscopic contacts the friction force is found to be independent of the sliding velocity, but no consensus has been reached on the velocity dependence at the nanometer scale. Since scanning velocities accessible by AFM are very small, typically from nm/s to few μm/s, it is relevant to study friction dynamics in this regime. The velocity dependence of friction is important both for applications and from a fundamental point of view, and has been discussed in several AFM [1, 2, 3, 4, 5, 6, 7, 8, 9] and Quartz Crystal Microbalance [10] experimental studies as well as theoretical works [7, 8, 9, 11, 12, 13, 14, 15, 16, 17]. Depending on the investigated systems and on the experimental conditions, different and somewhat contradictory results for the velocity dependence have been found. In the original experiments of Mate et al. [1] the authors state that the frictional forces of a tungsten tip on graphite show little dependence on velocity for scanning velocities up to 400 nm/s. A similar behaviour up to velocities of several μm/s has been reported also in the work of Zwörner et al. [8], where friction on different carbon structures has been studied. The authors of Ref. [8] claim that a $1D$ Tomlinson model at $T = 0$ can reproduce a velocity independent friction force for scanning velocities up to ~ 1 μm/s, while giving a linear increase of friction for higher velocities. At variance with the $1D$ case, in the $2D$ version of the Tomlinson model at $T = 0$, which has been recently analyzed by Prioli et al. [9], a smooth increase of friction for velocities lower than $\sim$ 300 nm/s has been found. In view of the results of Zwörner et al. for the $1D$ case, the authors argue that this effect should be peculiar of the $2D$ model, due to the non-linear coupling between the two degrees of freedom in the system. The role of damping has not been addressed in Refs. [8, 9]. In the underdamped regime, the velocity dependence can be quite complex, especially at intermediate-large velocities, where the system displays bifurcations, chaotic motion, resonances and hysteresis [12]. In the overdamped regime, Robbins and Müser [18] suggest velocity independent friction.

An increase of the friction force has been observed for small velocities also in Refs. [4, 5, 7] and it has been attributed to thermally activated processes [4, 5, 7, 17]. By means of a simple thermal activation probabilistic analysis in $1D$, Gnecco et al. [7] have obtained a logarithmic increase of friction with scanning velocity, which fits their experimental data quite well. A similar dependence had been obtained using a stress-modified thermally-activated Eyring model [4]. In a recent work, Sang et al. [17] have corrected this logarithmic relation at not too small velocities: they propose a $|\ln v_s|^{2/3}$ dependence of the friction force, where v_s is the scanning velocity. However, recent experiments showing an increase of friction with velocity [9] do not display the logarithmic behaviour related to thermal activation, but rather suggest an athermal power-law v_s^β behaviour, as found in related systems, such as charge density waves [19] and in boundary lubrication [20].

In view of the contradictory results presented above, here we reexamine this issue for Tomlinson-like models in $1D$ and $2D$, for different values of the damping, and both with and without thermal effects. In particular, we focus on the importance of the athermal contribution to the velocity dependence of friction, which is intrinsically present in the Tomlinson model. We show by means of a combined analytical and numerical analysis that the exponent β is independent of the spatial dimension and of the damping. Then we discuss the role of thermal fluctuations, establishing guiding rules to understand where thermal effects become dominant.

In Sec. 4.2 we illustrate the model studied and the numerical techniques. In Sec. 4.3 we discuss the results for the athermal velocity dependence of friction and in Sec. 4.4 we include thermal fluctuations. Finally, we present some concluding remarks in Sec. 4.5.

4.2 Model

In this chapter we will use the Tomlinson model, which we have described in Sec. 1.4.2. A cantilever tip of mass m interacts with the surface via a periodic potential V_{TS} and is attached by a spring of elastic constant K_x to a support moving at constant velocity v_s along the x direction (see the sketch in Fig. 4.1). Assuming that the elastic interaction between the tip and the support is

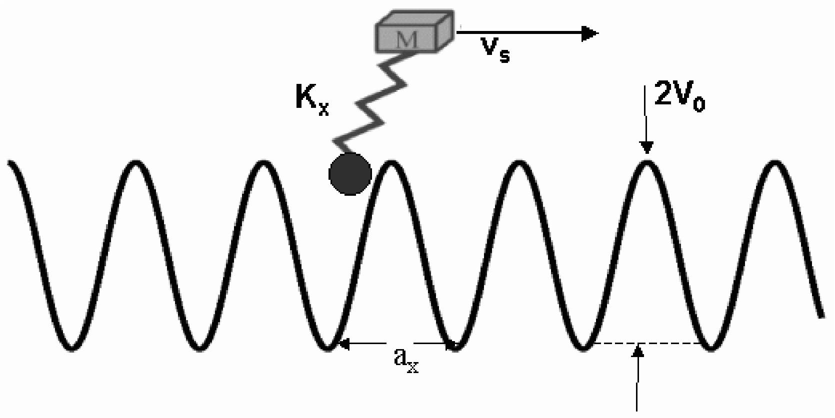

Figure 4.1: Sketch of the $1D$ Tomlinson model.

$$V_{el}(x) = \frac{1}{2}K_x(x - x_s)^2, \tag{4.1}$$

where x_s is the support position

$$x_s = v_s t, \tag{4.2}$$

and that the tip-substrate potential V_{TS} has the form

$$V_{TS}(x) = V_0[1 - \cos(2\pi x/a_x)], \tag{4.3}$$

the equation of motion in $1D$ becomes

$$\boxed{m\ddot{x} + m\eta\dot{x} + \frac{2\pi V_0}{a_x}\sin\left(\frac{2\pi x}{a_x}\right) + K_x(x - v_s t) = f(t)} \tag{4.4}$$

In Eq. (4.4) we have included thermal effects in the Langevin framework, with the random force $f(t)$ satisfying the conditions $< f(t) >= 0$ and $< f(t)f(0) >= 2m\eta k_B T\delta(t)$ (see Sec. 1.6). The static friction force in this model is simply given by the force needed to overcome the potential barrier:

$$F_{static} = \frac{2\pi V_0}{a_x}. \tag{4.5}$$

Stick-slip motion occurs when [21, 22]

$$K_x < -\left.\frac{\partial^2 V_{TS}}{\partial x^2}\right|_{x=x_{min}}, \quad \text{i.e.} \quad \tilde{V_0} \equiv \frac{4\pi^2 V_0}{K_x a_x^2} > 1, \tag{4.6}$$

where $x_{min} = na_x$ denotes the position of the minima of V_{TS}. In this case the kinetic friction force is finite in the limit $v_s \to 0$. Conversely, for $\tilde{V}_0 < 1$, uniform sliding occurs and energy dissipation comes only from the viscous term $m\eta v_s$, which vanishes for $v_s \to 0$. Notice that the kinetic friction force for $v_s \to 0$ is not equal to the static friction force F_{static}, since it results from dynamical effects and not by the interaction potential V_{TS}. The kinetic friction force F_{fric} is defined as [8, 12, 22]

$$F_{fric} =< F_x >\equiv \frac{v_s}{na_x} \int_0^{na_x/v_s} F_x dt, \tag{4.7}$$

where n is an integer number and $F_x = K_x(v_s t - x)$ is the lateral force. In the appendix of Chap. 1 we have shown that the definition Eq. (4.7) is equivalent to calculating the friction force from the energy dissipation ΔW in one period

$$\Delta W = m\eta \int_0^{na_x/v_s} \dot{x}^2 dt. \tag{4.8}$$

The friction force is then given by

$$F_{fric} = \frac{\Delta W}{na_x}. \tag{4.9}$$

Here we extend the model to deal with the motion at zero and finite temperature on a $2D$ lattice, as done in Refs. [9, 22] for $T = 0$. The tip-surface interaction is

$$V_{TS}(x, y) = V_0 \cos\left(\frac{2\pi x}{a_x}\right) \cos\left(\frac{2\pi y}{a_y}\right), \tag{4.10}$$

where a_x and a_y are the lattice parameters in the x and y directions respectively. When $a_y = \sqrt{3}a_x$, the substrate has the symmetry of a hexagonal closed-packed lattice. The elastic interaction is

$$V_{el}(x, y) = \frac{1}{2}K_x(x - v_s t)^2 + \frac{1}{2}K_y(y - y_s)^2, \tag{4.11}$$

where k_y denotes the spring constant in the y direction and y_s = constant represents the scanning line of the support. The equations of motion can be written in $2D$ as

$$\left\{ \begin{array}{rcl} m\ddot{x} + m\eta\dot{x} - (2\pi V_0/a_x)\sin(2\pi x/a_x)\cos(2\pi y/a_y) + K_x(x - v_s t) & = & f_x(t) \\ m\ddot{y} + m\eta\dot{y} - (2\pi V_0/a_y)\cos(2\pi x/a_x)\sin(2\pi y/a_y) + K_y(y - y_s) & = & f_y(t) \end{array} \right. \tag{4.12}$$

where f_x and f_y are independent stochastic forces satisfying the same properties as f in Eq. (4.4). In this case we also have a component of the lateral force along y, i. e. $F_y = k_y(y_s - y)$. The definition of the friction force in Eq. (4.7) can be generalized in $2D$ as

$$F_{fric} = \sqrt{< F_x >^2 + < F_y >^2} \tag{4.13}$$

We have solved the non-linear equations (4.4) and (4.12) using a Runge-Kutta 4 algorithm with initial conditions

$$x(0) = 0, \qquad \dot{x}(0) = 0, \qquad y(0) = 0, \qquad \dot{y}(0) = 0. \tag{4.14}$$

and for different values of the scanning velocity v_s and of the scanning line y_s.

4.3 Athermal velocity dependence of friction

At $T = 0$ the dynamics can be described by the equations of motion (4.4) and (4.12) without the stochastic forces. We choose values of the parameters which are typical of AFM experiments: $m = 10^{-10}$ kg, $K_x = 10$ N/m [5, 22, 23], $a_x = 0.316$ nm (in $2D$ we set $a_y = 0.548$ nm, corresponding to the hexagonal-packed structure of MoS$_2$(001) [22], and $K_x = K_y$), giving a resonance frequency $\sqrt{K_x/m}$ of the order of 10^5 Hz, which is characteristic of AFM experiments. In principle, the corrugation V_0 of the tip-surface potential depends on the loading force, which is not considered in $1D$ and $2D$ models: typically V_0 ranges from 0.2 eV to 2 eV, as found in different studies [24, 25]. Thus we take $V_0 = 1$ eV. These values of the parameters give $\tilde{V}_0 = 7$, yielding stick-slip motion ($\tilde{V}_0 > 1$) and allowing us to compare directly our results with those of Zwörner et al. in $1D$ [8]. The time step used in the calculations is ~ 0.1 ns, a value which is needed to account for the fast oscillations in the underdamped regime. The choice of η is quite delicate and it may affect the dynamical behaviour of the system. Usually a critical damping, $\eta = 2\sqrt{K_x/m}$ [22], is assumed. Here we study the problem for different values of η, in the underdamped, overdamped and critically damped regime. For each fixed scanning velocity v_s, we compute the friction force F_{fric}, averaging over many stick-slip periods (usually 10 at $T = 0$ and 100 at $T \neq 0$), according to Eqs. (4.7) and (4.13). The behaviour of F_{fric} as a function of v_s in $1D$ is shown for critical damping in Fig. 4.2(a) on a linear scale and in Fig. 4.2(b) on the most commonly used log-log scale [8]. Notice

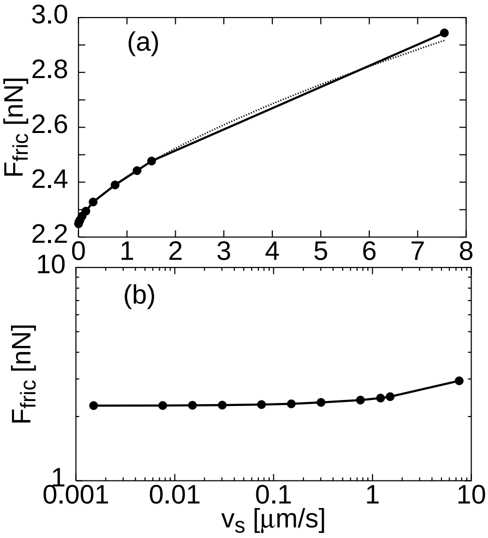

Figure 4.2: Frictional force F_{fric} as a function of sliding velocity v_s in the $1D$ Tomlinson model, plotted on a linear (a) and on a log-log scale (b) for $V_0 = 1$ eV, $m = 10^{-10}$ kg, $K_x = 10$ N/m, $a_x = 0.316$ nm ($\tilde{V}_0 = 7$) and $\eta = 2\sqrt{K_x/m} \simeq 6.3 \cdot 10^5$ s^{-1}. The increase of F_{fric} for small velocities is hidden using a log-log scale. The points connected by the solid lines are obtained from the simulations, while the dotted line in (a) is a power-law fit to the data of the form $F_{fric} - F_0 \propto v_s^{2/3}$ for $v_s < 2$ μm/s.

that the log-log scale hides the velocity dependence for small velocities ($v_s < 1.5\ \mu$m/s), where the friction force varies by more than 10%. The data in Fig. 4.2(a) can be fitted quite accurately by a power law of the form

$$\boxed{F_{fric} = F_0 + c v_s^{\beta}} \tag{4.15}$$

with $\beta \simeq 2/3$ and c a constant depending on the parameters of the model and on the space dimension.

To our knowledge the athermal velocity dependence of atomistic dry friction has been scarcely investigated from a theoretical point of view up to now: it has been studied in the limit of large velocities [12] and in the context of boundary lubrication [20]. Here we discuss the velocity dependence of dry friction for small scanning velocities, in the stick-slip regime, which is described by Eq. (4.15). In this case, the value of the exponent β can be calculated analytically for the Tomlinson model, yielding $\beta = 2/3$, as we will show below. The same kind of behaviour has been found in the field of elastic manifolds, for the dynamics of charge density waves driven by an electric field [19] and for the motion of a contact line on a heterogeneous surface [26, 27]. This law characterizes the athermal motion of strongly pinned systems ($\tilde{V}_0 > 1$ in our terminology), moving at constant velocity.

In order to get a flavour of the effect of scanning velocity on the dynamics of the tip, we plot the tip position as a function of the support position in Fig. 4.3 for different scanning velocities v_s. The important feature is that the slip events are not instantaneous for not

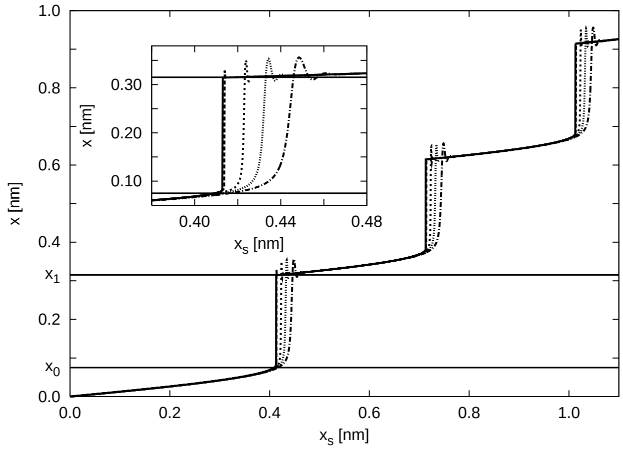

Figure 4.3: Tip position as a function of support position in the $1D$ Tomlinson model for different values of the scanning velocity (from left to right $v_s = 1.5$ nm/s, 15 nm/s, 300 nm/s, 750 nm/s, 1.5 μm/s), $\eta = 2\sqrt{K_x/m}$ and $\tilde{V}_0 = 7$. The lower horizontal line corresponds to the position x_0 of the tip before the first slip, calculated according to Eq. (4.28), while the upper one is the position of the tip x_1 after the first slip, calculated numerically from Eq. (4.26). The inset is a blow up of the region around the first slip event.

too small values of v_s, as highlighted in the inset of Fig. 4.3, showing a finite slip time depending on v_s. Furthermore the slip position tends to move rightwards for increasing v_s. This means that the integral of $F_x = K_x(x_s - x)$ over one period

$$F_{fric} = \frac{1}{na_x}\int_0^{na_x} F_x dx_s = \frac{K_x}{na_x}\frac{(na_x)^2}{2} - \frac{K_x}{na_x}\int_0^{na_x} x dx_s \tag{4.16}$$

increases with increasing v_s, since the second term on the right side of Eq. (4.16) decreases. We also notice that the effect of v_s on the tip coordinate is pronounced only in the proximity of the slip point, while in the sticking parts the different curves practically overlap. Thus, we might argue that the major contribution to the velocity dependence of friction comes from the regions close to the slip events. In the following we will make this heuristic considerations more quantitative.

Considering for simplicity the $1D$ case and following Ref. [19], we look for a solution $x(t)$ of Eq. (4.4) in the athermal case ($f(t) = 0$) of the form

$$x(t) = x_A(t) + \theta(t), \tag{4.17}$$

where θ is a perturbation to the adiabatic solution x_A of Eq. (4.4) for $v_s \to 0$. The limit $v_s \to 0$ means that x_A satisfies Eq. (4.4) neglecting the first (inertial) and second (damping) term, namely

$$K_x(x_A - v_s t) = -\frac{2\pi V_0}{a_x}\sin\left(\frac{2\pi x_A}{a_x}\right) \tag{4.18}$$

The average of the left hand side of Eq. (4.18) represents the friction force F_0 in the adiabatic limit. The kinetic friction force F_{fric} at finite v_s is given by

$$F_{fric} =< K_x(v_s t - x_A - \theta) >= K_x < (v_s t - x_A) > -K_x < \theta >= F_0 - K_x < \theta >, \tag{4.19}$$

having defined $F_0 \equiv F_{fric}(v_s \to 0)$. Thus, the final goal is to work out the dependence on v_s of

$$< \theta >\equiv \frac{v_s}{na_x}\int_0^{na_x/v_s} \theta(t)dt. \tag{4.20}$$

To evaluate Eq. (4.20) is not a simple task and requires some approximations. We will proceed as follows:
(a) we show that for $\tilde{V_0} \gg 1$, namely for a soft spring or a large corrugation of the substrate, the inertial term $m\ddot{x}$ can be neglected with respect to the damping term $m\eta\dot{x}$ near a slip event, leading to the condition (4.33);
(b) the previous step allows us to rewrite the problem as a Riccati equation (Eq. (4.39)) and use known results [19], in particular the fact that the solution of the Riccati equation has a divergence around a time corresponding to the slip;
(c) the dependence on velocity is mostly determined by the behaviour around the slip, leading to the final result Eq. (4.42).

(a) For $\tilde{V_0} \gg 1$ the inertial term $m\ddot{x}$ can be neglected with respect to the damping term

$m\eta\dot{x}$ near a slip event. This can be straightforwardly seen in the adiabatic limit. In fact, differentiating Eq. (4.18) with respect to time we obtain

$$K_x\dot{x}_A - K_x v_s = -\left(\frac{2\pi}{a_x}\right)^2 V_0 \cos\left(\frac{2\pi x_A}{a_x}\right)\dot{x}_A, \tag{4.21}$$

giving for $\dot{x}_A$ and $\ddot{x}_A$

$$z_A \equiv \dot{x}_A = \frac{K_x v_s}{K_x + \left(\frac{2\pi}{a_x}\right)^2 V_0 \cos\left(\frac{2\pi x_A}{a_x}\right)} \tag{4.22}$$

and

$$\ddot{x}_A = \dot{z}_A = \frac{dz_A}{dx_A} z_A = \frac{(K_x v_s)^2 \left(\frac{2\pi}{a_x}\right)^3 V_0 \sin\left(\frac{2\pi x_A}{a_x}\right)}{\left[K_x + \left(\frac{2\pi}{a_x}\right)^2 V_0 \cos\left(\frac{2\pi x_A}{a_x}\right)\right]^3} \tag{4.23}$$

respectively. Then the condition

$$|\ddot{x}_A| \ll \eta |\dot{x}_A| \tag{4.24}$$

becomes

$$\frac{K_x v_s V_0 \left(\frac{2\pi}{a_x}\right)^3 \left|\sin\left(\frac{2\pi x_A}{a_x}\right)\right|}{\left[K_x + \left(\frac{2\pi}{a_x}\right)^2 V_0 \cos\left(\frac{2\pi x_A}{a_x}\right)\right]^2} \ll \eta. \tag{4.25}$$

Since energy dissipation takes place mostly near the fast slip events, we focus on the behaviour of Eq. (4.25) near the slip point x_0, determined by

$$\frac{dV_{tot}}{dx} = K_x(x - x_s) + \frac{2\pi}{a_x} V_0 \sin\left(\frac{2\pi x}{a_x}\right) = 0 \tag{4.26}$$

$$\frac{d^2 V_{tot}}{dx^2} = K_x + \left(\frac{2\pi}{a_x}\right)^2 V_0 \cos\left(\frac{2\pi x}{a_x}\right) = 0. \tag{4.27}$$

where $V_{tot} = V_{TS} + V_{el}$ is the total potential energy. Eq. (4.27) can be used to calculate the position x_0 of the tip right before the slip:

$$\boxed{x_0 = \frac{a_x}{2\pi} \arccos(-1/\tilde{V}_0).} \tag{4.28}$$

Inserting this value in Eq. (4.26) we obtain the position $x_s^{(0)}$ of the support during the jump, which is supposed to be fixed in the quasi-static approximation:

$$x_s^{(0)} = \frac{a_x}{2\pi}\left[\sqrt{\tilde{V}_0^2 - 1} + \arccos\left(-\frac{1}{\tilde{V}_0}\right)\right]. \tag{4.29}$$

The position x_1 of the tip immediately after the jump is found by numerically solving Eq. (4.26) using $x_s^{(0)}$ from Eq. (4.29). It is clear from Fig. 4.3 that x_0 and x_1 are a good estimate of the points right before and after the slip respectively.

Near the slip point x_0 we can set

$$x_A(t) = x_0 + \xi_A(t) \tag{4.30}$$

with

$$|\xi_A| \ll \frac{a_x}{2\pi}. \tag{4.31}$$

Using Eqs. (4.6) and (4.27) and the relations

$$\sin\left(\frac{2\pi x_A}{a_x}\right) \simeq \sin\left(\frac{2\pi x_0}{a_x}\right) + \left(\frac{2\pi}{a_x}\right)\cos\left(\frac{2\pi x_0}{a_x}\right)\xi_A$$

$$\cos\left(\frac{2\pi x_A}{a_x}\right) \simeq \cos\left(\frac{2\pi x_0}{a_x}\right) - \left(\frac{2\pi}{a_x}\right)\sin\left(\frac{2\pi x_0}{a_x}\right)\xi_A$$

Eq. (4.25) becomes

$$\left|\frac{v_s}{\frac{2\pi}{a_x}\sqrt{\tilde{V}_0^2 - 1}\;\xi_A^2} - \frac{v_s}{(\tilde{V}_0^2 - 1)\xi_A}\right| \ll \eta. \tag{4.32}$$

Since Eq. (4.31) holds, we can neglect the second term with respect to the first, obtaining

$$|\xi_A| \gg \left(\frac{v_s a_x}{2\pi\eta\sqrt{\tilde{V}_0^2 - 1}}\right)^{1/2}. \tag{4.33}$$

Eq. (4.33) is easily fulfilled for large $\tilde{V}_0$ (or large η) and/or small v_s. For example, with our choice of parameters, yielding $\tilde{V}_0 \simeq 7$, and $\eta \simeq 6 \cdot 10^5$ s^{-1}, condition (4.33) is valid for velocities up to $v_s \sim 1$ μm/s. Notice that Eqs. (4.31) and (4.33) have to hold simultaneously.

(b) Having now demonstrated that we can neglect the inertial term, we can expand the equation of motion (4.4) (without the term $m\ddot{x}$) near x_0:

$$m\eta\dot{\xi} = K_x v_s \delta t + \frac{1}{2}\left(\frac{2\pi}{a_x}\right)^3 V_0 \sin\left(\frac{2\pi x_0}{a_x}\right)\xi^2, \tag{4.34}$$

where

$$\xi = x - x_0 \tag{4.35}$$

and

$$\delta t = t - t_0, \tag{4.36}$$

t_0 being the time at which the slip takes place. Following Ref. [19], with the change of variables

$$\xi = C^2 v_s^{1/3}\chi \tag{4.37}$$

$$\delta t = C v_s^{-1/3}\tau \tag{4.38}$$

where $C \equiv \frac{a_x}{2\pi}\left[\frac{V_0}{2m\eta}\sin\left(\frac{2\pi x_0}{a_x}\right)\right]^{-1/3}$, Eq. (4.34) takes the form of a Riccati equation:

$$\frac{d\chi}{d\tau} = \chi^2 + \frac{K_x}{m\eta}\tau. \tag{4.39}$$

From its definition Eq. (4.17), θ is linked to χ by the relation

$$\theta = x - x_A = \xi - \xi_A = C^2 v_s^{1/3}(\chi - \chi_A), \tag{4.40}$$

where the subscript A refers to the adiabatic solution. It can be shown [19] that the major contribution to the integral (4.20) comes from a time $\delta t = \delta t_s \equiv t_1 - t_0$ such that $\delta t_s \propto v_s^{-1/3}$. When $t \sim t_1$, the solution $\chi(\tau)$ of the Riccati equation has a divergence of the form $\chi(\tau) \sim \frac{1}{\tau_1 - \tau}$. Note that δt_s is the slip time, i. e. the time it takes for the tip to go from the metastable position $x = x_0$ to the next metastable position $x = x_1$. For the adiabatic solution the slip occurs instantaneously, while δt_s is finite for finite v_s and this is responsible for the velocity dependent correction of the friction force.
(c) In fact, when $t \sim t_1$

$$\xi \sim x_1 - x_0 \propto v_s^{1/3}\chi(\tau \sim \tau_1) \propto v_s^{1/3}\frac{1}{\tau_1 - \tau} \propto v_s^{1/3}v_s^{-1/3} = O(1) \tag{4.41}$$

is independent of v_s, and therefore, by virtue of Eq. (4.40), $\theta = O(1)$ as well. The independence of the amplitude of the slip $x_1 - x_0$ from the scanning velocity v_s is also evident from Fig. 4.3. Thus

$$\boxed{< \theta > \simeq \frac{v_s}{n a_x}\int_{t_0}^{t_1}\theta(t)dt \propto v_s \delta t_s O(1) \propto v_s v_s^{-1/3} \propto v_s^{2/3},} \tag{4.42}$$

which proves that the exponent β appearing in Eq. (4.15) is $\beta = 2/3$. This shows that the dependence of friction on velocity is a dynamical effect which is due to the finite (although small) scanning velocity, as it can be seen in Fig. 4.3. Only if the slip events were really instantaneous a velocity independent friction force would naturally follow from the definition Eq. (4.7), giving $F_{fric} = F_0$. Therefore, the source of athermal velocity dependence of friction is the non adiabaticity of the motion of the tip for finite v_s.

Fig. 4.4 shows the slip time δt_s as a function of v_s, as measured from the numerical solution of the equation of motion. The behaviour of δt_s is in very good agreement with the scaling relation

$$\boxed{\delta t_s \propto v_s^{-1/3},} \tag{4.43}$$

which is the law expected from the discussion following Eq. (4.39).

4.3.1 Effect of damping

The effect of the damping on the velocity dependence of friction has not been investigated so far in the literature, because the typical choice is to assume critical damping in order to damp out the fast oscillations of the tip after the slip events and to avoid jumps of the

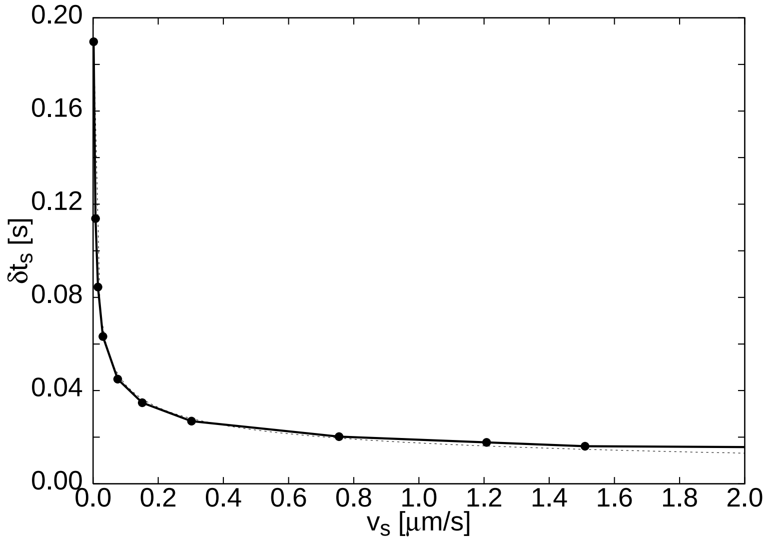

Figure 4.4: Slip time as a function of scanning velocity in the $1D$ Tomlinson model for critical damping and $\tilde{V}_0 = 7$. The points connected by the solid line are obtained by numerical simulations, while the dotted line is a power-law fit to the data of the form $\delta t_s \propto v_s^{-1/3}$.

tip of more than one lattice parameter. Nevertheless, it would be desirable to know the dynamical behaviour of the tip for a range of values of η, since experimental situations do not always meet the condition of critical damping and moreover the value of the damping is often not known. The behaviour of F_{fric} vs. v_s, for values of η ranging from strongly underdamped to strongly overdamped, is reported in Fig. 4.5. All curves start from the same value F_0, except for very low η (see discussion below), and can be fitted by Eq. (4.15) with the same value of $\beta = 2/3$, suggesting that the functional form of the velocity dependence of friction is robust with respect to the strength of the damping. The velocity range of validity of Eq. (4.15) decreases for large η, because the viscous regime ($F_{fric} \sim m\eta v_s$) sets in for smaller values of v_s (for example the data in Fig. 4.5 are fitted up to $v_s = 1.2$ μm/s for $\eta = 2\sqrt{K_x/m}$ and up to $v_s = 0.3$ μm/s for $\eta = 100\sqrt{K_x/m}$). As expected, at a fixed value of $v_s > 0$, F_{fric} increases with η, since energy dissipation increases by increasing the damping (see also Eq. (4.8)). Moreover the value of c in Eq. (4.15) is larger for larger η, reflecting the fact that the variation of F_{fric} is more pronounced for the highest values of η.

Note that for high damping we find a velocity dependent friction contrary to the qualitative expectation of Ref. [18]. The authors of Ref. [18] argue that in the overdamped regime the peak velocity of the tip, corresponding to a slip event, is a constant equal to $2\pi V_0/(m\eta a_x)$. This would imply that the amount of energy dissipated, which is proportional to the tip velocity according to Eq. (4.8), should not depend on v_s. On the contrary, we find appreciable dependence also in this case. As it can be seen from Fig. 4.6, the peak velocity of the tip is not a constant, but increases appreciably by increasing v_s. Actually,

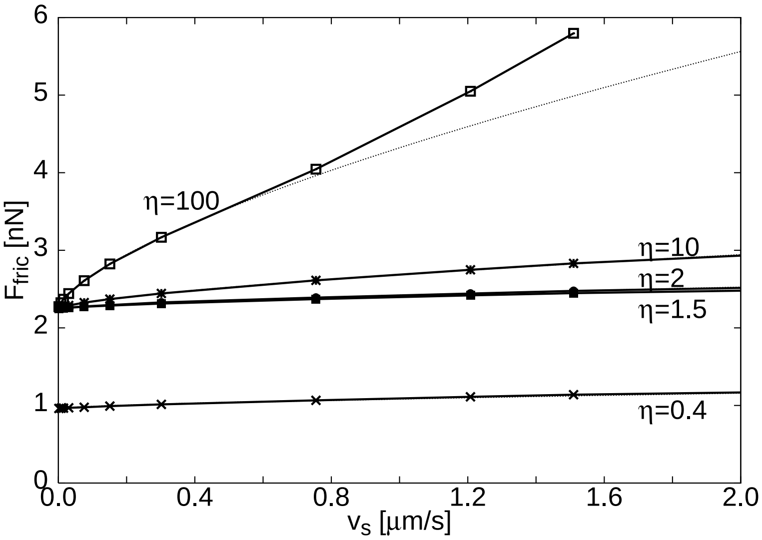

Figure 4.5: Frictional force F_{fric} as a function of sliding velocity v_s in the $1D$ Tomlinson model for $\tilde{V}_0 = 7$ and different values of the damping: from bottom to top $\eta/(\sqrt{K_x/m}) =$ 0.4, 1.5, 2, 10, 100. The dotted lines are fit to the numerical data of the form $F_{fric} - F_0 \propto v_s^{\beta}$, with $\beta = 2/3$. In the most underdamped case (lower line) the friction force is lower because the tip performs jumps of two lattice parameters.

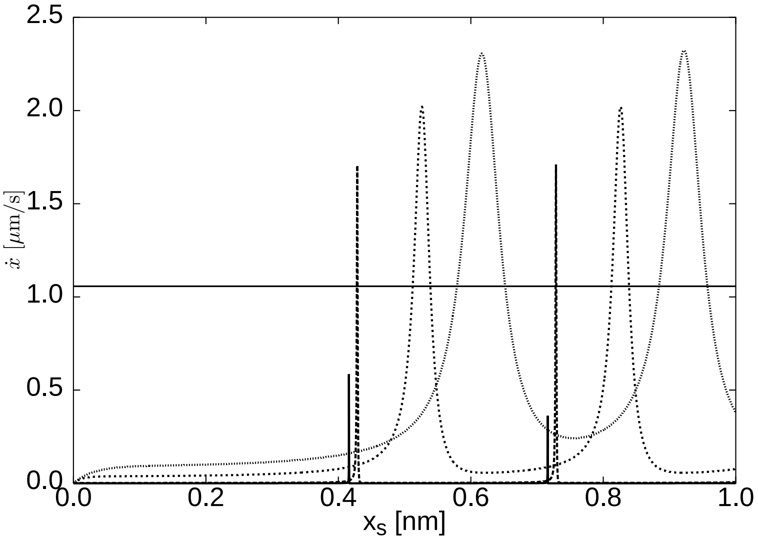

Figure 4.6: Tip velocity as a function of support position in the $1D$ Tomlinson model for different scanning velocities (from left to right v_s = 1.5 nm/s, 15 nm/s, 300 nm/s, 750 nm/s) in the overdamped case ($\eta = 100\sqrt{K_x/m}$) and for $\tilde{V}_0 = 7$. The horizontal line is the value $2\pi V_0/(m\eta a_x)$.

as we have shown by the analytical arguments leading to Eq. (4.33), the $v_s^{2/3}$ dependence of the friction force should be even more justified for the overdamped case.

The lower curve in Fig. 4.5, corresponding to the highly underdamped value $\eta = 0.4$, is characterized by a much lower friction force, because the tip in this case can perform jumps with periodicity of two lattice parameters. Notice that long jumps are characteristic of the underdamped dynamics, as we have also seen for surface diffusion in Sec. 2.4.2. This makes the lateral force drop to lower values after a slip event with respect to the critically damped situation, as shown in Fig. 4.7, resulting in a smaller F_0. In Fig. 4.7 we also plot the so-called "mechanistic Tomlinson loop", i. e. $F_x = \frac{2\pi V_0}{a_x} \sin\left(\frac{2\pi x}{a_x}\right)$ as a function of x, as obtained from Eq. (4.26). The slip events correspond to transitions between stable branches of this loop.

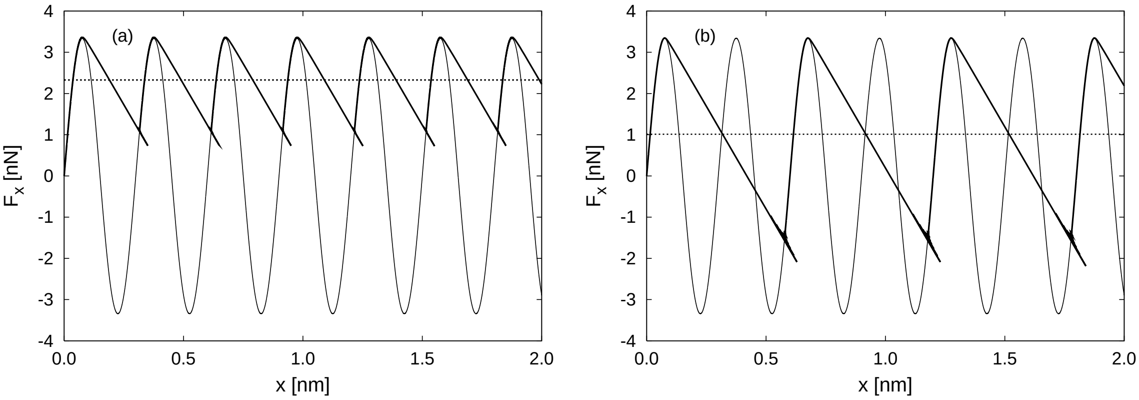

Figure 4.7: Lateral force as a function of tip position for two values of the damping: critically damped, $\eta = 2\sqrt{K_x/m}$ (a) and underdamped, $\eta = 0.4\sqrt{K_x/m}$ (b). The thick solid lines are obtained by the simulations for $\tilde{V}_0 = 7$ and $v_s = 300$ nm/s. Notice the presence of jumps with periodicity $2a_x$ in the underdamped case. The horizontal lines indicate the friction force for $\eta = 2\sqrt{K_x/m}$ ($F_{fric} = 2.33$ nN) and $\eta = 0.4\sqrt{K_x/m}$ ($F_{fric} = 1.01$ nN) respectively. The thin solid lines represent $F_x = \frac{2\pi V_0}{a_x} \sin\left(\frac{2\pi x}{a_x}\right)$, as obtained from Eq. (4.26).

In the underdamped regime, the velocity dependence of friction was also investigated in Ref. [12]: the results are reported in Fig. 4.8 and show a very complex nonlinear behaviour. The authors of Ref. [12] claim that a rough average of the friction force is velocity independent above the dashed line.

4.3.2 Role of dimensionality

As already mentioned in the introduction, this problem was recently studied in Ref. [9] using a $2D$ Tomlinson model, where a velocity dependent friction force was observed even for scanning velocities less than 300 nm/s. Since for $1D$ motion no velocity dependence had been previously found in Ref. [8], the authors attributed this dependence to the coupling

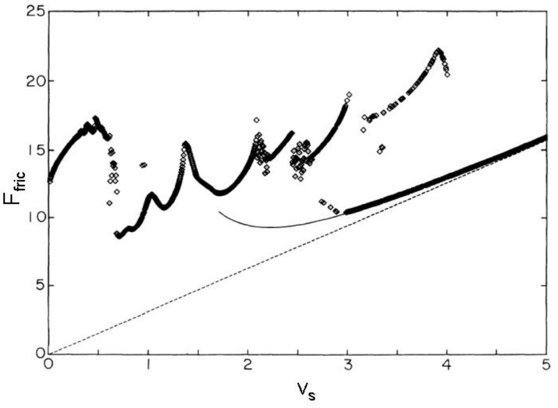

Figure 4.8: Friction force as a function of sliding velocity in the underdamped case: $\eta = 0.5\sqrt{K_x m}$ and $\tilde{V}_0 = 4$. The points are the result of the simulations, the dashed line is the viscous friction ($F_{fric} = m\eta v_s$) and the solid line is an analytic result for high velocities yielding $F_{fric} \propto v_s^{-3}$. All quantities are in dimensionless units (see the appendix of Chap. 1). [From Ref. [12]].

between the two degrees of freedom of the system. Our results for the $1D$ Tomlinson model already give a dependence on velocity, and it is interesting to look at the effect of an extra dimension on this dependence. Indeed, as it can be seen in Fig. 4.9, the behaviour of F_{fric} vs. v_s in $2D$ for different values of the scanning direction y_s is very similar to that in $1D$. Thus, in spite of the $2D$ character of the tip motion, clearly visible in Fig. 4.10, no dramatic effect of the dimensionality on the velocity dependence of friction can be noticed. This result is actually not surprising, because the Tomlinson model is a mean-field model and the functional form of constituent relations, such as $F_{fric}(v_s)$ should not change with dimensionality. Thus, Eq. (4.15) is expected to hold also in $2D$, with the same exponent $\beta = 2/3$. The values of the parameters F_0 and c can be different in $1D$ and $2D$. Specifically F_0 is always lower in $2D$. In fact, in $1D$ the tip is necessarily moved along an atom row, while in $2D$, depending on the scanning line y_s, the motion of the tip can occur also between atom rows. For the hexagonal lattice we have chosen, the interaction between the tip and the surface is the weakest when $y_s = a_y/4$ (bottom curve of Fig. 4.9), while it reaches its maximum value for $y_s = 0$, which coincides with the $1D$ case (upper curve of Fig. 4.9). Since the corrugation of the tip-surface interaction is directly related to the friction force [25], different scanning lines result in different values of friction. This feature allows for example to obtain $2D$ surface maps in AFM experiments (see for example Ref. [28]). We notice that the absolute variation of F_{fric} with velocity in the lowest curves of Fig. 4.9 is more pronounced, thus supporting to a certain extent the claim of Ref. [9]. But it is important that this variation is only due to the different value of the prefactor c in Eq. (4.15) and not to a change of the exponent β. Therefore, we can argue that no qualitative differences arise in the velocity dependence of friction in the $2D$ case and that the common mechanism that produces the observed behaviour at $T = 0$ can

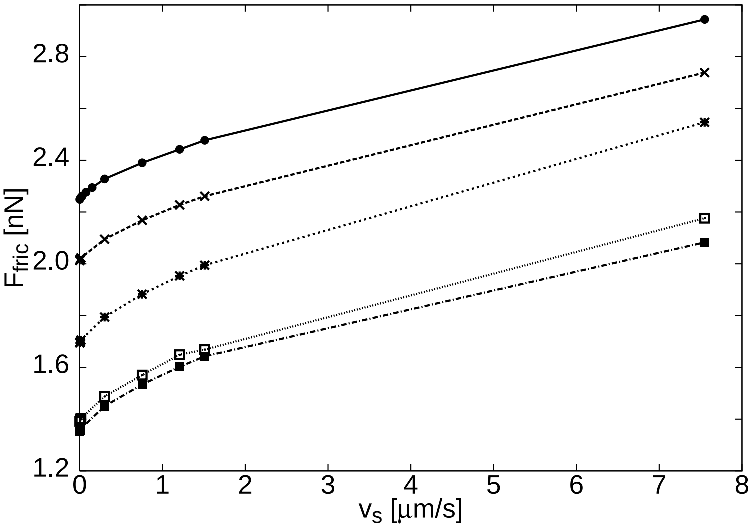

Figure 4.9: Friction force as a function of scanning velocity in the $1D$ (upper curve) and $2D$ Tomlinson model, for critical damping, $\tilde{V}_0 = 7$ and different values of y_s (from bottom to top $y_s = 0.137$ nm, 0.1 nm, 0.05 nm and 0.01 nm).

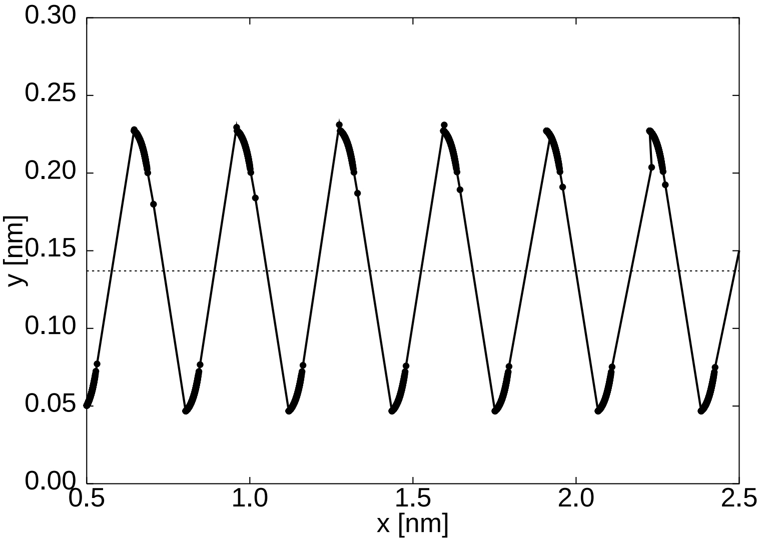

Figure 4.10: Trajectory of the tip in the $2D$ Tomlinson model for critical damping, $\tilde{V}_0 = 7$ and $v_s = 7.5$ nm/s. The circles connected by the solid line indicate the positions of the tip in the xy plane during the dynamics. The regions where the distribution of points is denser are the sticking domains, where the tip stays predominantly for most of the time. Note that the tip slips from one sticking domain to the other following a zig-zag pattern around the scanning direction $y_s = 0.137$ nm, indicated by the dashed line.

be ascribed to the delayed athermal motion of the tip with respect to the support.

4.4 Effect of thermal fluctuations

At finite temperature we integrate numerically the full equations of motion Eqs. (4.4) and (4.12). Due the presence of the stochastic forces, the motion of the tip is quite noisy and averages over long trajectories (containing up to 100 periods) have to be considered in order to have a reliable value of the friction force. A typical behaviour of the lateral force in $1D$ for different velocities and critical damping at $T = 300$ K is displayed in Fig. 4.11. The height of the maximum for a fixed v_s is not constant and the effect of the scanning velocity on the slip position is rather pronounced even for small v_s.

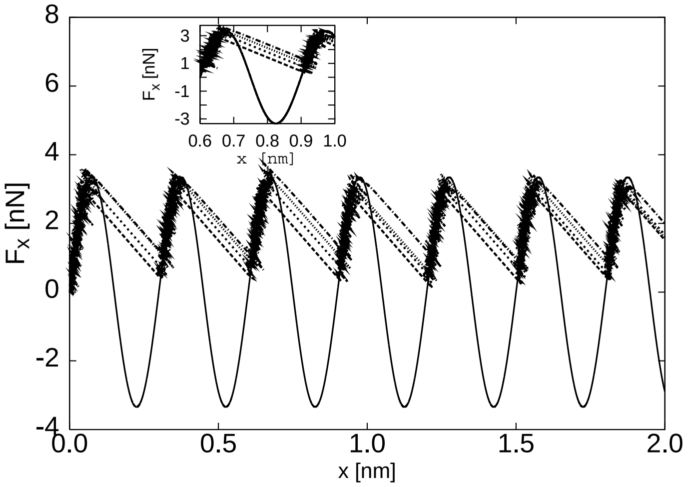

Figure 4.11: Lateral force as a function of tip position in the $1D$ Tomlinson model for critical damping, $T = 300$ K and $\tilde{V}_0 = 7$, for different scanning velocities (non-solid lines: from bottom to top $v_s = 1.5$ nm/s, 15 nm/s, 300 nm/s, 750 nm/s). The solid line represents $F_x = \frac{2\pi V_0}{a_x}\sin\left(\frac{2\pi x}{a_x}\right)$, as obtained from Eq. (4.26) (see also Fig. 4.7). The inset shows a blow up of the region around a slip event.

In fact, theoretical investigations based on simple analytical approaches in $1D$ [7, 17] and numerical simulations of the $1D$ Tomlinson model at $T \neq 0$ [17] have shown that temperature is effective in overcoming the energy barriers ΔE, activating jumps of the tip between minima of the total potential energy, for temperatures such that $\Delta E \simeq k_B T$. The thermal activation gives rise to a linearly logarithmic dependence of friction on velocity for very small scanning velocities [7]:

$$F_{fric} - F_c \propto \ln(v_s). \tag{4.44}$$

For a larger range of v_s, the following functional form has been proposed [17]:

$$\boxed{F_{fric} - F_c \propto |\ln(v_s)|^{2/3}.} \tag{4.45}$$

The constant value F_c is the lateral force corresponding to a slip event at $T = 0$. The appendix at the end of the chapter contains an analytical derivation of Eq. (4.45). Eq. (4.45) is obtained by assuming $\tilde{V}_0 > 1$ and $V_0 \gg k_B T$. As it is shown in Fig. 4.12, where we compare F_{fric} vs. v_s for $T = 0$ and $T = 300$ K, the main source of velocity dependence of friction is due to thermal fluctuations in the system. The data for $T = 300$ K can be fitted by a logarithmic behaviour with an exponent very close to the value 2/3 of Eq. (4.45). To our knowledge theoretical approaches of velocity dependence of friction at finite temperature have been restricted to $1D$ models. Here we report results of numerical simulations also for the $2D$ Tomlinson model, using the same parameters as for the model at $T = 0$. Not surprisingly, Fig. 4.13 shows that the velocity dependence of friction is very similar in $1D$ and $2D$, as we have found for $T = 0$. We can use Eq. (4.45) to fit the data of the $2D$ model as well. In fact, as we have discussed in Sec. 4.3.2, the mean field character of the Tomlinson model preserves the same form of the velocity dependence of energy dissipation.

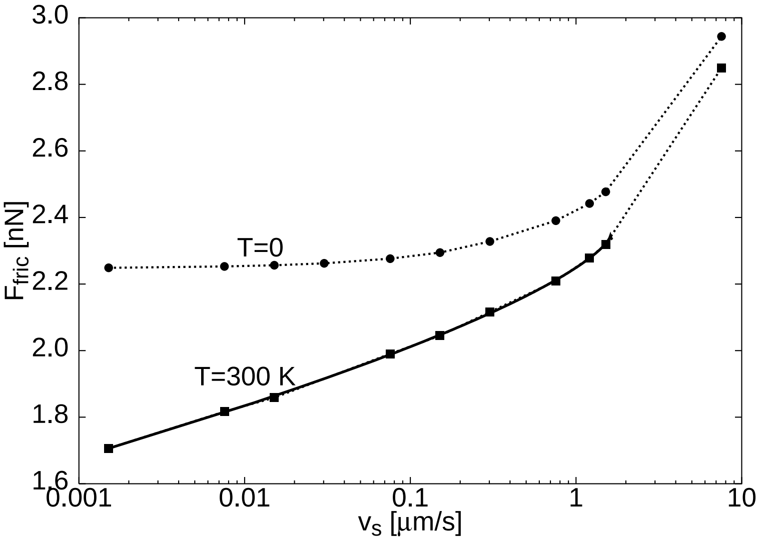

Figure 4.12: Velocity dependence of friction in the $1D$ Tomlinson model at $T = 0$ (upper curve) and $T = 300$ K (lower curve) for critical damping and $\tilde{V}_0 = 7$. The solid line is a fit of the data for $T = 300$ K, using Eq. (4.45) in the small velocity regime ($v_s < 2$ μm/s).

The different behaviour of friction with scanning velocity at $T \neq 0$ is due to the activated motion of the tip, which lowers the friction force with respect to the athermal situation. This can be easily understood from a sketch of the evolution of the total potential V_{tot} during the scanning, which is given in Fig. 4.14. While at $T = 0$ a slip event can occur only when the energy barrier ΔE (i. e. the difference between the maximum and the minimum of V_{tot}) vanishes, thermal fluctuations can activate jumps of the tip from

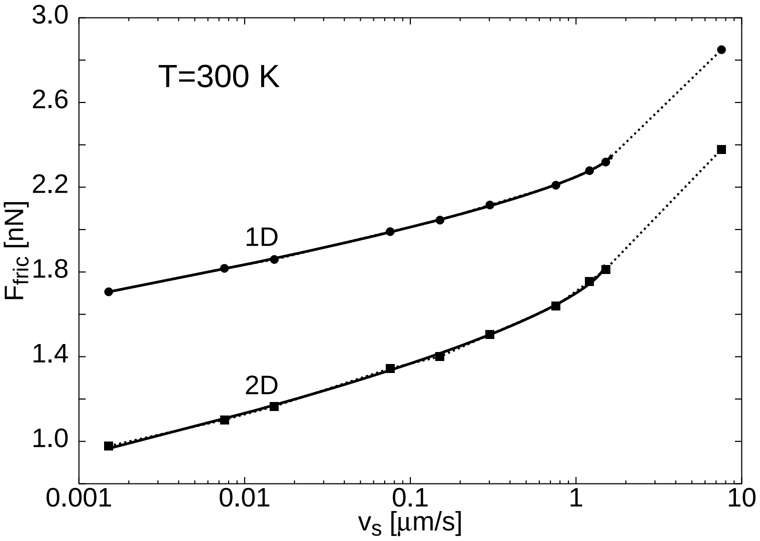

Figure 4.13: Velocity dependence of friction in the $1D$ (upper curve) and $2D$ (lower curve) Tomlinson model for $T = 300$ K, critical damping and $\tilde{V}_0 = 7$. The solid lines are fits to the data using Eq. (4.45) in the small velocity regime ($v_s < 2$ μm/s).

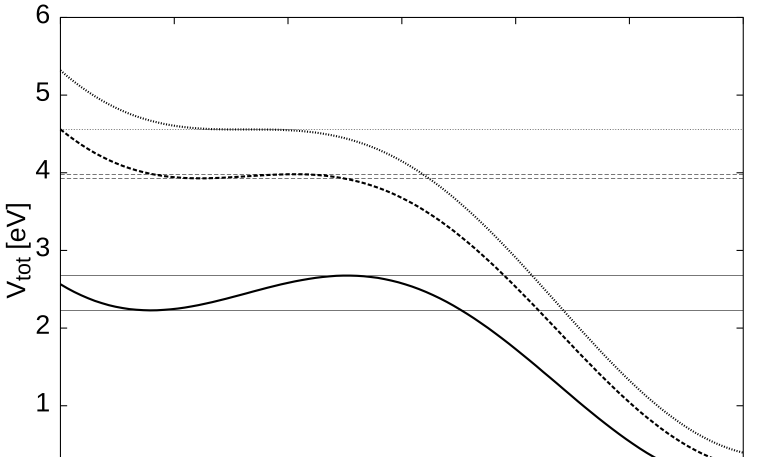

Figure 4.14: Total potential energy V_{tot} as a function of tip position x for three values of the cantilever position x_s (from bottom to top $x_s = 0.287$ nm, 0.382 nm, 0.413 nm). The horizontal lines indicate the values of the minimum (V_{min}) and the maximum (V_{max}) of the potential for each curve. The potential barrier is $\Delta E = V_{max} - V_{min}$. The upper curve corresponds to $\Delta E = 0$, while the middle curve to the case where $\Delta E \simeq k_B T$.

a metastable minimum to the next even for finite ΔE, when the cantilever has reached a position which is smaller than the one needed for a slip at $T = 0$: specifically, thermal effects start to be significant as soon as ΔE is few times $k_B T$. This has the effect to lower the energy dissipated in a jump, and thus the friction force. The energy barrier is given by

$$\Delta E(t) = V_{tot}(x_{max}(t)) - V_{tot}(x_{min}(t)), \tag{4.46}$$

where x_{min} and x_{max} are respectively the positions of a metastable minimum and maximum of V_{tot}.

In order to investigate in which conditions activated processes play a major role, it is useful to calculate the position of the cantilever x_s as a function of the energy barrier ΔE, and then to obtain the difference between x_s for $\Delta E = 0$ and x_s for $\Delta E \sim (2-3)k_B T$. For simplicity, we restrict ourselves to a $1D$ analysis. To determine x_{min} and x_{max} appearing in Eq. (4.46) we assume that $F_{static} > K_x a_x$ and expand dV_{tot}/dx around $x = a_x/4$, that is the point close to which an irreversible jump may occur. This approximation is plausible when the energy barrier ΔE is small, e.g. when $\Delta E \ll K_x a_x^2$. From Eq. (4.26), after expanding the sine term up to second order, we get

$$F_{static} - \frac{1}{2}\frac{4\pi^2}{a_x^2} F_{static} \left(x - \frac{a_x}{4}\right)^2 - K_x(v_s t - x) = 0 \tag{4.47}$$

Solving this equation, $x_{min}(t)$ and $x_{max}(t)$ can be found:

$$x_{min}(t) = \frac{a_x}{4}\left(1 + \frac{K_x a_x}{\pi^2 F_{static}} - \frac{2\sqrt{2}}{\pi}\sqrt{1 - \frac{K_x v_s t}{F_{static}} + \frac{K_x^2 a_x^2}{8\pi^2 F_{static}^2} + \frac{K_x}{4F_{static}}}\right) \tag{4.48}$$

$$x_{max}(t) = \frac{a_x}{4}\left(1 + \frac{K_x a_x}{\pi^2 F_{static}} + \frac{2\sqrt{2}}{\pi}\sqrt{1 - \frac{K_x v_s t}{F_{static}} + \frac{K_x^2 a_x^2}{8\pi^2 F_{static}^2} + \frac{K_x a_x}{4F_{static}}}\right). \tag{4.49}$$

Then, from Eq. (4.46) the energy barrier becomes

$$\Delta E(t) = \frac{4\sqrt{2}V_0}{3}\left(1 - \frac{K_x v_s t}{F_{static}} + \frac{K_x^2 a_x^2}{8\pi^2 F_{static}^2} + \frac{K_x a_x}{4F_{static}}\right)^{3/2}, \tag{4.50}$$

which is in agreement with the form proposed by Sang et al. [17], giving for F_{fric} the functional dependence of Eq. (4.45). In obtaining Eq. (4.50) we have assumed that F_{static} is quite large compared to $K_x a_x$. The expression of $x_s = v_s t$ as a function of ΔE can be determined by inverting Eq. (4.50):

$$x_s(\Delta E) = \frac{F_{static}}{K_x}\left[1 + \frac{K_x^2 a_x^2}{8\pi^2 F_{static}^2} + \frac{K_x a_x}{4F_{static}} - \left(\frac{3\Delta E}{4\sqrt{2}V_0}\right)^{2/3}\right] \tag{4.51}$$

Note that $x_s(\Delta E = 0)$ should coincide with the exact expression $x_s^{(0)}$ of Eq. (4.29). Indeed, it is possible to see that $x_s(\Delta E = 0)$ as given by Eq. (4.51) can be obtained by expanding $x_s^{(0)}$ for large $\tilde{V}_0$. Moreover, it is clear from Eqs. (4.48)-(4.50) that the values of $x_{min}(t)$ and

$x_{max}(t)$ are equal for $\Delta E = 0$; in particular, if $F_{static} \gg K_x a_x$, $x_{min} = x_{max} \simeq a_x/4$, which is the point around which the expansion in Eq. (4.47) was performed. From Eq. (4.51) it is straightforward to obtain the difference $\Delta x_s(\Delta E) \equiv x_s(\Delta E = 0) - x_s(\Delta E)$:

$$\Delta x_s(\Delta E) = \frac{F_{static}}{K_x} \left(\frac{3\Delta E}{4\sqrt{2}V_0} \right)^{2/3}. \tag{4.52}$$

Eq. (4.52) can be rewritten in a form depending only on the reduced corrugation $\tilde{V}_0$ of Eq. (4.6) and on the reduced energy barrier $\Delta\tilde{E} \equiv 4\pi^2 \Delta E/(K_x a_x^2)$:

$$\Delta x_s(\Delta\tilde{E}) = \frac{a_x}{2\pi} \tilde{V}_0^{1/3} \left(\frac{3\Delta\tilde{E}}{4\sqrt{2}} \right)^{2/3}. \tag{4.53}$$

The relative difference $\Delta x_s(\Delta\tilde{E})/x_s^{(0)}$ for $\Delta E = 2.5 k_B T$ (i. e. when the barrier is comparable to the thermal energy), as a function of $\tilde{V}_0$, is illustrated in Fig. 4.15. It decreases

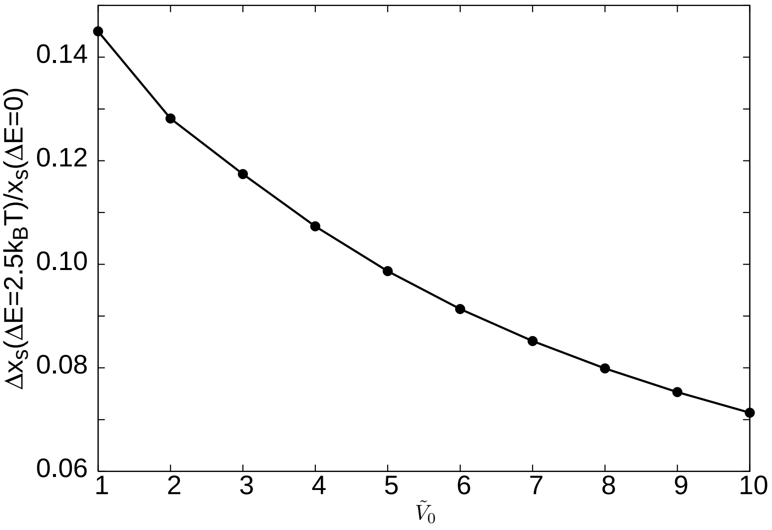

Figure 4.15: Relative difference between cantilever position x_s at $\Delta E = 0$ and x_s at $\Delta E = 2.5 k_B T$, as a function of the reduced corrugation $\tilde{V}_0$. The closed circles, connected by the solid lines, are calculated using Eq. (4.51) for $x_s(\Delta E \neq 0)$ and the exact expression Eq. (4.29) for $x_s(\Delta E = 0)$.

with increasing $\tilde{V}_0$, as it can be immediately derived from Eqs. (4.53) and (4.29):

$$\frac{\Delta x_s(\Delta\tilde{E} = 2.5 k_B T)}{x_s^{(0)}} \propto \tilde{V}_0^{-2/3}. \tag{4.54}$$

Since $F_{fric} =< K_x(x_s - x) >$, we expect that $\Delta F_{fric} \propto \Delta x_s$ and

$$\frac{\Delta F_{fric}}{F_{fric}(T=0)} \propto \frac{\Delta x_s}{x_s^{(0)}} \propto \tilde{V}_0^{-2/3}, \tag{4.55}$$

where we have defined $\Delta F_{fric} = F_{fric}(\Delta E = 2.5 k_B T) - F_{fric}(T = 0)$ (of course $F_{fric}(\Delta E = 0) = F_{fric}(T = 0)$). Thus, according to Eq. (4.55), the relative effect of thermal fluctuations on the value of the friction force is more pronounced for small $\tilde{V}_0$. Indeed, by increasing $\tilde{V}_0$, the friction force F_{fric}, in the limit $v_s \to 0$, tends to its maximum value F_{static}, and the relative variation in the stick-slip force decreases. As a consequence, the role of thermally activated processes will be less strong for large $\tilde{V}_0$.

Fig. 4.16 compares the velocity dependence of the friction force for three values of V_0 in the stick-slip regime ($V_0 = 0.28$ eV, 0.57 eV and 1 eV), with $K_x = 10$ N/m (yielding $\tilde{V}_0 = 2$, 4 and 7 respectively), both for $T = 0$ and $T = 300$ K. At the smallest scanning velocity considered, in going from $T = 0$ to $T = 300$ K, F_{fric} decreases only by a factor 1.2 for $\tilde{V}_0 = 7$, but by a factor 15 for $\tilde{V}_0 = 2$. Thus, the relative variation of F_{fric} with v_s is much more pronounced for the lowest value of $\tilde{V}_0$, and the velocity dependence of friction becomes weaker for larger $\tilde{V}_0$. The slope of the curves at $T = 300$ K slightly changes by increasing $\tilde{V}_0$ and we find that the value 2/3 of the exponent of the logarithmic behaviour (Eq. (4.45)) is recovered for the largest $\tilde{V}_0$ we have used. This is in compliance with the approximation used to derive Eq. (4.45), namely $\tilde{V}_0 > 1$ and $V_0 \gg k_B T$. More generally the data can be fitted by

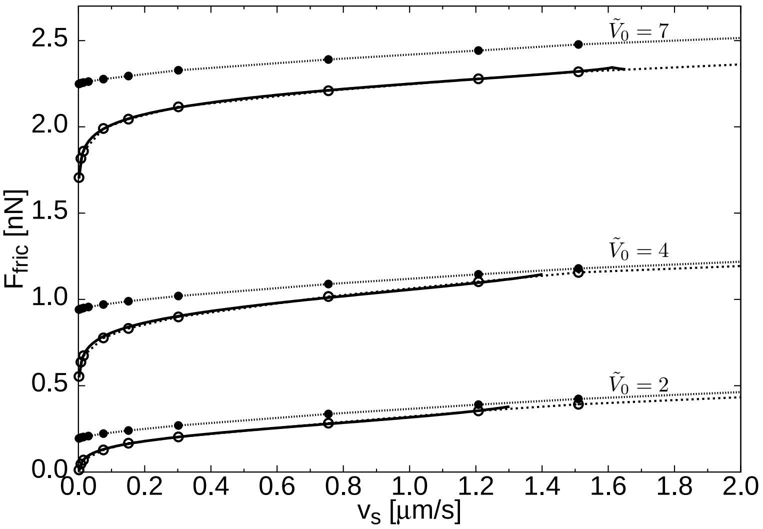

Figure 4.16: Friction force as function of scanning velocity for $\tilde{V}_0 = 2$, $\tilde{V}_0 = 4$ and $\tilde{V}_0 = 7$. The filled circles connected by the dotted lines are the data for $T = 0$, while the open circles connected by the dashed lines correspond to the data for $T = 300$ K. The solid lines are fits to the data at $T = 300$ K, according to Eq. (4.56) , with exponent $\alpha = 0.37$ for $\tilde{V}_0 = 2$, $\alpha = 0.56$ for $\tilde{V}_0 = 4$ and $\alpha = 0.67 \simeq 2/3$ for $\tilde{V}_0 = 7$. The minimum value of the scanning velocity in the plot is $v_s = 1.5$ nm/s.

$$F_{fric} - F_c \propto |\ln(v_s)|^{\alpha}, \tag{4.56}$$

where the exponent α depends on $\tilde{V}_0$. In particular, from our data we obtain $\alpha(\tilde{V}_0 = 2) = 0.37$, $\alpha(\tilde{V}_0 = 4) = 0.57$ and $\alpha(\tilde{V}_0 = 7) = 0.67$. A change of the slope of the velocity-friction curves can also be appreciated in Fig. 1(a) of Ref. [17], where data for different temperatures s are presented. This indicates that thermal effects critically depend on the surface corrugation and on temperature.

4.5 Discussion and conclusions

In this chapter we have investigated the velocity dependence of sliding friction at the atomic scale within the framework of the Tomlinson model. We have emphasized the role of the athermal processes characterizing the dynamics, which are responsible for a power-law velocity dependence of the friction force at small scanning velocities, and we have seen that at finite temperature a creep regime takes place, giving rise to a logarithmic behaviour of the friction force as a function of velocity. At variance with previous claims in the literature, these dependences apply both in $1D$ and $2D$. We have also suggested in a semi-quantitative manner in which conditions thermal effects are expected to be important for the frictional dynamics. Experimentally, the possibility to observe a velocity dependent frictional force may crucially depend on the nature of the system, which determines the corrugation V_0, on the stiffness of the cantilever and on the applied loading force, which in turns affects the value of V_0. Our model is simplified in the sense that the cantilever is treated as a point-like object and the form of energy dissipation, taken into account by introducing a damping term in the equations of motion, is purely phenomenological. Of course, in real situations finite contacts between the tip and the surface are involved and energy dissipation comes into play through more complex mechanisms. A more realistic approach to the frictional dynamics will be presented in the next chapter. However, a simple description based on the Tomlinson model contains the essential ingredients of the problem and can still capture the main dynamical features determining energy dissipation. We expect our study to stimulate further theoretical and experimental work on this issue.

Appendix: Derivation of the thermal velocity dependence of friction

Assuming $F_{static} \gg K_x a_x$ and noting that

$$F_x(t) = K_x(v_s t - x) \simeq K_x v_s t \tag{4.57}$$

the energy barrier given by Eq. (4.50) becomes

$$\Delta E(t) = \frac{4\sqrt{2}V_0}{3}\left(1 - \frac{F_x(t)}{F_{static}}\right)^{3/2} \equiv \lambda(F_{static} - F_x(t))^{3/2}. \tag{4.58}$$

When ΔE becomes comparable to the thermal energy $k_B T$, thermal fluctuations can activate jumps of the particle from the upper minimum A to the lower adjacent minimum B. Thus we can restrict ourselves to a double-well potential (see Fig. 4.17). If p is the probability to find the particle in A ($1-p$ is the probability to find the particle in B), the transition between the two states is governed by a master equation of the form

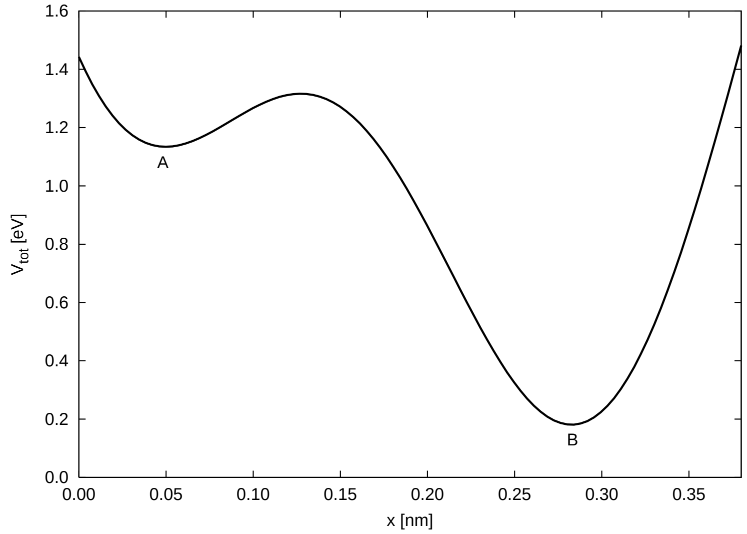

Figure 4.17: Sketch of the double-well potential used in the rate model to derive the thermal velocity dependence of friction. Thermal fluctuations can activate transition between A and B when the barrier $\Delta E \sim k_B T$.

$$\frac{dp(t)}{dt} = -f_0 \exp\left(\frac{-\Delta E(t)}{k_B T}\right) p(t), \tag{4.59}$$

where f_0 is the attempt jump frequency. Since $\frac{dF_x}{dt} \simeq K_x v_s$, we can write

$$\frac{dp}{dt} = \frac{dp}{dF}\frac{dF}{dt} \simeq \frac{dp}{dF} K_x v_s. \tag{4.60}$$

Thus Eq. (4.59) becomes

$$\frac{dp(F_x)}{dF_x} = -\frac{f_0}{K_x v_s} \exp\left(\frac{-\Delta E^+(F_x)}{k_B T}\right) p(F_x). \tag{4.61}$$

The maximum probability transition condition is expressed by

$$\frac{d^2 p(F_x)}{dF_x^2} = 0. \tag{4.62}$$

Working out this condition and using Eq. (4.58) it is possible to show that

$$\frac{\lambda(F_{static} - F_x)^{3/2}}{k_B T} = \ln\left(\frac{v_2}{v_s}\right) - \ln\sqrt{1 - \frac{F_{static}}{F_x}} \tag{4.63}$$

where $v_2 \equiv \frac{2 f_0 k_B T}{3\lambda K_x \sqrt{F_{static}}}$. For small sliding velocities, $v_s \ll v_2$, the term $\ln\sqrt{1 - \frac{F_{static}}{F_x}}$ in Eq. (4.63) can be neglected and, after performing the time average, a logarithmic dependence of the friction force on sliding velocity is obtained:

$$F_{fric}(v_s) \simeq F_{static} - \left(\frac{k_B T}{\lambda}\right)^{2/3} \left(\ln\left(\frac{v_2}{v_s}\right)\right)^{2/3} \tag{4.64}$$

In the limit of large velocities, $v_s \gg v_2$, the term $\frac{\lambda(F_{static} - F_x)^{3/2}}{k_B T}$ can be neglected, resulting in

$$F_{fric} \simeq F_{static} \left(1 - \frac{v_2}{v_s}\right)^2. \tag{4.65}$$

Bibliography

[1] C. M. Mate, G. M. McClelland, R. Erlandsson and S. Chiang, Phys. Rev. Lett. **59**, 1942 (1987).

[2] V. N. Koinkar and B. Bhushan, J. Vac. Sci. Technol. A **14**, 2378 (1996).

[3] F. Heslot, T. Baumberger, B. Perrin, B. Caroli and C. Caroli, Phys. Rev. E **49**, 4973 (1994).

[4] T. Bouhacina, J. P. Aimé, S. Gauthier, D. Michel and V. Heroguez, Phys. Rev. B **56**, 7694 (1997).

[5] R. Bennewitz, T. Gyalog, M. Guggisberg, M. Bammerlin, E. Meyer and H.-J. Güntherodt, Phys. Rev. B **60**, R11301 (1999).

[6] Y. Hoshi, T. Kawagishi and H. Kawakatsu, Jpn. J. Appl. Phys. **39**, 3804 (2000).

[7] E. Gnecco, R. Bennewitz, T. Gyalog, Ch. Loppacher, M. Bammerlin, E. Meyer and H.-J. Güntherodt, Phys. Rev. Lett. **84**, 1172 (2000).

[8] O. Zwörner, H. Hölscher, U. D. Schwarz and R. Wiesendanger, Appl. Phys. A **66**, S263 (1998).

[9] R. Prioli, A. F. M. Rivas, F. L. Freire Jr., A. O. Caride, Appl. Phys. A **76**, 565 (2003).

[10] C. Mak and J. Krim, Phys. Rev. B **58**, 5157 (1998).

[11] H. Matsukawa and H. Fukuyama, Phys. Rev. B **49**, 17286 (1994).

[12] J. S. Helman, W. Baltensperger and J. A. Hołyst, Phys. Rev. B **49**, 3831 (1994).

[13] M. R. Sørensen, K. W. Jacobsen and P. Stoltze, Phys. Rev. B **53**, 2101 (1996).

[14] F. Slanina, Phys. Rev. E **59**, 3947 (1999).

[15] J. N. Glosli and G. M. McClelland, Phys. Rev. Lett. **70**, 1960 (1993).

[16] M. S. Tomassone and J. B. Sokoloff, Phys. Rev. B **60**, 4005 (1999).

[17] Y. Sang, M. Dubé and M. Grant, Phys. Rev. Lett. **87**, 174301 (2001).

[18] M. O. Robbins and M. H. Müser, in Handbook of Modern Tribology, edited by Bharat Bhushan, CRC press (2001).

[19] D. S. Fisher, Phys. Rev. B **31**, 1396 (1985).

[20] M. H. Müser, Phys. Rev. Lett. **89**, 224301 (2002).

[21] D. Tománek, W. Zhong and H. Thomas, Europhys. Lett. **15**, 887 (1991).

[22] H. Hölscher, U. D. Schwarz and R. Wiesendanger, Surf. Sci. **375**, 395 (1997).

[23] K_x corresponds to an effective spring constant given by the series of the stiffness of the contact between the tip and the surface and the spring constant of the cantilever.

[24] E. Riedo, E. Gnecco, R. Bennewitz, E. Meyer and H. Brune, Phys. Rev. Lett. **91**, 084502 (2003).

[25] C. Fusco and A. Fasolino, Appl. Phys. Lett. **84**, 699 (2004).

[26] J. F. Joanny and M. O. Robbins, J. Chem. Phys. **92**, 3206 (1990).

[27] E. Raphaël and P. G. de Gennes, J. Chem. Phys. **90**, 7577 (1989).

[28] E. Gnecco, R. Bennewitz, T. Gyalog and E. Meyer, J. Phys.: Cond. Matt. **13**, R619 (2001).

Chapter 5

Atomic-scale friction on graphite

This chapter is based on the following papers:

- C. Fusco and A. Fasolino, Appl. Phys. Lett. **84**, 699 (2004).
- C. Fusco and A. Fasolino, in "Modeling and Simulating Materials Nanoworld" (Advances in Science and Technology), edited by P. Vincenzini and F. Zerbetto, Techna Group, Vol. 44, pp. 249-260 (2004).

We present a numerical study of the $3D$ dynamics of a tip scanning a graphite surface as a function of the applied load, in the framework of a generalized Tomlinson model with realistic interatomic interactions. We discuss the load dependence of atomic-scale friction for this system and show how it is possible to extract the corrugation of the effective tip-surface interaction potential from the analysis of the lateral forces. We also report interesting dynamical effects of the tip for extended contacts, which can affect the frictional behaviour.

5.1 Introduction: from macroscopic to microscopic load dependence of friction

It is well known that the macroscopic friction force F_{fric} between two objects sliding relatively to each other is proportional to the applied load F_{load} and that the friction coefficient

$$\boxed{\mu = \frac{F_{fric}}{F_{load}}} \tag{5.1}$$

is a constant independent of their sliding velocity and of their apparent contact area. This is the celebrated Amontons' law of friction, which dates back to 1700 [1]. Early attempts to account for Amontons' law, first by Amontons and later by Coulomb and Euler, were based on analyses of how the microscopic surface asperities of one surface would have to climb over those of the other to allow for two surfaces to slide past each other. Since the lateral local friction force needed to lift an asperity F_{fric} equals the normal (local) load F_{load} multiplied by $\tan\Phi$, where Φ is the maximum slope of the asperity junction, we immediately obtain $F^{(i)}_{fric}/F^{(i)}_{load} = \tan\Phi^{(i)}$ at the ith asperity. When averaged over all asperities, it was reasonable to expect the space-averaged angle Φ (and therefore $\tan\Phi$) to be a constant. Thus the total friction force F_{fric} is

$$F_{fric} = \sum_i F^{(i)}_{fric} = \sum_i F^{(i)}_{load} \tan\Phi^{(i)} =< \tan\Phi^{(i)} > F_{load} \equiv \mu F_{load}, \tag{5.2}$$

where the third equality follows from the assumption that the local values of $\tan\Phi^{(i)}$ and $F^{(i)}_{load}$ are uncorrelated. An example of such a linear relation between friction and load for a macroscopic system is reported in Fig. 5.1

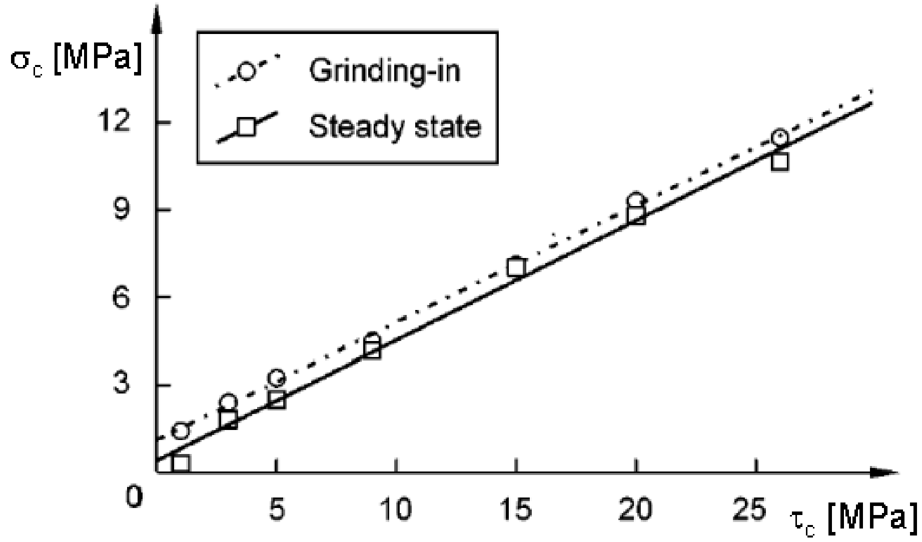

Figure 5.1: Relation between frictional force per unit area σ_c and normal pressure τ_c for a rail-wheel contact. The circles represent a measurement in the running-in stage, while the squares are obtained in the stationary state. The lines indicate a linear relation between friction and load, according to Eq. (5.1). The sliding velocity is $v_s = 5$ m/s. [From Ref. [2]].

Various arguments, both experimental and theoretical, were soon raised against this purely geometrical interpretation by Leslie in 1804, who argued that the energy expended on dragging an asperity on top of another is simply recovered when it falls down on the other side. Thus, no energy is ever lost. Some other "energy-dissipating" mechanism was therefore called for. In a series of classical experiments, Bowden and Tabor [3] found that the electrical conductivity at a metal-metal interface was proportional to the load pressing the two surfaces together and thereby concluded that the "real" contact area A is proportional to the load. The basic idea is that when two surfaces touch each other, the actual microscopic area of contact is much less than the apparent area by a factor of the order of 10^4. When the surfaces are forced to slide over each other, new contact regions are continuously formed, while others are broken. If the true contact area A is constant on average, and the contacting junctions are all subject to the same shear strength σ_c (frictional force per unit area), then the friction force is $F_{fric} = \sigma_c A$. Denoting with $\tau_c = F_{load}/A$ the compressive strain, i. e. the average pressure in a contact, the friction force becomes

$$F_{fric} = \sigma_c A = \frac{\sigma_c}{\tau_c} F_{load} \equiv \mu F_{load}, \tag{5.3}$$

which defines the friction coefficient μ as a quantity depending only on the properties of the material. For macroscopic contacts the real contact area is proportional to the load and the validity Amontons' law ($\mu =$ const.) is thus recovered. This is a phenomenological law which has been verified for a variety of systems [1].

The fundamental question we want to pose in this chapter is: *what is the load dependence of friction at the atomic-scale, i. e. for single asperities sliding over a clean, flat surface?* 300 years have passed since Amontons proposed his empirical law, and still the load dependence of friction at the nanoscale is an open problem. The usual way in which this problem has been treated is based on contact mechanics continuum theories, also known as Hertzian theories. The most well known of these were derived by Johnson, Kendall and Roberts [4] and Derjaguin, Muller and Toporov [5]. They predict that the relationship between the real contact area and the applied load for a spherical tip apex on contact with a flat surface has the form

$$A = \pi (R F_{load}/K)^{2/3}, \tag{5.4}$$

where R is the radius of the tip and K is the effective elastic modulus, which combines the elastic properties of the tip and the surface. This gives rise to the following load dependence of nanoscale friction:

$$\boxed{F_{fric} = \pi A (R F_{load}/K)^{2/3} = \nu R^{2/3} F_{load}^{2/3}} \tag{5.5}$$

where

$$\nu \equiv \pi A / K^{2/3}. \tag{5.6}$$

How can we now correlate the result given by Eq. (5.5), which holds at the nanometer scale, with the macroscopic law of friction Eq. (5.1)? The contradiction between these two results, each of which is valid at a different length scale, can be eliminated if we consider that the effective contact area between two macroscopically flat bodies, that are in motion, consists of a huge number of individual nanoscopic contacts. In fact, Greenwood and Williams [6] observed that a linear relation between friction and load is recovered for a *distribution* of elastic asperities. The linear relation arises because, as the load increases, not only the size of each individual contact spot increases, but also the number of contacting asperities. The mean size of a contact thus remains constant, as does the average contact pressure. Interestingly, the apparent contact area does not matter in this case. This argument provides an alternative explanation of Eq. (5.3)

Due to the development of AFM during the last decade (see Sec. 1.3.4), it has been possible to measure the load dependence of friction at the atomistic level. Actually, this issue is still under investigation and has been discussed in a limited number of experimental and theoretical works [7, 8, 9, 10, 11, 12, 13, 14, 15]. For example, the validity of Eq. (5.5) has been observed in some cases, of which we report one example in Fig. 5.2 [13]. However, as we have already said, the drawback of Eq. (5.5) is that it is derived under the assumption of a spherical tip, which is not always the case in real experimental situations. Moreover, Hertzian continuum theories do not give information about the atomic interaction in the sliding contact region: this is in fact the big unknown in AFM experiments. It has also been argued that, depending on the shape of the tip, power laws with different exponents can be found [13].

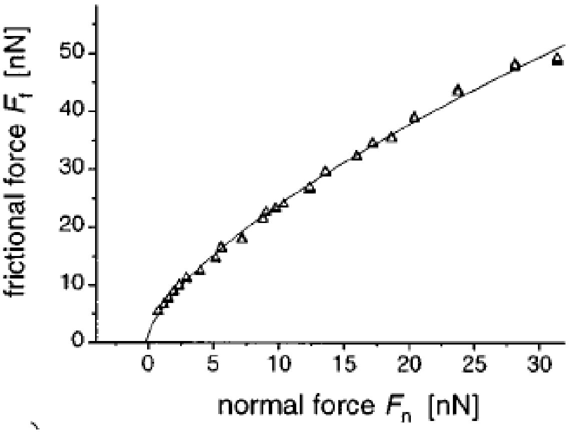

Figure 5.2: Relation between frictional force and load for amorphous carbon, obtained by AFM measurements in ultrahigh vacuum (points). The solid line is a fit using Eq. (5.5). [From Ref. [13]].

On the basis of these observations, we believe it is worthwhile to investigate the load dependence of friction up to the limit of a single atomic contact between the tip and the surface, where contact mechanics approaches lose their applicability: we can figure out that this situation is of interest in the case of a very sharp tip, whose contact with the substrate is estimated to be constituted only by few atoms [16]. Indeed, it has been observed in recent experiments on graphite [17, 30] that, as the tip (which is usually made of tungsten or silicon) is moved over the substrate, it cleaves small parts of the graphite, which remain attached to it. Thus, one is effectively studying the frictional behaviour between a graphite “flake” and a graphite layer. Graphite is well known to be a good solid lubricant and to have a low-friction behaviour, and it has been widely studied in AFM experiments [8, 13, 18, 19, 20, 21, 22, 23]. It is also used for testing and calibrating AFM machines.

In this chapter we present a detailed study of the load dependence of atomic-scale friction on graphite in the case of a sharp tip-surface contact, in particular for a single atomic contact and for small flakes. We also show how the effective tip-surface potential energy barriers can be derived from force measurements, thus establishing a connection between friction and the interatomic potential. Sec. 5.2 describes the model we have used

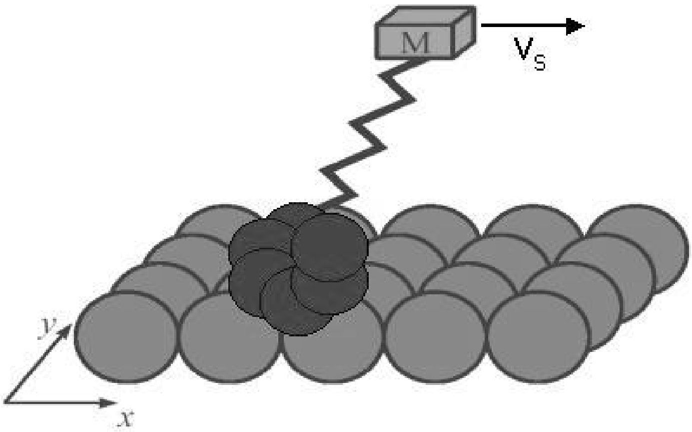

Figure 5.3: Sketch of the model of AFM on graphite used in our simulations.

in our simulations. Sec. 5.3 is devoted to the dynamics and load dependence of friction of the single-atom tip and describes the method to extract the surface corrugation from the force measurements. It also addresses the effects of finite temperature on the tip motion. Sec. 5.4 discusses dynamical effects occurring when the tip-surface contact is constituted by small flakes of graphite. We show that the dynamics of the flake can have important consequences on the frictional properties. In Sec. 5.5 we make some general remarks about the relation between friction and surface diffusion. We conclude with a discussion in Sec. 5.6.

5.2 A model of friction on graphite

We have seen in Chap. 4 that many features of the frictional dynamics can be captured by simple Tomlinson-like models, where the contact between the tip and the surface is constituted by a single atom, thermal fluctuations are neglected, the substrate is kept rigid and the motion is $1D$. Our purpose in this chapter is to develop an improved version of these kind of models, which is more realistic and can provide information about atomic-scale friction and energetics on graphite. Thus, at variance with the previous models, we aim at studying the full $3D$ dynamics of a tip scanning a monolayer graphite substrate at finite temperature. Our model is sketched in Fig. 5.3. Since, as explained in Sec. 5.1, the tip removes some graphite flakes from the substrate, we consider the tip-surface contact as constituted by one or a few carbon atoms. In this way, we can model the interaction between the tip and the surface by a specific empirical interatomic potential V_{TS} , which can accurately reproduce many properties of graphite [24]. It has the form

$$V_{TS} = \sum_{i=1}^{n_{flake}} \sum_{j=1}^{n_{sub}} \left[\theta_H(r_0 - r_{ij}) V_1(r_{ij}) + \theta_H(r_{ij} - r_0) V_2(r_{ij}) \right], \tag{5.7}$$

where r_{ij} is the distance between the ith atom of the flake and jth atom of the substrate, $\theta_H(r)$ is the Heaviside function, n_{flake} and n_{sub} are the number of carbon atoms in the flake and in the substrate respectively and

$$V_k(r) = \epsilon_i \left(e^{-2\beta_k(r-r_0)} - 2e^{-\beta_k(r-r_0)} \right) + v_k \qquad k = 1, 2 \tag{5.8}$$

with $v_1 = \epsilon_1 - \epsilon_2$ and $v_2 = 0$. The values of the parameters are $r_0 = 0.371$ nm, $\epsilon_1 = 5.355$ meV, $\epsilon_2 = 2.614$ meV, $\beta_1 = 14.693$ nm^{-1} and $\beta_2 = 21.029$ nm^{-1}. The potential V_{TS} has a cut-off at $r = r_{cut} = 0.7$ nm. Notice that periodic boundary conditions are imposed on the substrate and that the number of surface atoms n_{sub} is chosen in such a way that the length of the substrate in both x and y directions is larger than $2r_{cut}$. The tip is connected via harmonic interactions with force constants K_x, K_y and K_z to a support moving along the scanning direction. The tip support is moved with constant velocity v_s along the scanning line $x_s = v_s t$, $y_s =$constant. In our simulations we keep the substrate atoms fixed at their equilibrium positions and we do not allow the flake atoms to vibrate. We solve numerically the equations of motion in the constant force mode, i. e. we set $K_z = 0$ and add a constant force F_{load} in the downward z direction, including also a damping term proportional to the atom velocity, which takes into account dissipation mechanisms, and a stochastic force (white noise). For the single-atom tip of coordinates (x, y, z) the equations of motion have the form

$$\begin{cases} m\ddot{x} = -\frac{\partial V_{TS}}{\partial x} + K_x(x_s - x) - m\eta\dot{x} + f_x \\ m\ddot{y} = -\frac{\partial V_{TS}}{\partial y} + K_y(y_s - y) - m\eta\dot{y} + f_y \\ m\ddot{z} = -\frac{\partial V_{TS}}{\partial z} - F_{load} - m\eta\dot{z} + f_z \end{cases} \tag{5.9}$$

For the rigid flake we have only one more degree of freedom, which we choose as the angle θ formed between the line connecting one flake atom to the centre of mass (CM) of the flake and the y direction. In this case we have the following equations of motion for the CM and the angular coordinate:

$$\begin{cases} m\ddot{x}_{CM} = -\frac{1}{n_{flake}} \sum_{i=1}^{n_{flake}} \frac{\partial V_{TS}}{\partial x_i} + K_x(x_s - x_{CM}) - m\eta\dot{x}_{CM} + f_{x_{CM}} \\ m\ddot{y}_{CM} = -\frac{1}{n_{flake}} \sum_{i=1}^{n_{flake}} \frac{\partial V_{TS}}{\partial y_i} + K_y(y_s - y_{CM}) - m\eta\dot{y}_{CM} + f_{y_{CM}} \\ m\ddot{z}_{CM} = -\frac{1}{n_{flake}} \sum_{i=1}^{n_{flake}} \frac{\partial V_{TS}}{\partial z_i} - F_{load} - m\eta\dot{z}_{CM} + f_{z_{CM}} \\ I\ddot{\theta} = M_{TS,z} - I\eta\dot{\theta} + f_\theta \end{cases} \tag{5.10}$$

(x_{CM}, y_{CM}, z_{CM}) are the coordinates of the CM of the flake, I is the moment of inertia of the flake, and $M_{TS,z}$ is the torque along z exerted by the tip-substrate force:

$$\mathbf{M}_{TS} = \sum_{i=1}^{n_{flake}} (\mathbf{r}_i \times \mathbf{F}_{TS_i}) \tag{5.11}$$

where $\mathbf{r}_i = (x_i, y_i, z_i)$ indicates the position vector of particle i of the flake, and $\mathbf{F}_{TS_i} = -\left(\frac{\partial V_{TS}}{\partial x_i}, \frac{\partial V_{TS}}{\partial y_i}, \frac{\partial V_{TS}}{\partial z_i} \right)$ is the force due to the tip-substrate interaction acting on particle i.

The statistical properties of the stochastic forces are identical to those defined by Eqs. (3.4) and (3.5).

We adopt an atomistic approach, assuming for m the mass of a single carbon atom ($m = 1.92 \cdot 10^{-26}$ kg) and for the damping parameter $\eta = 1$ ps^{-1}, which is a value appropriate for dissipation of energy and momentum at the atomic scale (see e. g. [25]). Actually, in AFM problems two kinds of dynamics are present: the slow motion of the massive cantilever, with typical resonant frequency of $10^3 - 10^4$ Hz and the fast vibrations of atoms in the contact area, with typical frequency of 10^{12} Hz [26]. Due to the extremely large difference of time scales, these two dynamical modes can be decoupled. Since we use an atomistic approach, our time scales are of the order of picosecond, and this is also the reason for which $\eta = 1$ ps^{-1}. This approach does not allow to reach velocities as low as those in AFM. On the other hand, considering the entire mass of the cantilever ($m \simeq 10^{-10}$ kg) one should end up with a damping of the order $\eta \simeq 10^3 - 10^4$ ps^{-1}. Indeed, it can be shown that for Tomlinson-like models the equations of motion can be written in a such a way that they do not depend on the mass of the object (see also the appendix of Chap. 1). Thus, in the framework of this kind of models, the dynamics of an object having the typical mass of a cantilever, with resonance frequency $\sqrt{K_x/m}$ of the order of 10^4 Hz should be the same as that of a single atom with associated frequency of the order of 10^{12} Hz. Here we show results for $K_x = K_y = 1$ N/m, which are typical values of AFM, whereas our scanning velocity $v_s = 0.4$ m/s is much higher than in experiments. Our choice of parameters makes the dynamics underdamped, which is an interesting case, because dynamical effects can play a more important role.

5.3 Dynamics of a single-atom tip

In this section the effects of load and temperature on the single-atom tip dynamics are considered and a heuristic method to extract the interaction potential from the lateral forces is provided. Although the case of a single atom tip is rather extreme, it is instructive and can serve as a basis for a more sophisticated modelling of the tip-substrate contact.

5.3.1 Energetics and trajectories of the tip

The energetic landscape gives us an idea about the interaction that is at play between the tip and the surface. The energetics characterizing the tip motion for different loads is illustrated in Fig. 5.4, where we present the tip-surface potential V_{TS} as a function of the vertical tip-surface distance z. Figs. 5.4(a)-(b) show that the tip probes the attractive part of V_{TS} for $F_{load} = 0.1$ nN and the whole region around the minimum for $F_{load} = 1$ nN. By further increasing the load the tip moves closer and closer to the repulsive core of the substrate atoms, as shown in Fig. 5.4(c). These results clearly indicate that the whole tip-surface potential is probed by the motion of the tip for different loads, as also suggested by the experimental work of Fujisawa et al. [8].

The effect of the load on the actual trajectories of the tip is reported in Fig. 5.5. At very low F_{load} the tip hardly feels the surface potential and the trajectory is rather continuous, without a clear lattice periodicity. For intermediate loads the trajectory has

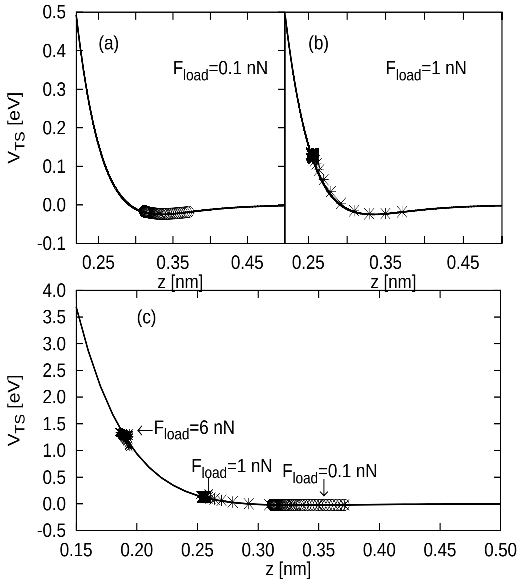

Figure 5.4: Tip-surface potential V_{TS} as a function of the vertical tip-surface distance z. The different types of points represent the values of V_{TS} at several positions along the actual trajectory as a function of the instantaneous value of z for different loads at $T = 0$. The solid lines have been obtained by a static calculation of the tip-surface potential at the hollow site (centre of a hexagon).

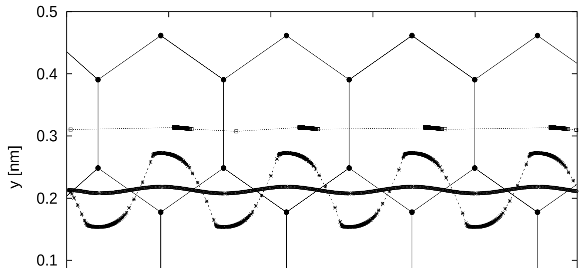

Figure 5.5: Tip in-plane trajectories at $T = 0$ for $y_s = 0.21$ nm and different values of the load: the solid line starting at $y = 0.21$ nm corresponds to $F_{load} = 0.1$ nN, the zig-zag trajectory to $F_{load} = 1$ nN and the dotted line at $y \simeq 0.31$ nm to $F_{load} = 6$ nN. Notice the transition from $1D$ continuous motion to $1D$ stick-slip motion, through $2D$ stick-slip, by increasing the load.

a zigzag behaviour with significant excursions in the y direction, sticking domains (parts of the trajectory with a denser concentration of points) appear and the motion starts revealing the underlying periodicity. If F_{load} is further increased the sticking domains become very localized, and the trajectory acquires a $1D$ character along the hollow sites (centre of hexagons), with periodicity $a = 0.246$ equal to the distance between the hollow sites. The transition from continuous to stick-slip motion and from $2D$ to $1D$ trajectories by increasing the load is consistent with the experimental results of Fujisawa et al. [8] and the static calculations of Sasaki et al. [10] on graphite. A similar kind of transition is obtained by fixing the load and changing the spring constant of the cantilever. In this sense, soft spring constants produce the same effect as large loading forces, as it can be seen in Fig. 5.6. The occurrence of different types of motion by changing the load is rather useful, because a certain dynamical pattern of the tip can identify a specific frictional regime. In fact, the $1D$ stick-slip motion for example is characterized by a larger friction force than the $2D$ zig-zag trajectory.

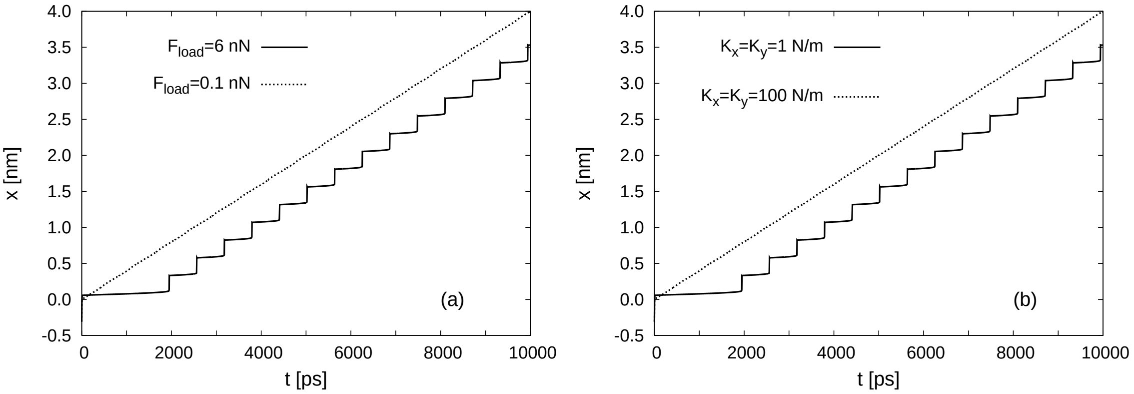

Figure 5.6: Time behaviour of the lateral coordinate of the tip x for (a) two values of the loading force [$F_{load} = 0.1$ nN (upper curve) and $F_{load} = 6$ nN (lower curve), with $K_x = K_y = 1$ N/m], and (b) two values of the cantilever spring constant [$K_x = K_y = 1$ N/m (lower curve) and $K_x = K_y = 100$ N/m (upper curve), with $F_{load} = 6$ nN] at $T = 0$. Notice the transition from sliding to stick-slip motion by increasing F_{load} (or decreasing K_x). In particular, a soft spring constant has the same effect as a large load.

In Fig. 5.7 we show the contour plots of V_{TS} , calculated for z given by the average value of the tip height at two values of the load. The scanning line $y_s = 0.17$ nm corresponds to scanning along a row of atoms. The actual trajectory is also reported: for the smaller load the motion follows a zig-zag-like pattern, while the trajectory acquires a one-dimensional stick-slip character for the higher load. It is clear that the atomic tip does not follow the scan line $y = y_s$, since it prefers to move along the hollow sites.

5.3.2 Load dependence of friction

As it was already discussed in Secs. 1.1 and 5.1, one of the main goals of AFM studies is to check whether the macroscopic laws of friction can be still applied at the nanoscale.

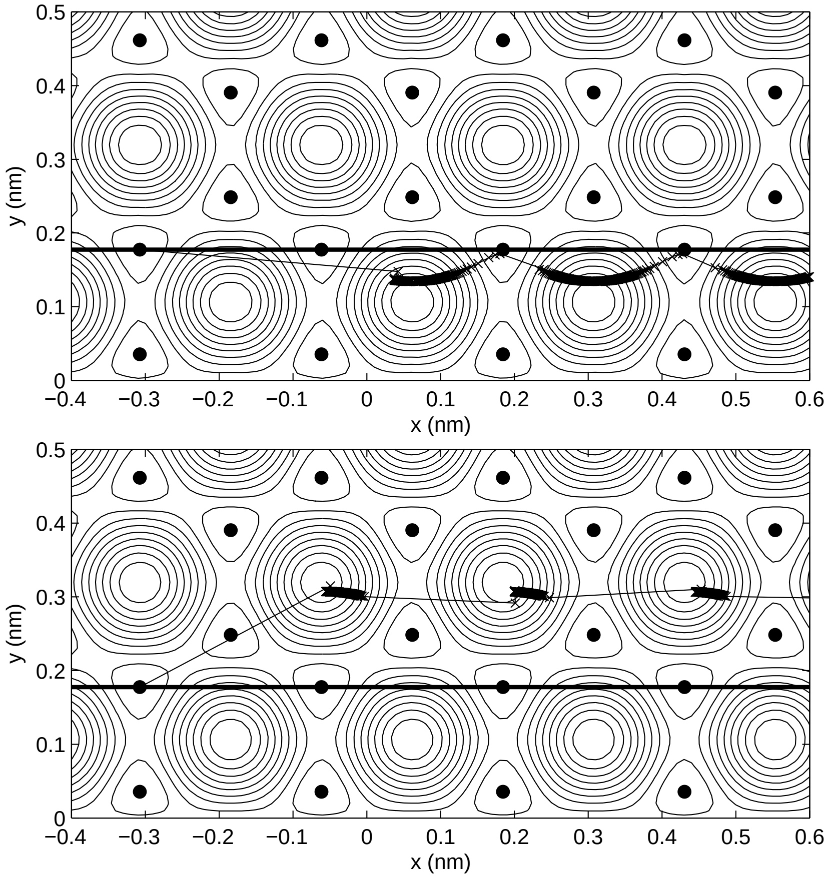

Figure 5.7: Contour plot of the potential V_{TS} for $F_{load} = 1$ nN (top) and $F_{load} = 4$ nN (bottom) with z fixed at the average value $< z >$ of the height obtained by the simulations ($< z >= 0.25$ nm for $F_{load} = 1$ nN and $< z >= 0.2$ nm for $F_{load} = 4$ nN). The minimum V_{min} and the maximum V_{max} of V_{TS} are located respectively at the hollow site and on top of one atom. We show 10 contour lines between V_{min} and V_{max}, separated by an energy interval Δ. $V_{min} = 123.5$ meV, $V_{max} = 158.5$ meV and $\Delta = 3.2$ meV for $F_{load} = 1$ nN, while $V_{min} = 774$ meV, $V_{max} = 1.01$ eV and $\Delta = 23.7$ meV for $F_{load} = 4$ nN. The horizontal thick solid lines indicate the scanning direction ($y_s = 0.17$ nm), while the crosses are points along the actual atomic trajectory taken every 4 ps.

Here, we address the problem of the load dependence of friction. The friction force F_{fric} is calculated by averaging the lateral forces F_{el}^x and F_{el}^y over several lattice parameters, by using

$$F_{fric} = \sqrt{< F_{el}^x >^2 + < F_{el}^y >^2}. \tag{5.12}$$

for each value of the applied load F_{load}. The behaviour of F_{fric} vs. F_{load}, as found by our numerical simulations, is illustrated in Fig. 5.8. The data can be fitted by a power law of the form

$$\boxed{F_{fric} \propto F_{load}^{\alpha}}, \tag{5.13}$$

with $\alpha \simeq 1.6$. This exponent is different both from the one expected for macroscopic friction, $\alpha = 1$ (see Eq. (5.2)), and from that of Hertzian contacts, $\alpha = 2/3$ (see Eq. (5.5)).

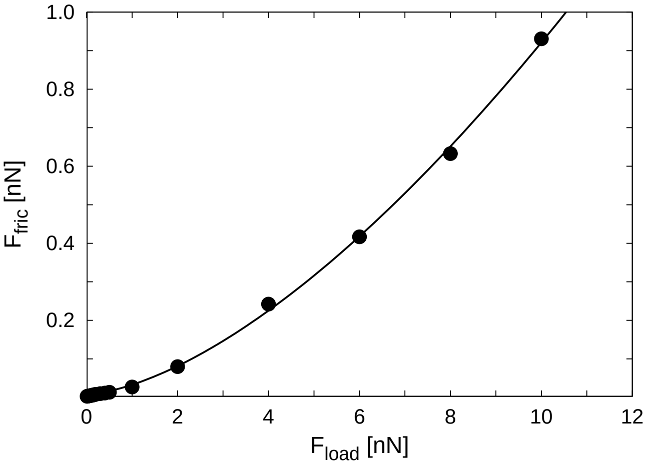

Figure 5.8: Friction force as a function of the applied load at $T = 0$. The circles are the result of the numerical simulations, and the line is a power-law fit to the data with exponent ~ 1.6. Notice that F_{fric} is very low up to $F_{load} \simeq 0.5$ nN, where the dynamics is dominated by sliding motion.

Therefore, although we cannot justify the exponent found in our simulations in an analytical way, we infer that an exponent larger then 1 is characteristic of very sharp and undeformable tip-surface contacts, of which our case is a prototype. In fact, since it has been suggested that the shape of the tip can be crucial in determining the exponent α, a detailed study of the load dependence of friction can be useful to provide information about the morphology of the tip-surface contact: the exponent 2/3 is recovered only for perfectly spherical tips, elastically in contact with the substrate [13]. This means that wear should be avoided, restricting the applicability of Eq. (5.5) only to low loading forces.

In Fig. 5.8 we can clearly appreciate a bunch of points for $F_{load} < 0.5$ nN, where the friction force is rather low, and more or less constant. This is an interesting observation, because for these very small loads the tip performs a sliding motion and the dissipation of energy is very low (see also Fig. 5.6(a), showing the comparison of the tip motion for two loads). Thus, by reducing the load we can drive a transition from a stick-slip regime with high friction force to a sliding state with very low friction. This kind of transition has also been discussed in Sec. 1.4.2 in the framework of the Tomlinson model and has been reported very recently in an AFM experimental work on NaCl [15]. Besides, the relation between friction and load has been measured for graphite up to loads $F_{load} = 50$ nN, finding that F_{fric} does not increase appreciably with F_{load} for $F_{load} < 40$ nN, as illustrated in Fig. 5.9. In order to compare these results with ours we notice that the tip-surface contact has been estimated to be of the order of 100 atoms in the experiments. Thus, the load per particle and the friction force per particle are the experimental values divided by 100. This means that the value of $F_{load} = 40$ nN up to which the friction is constant in Fig. 5.9 corresponds to the value $F_{load} = 0.4$ nN in our simulations presented in Fig. 5.8. Indeed, we also find that F_{fric} is almost constant in this region and that it is very low, e. g. of the order of few pN. In fact, examining Fig. 5.9 we see that the experimental friction force per particle is of the order of pN. The occurrence of these these extremely low friction forces, which in modern AFM machines can be measured with a precision of the order of 10^{-3} pN, has given rise to the concept of *superlubricity*, first introduced by Hirano et al. [28], which implies the possibility to slide without energy dissipation [17]. Actually, we refrain from using this term, since the average friction is not zero, even in the limit of very small loads: there is always a damping mechanism due to the finite velocity of the support. What disappears however are the elastic instabilities in the stick-slip regime, which we have discussed for the Tomlinson model in Secs. 1.4.2 and 4.2, and which represent the dominant contribution to energy dissipation.

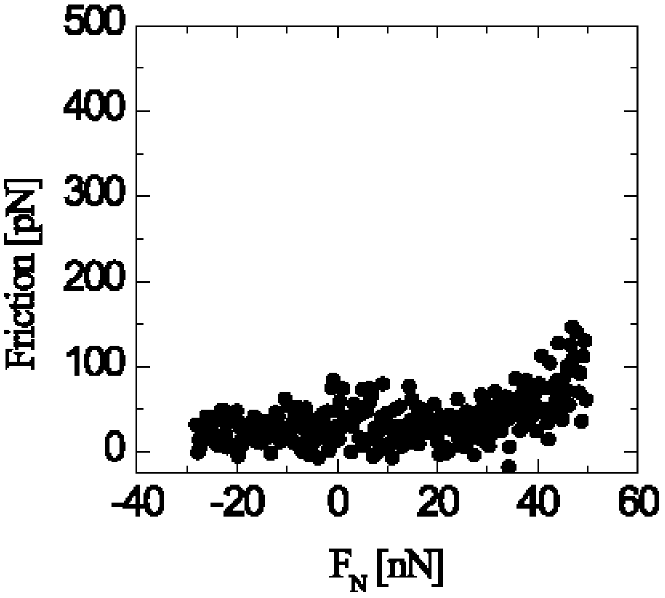

Figure 5.9: Friction force as a function of the applied load from AFM measurements on graphite. The friction force is constant for $F_{load} < 40$ nN. In this experiment the tip-surface contact is estimated to be formed by about 100 atoms. [From Ref. [27]].

5.3.3 Reconstructing the surface corrugation

As shown in Fig. 5.7, the actual trajectory does not necessarily follow the scanning line, so that the potential energy landscape during the motion is not known a priori. A detailed theoretical/experimental study [22] of AFM images obtained in the stick-slip regime on graphite substrates shows indeed that, strictly speaking, the AFM images are not ”atomically resolved”, since they reveal the periodicity of the potential minima of the hexagonal lattice rather than the atomic positions. Here we show that this apparent drawback of the technique can be turned into an advantage, since the information provided by the force measurement can be used to reconstruct the effective interaction potential.

Only few experimental studies employing contact mode AFM have attempted to establish a relationship between friction forces and interatomic potentials [8]. On the other hand, recent works using noncontact mode AFM have shown the possibility to reconstruct the tip-surface potential [29]. In this technique, which was already introduced Sec. 1.3.4, the measured quantity is the shift of the resonance frequency Δf caused by the tip-sample interaction rather than the deflection of the cantilever, as in contact mode. Δf is directly linked to the tip-surface force $F_{TS}(z) = -\frac{\partial V_{TS}}{\partial z}$ by the relation

$$\Delta f = \frac{1}{\sqrt{2\pi}} \frac{f_0}{A^{3/2}} \int_D^\infty \frac{F_{TS}(z)}{\sqrt{z-D}} dz, \tag{5.14}$$

where f_0 and A are the frequency and the amplitude of oscillation of the cantilever respectively, and D is the nearest tip-surface distance. However, this approach lacks the link between the corrugation of the potential and the friction force. The ideal way to achieve this goal is provided by a study of the load dependence. We show how to extract the effective value of the energetic barrier V_0 for a given F_{load} from the force plots, as if they were experimental data.

The stick-slip dynamics results from the competition of the forces $\mathbf{F}_{el}$ and $\mathbf{F}_{TS}$ due to the cantilever and to the tip-surface potential V_{TS} respectively. While the tip is driven in a given direction, elastic energy accumulates in the spring but it is counterbalanced by the substrate attraction, until, suddenly, the tip slips to another minimum. Therefore, while sticking, $\mathbf{F}_{el}$ mirrors $\mathbf{F}_{TS}$. This fact can be used to derive the surface corrugation V_0. Fig. 5.10 presents typical force plots as a function of x_s and x for $F_{load} = 2$ nN and $F_{load} = 4$ nN. Note that experimental force plots data are often given as a function of x_s. However, since $F_{el}^x = K_x(x_s - x)$, it is straightforward to rewrite the data $F_{el}^x(x_s)$ as $F_{el}^x(x)$. The solid lines in Fig. 5.10 represent the lateral force along the scanning direction, F_{el}^x, as obtained by our simulations. Increasing the load enhances the sawtooth behaviour of the stick-slip motion and gives rise to a larger initial sticking region, related to the static friction force, which is often observed experimentally (see e. g. [30]).

To proceed towards our goal we note that in several *ab-initio* calculations, the force felt by a tip scanning a surface is well approximated by a sinusoidal function (see e. g. Refs. [11, 31]). Therefore, we can assume that the substrate interaction at fixed y and z has a sinusoidal shape. Moreover F_{TS} should average to zero for a periodic substrate. As already noted, the cantilever elastic force and the tip-substrate force sum to zero in the stick interval, the elastic force reaching its maximum when the tip-surface force is at

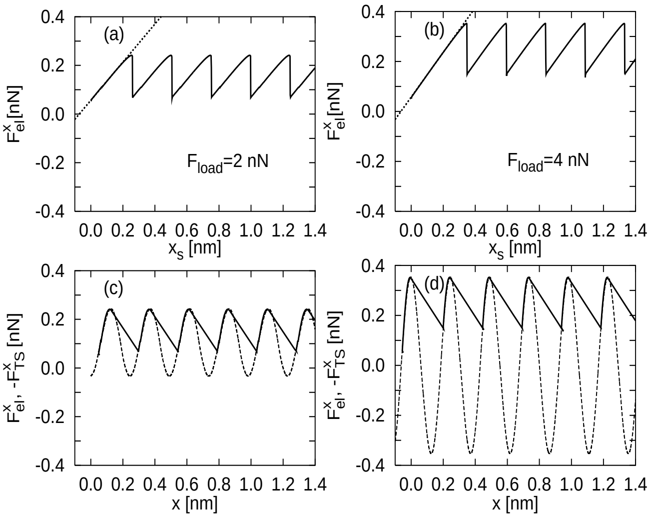

Figure 5.10: Lateral forces along the scanning direction for $F_{load} = 2$ nN [(a),(c)] and $F_{load} = 4$ nN [(b),(d)], plotted as a function of x_s [(a),(b)] and x [(c),(d)], for $y_s = 0.17$ nm and $T = 0$. Solid lines are the elastic forces F^x_{el} obtained by simulations, while the dashed lines in (c) and (d) are static calculations of the tip-surface force (with reverted sign) $-F^x_{TS}$ at (y, z) determined by averaging $y(t)$ and $z(t)$ given by the dynamics. The dotted lines in (a), (b) give the slope K_{eff} of the sticking part ($K_{eff} = 0.78$ N/m for $F_{load} = 2$ nN and $K_{eff} = 0.89$ N/m for $F_{load} = 4$ nN).

the minimum. Given these facts, we can obtain the amplitude F_0, the average value and the period a of the tip-surface force along the scanning direction, i.e. we can reconstruct F^x_{TS} completely. Then, the tip-surface potential V_{TS} is simply given, up to a constant, by integrating F^x_{TS}:

$$V_{TS}(x) = \frac{V_0}{2} \sin\left(\frac{2\pi x}{a}\right) + const. \tag{5.15}$$

with $V_0 = \frac{F_0 a}{2\pi}$. In Figs. 5.10(c)-(d) we show $-F^x_{TS}$ (dashed lines) obtained by static calculations for (y, z) determined by averaging $y(t)$ and $z(t)$ given by the dynamics. Indeed, $-F^x_{TS}$ follows the sticking parts of F^x_{el} quite well. The first stick signal, of larger amplitude, is the most suitable to estimate the amplitude of F^x_{TS}.

This procedure enables us to estimate the effective energy barrier along the tip trajectory. The resulting dependence of the energy barrier V_0 on the load is shown in Fig. 5.11. Interestingly, the data can be fitted by a power law

$$\boxed{V_0 \propto F^{\gamma}_{load}}, \tag{5.16}$$

with $\gamma \simeq 1.6 \simeq \alpha$. Thus, the relation between load and energy barrier is the same as that between load and friction. Fig. 5.12 substantiates this statement, showing that the friction force is linearly dependent on the surface energetic barrier. This result indicates a direct link between friction and surface corrugation, which is the essence of the microscopic

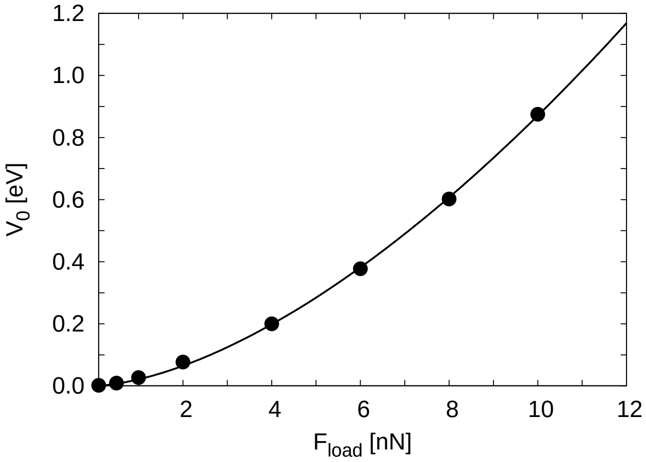

Figure 5.11: Load dependence of the energetic barrier at $T = 0$. The solid circles are the result of the simulations, while the solid line is a power law fit with exponent ~ 1.6.

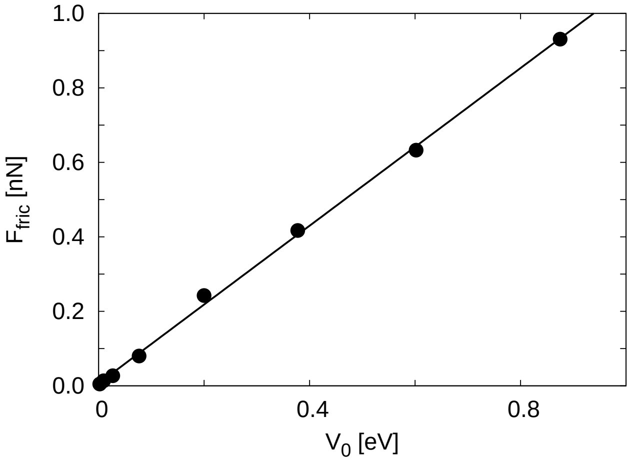

Figure 5.12: Relation between friction and surface corrugation at $T = 0$. The solid circles are the result of the simulations, while the solid line is a linear fit to the data.

description of sliding friction in terms of atoms in the contact area moving on a corrugated potential, similar to surface diffusion of adsorbates (see also Sec. 5.5). An increase of V_0 with F_{load} has also been found experimentally in recent works [8, 32]. We report for comparison the dependence of V_0 on F_{load} for a mica surface in Fig. 5.13 [32], which shows that the data can be fitted by a power law with exponent ~ 1.2, thus suggesting a behaviour quite similar to that found in our simulations.

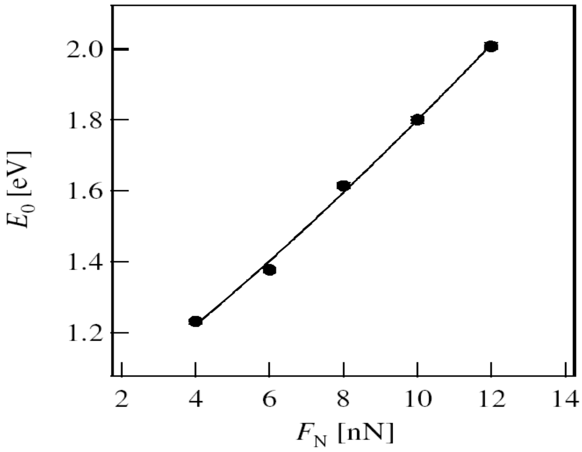

Figure 5.13: Load dependence of the energetic barrier (E_0 is the analogous of V_0 in our notation and F_N corresponds to F_{load}) as measured by AFM experiments on mica. The solid line is a power-law fit with exponent ~ 1.2. [From Ref. [32]].

5.3.4 Determination of the cantilever lateral stiffness

We propose a method to determine the lateral spring constant of the cantilever K_x from the knowledge of the surface corrugation V_0, which we are able to obtain by the method described in Sec. 5.3.3. From the slope of the lateral force F_{el}^x in the stick-slip regime one usually obtains an effective stiffness K_{eff} of the cantilever which is lower than the lateral spring constant K_x. This apparent contradiction is due to the fact that there is a further contribution to the lateral stiffness coming from the elastic compliance of the tip-surface contact. Thus, the effective spring constant arises from the series of the cantilever spring constant K_x and the spring constant $K_{contact}$ formed by the contact between the tip and the surface, which is called *contact stiffness* [33]:

$$K_{eff} = \left(\frac{1}{K_x} + \frac{1}{K_{contact}} \right)^{-1} . \tag{5.17}$$

$K_{contact}$ is the curvature of the potential V_{TS} at the local minimum. Therefore, given the validity of Eq. (5.15), it is easily found

$$\boxed{K_{contact} = \frac{2\pi^2 V_0}{a^2}} . \tag{5.18}$$

Thus, the contact stiffness is proportional to the surface corrugation, meaning that the higher is the load, thus the higher is the energy barrier, the stiffer is the contact. Since it is possible to estimate K_{eff} from the slope of the sticking part of the lateral force (see dotted lines in Fig. 5.10(a)) and to reconstruct the corrugation from the lateral forces as well, it is straightforward to obtain K_x using Eqs. (5.17) and (5.18). The values of K_{eff} and $K_{contact}$ are plotted in Fig. 5.14 as a function of F_{load}. Note that for low loads the contact stiffness $K_{contact}$ can be comparable to the lateral stiffness of the tip K_x, whereas at high loads K_{eff} tends to K_x.

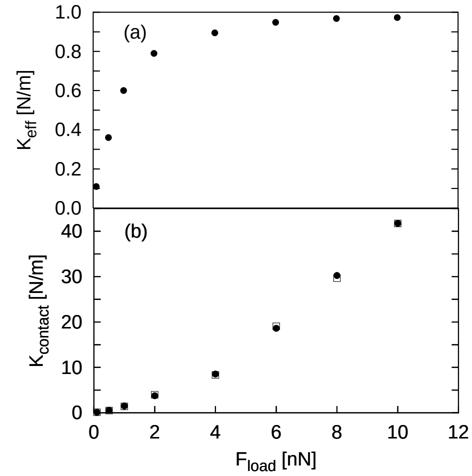

Figure 5.14: (a) Effective lateral spring constant obtained from the slope of the sticking part of the lateral force. (b) Solid circles: contact stiffness obtained from Eq. (5.17) assuming K_x to be known ($K_x = 1$ N/m). Open squares: contact stiffness obtained from Eq. (5.18). The agreement between the two determinations is excellent. Thus Eq. (5.18) can be used to calculate $K_{contact}$ and then K_x can be determined by Eq. (5.17), using the values of K_{eff} shown in (a). The scanning direction is $y_s = 0.17$ nm.

5.3.5 Thermal effects

The analysis that we have shown was performed at $T = 0$. By adding thermal fluctuations we observe a more irregular behaviour of the lateral forces and of the trajectories, characterized by straight and diagonal jumps, as shown in Fig. 5.15. As a consequence, the periodicity of F_{el}^{x} is not well defined, reflecting the occurrence of straight and of shorter diagonal jumps from one hollow site to the next. Moreover, the time spent by the tip in each sticking domain is not constant, causing variations of the height of the sticking parts up to 20% from one maximum to another. Yet it is still possible to get useful information about atomistic friction and energy barriers also in this case, thus making our method applicable to raw experimental data. In Fig. 5.16 a comparison of the sinusoidal fit to the sticking part between the data for $T = 0$ and $T = 300$ K is shown. The amplitude

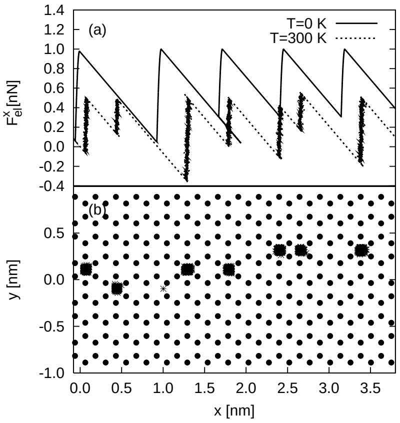

Figure 5.15: Comparison of the lateral force for $T = 0$ (solid line) and $T = 300$ K (dashed line) (a) and in-plane trajectory of the tip for $T = 300$ K (b) for $F_{load} = 8$ nN. The solid circles in (b) denote the substrate atoms positions. Notice the more irregular behaviour of the trajectory and of the lateral force at finite temperature.

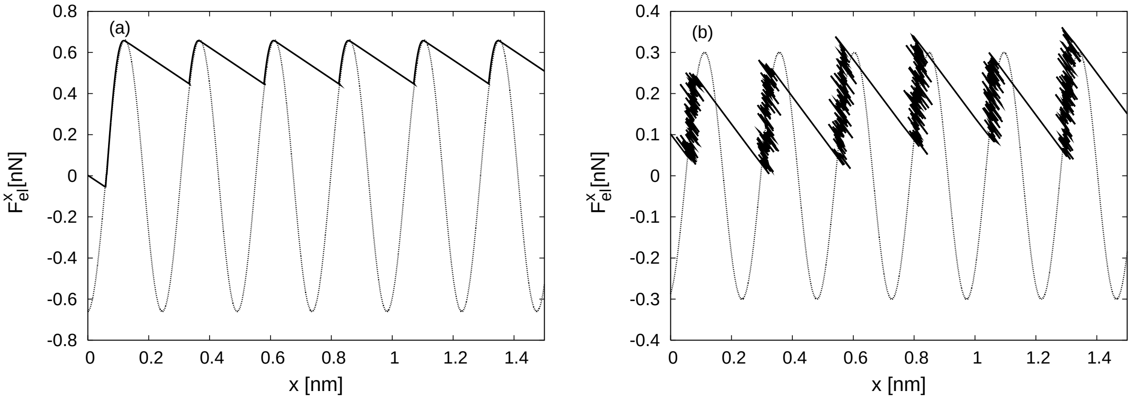

Figure 5.16: Lateral force along the scanning direction F^x_{el} at $T = 0$ K (a) and $T = 300$ K (b) for $F_{load} = 6$ nN. The solid lines are obtained by the simulations, while the dotted lines are sinusoidal fits to the sticking parts of F^x_{el}. Notice that the amplitude of the force is much lower in the case of finite temperature ($F_0 = 0.66$ nN at $T = 0$ and $F_0 = 0.3$ nN at $T = 300$ K).

of the fitting function at $T = 300$ K has been obtained by averaging the different heights of the sticking parts over a long trajectory. We notice that finite temperature results in a reduction of the effective corrugation V_0. In fact, from Fig. 5.16 it is seen that $F_0 = 0.66$ nN for $T = 0$ and $F_0 = 0.3$ nN for $T = 300$ K, which implies that the value of V_0 is more than halved in going from $T = 0$ to $T = 300$ K. From the discussion of Sec. 5.3.3 it immediately results that *thermal fluctuations lower the friction force*: this has been also observed in Sec. 4.4 for the Tomlinson model. Fig. 5.17 clarifies this point.

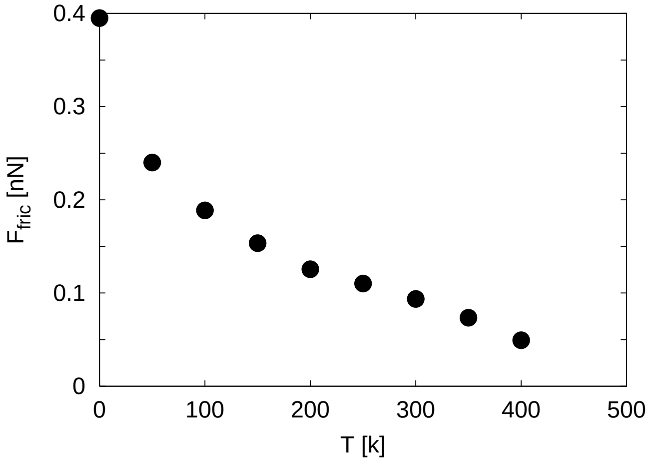

Figure 5.17: Temperature dependence of friction found from the numerical simulations for $F_{load} = 6$ nN. Temperature effectively reduces the friction force.

Finally, we have calculated the load dependence of friction at finite T. From Fig. 5.18 we see that the friction force at finite T is always lower than that for $T = 0$, as expected. Surprisingly, the behaviour at finite T can still be fitted by the functional form Eq. (5.13) with the same exponent $\gamma \simeq 1.6$. What changes is only the prefactor in front of the power law. Thus, the behaviour found at $T = 0$ seems to be robust and linked only to the specific form of our tip-surface potential and to the choice of a single-atom tip.

5.4 Dynamics of rigid graphite flakes

Recent experimental works [17, 27] have shown puzzling results: the friction force between a tungsten tip and an atomically flat graphite surface was ultralow (less than 50 pN) for most relative orientations of the flake with respect to the substrate, except for a narrow range of orientations where the friction was very high (of the order of 250 pN). Previous experiments had already found that the sliding of MoO_3 nanocrystals in contact with a MoO_2 surface occurred along specific directions for which a very low shear stress was measured [34]. Furthermore, total-energy minimization calculations performed at $T = 0$ of a flat Cu(111) terminated asperity over a Cu(111) surface have demonstrated that, when the asperity was rotated out of registry with respect to the substrate, the friction force vanished for sufficiently large contacts. These findings underline the importance of the

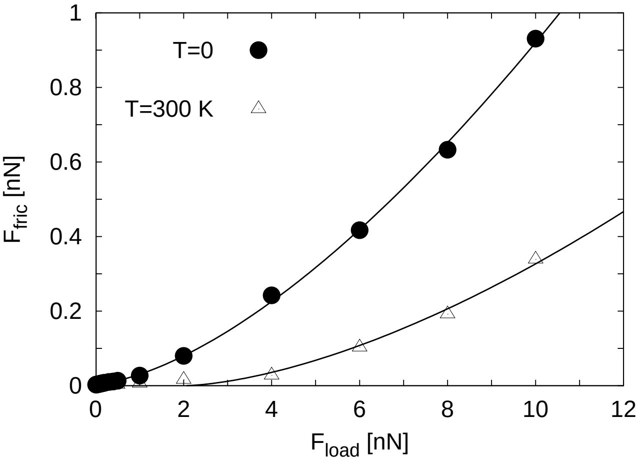

Figure 5.18: Load dependence of friction at $T = 0$ (solid circles) and $T = 300$ K (open triangles). The solid lines are fit to the numerical data of the form (5.13) both with the same exponent $\gamma \simeq 1.6$, but with different prefactors.

finite size and of the degree of commensurability of the tip-surface contact on the frictional behaviour.

In order to make contact with the experimental results, in particular those found in Refs. [17, 27], we will show some peculiar features of the dynamics of rigid graphite flakes attached to the tip and we will discuss another way to control friction, which relies on the orientational degree of freedom of the flake. Thus, for our purposes, we can consider the flake as a rigid object where internal vibrations are negligible, restricting our analysis to zero temperature. Fig. 5.19 displays the symmetric flakes we have used in our calculations. The flake dynamics is studied by solving Eq. (5.10) for $T = 0$. As a first step we fix the angle θ of the flake with respect to the substrate to a given value θ_0 and calculate the resulting friction force on the flake. Repeating this procedure for different values of θ, we can plot the friction force as a function of the rotation angle. This is illustrated in Fig. 5.20(a). The striking feature of this figure is the occurrence of two peaks at $\theta = 0°$ and $\theta = 60°$, where the friction force is maximum ($F_{fric} \simeq 160$ pN). These are the angles at which the flake is commensurate, i. e. “in registry”, with respect to the substrate and

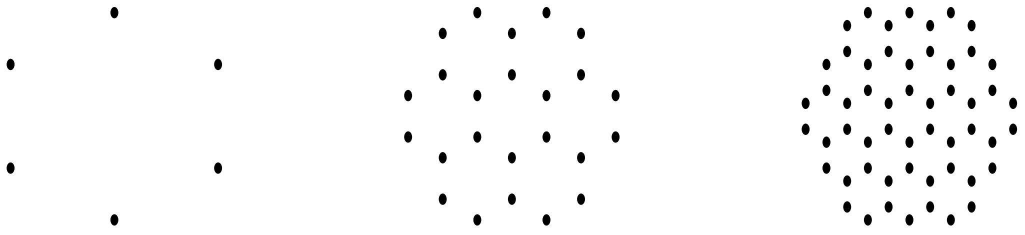

Figure 5.19: Symmetric flakes used in our calculations, consisting (from left to right) of 6, 24 and 54 atoms.

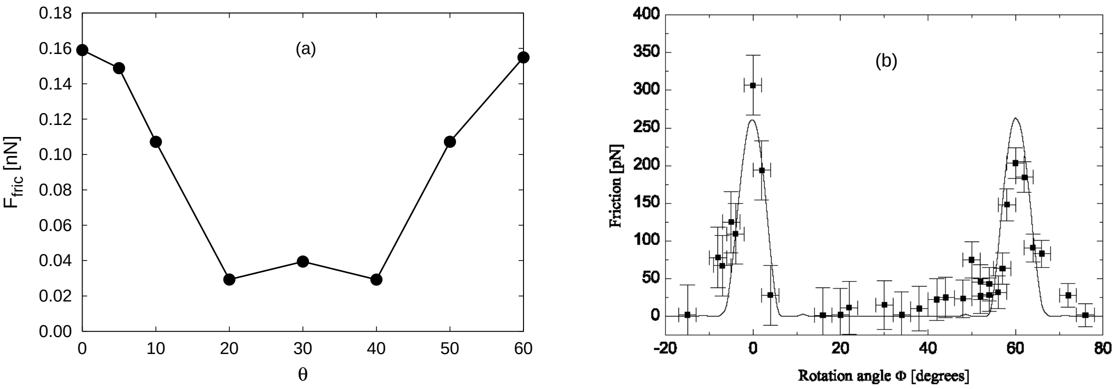

Figure 5.20: Dependence of the friction force on the rotational angle θ of the graphite flake with respect to the graphite lattice. The results of our simulations are plotted in (a). The friction force is maximum at $\theta = 0°$ and $\theta = 60°$ (flake in registry with the lattice) and is very low when the flake is not commensurate with the substrate (especially around $\theta = 30°$). The loading force used in the simulations is $F_{load} = 40$ nN. For comparison we report in (b) the experimental data on graphite from Ref. [17].

their values are related to the hexagonal symmetry of the graphite lattice. On the other hand, the friction is very low ($F_{fric} \simeq 3$ pN) when the flake is rotated out of registry, e. g. for an interval of angles centered around $\theta = 30°$. For clarity's sake, we illustrate in Fig. 5.21 two configurations of the flake which are respectively in registry ($\theta = 0°$) and out of registry ($\theta = 30°$) with respect to the substrate, and correspond to the maximum and minimum friction in Fig. 5.20. These features have been observed experimentally, as shown in Fig. 5.20(b) [17]. The results displayed in Fig. 5.20(a) are obtained using a flake with 24 atoms. Increasing the number of flakes does not change qualitatively the observed pattern. Actually, the angular width of the peaks $\Delta\theta$ is related to the size of the flake D by [17]

$$\tan(\Delta\theta) = a/D \simeq n_{flake}, \tag{5.19}$$

where $a = 0.142$ nm is the lattice constant of graphite. From this relation it was concluded that in typical cases $n_{flake} \simeq 100$. Moreover, if the flake is not symmetric the height of the two maxima at $\theta = 0°$ and $\theta = 60°$ can be different [35]. The dramatic reduction of friction obtained by rotating the flake out of registry for a case with $n_{flake} = 54$ is shown in Fig. 5.22, where we compare the lateral force for $\theta = 0°$ and $\theta = 30°$. In the latter case the friction force is almost one order of magnitude smaller than for the commensurate case.

The possibility to achieve a range of states of very low friction when the flake is rotated out of the commensurate locking angle has very important practical consequences, because it implies that friction can be potentially controlled by the orientation of the two contacting surfaces. In fact, while a single-atom tip should show high friction for all orientations, an infinitely large contact would experience almost vanishing dissipation, expect for infinitely narrow angular ranges around perfect registry. In particular, one may speculate that

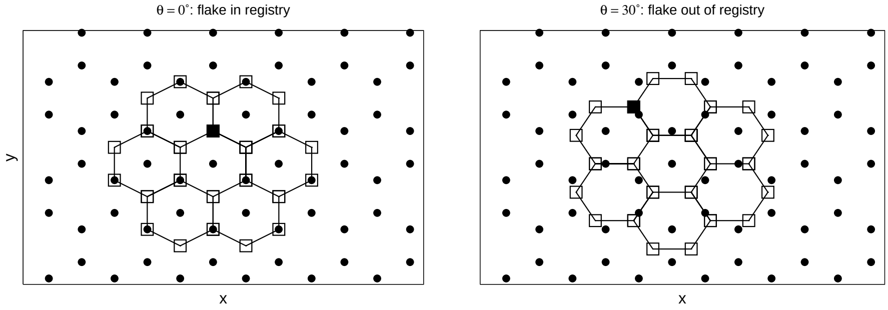

Figure 5.21: Two configurations of a graphite flake with $n_{flake} = 24$. The flake is formed by the squares connected by the solid line, while the filled circles indicate the positions of the atoms in the substrate. The flake on the left is commensurate with the substrate and corresponds to the configuration of maximum friction, whereas the flake on the right is out of registry and experiences very low friction. θ is the angle formed between the line parallel to the y axis passing through the CM of the flake and the line connecting the CM of the flake to the atom of the flake denoted by a filled square.

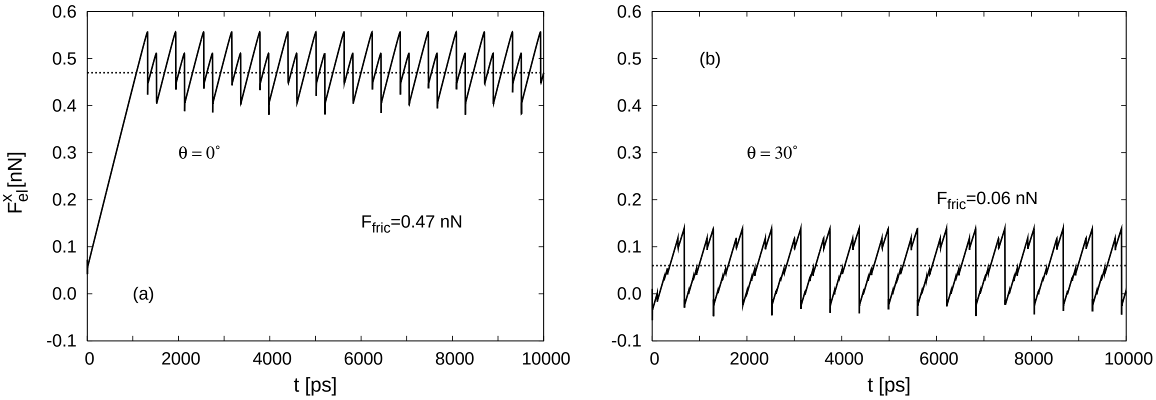

Figure 5.22: Time dependence of the lateral force for $\theta = 0°$ (a) and $\theta = 30°$ (b) for $n_{flake} = 54$ and $F_{load} = 100$ nN (solid lines). The dotted lines denote the value of the friction force (average of stick-slip signal) in the two cases. Notice that F_{fric} is almost one of order of magnitude smaller when $\theta = 30°$, in compliance with the results of Fig. 5.20.

in the macroscopic case, which involves multiple microcontacts with different sizes and orientations, a large fraction of the graphite-graphite contacts will be in a low-friction state, while only a small fraction will be in registry. This should lead to a tremendous reduction in the average friction force, experienced in the ensemble of microcontacts, and thus might explain the excellent lubrication of graphite.

However, in our simulations we found that for flakes loosely attached to the tip it is not always possible to keep the rotational coordinate θ under control. Specifically, we have observed that in some cases, a flake initially displaced out of registry tends to rotate back into a commensurate state ($\theta = 0°$) after a certain time t^*. This is clearly visible in Fig. 5.23(a), where the flake starts at $\theta = 30°$ and after some dynamical rearrangement it drops to $\theta = 0°$. We interpret this event as the effect of the torque exerted by the surface on a misaligned flake, which is attached to the tip sufficiently loosely to rotate. In fact, the torque plotted in Fig. 5.23(b) has a peak at the time $t = t^* \simeq 570$ ps at which the rotation of the flake takes place and causes a *dynamical locking* of the flake. This effect can significantly affect the friction force: a dynamical transition from low friction to high friction occurs when the flake rotates, as it is evident in Fig. 5.24. Just before the time t^*, the lateral force exhibits irregular sharp peaks, caused by the dynamic process of reorientation of the flake observed in Fig. 5.23. Interestingly, this phenomenon was also observed in the experiments: in the course of a few scan lines, the friction force restored

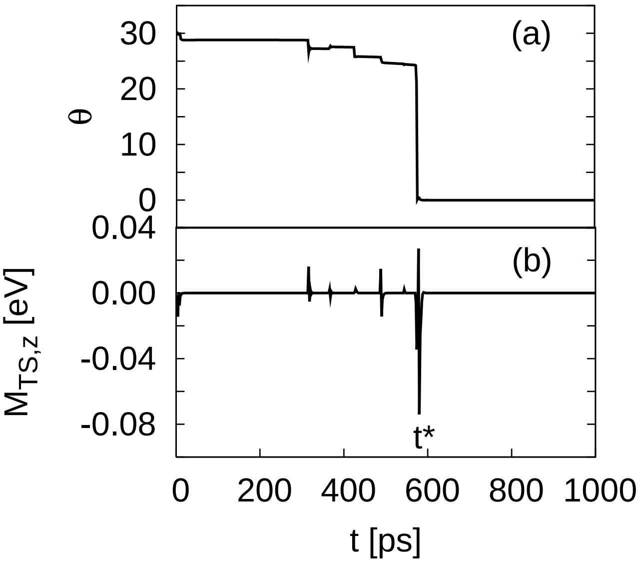

Figure 5.23: Time dependence of the angular coordinate θ (a) and of the torque $M_{TS,z}$ exerted by the tip-substrate force along z (b). At $t = t^*$ the angle θ, which starts at $\theta = \theta_0 = 30°$, drops to the value $\theta = 0°$ of a commensurate flake. Correspondingly, the torque has a sharp peak at $t = t^*$. Here $n_{flake} = 24$, $v_s = 0.4$ m/s and $F_{load} = 40$ nN.

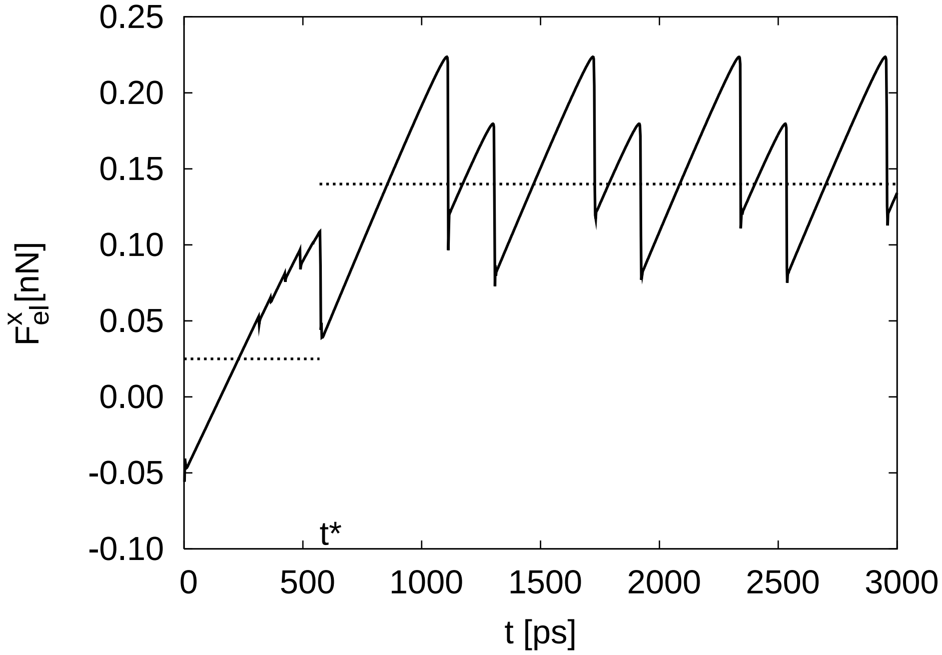

Figure 5.24: Time dependence of the lateral force (solid line) for the case illustrated in Fig. 5.23. Notice the transition from low to high friction at $t = t^* \simeq 570$ ps, where the flake rotates back to the commensurate state. The two horizontal dashed lines indicate the values of the friction force for $t < t^*$ ($F_{fric} = 0.025$ nN) and for $t > t^*$ ($F_{fric} = 0.14$ nN).

back to high values and, furthermore, reproducible measurements, such as those shown in Fig. 5.20(b), in which the same relative orientation always led to the same friction loops, were quite rare, the fixed-flake situation occurring as the exception rather than the rule [17, 27]. The dynamical nature of these findings is even clearer in Fig. 5.25(a), which shows the time dependence of the angle θ for the same situation as in Fig. 5.23(a), but for a velocity ten times larger: the transition time t^* is ten times smaller, implying that, in order to keep the initial alignment, very small scanning velocities have to be used. Moreover, the possibility to rotate crucially depends on the size of the flake: for $n_{flake} = 54$ we have not observed any reorientation on the time scale of our simulation (see Fig. 5.25(b)). We are currently investigating the origin and the implications of this intriguing rotational dynamics of the graphite flakes.

5.5 Relation between friction and surface diffusion

In this work, we have presented microscopic models to describe the dynamics of diffusion and friction on flat surfaces. Here we want to emphasize the conceptually common nature of this description for diffusion and friction. In fact, from a basic point of view, we

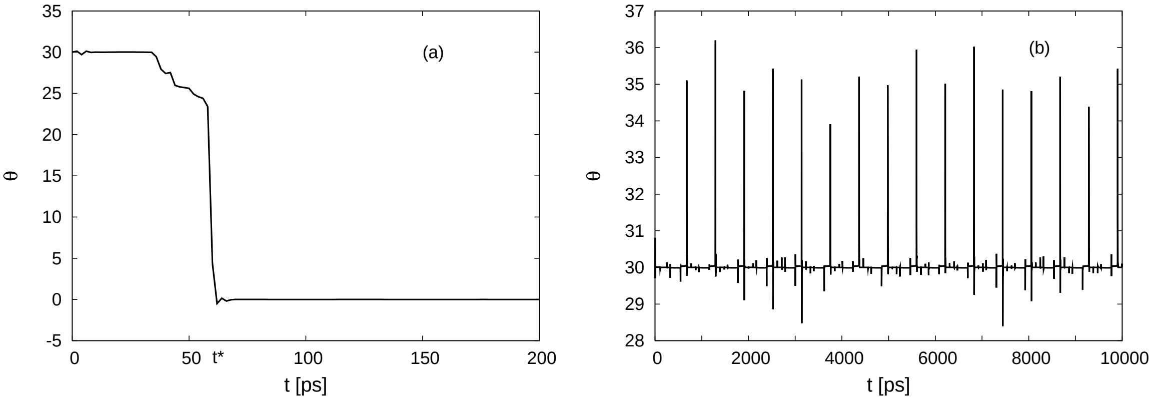

Figure 5.25: Time dependence of the angular coordinate for $n_{flake} = 24$, $F_{load} = 40$ nN and $v_s = 4$ m/s (a) and $n_{flake} = 54$, $F_{load} = 100$ nN and $v_s = 0.4$ m/s (b). The case shown in (a) is the same as that illustrated in Fig. 5.23(a), but with a scanning velocity ten times larger. Notice that here $t^* \simeq 57$ ps, which is ten times smaller than t^* found in Fig. 5.23(a). Thus we can argue that $t^* \propto 1/v_s$. For the larger flake in (b) no crossover to $\theta = 0°$ is observed on the time scale of the simulation. However, variations of the order of $5°$ around $\theta = \theta_0 = 30°$ periodically occur.

are dealing in both cases with the motion of few (interacting) adsorbates atoms over a corrugated potential: this is the essence of our treatment of these phenomena. Most importantly, the typical potential barriers encountered in AFM are of the same order of the barriers for surface diffusion of adsorbates [32].

Now we substantiate the above statement in a very simple way in the framework of the model of Fig. 5.3 used in our AFM simulation. If we set $K_x = K_y = 0$ and $F_{load} = 0$ in Eqs. (5.9)-(5.10), i. e. we remove the cantilever and we do not apply any external load, we are left with the problem of thermal diffusion of a cluster on a $2D$ substrate. For simplicity, we consider only a single atom, i. e. $n_{flake} = 1$. For this case we study the behaviour of the diffusion coefficient

$$D = \lim_{t \to \infty} \frac{< x^2 > + < y^2 > + < z^2 >}{6t} \tag{5.20}$$

as a function of temperature. From Sec. 2.4 we expect a Arrhenius behaviour of diffusion of the form

$$D = D_0 \exp(-E_a/k_B T). \tag{5.21}$$

This is indeed what we find from the simulations presented in Fig. 5.26(a), from which we extract the value of the activation energy E_a as the slope of the curve plotted in lin-log scale. For $\eta = 1$ ps^{-1} we obtain $E_a \simeq 2$ meV. Now we compare this value with the height of the barrier of the potential V_{TS} obtained by fixing z to the average value $< z > \simeq 0.33$ nm found in the simulations of thermal diffusion: the plot in Fig. 5.26(b) shows that the height of the potential V_0 is comparable to the activation energy E_a, thus underlining that the diffusion barrier is the same as the potential barrier in AFM experiments. In other words, *we might think of AFM as a driven diffusion process.*

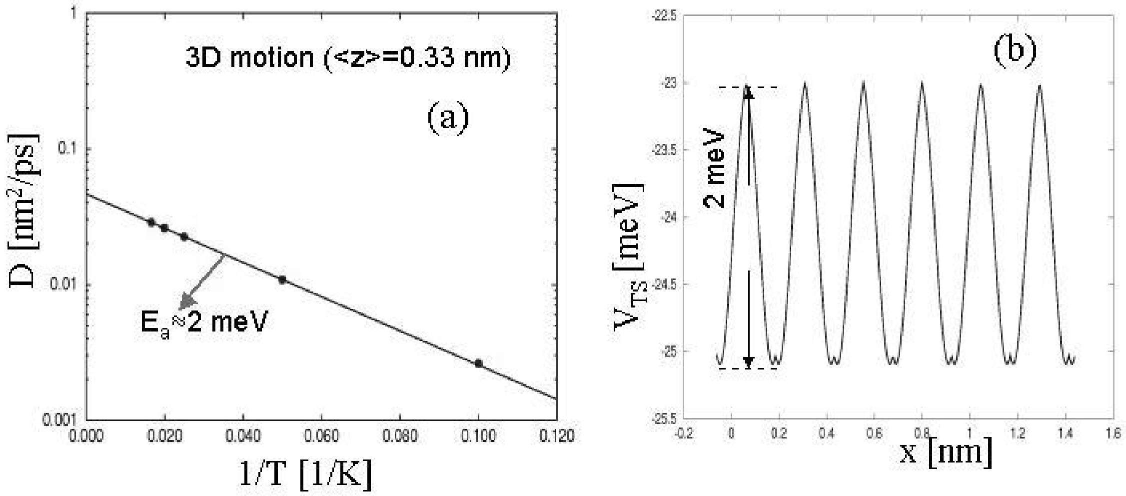

Figure 5.26: (a) Diffusion coefficient as a function of inverse temperature for $K_x = K_y = 0$ and $F_{load} = 0$. The circles are the points obtained by the simulations and the solid line is the Arrhenius fit from which the activation energy $E_a \simeq 2$ meV can be extracted. (b) Static calculation of the tip-surface potential as a function of x fixing z to the average value $< z >= 0.33$ nm found in the simulations of thermal diffusion. The value of the potential barrier V_0 from (b) is found to be the same as the activation energy E_a.

5.6 Discussion and conclusions

In this chapter we have introduced a microscopic model to simulate AFM dynamics at the nanoscale. Our atomistic description provides us with a powerful tool to understand the complex processes of energy dissipation taking place in the contact area between the tip and the surface, a region which is not easily accessible by experiments. The results of our simulations indicate a qualitative agreement with the experimental findings and emphasize the role of the dynamical effects of the tip on the frictional behaviour.

The ultimate goal of nanotribology is to control the frictional properties. We have discussed two ways by which this can be done. It is possible to drive a transition between sliding motion with low friction to stick-slip with high friction by increasing the applied load. Experiments have demonstrated that states of ultralow friction can be realized by this method [15]. Since we have shown that the surface corrugation depends itself on the load, a proper choice of the surface structure (characterized by a specific value of the corrugation) will lower the corrugation and thus will result in very low frictional forces. This is the case of graphite which we have analysed here. The second way is applicable to extended contacts, where the rotational degree of freedom with respect to the substrate is effective to achieve almost “superlubric” sliding. We would like to underline that both these ways are intended for *dry friction*, i. e. they do not rely on the presence of lubricants, which are commonly used to lower the friction between two macroscopic surfaces [1]. The effect of the interplay between translational and rotational motion of finite contacts on the frictional behaviour is also triggered by tribological properties of nanoscale systems such as C_{60} molecules [23] and nanotubes [36, 37], in which transitions from sliding-rotating motion to rolling motion have been observed, with very drastic corresponding changes in friction forces. Therefore, finding the dynamical conditions that reduce nanoscale friction could be very promising for the realization of nano- and micromachines. Furthermore, these concepts can find applications for the construction of nanodevices powered by biomolecular motors [38] and for molecular-based mechanical devices [39].

Finally, we would like to discuss our assumption of rigidity of the flake and of the substrate. Graphite consists of stacked sheets of carbon atoms, separated by a relatively large distance. The van der Waals force between sheets are weak when compared to the covalent bonding between atoms within the sheet. This causes a high Young's modulus in the direction parallel to the sheet. Calculations performed on double-walled nanotubes, where the outer layer incommensurably slides over the inner layer, for both rigid and relaxed layers, suggest that relaxation induces only moderate changes [40]. This is attributed to the extreme rigidity of the graphite layers and to the weakness of the interlayer interaction. Furthermore, experimentally observed rolling, rotating and sliding of carbon nanotubes on a graphite surface have been modelled assuming the nanotube to be rigid [37]. On the other side, we expect that dynamical effects related to the resonant coupling between interatomic vibrations and translational motion of the flake could be relevant at high sliding velocities.

Bibliography

[1] See for example F. P. Bowden and D. Tabor, *The Friction and Lubrication of Solids*, Clarendon Press, Oxford (1986).

[2] V. L. Popov, S. G. Psakhie, E. V. Shilko, A. I. Dmitriev, K. Knothe, F. Bucher and M. Ertz, Phys. Mesomechanics **5**, 17 (2002).

[3] F. P. Bowden and D. Tabor, *An Introduction to Tribology*, Anchor Press/Doubleday, Garden City (1973).

[4] K. L. Johnson, K. Kendall and A. D. Roberts, Proc. R. Soc. London, Ser. A **324**, 301 (1971).

[5] B. V. Derjaguin, V. M. Muller and Yu. P. Toporov, J. Colloid Interface Sci. **53**, 314 (1975).

[6] J. A. Greenwood and J. B. Williams, Proc. R. Soc. London, Ser. A **295**, 300 (1966); J. A. Greenwood, in *Fundamentals of Friction: Macroscopic and Microscopic Processes*, edited by I. L. Singer and H. M. Pollock, Kluwer Academic Publishers, Doordrecht (1992).

[7] S. Fujisawa, E. Kishi, Y. Sugawara and S. Morita, Phys. Rev. B **52**, 5302 (1995).

[8] S. Fujisawa, K. Yokoyama, Y. Sugawara and S. Morita, Phys. Rev. B **58**, 4909 (1998).

[9] M. Ishikawa, S. Okita, N. Minami and K. Miura, Surf. Sci. **445**, 488 (2000).

[10] N. Sasaki, M. Tsukada, S. Fujisawa, Y. Sugawara, S. Morita and K. Kobayashi, Phys. Rev. B **57**, 3785 (1998).

[11] W. Zhong and D. Tománek, Phys. Rev. Lett. **64**, 3054 (1990).

[12] M. R. Sørensen, K. W. Jacobsen and P. Stoltze, Phys. Rev. B **53**, 2101 (1996).

[13] U. D. Schwarz, O. Zwörner, P. Köster and R. Wiesendanger, Phys. Rev. B **56**, 6987 (1997).

[14] M. Enachescu, R. J. A. van den Oetelaar, R.W. Carpick, D. F. Ogletree, C. F. J. Flipse and M. Salmeron, Phys. Rev. Lett. **81**, 1877 (1998).

[15] A. Socoliuc, R. Bennewitz, E. Gnecco and E. Meyer, Phys. Rev. Lett. **92**, 134301 (2004).

[16] E. Gnecco, R. Bennewitz, T. Gyalog, Ch. Loppacher, M. Bammerlin, E. Meyer and H.-J. Güntherodt, Phys. Rev. Lett. **84**, 1172 (2000).

[17] M. Dienwiebel, G. S. Verhoeven, N. Pradeep, J. W. M. Frenken, J. A. Heimberg and H. A. Zandbergen, Phys. Rev. Lett. **92**, 126101 (2004).

[18] C. M. Mate, G. M. McClelland, R. Erlandsson and S. Chiang, Phys. Rev. Lett. **59**, 1942 (1987).

[19] J.-A. Ruan and B. Bhushan, J. Mater. Res. **8**, 3019 (1993).

[20] E. Liu, B. Blanpain, J.-P. Celis and J. R. Roos, J. Appl. Phys. **84**, 4859 (1998).

[21] R. Buzio, E. Gnecco, C. Boragno and U. Valbusa, Carbon **40**, 883 (2002).

[22] H. Hölscher, U. D. Schwarz, O. Zwöner and R. Wiesendanger, Phys. Rev. B **57**, 2477 (1998).

[23] K. Miura, N. Sasaki and S. Kamiya, Phys. Rev. B **69**, 075420 (2004).

[24] J. H. Los and A. Fasolino, Comp. Phys. Comm. **147**, 178 (2002); Phys. Rev. B **68**, 024107 (2003).

[25] R. Guantes, J. L. Vega, S. Miret-Artés and E. Pollak, J. Chem. Phys. **119**, 2780 (2003); H. Xu and I. Harrison, J. Phys. Chem. B **103**, 11233 (1999).

[26] Y. S. Leng and S. Jiang, Phys. Rev. B, **63**, 193406 (2001).

[27] M. Dienwiebel, PhD Thesis, University of Leiden, The Netherlands (2003).

[28] M. Hirano, K. Shinjo, R. Kaneko and Y. Murata, Phys. Rev. Lett. **78**, 1448 (1997).

[29] H. Hölscher, W. Allers, U. D. Schwarz, A. Schwarz and R. Wiesendanger, Phys. Rev. Lett. **83**, 4780 (1999); Phys. Rev. B **62**, 6967 (2000); H. Hölscher, A. Schwarz, W. Allers, U. D. Schwarz and R. Wiesendanger, ibid. **61**, 12678 (2000); U. D. Schwarz, H. Hölscher and R. Wiesendanger, ibid. **62**, 13089 (2000).

[30] S. Morita, S. Fujisawa and Y. Sugawara, Surf. Sci. Rep. **23**, 1 (1996).

[31] S. H. Ke, T. Uda, R. Pérez, I. Štich and K. Terakura, Phys. Rev. B **60**, 11631 (1999).

[32] E. Riedo, E. Gnecco, R. Bennewitz, E. Meyer and H. Brune, Phys. Rev. Lett. **91**, 084502 (2003).

[33] M. A. Lantz, S. J. O'Shea, A. C. F. Hoole and M. E. Welland, Appl. Phys. Lett. **70**, 970 (1997).

[34] P. E. Sheehan and C. M. Lieber, Science **272**, 1158 (1996).

[35] G. S. Verhoeven, M. Dienwiebel and J. W. M. Frenken, Phys. Rev. B **70**, 165418 (2004). bibitemmiura K. Miura, S. Kamiya and N. Sasaki, Phys. Rev. Lett. **90**, 055509 (2003).

[36] M. R. Falvo, R. M. Taylor II, A. Helser, V. Chi, F. P. Brooks Jr., S. Washburn and R. Superfine, Nature **397**, 236 (1999);

[37] A. Buldum and J. P. Lu, Phys. Rev. Lett. **83**, 5050 (1999).

[38] R. K. Soong, G. D. Bachand, H. P. Neves, A. G. Olkhovets, H. G. Craighead and C. D. Montemagno, Science **290**, 1555 (2000).

[39] J. K. Gimzewski, C. Joachim, R. R. Schlittler, V. Langlais, H. Tang and I. Johannsen, Science **281**, 531 (1998).

[40] A. N. Kolmogorov and V. H. Crespi, Phys. Rev. Lett. **85**, 4727 (2000).

Summary

This work presents an atomistic study of the motion of adsorbates on solid surfaces. Specifically, we consider from a theoretical perspective two important phenomena occurring at surfaces, namely *surface diffusion* and *atomic-scale friction*. Surface diffusion of atoms, molecules and clusters is a topic of great importance both from a fundamental point of view and for its technological applications, such as crystal growth and catalysis. When an atomic or molecular adsorbate diffuses, or is pulled, on a surface it unavoidably experiences friction, which opposes its motion. Therefore, surface diffusion and friction are two inextricably linked issues. Since the adsorbate typically extends over the length scale of nanometers, the simple, empirical laws of friction known for the macroscopic world do not hold. Thus, a microscopic explanation of these laws and an understanding of the fundamental mechanisms of diffusion and frictional dynamics of adsorbates at the atomic scale are called for, and have given rise to the field of *nanotribology*, i. e. the science of friction, wear and lubrication at the nanoscale. Due to the development of powerful experimental techniques in the last two decades, it has been possible to follow the dynamical details of surface diffusion (by Scanning Tunnelling Microscopy) and to study the frictional properties of single atomistic asperities in contact with flat surfaces (by Atomic Force Microscopy). In spite of this progress, a deep understanding of the dynamical mechanisms involved in these processes and a theoretical modelling of energy dissipation at the atomic scale are still a challenge. At this scale, in fact, a description based on purely linear, equilibrium theories is not possible, since the dynamics is dominated by highly nonlinear interatomic interactions, which are responsible for anomalous behaviour of the diffusion, for chaos and for nonlinear dependence of friction on sliding velocity and on loading force. The commensurability of the adsorbate to the substrate and its surface registry are also key ingredients that determine the diffusion dynamics and the frictional properties. The aim of the present work is to unravel, by means of simple theoretical models, the importance of nonlinear effects and of the interparticle interaction in the dynamical behaviour of adsorbates diffusing on periodic surfaces and to understand how the macroscopic laws of friction are modified at the nanoscale.

The above problematics are explained in Chapter 1, where we also review the experimental techniques and the computational methods to probe surface diffusion and to study nanoscale friction. In that chapter we introduce the models we have employed in our study, which have the advantage to be simple enough to allow a unified description of surface diffusion and frictional dynamics within the same theoretical framework. The treatment of thermal effects in computer simulations, which is crucial in surface diffusion, is discussed

and an effective way to include temperature as a heat bath coupled to a damping term, known as Langevin approach, is presented.

Chapter 2 illustrates the basic concepts of the diffusion of an adatom (e. g. an atom adsorbed on a substrate) on a periodic surface, with particular emphasis on the one-dimensional case. The adatom dynamics is studied comparing numerical results with existing analytical theories, both in the deterministic case (zero temperature) and at finite temperature. The expressions of the mobility of the adatom in the presence of an external driving force and of the diffusion coefficient in the case of purely thermal motion are derived in different damping regimes. At very low temperatures compared to the potential barrier, the adatom dynamics is activated by thermal fluctuations, and a rate description, first introduced by Kramers, can be applied. It is shown that in this regime the diffusion coefficient follows a Arrhenius behaviour. In the last part of the chapter we discuss the possible occurrence of long jumps in surface diffusion. This issue is of interest to understand the low-friction diffusional dynamics and it is still a matter of open debate.

Chapter 3 deals with the problem of interacting particles moving on a periodic surface. We consider a dimer, i. e. two coupled adatoms, in a one-dimensional sinusoidal potential. Even for this very simple case, complex features related to the interparticle adsorbate interaction are observed and the dynamics is strongly affected by the coupling between the translational motion of the dimer and the internal degrees of freedom. We start by studying the dynamics in the case of zero temperature and without damping, finding a rich dynamical behaviour as a function of the energy of the dimer: oscillatory and drift regime of the centre of mass are separated by a region of where the trajectory behaves in a chaotic fashion. The nonlinear aspects are also connected to resonance mechanisms between the vibrational and the drift motion of the adsorbate on the periodic potential. The role of the internal degrees of freedom has interesting consequences on the thermal diffusive dynamics, revealing deviations from the Arrenhius law. The relation between chaos and anomalous diffusion is also discussed.

In Chapter 4 we investigate the velocity dependence of atomic-scale friction. For a pair of macroscopic objects, friction is independent of their relative sliding velocity. However, at the nanoscale an appreciable dependence of friction on velocity can be found, and different and somehow contradictory results are available in the literature. We study this problem in the context of the Tomlinson model, which is widely used to describe the frictional dynamics. We characterize quantitatively the dependence of friction on velocity both at zero and finite temperatures, as a function of the damping, and in one and two spatial dimensions. Specifically, a power law behaviour with exponent $2/3$ is found in the athermal case and a logarithmic relation at finite temperatures. We present analytical arguments to justify these dependences and we underline the role of the surface potential in this problem.

Chapter 5 is devoted to a more realistic model to study nanoscale friction, which is applied to Atomic Force Microscopy on graphite. We focus on the load dependence of friction, which turns out to be nonlinear at variance with the behaviour of macroscopic systems, and which has the form of a power law with exponent larger than one. We propose a method to extract the effective surface potential as a function of the applied load and we establish a connection between friction and the interatomic potential. In the last part of the chapter we consider dynamical effects observed in the motion of extended flakes of graphite, where the role of surface registry is important to achieve very low friction. The connection to recent experimental works on this topic and the possibility to control friction without lubricants are discussed.

Samenvatting

In dit proefschrift wordt de beweging van op oppervlakken geadsorbeerde deeltjes op atomaire schaal bestudeerd. We zijn in het bijzonder geinteresseerd in twee aspecten, namelijk *oppervlaktediffusie* en *wrijving op atomaire schaal*. Oppervlaktediffusie van atomen, clusters en moleculen is van groot belang, niet alleen vanwege de fundamentele waarde maar ook om de technologische toepassingen zoals kristalgroei en katalyse. Een op een oppervlak geadsorbeerd atoom (adatoom) of molecuul dat diffundeert door thermische beweging of een externe kracht, zal onvermijdelijk wrijving ondervinden die de beweging zal tegengaan. Oppervlaktediffusie en atomaire wrijving zijn dan ook twee aspecten die nauw met elkaar zijn verbonden. De natuurwetten die wrijving in de macroscopische wereld beschrijven, zijn echter niet meer geldig in de microscopische wereld waar een geadsorbeerd deeltje een typische afmeting heeft van nanometers. Het is dus belangrijk om wrijving op het microscopische niveau beter te begrijpen, en meer inzicht te verkrijgen in de fundamentele mechanismen van diffusie en atomaire wrijving. Dit heeft geleid tot een heel nieuw onderzoeksgebied: *nanotribologie*, de wetenschap die zich bezig houdt met wrijving, slijtage en smering op de nanoschaal. Door de ontwikkeling van nieuwe, krachtige experimentele technieken gedurende de laatste twee decennia, is het nu mogelijk om de details van de dynamica van diffusie te volgen door middel van Scanning Tunneling Microscopy (STM), en om de eigenschappen van atomaire oneffenheden op vlakke oppervlakken te bestuderen door middel van Atomic Force Microscopy (AFM). Hoewel er dus reeds een grote vooruitgang is geboekt, ligt er nog steeds een uitdaging om de mechanismen van de dynamica van deze processen beter te begrijpen. Een andere uitdaging is het opstellen van een atomair model om het weglekken van energie te kunnen beschrijven. Op atomaire schaal is het niet meer mogelijk om een beschrijving te baseren op alleen lineaire evenwichtstheorieën omdat de dynamica wordt overheerst door sterke niet-lineaire wisselwerkingen tussen de atomen. Deze sterke niet-lineaire wisselwerkingen zijn verantwoordelijk voor chaotische gedrag, afwijkend gedrag van diffusie, en voor de niet-lineaire afhankelijkheid van wrijving als functie van de glijsnelheid en de drukkracht. De eigenschappen van diffusie en wrijving worden ook in hoge mate bepaald door het al of niet commensurabel zijn van het geadsorbeerde deeltje ten opzichte van het oppervlak. Dit proefschrift heeft als doel om, door middel van simpele theoretische modellen, het belang te ontrafelen van niet-lineaire effecten en van de wisselwerking tussen de geadsorbeerde deeltjes op hun dynamisch gedrag tijdens de diffusie, en om te begrijpen hoe de macroscopische wetten van wrijving zich verhouden tot wrijving op nanoschaal.

De hier bovenstaande problemen worden besproken in Hoodfstuk 1, waar ook een overzicht wordt gegeven van de beschikbare experimentele technieken en rekenkundige methoden om oppervlaktediffusie en wrijving op nanoschaal te onderzoeken. In datzelfde hoofdstuk worden tevens de door ons gebruikte modellen besproken, die als voordeel hebben dat ze eenvoudig genoeg zijn om een beschrijving van oppervlaktediffusie en wrijving binnen hetzelfde raamwerk mogelijk te maken. Verder laten we zien hoe temperatuursafhankelijke effecten kunnen worden meegenomen in de computerberekeningen. Temperatuursafhankelijke effecten spelen een cruciale rol in oppervlaktediffusie, en een effectieve manier om temperatuur te modelleren is de Langevin methode waarmee het systeem wordt gekoppeld aan een warmtebad.

Hoofstuk 2 illustreert de basisconcepten van diffusie van een adatoom op een periodiek oppervlak, waarbij de nadruk ligt op het één-dimensionale geval. De dynamica van het adatoom wordt bestudeerd door numerieke resultaten te vergelijken met bestaande analytische resultaten, zowel voor 0 graden Kelvin als voor hogere temperaturen. Uitdrukkingen voor de mobiliteit van het adatoom in de aanwezigheid van een externe drijvende kracht, en voor de diffusiecoëfficient in het geval van een zuivere thermische beweging, worden afgeleid voor verschillende dempingsgebieden. Als de temperatuur veel lager is dan de barriere, wordt de dynamica van het adatoom bepaald door thermische fluctuaties, en een beschrijving die voor het eerst werd opgesteld door Kramers is dan van toepassing. Er wordt aangetoond dat voor dit geval de diffusiecoefficient een Arrheniusgedrag vertoont. In het laatste deel van dit hoofdstuk bespreken we de mogelijkheid van het optreden van lange sprongen in oppervlaktediffusie, een onderwerp dat van belang is om de dynamica van diffusie in het geval van lage wrijving te begrijpen, en dat nog steeds een open kwestie is.

Hoofdstuk 3 is gewijd aan het probleem van twee wisselwerkende deeltjes die op een periodiek oppervlak bewegen. We beschouwen een dimeer, d.i. twee gekoppelde adatomen, die in een één-dimensionale, sinusoïde potential beweegt. Zelfs voor dit eenvoudige geval vinden we complex gedrag dat zijn oorsprong heeft in de wisselwerking tussen de adatomen. Het dynamische gedrag van het dimeer blijkt sterk beïnvloed te worden door de koppeling tussen de translationele en vibrationele vrijheidsgraden van het dimeer. Het hoofdstuk begint met het bestuderen van het gedrag van een dimeer in een periodieke potentiaal bij 0 graden Kelvin. Voor dit speciale geval vinden we dat het dimeer als functie van energie een zeer rijk gedrag vertoont, welke onder te verdelen is in drie verschillende regimes: een oscillerend en een drift regime, gescheiden door een regime waarin het dimeer chaotische gedrag vertoont. De niet-lineaire aspecten die gevonden worden, kunnen worden toegeschreven aan resonantiemechanismen tussen de vibratie modes en de driftbeweging van het geadsorbeerde dimeer. De vibrationale vrijheidsgraad van het dimeer heeft als interessante consequentie dat thermische geactiveerde diffusie gedrag vertoont dat afwijkt van Arrheniusgedrag. Verder wordt het verband tussen chaos en afwijkende diffusie ('anomalous diffusion') besproken.

In Hoofdstuk 4 wordt onderzocht hoe wrijving op atomaire schaal afhangt van snelheid. Voor twee macroscopische objecten hangt de wrijving niet af van hun onderlinge glijsnelheid. Op nanoschaal, echter, kan wrijving aanmerkelijk van de glijsnelheid afhangen. In de literatuur komen verschillende, en soms ook elkaar tegensprekende, resultaten voor. Wij bestuderen dit probleem binnen de context van het Tomlinsonmodel, dat veel gebruikt wordt om de dynamica van wrijving te beschrijven. Wrijving bij zowel 0 graden Kelvin als voor hogere temperaturen, wordt kwantitatief gekarakteriseerd op snelheidsafhankelijkheid in één en twee ruimtelijke dimensies als functie van de demping. Een machtsafhankelijkheid ('power law') met een exponent van 2/3 wordt gevonden voor 0 graden Kelvin. Voor hogere temperaturen wordt een logaritmische afhankelijkheid gevonden. De gevonden resultaten worden onderbouwd met een zorgvuldige analyse van het probleem, waarbij de rol van de potentiaal wordt benadrukt.

Het laatste hoofdstuk, Hoofdstuk 5, staat in het teken van een meer realistisch model om wrijving op de nanoschaal te bestuderen. Dit model wordt toegepast op AFM op grafiet. De nadruk ligt hierbij op hoe wrijving afhangt van de drukkracht. Deze afhankelijkheid blijkt niet-lineair te zijn, in tegenspraak met het gedrag van macroscopische systemen, maar kan beschreven worden door een machtsafhankelijkheid met een exponent groter dan 1. We stellen een methode voor om de effective oppervlaktepotentiaal te bepalen als functie van de toegepaste drukkracht, en we leggen een verband tussen wrijving en de potential tussen de atomen. Als laatste bespreken we dynamische effecten die zijn waargenomen in de beweging van vlokken van grafiet, waarbij de rol van het oppervlakteregister van belang is voor het bereiken van zeer lage wrijving. Het verband met recente experimenten aan dit soort systemen en de mogelijkheid om wrijving te kunnen beïnvloeden zonder het gebruik van smeermiddel wordt besproken.

List of publications

1. C. Fusco, P. Gallo, A. Petri and M. Rovere, *Random sequential adsorption and diffusion of dimers and $k-$mers on a square lattice*, Journal of Chemical Physics **114**, 7563 (2001).
2. C. Fusco, P. Gallo, A. Petri and M. Rovere, *Stretched exponential relaxation in a diffusive lattice model*, Physical Review E **65**, 026127 (2002).
3. C. Fusco, P. Gallo, A. Petri and M. Rovere, *Slow dynamics of $k-$mers on a square lattice*, Philosophical Magazine B **82**, 375 (2002).
4. C. Fusco, A. Fasolino, P. Gallo, A. Petri and M. Rovere, *Microscopic two-dimensional lattice model of dimer granular compaction with friction*, Physical Review E **66**, 031301 (2002).
5. C. Fusco, A. Fasolino and T. Janssen, *Nonlinear dynamics of dimers on periodic substrates*, European Physical Journal B **31**, 95 (2003).
6. C. Fusco and A. Fasolino, *Microscopic mechanisms of thermal and driven diffusion of non rigid molecules on surfaces*, Thin Solid Films **428**, 34 (2003).
7. C. Fusco and A. Fasolino, *Power-law load dependence of atomic friction*, Applied Physics Letters **84**, 699 (2004).
8. C. Fusco and A. Fasolino, *Diffusion and nonlinear dynamics of adatoms and dimers on periodic surfaces*, in “Modeling and Simulating Materials Nanoworld” (Advances in Science and Technology), edited by P. Vincenzini and F. Zerbetto, Techna Group, Vol. 44, pp. 293-300 (2004).
9. C. Fusco and A. Fasolino, *Dynamics and friction at the nanoscale: new phenomena and challenges*, in “Modeling and Simulating Materials Nanoworld” (Advances in Science and Technology), edited by P. Vincenzini and F. Zerbetto, Techna Group, Vol. 44, pp. 249-260 (2004).
10. C. Fusco and A. Fasolino, *Velocity dependence of atomic-scale friction: a comparative study of the one- and two-dimensional Tomlinson model*, Physical Review B **71**, 045413 (2005).

11. C. Fusco and A. Fasolino, *Nonlinear dynamics and surface diffusion of diatomic molecules*, to be published in ChemPhysChem.
12. S. Gonçalves, C. Fusco, V. M. Kenkre and A. R. Bishop, *Bistability and hysteresis in the sliding friction of a dimer*, submitted.

Curriculum Vitae

Claudio Fusco
born in Rome (Italy) on 11 June 1976

1990-1995	Secondary school at “Liceo Scientifico F. Enriques” in Rome
July 1995	Secondary school degree with mark 60/60
1995-2000	Physics studies at “Roma Tre” university in Rome
October 2000	Master’s Degree in Theoretical Physics *cum laude*
January 2001 - March 2005	Onderzoeker in opleiding (Junior scientist) at the department of Theoretical Physics, University of Njmegen. PhD project: Friction and diffusion dynamics of adsorbates at surfaces
May 2002	Award ”Best Master’s thesis of scientific faculties in Rome” in the academic year 2000-2001
September - November 2004	Visiting scientist at the University of New Mexico, Albuquerque (USA)

Acknowledgments

The work reported in this thesis has been carried out in the department of theoretical physics at the Radboud University Nijmegen. During the four years that I spent there, I enjoyed the stimulating international environment of the department, the weekly meetings, the seminars and the informal discussions, which have contributed to my scientific education. In particular, I would like to thank the people who have been closer to me in a more or less direct way: Jan Los, who has given me some useful hints for this work and who has developed the interaction potential that I have used for my simulations of friction on graphite (we still have an ongoing collaboration on this topic); Misha Katselson, our new group leader, whose ideas are always stimulating and with whom I had many interesting discussions about my work; Hubert Knops, who has given me some beneficial insights in statistical mechanics and who has supported me in many circumstances. I am also grateful to the experimentalists, from whom I could learn many things about friction in real systems, specifically Sylvia Speller, Markus Travaille and Jan Gerritsen, who showed to me "hot" AFM experiments in our university. Then, I would like to mention the people outside Nijmegen, with whom I have been in contact: Joost Frenken (Leiden University), who has enlightened me about very interesting experimental findings on friction on graphite, has supported me and with whom I had exciting discussions, and also other members of his group, i. e. Jinesh, Tjerk Oosterkamp and Martin Dienwiebel. Sergey Krylov has also been very illuminating on some theoretical aspects of surface diffusion and friction. Furthermore, I wish to thank Elisa Riedo for hosting me at the EPFL in Lausanne and for the interesting discussions we had during my stay there. I am grateful to the Consortium of the Americas for Interdisciplinary Science for the hospitality during my stay at the University of New Mexico and, in particular, V. M. Kenkre, Sebastian Gonçalves and Alan Bishop for the work we have been doing together. Since my work has been mainly based on computer simulations, many thanks go to the computer department C&CZ, providing our computer resources and always ready to solve any kind of problems. Marcella Haerkens, our secretary, has also been very helpful for technical and administrative questions. Finally, I would like to thank the Institute for Molecules and Materials (IMM), who has created an interdisciplinary environment at the university, underlining the contact areas between physics, chemistry and biology, and for giving me the opportunity to present my work in the annual symposium. Of course, I will not forget to mention my employer, the FOM, organizing many activities, in particular the annual meeting of Condensed Matter Physics, and without which this work would have never been possible.

The picture on the cover is entitled “Children play in the Roviana Lagoon at Munda, New Georgia in the Western Province of the Solomon Islands”. Photograph Jocelyn Carlin (2003). http://www.carlin.co.nz.
I would like to thank personally Jocelyn Carlin for her kind permission to use this suggestive picture for my thesis.